THE MECHANISM OF RADIATION-INDUCED NANOCLUSTER EVOLUTION IN OXIDE DISPERSION STRENGTHENED AND FERRITIC-MARTENSITIC ALLOYS

by

Matthew John Swenson

A dissertation

submitted in partial fulfillment

of the requirements for the degree of

Doctor of Philosophy in Materials Science and Engineering

Boise State University

August 2017

BOISE STATE UNIVERSITY GRADUATE COLLEGE

DEFENSE COMMITTEE AND FINAL READING APPROVALS

of the dissertation submitted by

Matthew John Swenson

Dissertation Title: The Mechanism of Radiation-Induced Nanocluster Evolution in Oxide Dispersion Strengthened and Ferritic-Martensitic Alloys

Date of Final Oral Examination: 17 May 2017

The following individuals read and discussed the dissertation submitted by student Matthew John Swenson, and they evaluated his presentation and response to questions during the final oral examination. They found that the student passed the final oral examination.

Janelle P. Wharry, Ph.D.	Co-Chair, Supervisory Committee
Hui Xiong, Ph.D.	Co-Chair, Supervisory Committee
Yaqiao Wu, Ph.D.	Member, Supervisory Committee
James Cole, Ph.D.	Member, Supervisory Committee

The final reading approval of the dissertation was granted by Janelle P. Wharry, Ph.D., Chair of the Supervisory Committee. The dissertation was approved by the Graduate College.

DEDICATION

The culmination of the effort to create this dissertation is dedicated to my wife, Sarah Swenson, and my parents, John and Lori Swenson. Both have made tremendous sacrifices and have provide endless encouragement to help me achieve goals for both my life and career. For their patience and belief in me, I am sincerely grateful.

ACKNOWLEDGEMENTS

The most important person to acknowledge for the success of dissertation is my advisor, Dr. Janelle Wharry. I am so grateful to have been aligned with her throughout this experience. She has been a relentless source of encouragement throughout the process, showing patience and willingness to listen to my new ideas. The times we have spent using each other as a sounding board for ideas will always be cherished. Dr. Wharry has taught me much about how to be a better writer, a disciplined scientist, and an improved leader of students.

Next, I must acknowledge my fellow students who were instrumental in my ability to learn new skills and navigate my way through graduate school. For the first two years of my time at BSU, Corey Dolph and I spent a great deal of time together in the lab and traveling to and from CAES in Idaho Falls. We enjoyed some good laughs, but most importantly grew up together in learning how to use the focused ion beam and transmission electron microscopy (TEM). For the past two years, Kayla Yano and I have spent a lot of time together advancing our TEM ability and applying in situ TEM mechanical testing. Kayla is such a quick learner, is easy to get along with, and has been an encouraging friend. I with her all the best in her future endeavors at Purdue University.

I want to extend my sincere gratitude to the faculty and staff in the Micron School of Materials Science and Engineering at BSU. From the very beginning, the MSMSE department has made me feel very welcome and secure, even as a non-traditional student.

Everyone makes me feel like they are glad I am here. This means a lot to someone who took the risk to give up a successful career in industry to come back to graduate school.

I would remiss to not acknowledge the staff of scientists for their above-and-beyond assistance in the Microscopy and Characterization Suite (MaCS) at the Center for Advanced Energy Studies (CAES) in Idaho Falls. Both Jatu Burns and Alyssa Bateman have taught me everything I know about operating the focused ion beam, while Yaqiao Wu has been my personal mentor in learning a variety of techniques on the transmission electron microscope. Yaqiao was also responsible for conducting all of the LEAP data analysis on my APT samples, enabling me to come home while this process was carried out. These people are so talented at what they do, but also a group of the most encouraging people I have ever worked with. I could always count on coming home with valuable data and progress after every trip I ever made to CAES. Finally, the Lab Manager, Joanna Taylor, has been one of my most prized working relationships, as she always ensured I accomplished all of my goals with every visit I made to MaCS.

Finally, several others have participated in my progress throughout the past four years. At the Michigan Ion Beam Laboratory (MIBL), the team of people including Anthony Monterrosa, Liz Getto, Shyam Dwaraknath, Ovidiu Toader, Fabian Naab, and Dr. Gary Was all helped greatly with the ion irradiation experiments.

This research was sponsored in part by the US Nuclear Regulatory Commission Grant NRC-HQ-84-14-G-0056, the Micron Foundation, and by the US DOE, Office of Nuclear Energy under DOE Idaho Operations Office Contract DE-AC07-05ID14517, as part of the Nuclear Science User Facilities experiments 13-419, 14-486, 15-540, 15-569, 16-625, and 16-720.

ABSTRACT

The objective of this study is to evaluate the mechanism of irradiation-induced nanoparticle evolution in a model Fe-9%Cr oxide dispersion strengthened steel and commercial ferritic-martensitic alloys HCM12A and HT9. Each alloy is irradiated with Fe^{2+} ions, protons, or neutrons to doses ranging from 1-100 displacements per atoms at 500°C. The morphology of nanoclusters are characterized using atom probe tomography. The evolution of clusters in each alloy are notably different with each irradiating particle, and the competing effects of ballistic dissolution and radiation-enhanced, diffusion-driven growth are attributed to the respective differences in cluster evolution. A phase evolution model, originally theorized by Nelson, Hudson, and Mazey, is used to simulate time-dependent nanocluster irradiation evolution in each alloy, with useful insights achieved to inform future alloy development. In all cases, a downward temperature shift is required to emulate low-dose-rate nanocluster evolution using higher-dose-rate irradiations.

TABLE OF CONTENTS

LIST OF TABLES

LIST OF FIGURES

LIST OF ABBREVIATIONS

APT	atom probe tomography
ATR	Advanced Test Reactor
b.c.c.	body-centered cubic
BSU	Boise State University
CAES	Center for Advanced Energy Studies
dpa	displacements per atom
EELS	electron energy loss spectroscopy
EFTEM	energy-filtered transmission electron microscopy
FEG	field emission gun
F-M	Ferritic-martensitic
FIB	focused ion beam
FWHM	full-width half maximum
GIXRD	glancing-incident angle x-ray diffraction
HRTEM	high-resolution transmission electron microscopy
ICF	image compression factor
INL	Idaho National Lab
IVAS	Integrated Visualization and Analysis Software
LSW	Lifshitz-Slyokov and Wagner
MIBL	Michigan Ion Beam Laboratory
NFA	nanofeatured ferritic alloy

ODS	oxide dispersion strengthened
PAS	positron annihilation spectroscopy
PKA	primary knock-on atom
SANS	small angle neutron scattering
SEM	scanning electron microscopy
SICRD	size-independent cascade re-dissolution parameter
SRIM	Stopping and Range of Ions in Matter
STEM	scanning transmission electron microscopy
TDC	Thesis and Dissertation Coordinator
TEM	transmission electron microscopy
TOF	time-of-flight
TTP	time-temperature-precipitation (isothermal transformation)
TTT	time-temperature-transformation
XAFS	x-ray absorption fine structure

CHAPTER ONE: INTRODUCTION

Advanced nuclear fusion and fission reactors have the potential to safely and reliably fulfill the growing worldwide energy demand. But these reactor designs demand their component materials (e.g. fission reactor cladding, fusion first wall and blanket structures) perform under extreme conditions, including temperatures up to 700°C and irradiation doses up to several hundred displacements per atom (dpa) [1–3]. Oxide dispersion strengthened (ODS) steels [4–13] and ferritic/martensitic (F-M) Fe-Cr b.c.c. alloys [11,14–21] are leading candidates for these applications because of their high-temperature strength and dimensional stability under irradiation.

The extreme performance of ODS steels is attributed to their high density of Ti-Y-O-rich nanoparticles, which: 1) act as localized sinks for point defects, providing resistance to irradiation swelling [4–6,8–10,12], and 2) strengthen the material without significantly compromising ductility. Since the properties and performance of ODS steels are highly dependent upon the oxide nanoparticles, it is imperative that the integrity of the nanoparticles under high temperature irradiation be well understood. Previous investigations have shown that irradiation can induce considerable morphological and chemical changes in the oxide nanoparticles [22]. However, a wide variety of irradiation-induced changes have been observed, making it difficult to discern the mechanisms of nanoparticle irradiation evolution.

In F-M alloys, a multitude of nanoscale irradiation-induced phases can be found. First are G-phase precipitates, rich in Si, Ni, and Mn, which have been reported in

commercial F-M alloys containing as low as nominally 9 wt% Cr, irradiated at temperatures between 400°C and 500°C [11,20,21,23–30]. Chromium-rich α' phases are also observed [11,20,24–29,31–33] and their formation predicted by computational approaches [34] in both commercial and high-purity Fe-Cr b.c.c. alloys at irradiation temperatures <500°C. Cu-rich nanoclusters are also observed to nucleate, often alongside G-phases [16,23–25,35], although their formation has been ascribed to the low solubility limit of Cu in Fe, rather than to irradiation.

Ion irradiations, including protons and heavier species, are widely utilized to emulate neutron irradiation effects in F-M and ODS alloys, especially to access irradiation damage levels ≥100 dpa [30,36–39]. Ions can deliver high irradiation damage rates in short experimental time frames, at lower costs, and with little to no residual radioactivity. However, questions remain about the ability of ions to comprehensively emulate the damage introduced by neutrons in a reactor environment. Studies on the efficacy of charged particles to emulate neutron damage have tended to focus primarily on void nucleation and growth. For example, Was, et al. [36] is able to obtain a relatively consistent void morphology in a commercial heat of F-M alloy HT9 between neutron and self-ion irradiations. But in the same study, the G-phase (Si-Ni-Mn-rich nanoclusters) morphologies are markedly different between irradiation types. Likewise, irradiation evolution of ODS oxide nanoclusters has also been noted to differ between neutron and ion irradiations [40].

Given that nanoclusters contribute significantly to the mechanical performance – especially under irradiation – of F-M [23] and ODS alloys [41], it is critical that we understand whether charged particle irradiations can appropriately emulate neutron

irradiation-induced nanocluster evolution. Charged particle and neutron irradiations have several key differences that affect resultant nano/microstructures: a) dose rates typically differ by at least two orders of magnitude, and b) differences in irradiating particle type introduce differences in damage cascade parameters. The consequences of these dose rate and damage cascade differences are largely unknown, particularly with respect to the mechanisms of nanocluster evolution. But attaining this mechanistic understanding is a vital step toward accomplishing the greater challenge of predicting the performance of ODS and F-M components over reactor lifetimes.

The objective for this dissertation is to determine the mechanism of radiation-induced nanocluster evolution in oxide dispersion strengthened and ferritic-martensitic alloys. A series of irradiation experiments are conducted, with characterization of the microstructure and cluster morphology measured. These results are coupled with cluster evolution modeling efforts to describe the observed cluster evolution as a result of each irradiation. Chapter 2 of this thesis will first outline the relevant background information, including details about the alloys in question, existing literature on the mechanisms and modeling of cluster evolution, and current experimental results of cluster evolutions. Chapter 3 outlines the objective of this thesis. Chapter 4 presents the detailed experimental procedures applied. The results of the irradiation and characterization experiments are presented in Chapter 5, while the detailed approach for the modeling efforts and analysis of the model results is outlined in Chapter 6. Chapter 7 reviews and discusses the experimental results and related interpretation of the model predictions, including limitations of the model. Finally, a set of conclusions and recommended future work are provided in Chapter 8.

CHAPTER TWO: BACKGROUND

Structural and cladding components in advanced nuclear reactor applications will be subjected to a high fluence of fast neutrons at temperatures higher than previous reactor designs. Damage from neutron bombardment in these applications is capable of producing considerable changes in the microstructure and mechanical properties of such components, impacting their long-term durability and useful life. Within prior generation reactors, structural and cladding components have been observed to experience undesirable irradiation-induced side effects including swelling, embrittlement, and enhanced creep. These changes in mechanical properties have been traced to irradiation-induced evolution in the microstructure, including the nucleation and growth of dislocation loops and voids, phase transformations, and composition gradients present at grain and sink boundaries.

A variety of advanced alloys are actively under development for structural and cladding applications for Generation IV nuclear reactors that will ideally provide enhanced resistance to neutron bombardment, leading to longer-term stability in their mechanical properties and increasing their useful life in these applications. The microstructure of these advanced alloys are generally distinguished by having a high sink strength for irradiation-induced defects, which is generally accomplished through the presence of smaller laths, high dislocation density, and/or nanoscale phases embedded within the matrix. Commercial ferritic-martensitic (F-M) alloys and ferritic oxide dispersion strengthened (ODS) alloys are considered candidates for these applications

due to their high temperature strengths and dimensional stability upon irradiation. Additionally, ODS and other nanostructured ferritic alloys (NFAs) contain a high density of nanoparticles, which: 1) act as localized sinks for point defects, providing resistance to irradiation swelling, and 2) strengthen the material without significantly compromising ductility. However, the long-term irradiation stability of the microstructure of these alloys is still not well understood, particularly the irradiation-induced evolution of nanoscale phases that may be present.

This chapter will provide an overview of the mechanisms of irradiation damage and its effects on b.c.c. Fe-based alloys, and the mechanisms of nanocluster evolution in an irradiation environment. An overview of commercial F-M and ODS alloys will be provided, including an assessment of existing literature covering irradiation-induced microstructure and nanocluster evolution.

2.1 Mechanisms of Irradiation Damage

The bombardment of neutrons onto a structural component in a nuclear reactor will induce the localized displacement of atoms within the microstructure of the target alloy. As a result, for the development of any alloys for nuclear reactors, a clear understanding of the irradiation response of the microstructure is required to validate an alloy for use. However, neutron irradiation experiments are time-consuming (10+ years in a fast neutron spectrum to accumulate up to 100 displacements per atom), extremely costly, and specimens become highly activated and thus difficult to handle and characterize [42]. In order to accelerate the evaluation process for F-M and ODS alloys, charged particles are increasingly being used to emulate neutron irradiations. Charged particle irradiations allow the possibility of conducting irradiation experiments within a

shorter time period (i.e. over a few hours or days) and will typically not cause activation of the material, accommodating faster turnaround in post irradiation examination and analysis. This section will provide an overview of the mechanism of irradiation damage accumulation, then discuss the relevant similarities and differences between neutron irradiation and charged particle irradiation experiments.

2.1.1 Irradiation Damage

Irradiation damage is incurred when an incident particle (i.e. neutron, proton, or ion) interacts with the atomic structure of the target alloy. The incident particle will initially translate through the matrix of the target material before eventually colliding with the nucleus of a target matrix atom (i.e. the primary knock-on atom, or PKA). If enough energy is transferred from the incident particle to the PKA, it will be dislodged from its original lattice position and relocated elsewhere with the matrix, likely as an interstitial defect. A corresponding vacancy defect remains at this original lattice position. The coupling of these interstitial and vacancy defects is referred to as a Frenkel pair (Figure 2.1). Furthermore, if the amount of energy transferred to the PKA is sufficiently high, the high-energy PKA will impact additional target matrix atoms, creating a chain reaction, or cascade, of multiple Frenkel pair defects.

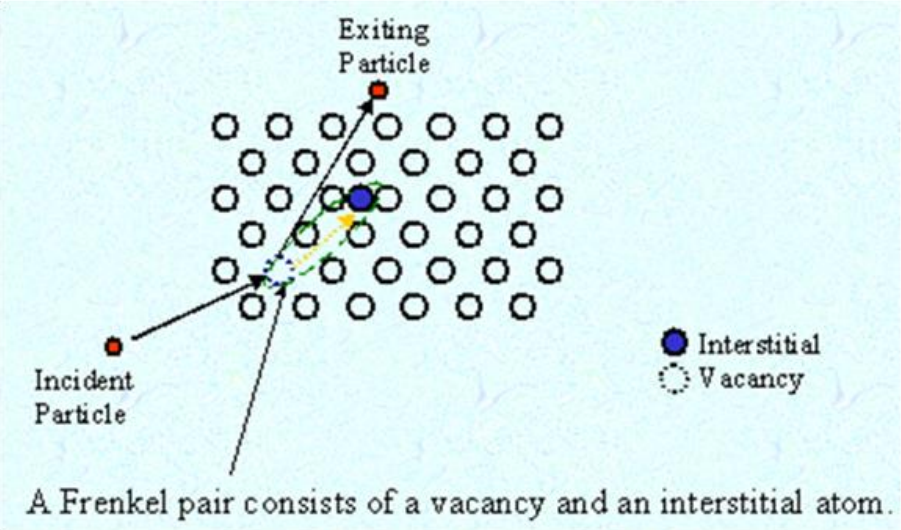

Figure 2.1. Illustration of Frenkel pair generation by an incident particle on a target alloy matrix, from [43]**.**

If a continuous fluence of incident particles is present, the generation of Frenkel pair defects will accumulate at a rate that is proportional to the particle fluence. The rate of damage accumulation is typically quantified in terms of displacements per atom per sec (dpa/s). When the fluence of incident particles is applied over a fixed period of time, the resultant dose (in dpa) may be determined.

Through the ongoing accumulation of Frenkel pair defects during irradiation, a non-equilibrium, higher concentration of vacancy and interstitial defects will result. Given that most alloying solutes in F-M and ODS alloys diffuse via the vacancy diffusion mechanism [42], a higher concentration of vacancies will result in radiation-enhanced diffusion rates for each of the substitutional solutes. The vacancy defects also have the ability to diffuse within the matrix of the material. The diffusion of each vacancy defect may result in one of the following: 1) recombination with an existing interstitial defect, 2) clustering with other vacancy defects to create voids or dislocation loops, or 3) migration to a sink where it may become "trapped" and is no longer mobile. The relative likelihood of each of these results depends upon many factors in the irradiation process.

2.1.2 Charged Particles as Surrogates for Neutron Irradiation

Charged particle irradiations offer several opportunities for earlier verification of alloys under development for structural and cladding applications. Higher dose rates enable faster turnaround time for irradiation experiments, which provides the opportunity to gain information about the irradiation response of alloys much quicker. With the ability to conduct experiments more quickly, development through iterative experiments and ultimately the complete design cycle may be expedited, potentially saving large amounts of product development resources. Despite these important benefits, it is critical to recognize that some inherent differences exist between in-lab charged particle irradiation experiments and the in-reactor neutron irradiation environment components will be exposed to. In particular, the irradiation dose rate, depth profiles, and damage cascade morphologies all differ widely between proton, self-ion, and neutron irradiation. Currently, there is limited understanding of the significance of these physical differences and how they manifest in the resultant microstructure and mechanical properties of F-M and ODS steels.

As charged particles such as protons or Fe^{2+} self-ions are incident on the target alloy, the inherent charge of the ions will encounter coulombic interactions with both the positive charged nuclei and negatively charged electron clouds of the target matrix atoms. These coulombic effects will tend to naturally reduce the momentum of the incident particle, until the particle eventually collides with the PKA. This reduction in momentum will limit the depth that each particle is able to translate through the matrix before colliding with the PKA. The displacement damage caused by charged particle irradiations may be calculated using the Stopping and Range of Ions in Matter (SRIM) [44], which is

a Monte Carlo simulation of incident ion interactions with the target. The representative depth profiles of irradiation with either 5 MeV Fe^{2+} ions or 2 MeV protons on a target Fe-9%Cr alloy using are provided in Figure 2.2. Upon irradiation with 5 MeV Fe^{2+} ions, the damage will be limited to only the top ~1-1.5 μm of depth. Likewise, upon proton irradiation with 2 MeV protons, the damage is limited to a depth of ~20 μm. On the other hand, neutrons are charge neutral and do not encounter these same coulombic interactions with the target matrix atoms. Accordingly, the momentum of the incident neutron encounters little resistance to impede its inertia and will translate through the target material until colliding with the PKA at a random depth. The result of neutron irradiation is a generally flat damage profile through the thickness of the material (Figure 2.2).

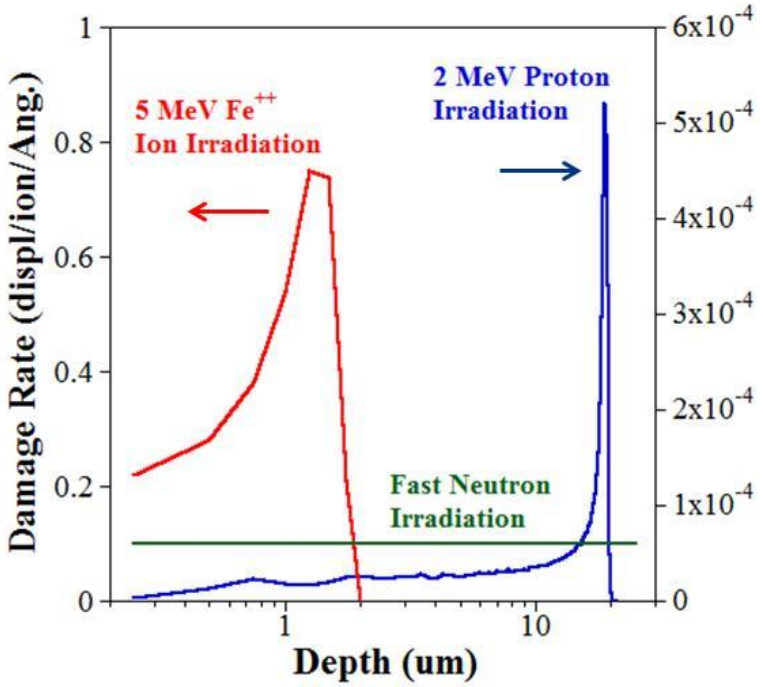

Figure 2.2. Simulated damage profiles for 5.0 MeV Fe^{++} ions and 2.0 MeV protons incident on Fe-9%Cr, with a flat neutron damage profile of arbitrary magnitude for reference, from SRIM [44].

It has been estimated that different irradiating particles, and their respective momentums at the time of incidence, are responsible for generating different morphologies of damage cascades [42] and in some cases (e.g. protons), generate only Frenkel pair damage rather than damage cascades [45]. The cascade process has been studied extensively by molecular dynamics simulations [46–48], and these studies consistently reveal intricate and complex cascade shapes that are dependent not only on the particle type, but also on its energy and the target composition. Furthermore, the extent of damage remaining in the material following cascade collapse is not easily quantifiable relative to the size or expanse of the original cascade. In short, for a given set of experimental parameters, it is not easy to understand damage cascade formation and evolution without conducting cascade dynamics simulations. A simplified approximation may be applied based on the work of Norgett, et al. [49] and Lindhard [45,50,51] and summarized in [42], in which the relative size, l (i.e. effective diameter) of a single damage cascade for each irradiation condition may be estimated using [42]:

$$l = 2\left(\frac{3}{4\pi}\frac{E_D}{U_a N}\right)^{1/3} \tag{2.1}$$

where U_a is the energy per atom (~0.3 eV [42]), N is the atomic density of the target (85.2 atoms/nm^3 for b.c.c. Fe). The damage energy (E_D) of the cascade may be approximated as [42]:

$$E_D = \frac{T}{1+k_N g} \tag{2.2}$$

For Eq. 2.2, T is the energy transferred to the primary knock-on atom (PKA), while k_N and g are each a numerical approximation given by [42]:

$$k_N = 0.1337 Z_1^{1/6}\left(\frac{Z_1}{A_1}\right)^{1/2} \tag{2.3}$$

and

$$g = 3.4008\varepsilon_N^{1/6} + 0.40244\varepsilon_N^{3/4} + \varepsilon_N \quad (2.4)$$

in which Z_1 and A_1 are the atomic number and atomic weight, respectively, of the incident particle. The value for ε_N may be calculated as [42]:

$$\varepsilon_N = \left(\frac{A_2 T}{A_1 + A_2}\right)\left(\frac{a}{Z_1 Z_2 \varepsilon^2}\right) \quad (2.5)$$

where Z_2 and A_2 are the atomic number and atomic weight, respectively, of the target atoms (Fe), ε is the unit electronic charge (1.44 eV·nm). The screening radius (a) is calculated by [42]:

$$a = \left(\frac{9\pi^2}{128}\right)^{1/3} a_0\left(Z_1^{2/3} + Z_2^{2/3}\right)^{-1/2} \quad (2.6)$$

in which a_0 is the Bohr radius (0.053 nm). The values for each of these variables and the estimated effective diameter of cascades resulting from common irradiating particles are given in Table 2.1. By this estimation, the cascades resulting from proton irradiation are the smallest (~2.3 nm), while those from Fe^{2+} irradiation are larger (~6.8 nm), and typical cascades created by fast neutron irradiation are the largest at ~10.4 nm. One should note that this volume does not describe a true irradiation damage *cascade* that envelops the region, but rather describes a space over which Frenkel pairs are produced.

Table 2.1 Summary of calculation variables and estimated effective diameter for different irradiating particles.

Irradiating particle	***PKA Energy,T* (eV), from** [42]	***Screening Radius, a* (nm)**	ε_N	k_N	g	***Cascade Damage Energy,* E_D (eV)**	**Estimated effective cascade diameter,** l **(nm)**
1 MeV electrons	60	0.016	60.00	0.000	75.4	60	1.65
2 MeV protons	200	0.015	0.026	0.134	1.90	159	2.28
5 MeV Fe2+	5000	0.009	0.004	0.157	1.34	4134	6.76
Fast neutrons	35000	0.015	4.520	0.134	10.1	14857	10.36

2.2 Ferritic-Martensitic Alloys

High-Chromium (9-12%) ferritic-martensitic (F-M) alloys have been in use as early as 1912. At that time, it was discovered that Fe-based alloys with such high Cr content were resilient against rusting, while also producing a hard and sharp cutting edge. As a result, F-M alloys were first used in knife and blade applications [11]. Later, in the 1930's, it was discovered that adding solutes to F-M alloys, including small amounts of C (<0.1%), Mo, W, V, Nb, and N, would yield increased creep-rupture strength and further improve resistance to corrosion and oxidation. With these improvements, F-M alloys have found many uses in a variety of applications including chemical plants, gas turbines, boilers, steam power plants, aircraft/aerospace, and nuclear reactor components [11].

More recently, in the 1970's, interest in use of F-M steels in nuclear reactor applications increased even further. At that time, austenitic stainless steels were the prominent materials of choice for fuel and cladding applications, but were found to exhibit swelling over long periods of exposure to irradiation [11]. On the other hand, F-M

alloys have demonstrated much better resistance to swelling, while also having a higher thermal conductivity and lower coefficient of thermal expansion [11]. For these reasons, F-M steel alloys are considered more viable alternatives for structural components in advanced nuclear reactors moving forward.

As the development of F-M alloys advances, many factors in the metallurgy of these alloys will influence the macroscopic properties and performance of the materials. In this section, an overview of the metallurgical considerations will be presented, along with reflection on the limitations of F-M alloys and the current developmental directions.

2.2.1 Physical Metallurgy

Ferritic-martensitic alloys are generally produced following a three step process: 1) austenitizing at elevated temperature, 2) transformation from austenite to martensite via rapid cooling to room temperature, and 3) tempering at a moderately elevated temperature to obtain desirable microstructure and macroscopic properties [11]. Within this framework, many variables may be adjusted in the alloys and the production process to enable "tuning" of the properties to help meet desired requirements.

The equilibrium phase diagram of the Fe-Cr system is shown in Figure 2.3. High Chromium (9%) F-M alloys will generally have an austenitic structure (γ-phase) at temperatures between 850 - 1200°C, with the γ-phase loop extending out to approximately 12% Cr [11]. This loop can be extended to entail higher Cr contents through alloying with elements such as C, N, Ni, Mn, Cu, and Co, while addition of elements including Mo, Nb, V, W, Si, Ti, and Al will reduce the Cr limit of this loop [11].

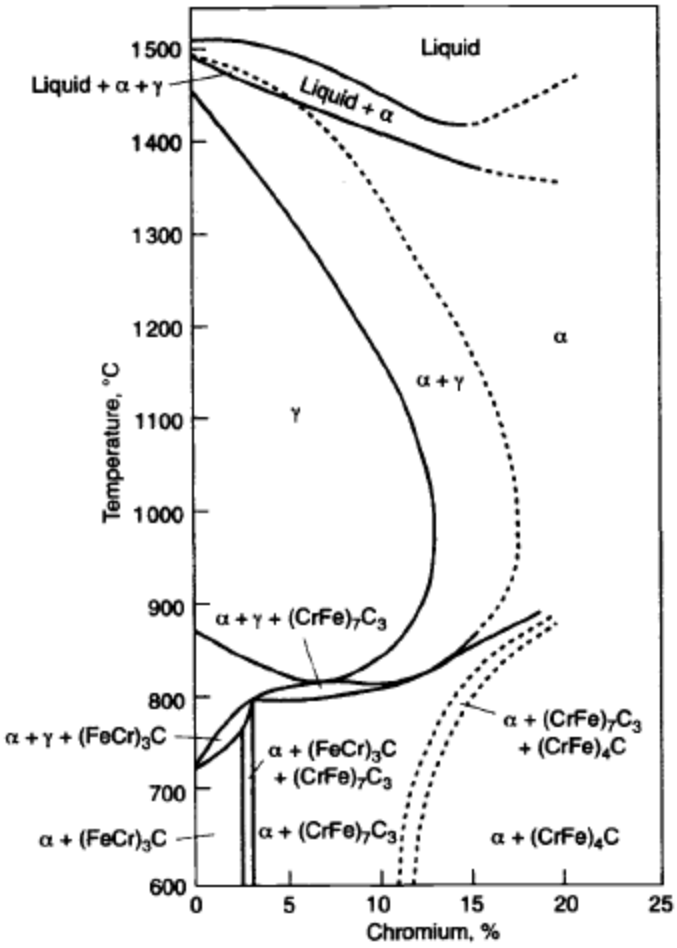

Figure 2.3. Fe-Cr equilibrium phase diagram, from [11]**.**

The resultant phases following the rapid cooling of an austenized F-M alloy will also depend upon the solute content of the alloy. The predicted phases are illustrated by the Schaeffler-Schneider diagram in Figure 2.4, in which phase boundaries are differentiated by the relative Ni-equivalent and Cr-equivalent of the alloying components, which may be calculated using [11]:

$$Ni\ equivalent\ (wt\%) = (\%Ni) + (\%Co) + 0.5(\%Mn) + 0.3(\%Cu) + 30(\%C) + 25(\%N) \quad (2.7)$$

$$Cr\ equivalent\ (wt\%) = (\%Cr) + 2(\%Si) + 1.5(\%Mo) + 5(\%V) + 1.75(\%Nb) + 0.75(\%W) + 1.5(\%Ti) + 5.5(\%Al) + 1.2(\%Ta) + 1.2(\%Hf) +$$

$$1.0(\%Ce) + 0.8(\%Zr) + 1.2(\%Ge) \quad (2.8)$$

Depending on the solute content of the alloy, the resultant microstructure upon cooling may be a combination of martensite (α'), ferrite (δ), or austenite (γ).

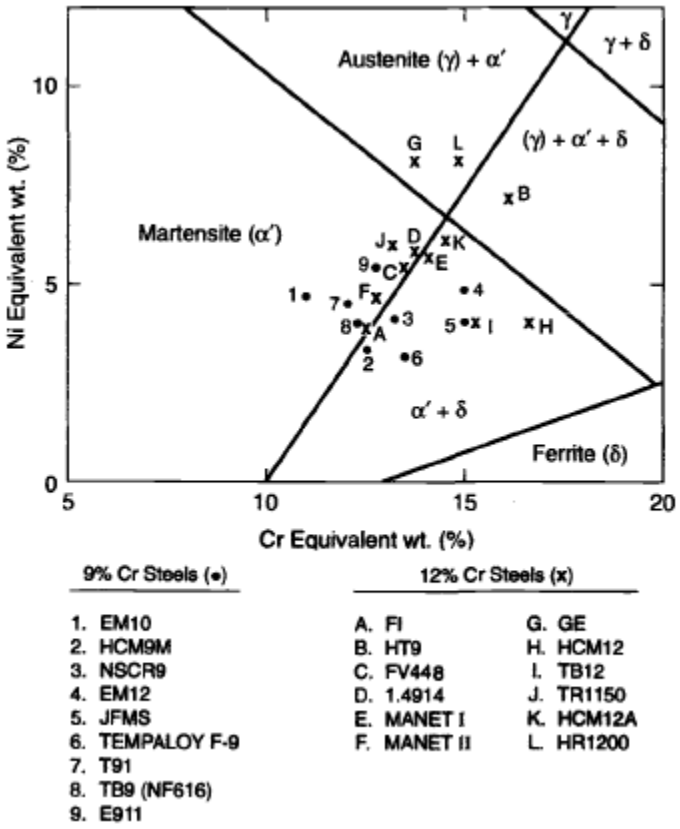

Figure 2.4. Schaeffler-Schneider diagram, predicting resultant microstructure following rapid cooling from austenite based on Ni-equivalent and Cr-equivalent content, from [11]**.**

Another key consideration when alloying F-M steels is controlling the start and finish temperatures of the martensitic transformation, which must be maintained above room temperature, ensuring full transformation will occur upon cooling. Generally, the addition of solutes will lower both the start (M_s) and finish (M_f) temperatures of the martensitic transformation, thus, there are limits to the amount of alloying which is feasible. For F-M alloys, M_s typically ranges from 250° - 350°C, while M_f ranges from 80° - 190°C [11].

A representative isothermal transformation (TTT) diagram for a 12Cr-MoVNb ferritic-martensitic alloy is illustrated in Figure 2.5. In this case, the nose of the pearlite transformation region is at approximate 700°C at an isothermal cooling time of almost 10^4 seconds (~2 hours). Since this is a relatively long duration, it is possible to use air cooling to facilitate the transformation from austenite (A) to martensite (M), without any formation of pearlite (P) or bainite. And, since air cooling is a slower process than traditional water or oil quenching, the martensitic microstructure will result in laths which are thicker than typical rapid quenched steels [11].

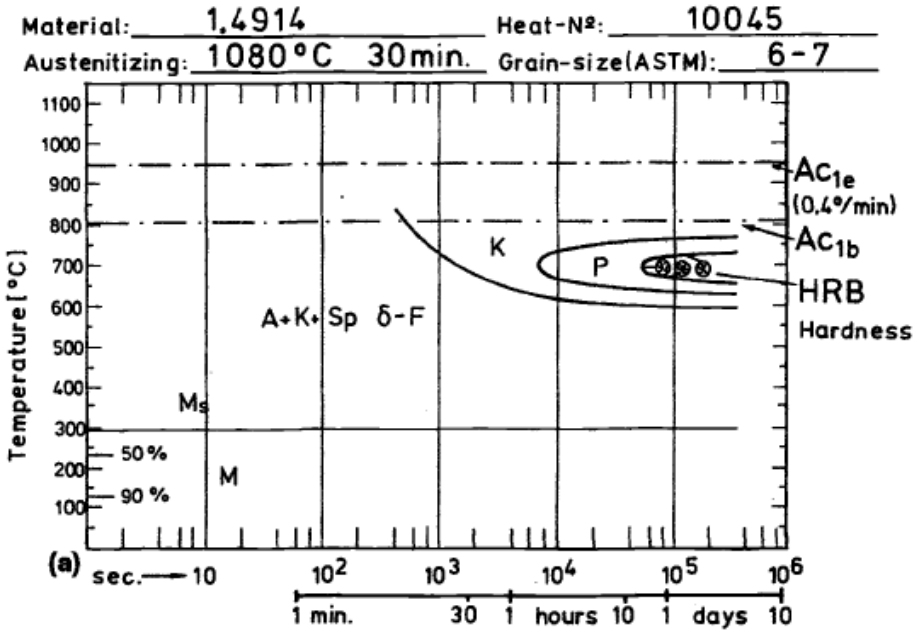

Figure 2.5. Isothermal transformation (TTT) diagram for 12Cr-MoVNb martensitic steel (A = Austenite, K = Carbide, Sp δ-F = Trace of ferrite, M = Martensite, P = Pearlite, Ac_{1b} = Start of austenite formation on heating, Ac_{1e} = Completion of austenite formation on heating), from [11]**.**

Once the transformation to a martensitic structure is completed, the material is brittle and generally not useful. A tempering process is necessary to enable recrystallization of the microstructure and obtain more desirable and useful properties. In order to avoid re-austenitizing of the material, the temperature of the tempering process

needs to be below the point at which austenite formation (Ac_1) will start (ref. Figure 2.5). It is important to recognize that addition of alloying elements will also influence Ac_1, thus affecting the range of temperatures available for the tempering process. A summary of the alloying species influence on austenite formation temperature (Ac_1) is provided in Table 2.2. Typical temperatures for Ac_1 in F-M steels range from 760 - 850°C, while typical values for the completion of austenite transformation upon heating (Ac_3) range from 870 - 960°C [11].

Table 2.2 The influence on austenite formation temperature upon heating by several alloying elements, from [11]**.**

Element	**Change in Ac_1 (°C) per mass %**
Ni	-30
Mn	-25
Co	-5
Si	+25
Mo	+25
Al	+30
V	+50

In the end, the tempering temperature may also be strategically selected to induce different types of microstructure development. Softening due to tempering at temperatures below ~500°C will be slow, but increases dramatically at temperatures in the range between 500° - 550°C as annealing is more pronounced [11]. At temperatures above 550°C, the response of the microstructure will be a combination of annealing (i.e. softening) along with precipitation of secondary phases including $M_{23}C_6$ carbides or nitrides such as VN or Nb(CN), which contribute to hardening of the alloy [11]. In

general, the extent of precipitation will depend on the tempering temperature and the amount of C and N in the alloy (e.g. higher C or N content will give way to more precipitation) [11]. The final microstructure will consistent of tempered martensitic laths decorated with $M_{23}C_6$ particles along the prior austenite and ferrite grain boundaries. Finer precipitates may also be found either within the laths or on the boundaries of the martensitic laths and subgrains [11].

2.2.2 Limitations & Development

Advanced Generation IV nuclear fission reactors are expected to operate at temperatures potentially as high as 700°C. Therefore, materials utilized in reactor core applications as fuel cladding and structure components will need to exhibit long-term thermal stability (along with irradiation resistance) at these extreme conditions. In the case of high-chromium ferritic-martensitic steels, the application of aging and creep straining at temperatures from 400° - 750°C leads to further precipitation of several possible new phases in the microstructure (summarized in Figure 2.6) [11]. One notable group of secondary phases that develop are the Laves phases, which typically nucleate and grow at temperatures ranging from 450° - 650°C. Isothermal time-temperature-precipitation (TTP) diagrams are provided for several F-M steels in Figure 2.7. The nose of the curves for T91 and HT9 are at approximately 550° to 600°, which gives way to precipitation of laves phases in these alloys after only ~2 hours of operation at these temperatures. Another example of an isothermal TTP diagram for P92 (NF616) is provided in Figure 2.8. In this case, curves representing increasing amounts of laves phase precipitation are calculated to show that, depending on the aging temperature, the phase amount increases to an equilibrium value.

Precipitate Phase	Crystal Structure and Lattice Parameter	Typical Composition	Distribution of Precipitates
$M_{23}C_6$	fcc a =1.066 nm	$(Cr_{16}Fe_6Mo)C_6$ $(Cr_4Fe_{12}Mo_4Si_2WV)C_6$	Coarse particles at prior austenite grain and martensite lath boundaries and fine intra-lath particles
MX	f.c.c. a = 0.444-0.447 nm	NbC, NbN, VN, (CrV)N, Nb(CN) and (NbV)C	Undissolved particles and fine precipitates at martensite lath boundaries
M_2X	Hexagonal a = 0.478 nm c = 0.444 nm	Cr_2N, Mo_2C and W_2C	Martensite lath boundaries (Cr_2N and Mo_2C); prior austenite grain boundaries (Mo_2C); intra-lath (Mo_2C and W_2C); δ-ferrite in duplex steels [Cr_2 (CN) and $(CrMo)_2(CN)$]
Z-phase	Tetragonal a = 0.286 nm c = 0.739 nm	(CrVNb)N	Large plate-like particles in the matrix after creep straining at 600°C
η-carbide	Diamond cubic a = 1.07-1.22 nm	M_6C $(Fe_{39}Cr_6Mo_4Si_{10})C$	Prior austenite grain and martensite lath boundaries and intra-lath
Vanadium carbide	f.c.c. a = 0.420 nm	V_4C_3	Low number density in matrix
Laves	Hexagonal a = 0.4744 nm c = 0.7725 nm	Fe_2Mo Fe_2W and $Fe_2(MoW)$	Prior austenite grain and martensite lath boundaries and intra-lath; δ-ferrite in duplex steels
Chi (χ)	b.c.c. a = 0.892 nm.	$M_{18}C$ or $Fe_{35}Cr_{12}Mo_{10}C$	Intra-martensite lath; δ-ferrite in duplex steels

Figure 2.6. Precipitation phases observed in tempered, aged, and creep-rupture tested ferritic-martensitic steels, from [11]**.**

Based on the manifestation of precipitates at higher operating temperatures, F-M steels are typically limited in thermal creep-rupture strengths above ~550°C [11] and are currently only approved for applications operating below these temperatures. Further development of F-M alloys continues to strive to increase this threshold, particularly in light of goals for advanced nuclear reactors to operate at temperatures as high as 700°C.

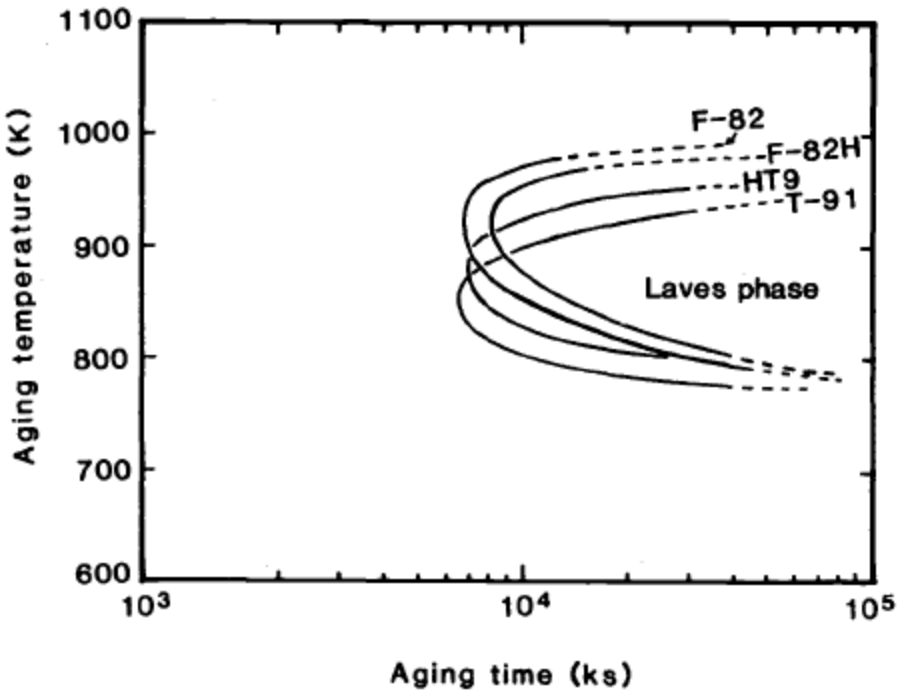

Figure 2.7. Isothermal TTP curves for laves phases in several ferritic-martensitic steels, from [11]**.**

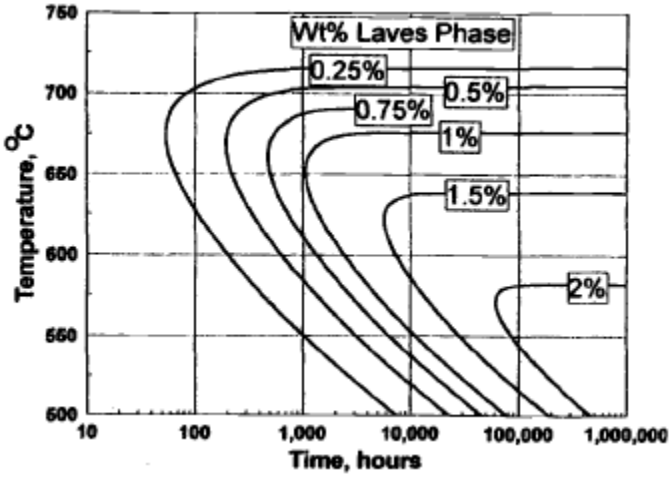

Figure 2.8. Isothermal TTP curves for laves phases in P92 (NF616) steel, from [11]**.**

In summary, it has been shown that the relative amounts of alloying solutes in high-chromium F-M steels will greatly influence a multitude of properties including the:

a) Austenite solubility limit of Cr (Figure 2.3)

b) Resulting phases (α', γ, and δ) after the austenite-to-martensite transformation (Figure 2.4)

c) Martensite transformation temperatures (M_s and M_f) upon cooling

d) Austenite transformation temperatures (Ac_1, Ac_3) upon heating (Table 2.2)

e) Phases of precipitates and relative amounts formed during tempering

f) Phases of precipitates and relative amounts formed upon aging and creep straining (Figures 2.6, 2.7, and 2.8).

Based on these strong dependencies on alloying content, much of the future development of F-M alloys is aimed at the elemental tailoring of the alloying elements to achieve the following goals [11]:

1) Optimize the final constituents, particularly the δ-ferrite content (e.g. adding Cu, Co).
2) Maximize the solid solution strengthening (e.g. adding W, Mo, N).
3) Stabilize the martensite dislocation structure and $M_{23}C_6$ precipitates (e.g. adding B).
4) Enhance dispersed precipitate strengthening with fine VN or Nb(CN), which are more resistant to coarsening during ageing.
5) Reduce activation by replacing higher activation elements including Mo, Nb, and Ni with more resistant elements such as W, V, Mn, Si, Ta, and Ti.

Although these are important directions for research and development, F-M steels are unlikely to be approved for applications at dramatically higher temperature limits within the foreseeable future [11]. As a result, variations of F-M steels containing small, nanoscale particles have gained more attention due to their increased strength and stability at higher temperatures. The next section will provide an overview of how the development of ODS alloys has complemented F-M steels, potentially presenting a

solution to the requirement for irradiation-resistant structural materials capable of operating at higher temperatures.

2.3 Oxide Dispersion Strengthened Alloys

Oxide dispersion strengthened (ODS) alloys are variations of F-M alloys, modified with a distribution of small, nanoscale particles intended to enhance the strength of the material at elevated temperatures where traditional F-M alloys are limited [11]. Initial versions of these steels were developed in the 1960's, with compositions of 13%Cr-1.5%Mo and 11-13%Cr-3%W, and included small oxide dispersions of Ti_2O_3 and/or Y_2O_3 particles [11]. These small Ti and Y oxide particles provide additional strength at elevated temperatures, as they effectively inhibit dislocation motion. At that time, these alloys were found to possess strong swelling resistance upon irradiation, even when He was known to be present [11], as the oxides provide sites for the nucleation and "trapping" of He bubbles. Today, development of ODS alloys is actively underway in Japan, Europe, and the United States [52], while only a handful of commercially available ODS alloys are currently produced, including MA956, PM2000 and MA957 (which has been discontinued).

Although the development of ODS alloys is still in a relatively early stage, interest in ODS alloys continues to grow in the field of nuclear materials due to their irradiation resistance and improved mechanical performance at higher temperatures. In this section, an overview of the unique manufacturing and microstructural implications of ODS alloys will be presented, along with a brief review of current development thrusts and directions moving forward.

2.3.1 Metallurgy

One of the key challenges for ODS is the development of a standardized process for creating a semi-homogeneous distribution of secondary phase particles throughout the microstructure of the material. This is typically accomplished through a process of mechanical alloying by ball milling fine powders of the metal along with ultrafine oxide powders (often Y_2O_3) [11,52]. Subsequently, the powdered mix is consolidated through either hot extrusion, hot isostatic pressing (HIP), or spark plasma sintering at elevated temperature [11,52,53]. As with traditional F-M steels, the alloy is rapidly cooled to achieve a martensitic structure, followed by tempering at elevated temperature to achieve the final microstructure.

The resultant microstructure generally contains fine grains less than 1 μm in length, resulting in enhanced uniaxial creep-rupture strength and ductility. However, elongated grains tend to lead to anisotropy in mechanical properties, which is one of the primary concerns with ODS alloy development [11,52]. The size of the nanoscale oxide phase is generally on the order of a few nm, and are typically enriched with Ti content often higher than Y, which suggests that Ti solutes have an influence on the dissolution process of the oxide powders [52]. The oxide phases present in ODS have been shown to improve radiation resistance in F-M alloys. The oxides provide a high density of interfaces, which act as sinks for the point defects generated by irradiation. As a result, the formation of defect clusters is less favorable, thus delaying the nucleation of voids, which lead to swelling. Ideally, the microstructure is most effective when the oxide nanoclusters are smallest (few nm) and homogeneously distributed, to maximize the sink strength of the microstructure.

2.3.2 Limitations and Development

By comparison to traditional F-M alloys, the development of ODS alloys are still in a relatively early stage. One of the key challenges is to overcome the anisotropy of mechanical properties, which are attributed to the elongated grain structure [11,52]. Development is underway for fabrication of ODS alloys with a more equiaxed grain structure by tailoring the microstructure through composition, warm rolling, and heat treatment processes [11]. Generally, compositions with 9-11% Cr and 2-3% W have exhibited improved anisotropy and resulted in excellent tensile strengths [11].

Additionally, methodologies for producing thick-walled components out of ODS alloys has not yet been established, nor has a process for joining (i.e. welding) ODS alloys to make complex fabricated assemblies [11]. However, due to the clear advantages and irradiation resistance potential of ODS alloys, several thrusts of development are occurring in parallel to develop production capability for ODS alloys and optimize microstructure to maximize irradiation resistance while ensuring isotropic mechanical properties for nuclear reactor applications.

2.4 Mechanisms of Cluster Evolution

As discussed above, the distribution of nanoscale phases within the matrix of ODS alloys provide a number of benefits, making them potential alternatives to traditional F-M alloys as they enable higher strength and creep resistance at higher operating temperatures [52,54–56]. These dispersed nanoclusters inhibit dislocation motion, strengthening the material without dramatically compromising ductility, and offering sites for vacancy and He clusters to nucleate, limiting the ability of voids and bubbles to grow and cause substantial swelling of the material [52,54–56]. Although

traditional F-M alloys do not contain any nanoscale phases in their "as manufactured" condition, several irradiation studies have shown that irradiation-induced nanoscale phases rich in Si, Mn, and Ni (referred to as G-phase), Cu-rich clusters, or Cr-rich clusters (α'-phase) may nucleate within the material matrix. Subsequently, these phases are believed to provide similar benefits as the oxide nanoclusters in ODS alloys, namely, increased strength and resistance to swelling via voids and bubble formation.

Due to the benefits of these dispersed phases, one of the over-arching questions in the development of nanofeatured ferritic alloys (NFA) such as ODS and F-M alloys for nuclear applications is whether these nanoscale phases will remain stable upon long-term irradiation to higher doses at the elevated temperatures planned for advanced nuclear reactors. It has been hypothesized that the stability of nanoclusters in b.c.c. Fe-based alloys upon irradiation is influenced by multiple factors, including: a) ballistic dissolution due to nuclear displacements, b) radiation-enhanced diffusion, c) nucleation, and d) Ostwald ripening. Upon irradiation, each of these influences are potentially in effect, and the resulting evolution of nanoclusters likely depends on the relative extent of the influence of these factors. In this section, a brief overview of each mechanism will be provided, with a discussion on the potential implications to oxide nanoclusters in ODS or G-phase, Cu-rich and α'-phase clusters in F-M alloys.

2.4.1 Ballistic Dissolution

Incident irradiation particles impact PKA atoms and (at high enough energies) can generate cascades of collisions in which target atoms are displaced from their original lattice positions. These cascades will occasionally overlap with the distributed nanoclusters of the material, potentially leading to the physical dissolution of solutes

from the nanoclusters to the surrounding matrix and thus, the reduction in size of the nanoclusters. This process is described as ballistic dissolution and should be considered as two separate, complimentary mechanisms: 1) recoil dissolution, and 2) disordering dissolution [57]. Recoil dissolution refers to the ejection of solute atoms from the nanocluster due to the physical displacement of knock-on atoms within the damage cascades to a position outside of the nanocluster. Heinig, et al. [58] developed a method to estimate the average distance a solute atom travels upon ejection ($\bar{x}$). By executing a SRIM calculation [44] on a thin slab of the cluster composition imbedded in an Fe-matrix, a recoil distribution is created and an average recoil distance may be determined [59]. Typical values for $\bar{x}$ are approximately 0.25 - 0.35 nm [59], depending on the solute, which is on the same order as the lattice parameter of b.c.c. Fe (0.286 nm).

On the other hand, disordering dissolution refers to the localized disordering of atoms within the damage cascade. Although not physically ejected, disordered atoms are no longer strongly bound to the nanoclusters, thus enabling them to more readily diffuse away, resulting in cluster size reduction. In either case, once an atom has been displaced, it is free to diffuse within the matrix and either: a) rejoin the original nanocluster, b) join a different nanocluster, c) move to another nanocluster via subsequent recoil events, or d) remain in the matrix.

Finally, Dai, et. al [34] has shown through Molecular Dynamics and Metropolis Monte Carlo simulations that overlapping cascades will lead to a higher rate of Frenkel pair production, also giving way to a higher size and number density of vacancy clusters. This insight suggests that damage cascade size and morphology may have a direct

influence on the amount of cascade overlaps and thus, the ability of irradiation to influence the evolution of the microstructure.

2.4.2 Radiation-Enhanced Diffusion

As discussed in Section 2.1, irradiation will result in a concentration of defects that exceeds those driven purely by thermodynamics. This higher concentration provides additional vacancies that enable atomic transport via diffusion at a higher rate [57]. This increased mobility of atoms enables solutes to migrate more quickly, thus influencing the microstructure. Solutes have an opportunity to diffuse towards or away from existing nanoclusters, potentially enlarging or shrinking such clusters, depending on chemical composition gradients. Since irradiation results in a non-equilibrium condition, the resulting evolution of nanoclusters may also be in a non-equilibrium state.

Quantifying radiation-enhanced diffusion (D^{irr}) is typically accomplished through comparison of the concentration of vacancies present in the microstructure with and without irradiation [59,60]:

$$D^{irr} = \frac{C_v^{irr}}{C_v^{eq}} D^{th} \tag{2.9}$$

where C_v^{eq} and C_v^{irr} are the concentration of vacancies at thermal equilibrium and during irradiation, respectively. The thermal diffusion rate (D^{th}) is the solute diffusion rate following typical arrhenius behavior. The value for C_v^{irr} may be estimated as [59]:

$$C_v^{irr} = R\tau \tag{2.10}$$

in which R is the defect production rate (dpa/s) and τ is the characteristic amount of time required for defects to react with sinks in the microstructure. This time can be written as [59]:

$$\tau = \frac{1}{k^2 D_v} \tag{2.11}$$

with k^2 as the sink strength of the microstructure and D_v is the thermal diffusion rate for vacancies. In these relationships, it is important to recognize that microstructures with higher sink strengths will result in lower values for τ, C_v^{irr}, and thus, D^{irr}. This suggests high sink strength alloys will inherently be more resistant to radiation-enhanced diffusion.

2.4.3 Ostwald Ripening

Ostwald ripening can be described as the coarsening of particles within either a solid or liquid solution. In this mechanism, smaller particles within solution tend to dissolve, while larger particles tend to grow due to redeposition of dissolved solutes from the smaller particles. The net result is an increase in average size of the particles, along with a decrease in number density, as illustrated in Figure. 2.9 [61]. The Ostwald ripening mechanism is driven by the relative difference of particle interfacial energy. Smaller particles have higher interface energy and are less stable. Thermodynamically, the system is driven to minimize surface area and surface tension (i.e. interfacial energy) and thus sacrifices smaller, incoherent particles in favor of larger ones.

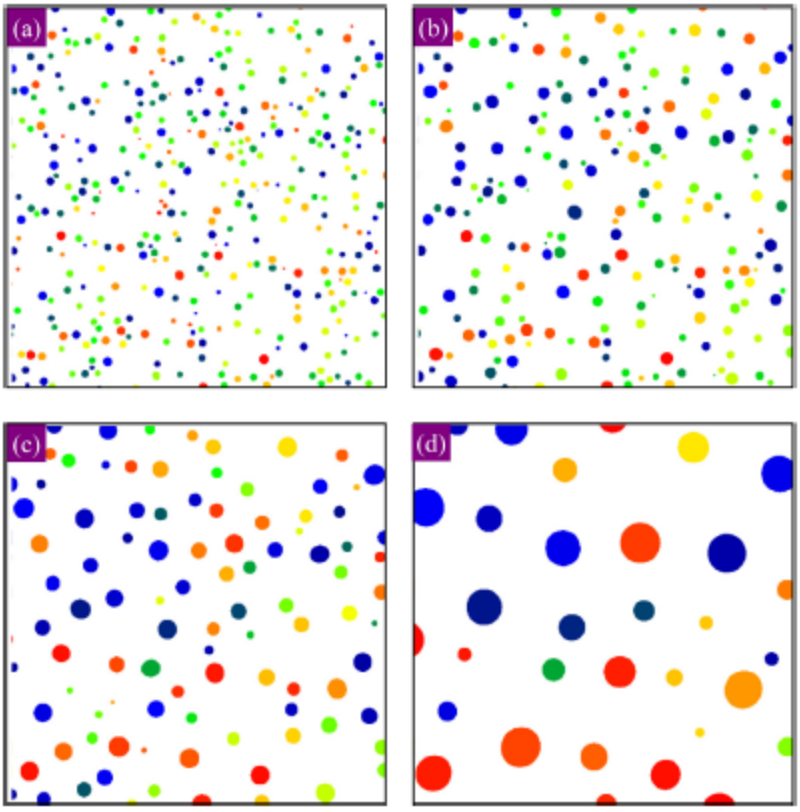

Figure 2.9. Illustration of typical nanocluster size and number density evolution that is characteristic of Ostwald ripening with time progressing from a) to d), from [61]**.**

Classical theory of Ostwald ripening was originally developed in ~1958 for two different extreme conditions. The Lifshitz-Slyokov theory accounts for the case for which the reaction rate for Ostwald ripening is limited by diffusion of atoms in the solution. On the other hand, the Wagner theory assumes that the reaction rate is only limited by the kinetics of the particle-matrix interface [62,63]. The most complete solution for modeling Ostwald ripening is with combining the classical Lifshitz-Slyokov and Wagner (LSW) models, but this solution is only applicable for the situation of low particle fraction that is vanishing. The general solution of this combined model can be written as [64]:

$$\langle r_p(t)\rangle^3 - \langle r_p(o)\rangle^3 = K_{LSW}t \tag{2.12}$$

where $\langle r_p \rangle$ is the average particle radius, K_{LSW} is the coarsening rate constant, and t is time.

Since the development of the LSW theory, much effort has occurred to further enhance and apply the theory in a more general form for multiple circumstances. Most literature involves an abundance of theory and mathematics attempting to enhance existing models or create new models to develop better prediction methods for Ostwald ripening in such cases as in binary alloys [62], ternary alloys [65], multi-component alloys [66], as well as ripening in liquid solutions [61,64]. Unfortunately, few studies in literature evaluate irradiation experiments and attempt to correlate calculating models with observed results.

The most common theoretical model utilized for simulating Ostwald ripening is the phase-field model. Key assumptions with this model are: 1) the transport of mass occurs by diffusion only, and 2) the different nanoparticles are not allowed to coalesce. As a result of the second assumption, each particle is allowed to have its own crystallographic orientation, which brings about the introduction of multiphase fields [64]. Another key assumption of the classical LSW theory is that the volume fraction of the nanocluster particles is vanishing, which creates some limitation. In a refinement to the phase-field model developed by Kim [64], a correction to the rate constant has been included that allows the volume fraction to evolve over time. In the model by Kim, $\langle r_p \rangle$ is dependent on the volume fraction, $f_p(t)$, and the number density, $n_p(t)$. This revised model was simulated on a solid-cluster in liquid system to assess its applicability and compared to the classical LSW model. The evolution of f_p and n_p over time in this simulation are shown in Figure 2.10. The volume fraction of particles increases initially and then

stabilizes after longer durations. Meanwhile, the number density dramatically declines, which is consistent with the coarsening mechanism of Ostwald ripening [64].

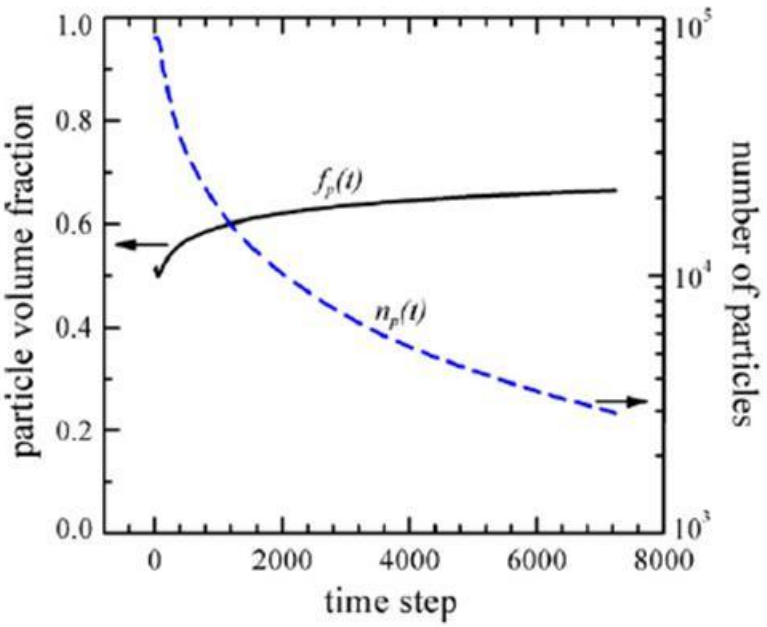

Figure 2.10. Evolution of the particle volume fraction (f_p) and number of particles (n_p) in a typical simulation, from [64]**.**

Additionally, the results for four different simulations with different starting volume fractions are illustrated in Figure 2.11 as a plot of the evolution of $\langle r_p \rangle^3$ over time [64]. Based on the classical LSW theory from Eq. 2.12, these plots would be expected to follow a linear trend. For lower volume fractions, the trend appears to be close to linear, but at higher volume fractions, the slope appears to continue to slightly increase throughout the duration of the simulation [64]. This also demonstrates the rate constant has a strong dependence upon the volume fraction, f_p. Therefore, additional factors need to be considered for estimating the rate constant for Ostwald ripening.

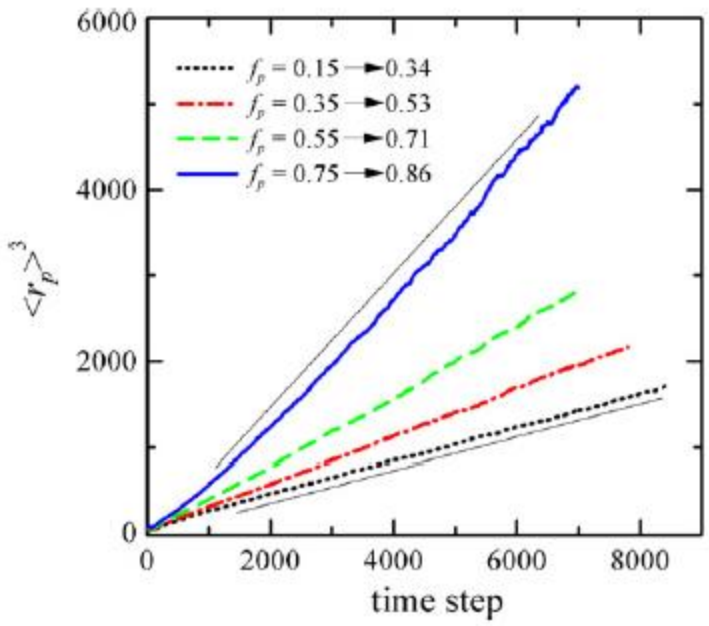

Figure 2.11. Evolution of $\langle r_p \rangle^3$ over time for four different initial particle fractions, from [64]**.**

Kim wrote an expression for an adjustment to the rate constant as [64]:

$$K^{app} = K_{LSW} + \Delta K \tag{2.13}$$

where K^{app} is the apparent (i.e. observed) rate constant, K_{LSW} is the classical rate constant and ΔK is an adjustment due to change in particle volume fraction. Each of these terms can be replaced and the following equation can be written [64]:

$$\frac{d\langle r_p \rangle^3}{dt} = \left.\frac{\delta\langle r_p \rangle^3}{\delta n_p}\right|_{f_p=const} \cdot \frac{dn_p}{dt} + \left.\frac{\delta\langle r_p \rangle^3}{\delta f_p}\right|_{n_p=const} \cdot \frac{df_p}{dt} \tag{2.14}$$

where the left side of the equation is K^{app}, the first term on the right hand side is K_{LSW} and the second term on the right hand side is ΔK. Through mathematical rearranging and using the definition for f_p, we can write [64]:

$$\Delta K = \frac{\langle r_p \rangle^3}{f_p} \frac{df_p}{dt} \tag{2.15}$$

Through experimentation, $\langle r_p \rangle$, f_p, and df_p/dt can be measured and thus ΔK may be calculated.

Irradiation studies of ODS have also been observed to exhibit nanocluster coarsening consistent with the Ostwald ripening mechanism [67,68]. Observations such as these have led to hypotheses that irradiation-induced coarsening should be proportional to $\varphi^{1/3}$ (i.e. K_{LSW} from Eq. 2.13 is proportional to φ), where φ is the irradiation flux [59,69]. Conversely, other irradiation studies have shown evidence of reduction in average nanocluster size [70] and even of haloing [71,72], in which a high density of smaller nanoclusters nucleate around, and at the expense of, larger nanoclusters. This trend is fundamentally the opposite that of Ostwald ripening, and is commonly referred to as inverse Ostwald ripening (Section 2.4.5).

It appears the existing theoretical models for Ostwald ripening could provide a strong foundation for the prediction of Ostwald ripening behavior in irradiated materials. Since the nanoclusters are under the additional influence of ballistic dissolution during irradiation, the Kim model, which allows for change in the particle volume fraction, could provide additional accuracy. The key challenge in developing a predictive model for radiation-induced Ostwald ripening will likely require the overlay of ballistic dissolution along with radiation-enhanced diffusion effects due to the higher concentration of vacancies produced (Section 2.4.5).

2.4.4 Nucleation

The process of nucleation may be described as the condensation or adsorption of solutes into a precipitate embryo. The free energy barrier to nucleation consists of two parts: a) volume free energy, and b) surface free energy [73]. The volume free energy is the difference in free energy of each respective phase, while the surface free energy is a

function of the interface between each phase. If the precipitate embryo grows beyond the critical radius, growth of the precipitate is favored by thermodynamics.

Two different types of nucleation mechanisms are possible: homogeneous and heterogeneous [73]. Homogeneous nucleation involves precipitate nuclei forming in the interior of the solvent phase, while heterogeneous nucleation is facilitated by the presence of a local, pre-existing surfaces or interfaces. Due to the reduction of surface free energy present in heterogeneous nucleation, the activation barrier for heterogeneous nucleation is typically considerably lower than homogeneous nucleation. As a result, heterogeneous nucleation is more kinetically favorable. In either case, the rate of nucleation and growth of precipitate nuclei is highly dependent on the diffusion rates of the respective solutes.

2.4.5 Multiple Active Mechanisms

In considering each of these mechanisms in isolation, the nanoclusters in F-M alloys could take any number of conflicting evolution paths. On its own, ballistic dissolution will result in the complete dissolution of all nanoclusters over time. Conversely, the mechanism of Ostwald ripening alone would lead to indefinite coarsening of the nanoclusters over time, at least until some saturation point is achieved. As irradiation is introduced, diffusion rates of solutes will be enhanced, giving way to increased rates for Ostwald ripening and nucleation even further. None of these mechanisms in isolation are capable of explaining the results of nanocluster evolution observed in literature (see Section 2.5). Consequently, multiple authors [57,60,74] have hypothesized that nanocluster evolution upon irradiation is governed by a balance between these competing mechanisms.

The concept of multiple active mechanisms has also been hypothesized in an emerging fields of nanoelectronics, in which ion-beam irradiation is used for size refinement of embedded metallic nanoparticles [58,75–78]. In this context, smaller nanoparticles are observed to nucleate and grow at the expense of larger nanoparticles, a mechanism described as "inverse Ostwald ripening". The framework of this mechanism involves multiple steps: 1) ion irradiation induces solute ejection (i.e. ballistic dissolution), 2) ejected solutes nucleate into new particles (i.e. nucleation), and 3) new nanoparticles grow and coarsen (i.e. Ostwald ripening). Over time, a steady, refined particle size distribution is obtained as each of these competing influences arrive at a new equilibrium state. Therefore, inverse Ostwald ripening is consistent with the notion of several cluster evolution mechanisms acting in parallel, culminating in an altered system equilibrium.

2.4.6 Cluster Evolution Modeling in Literature

Since the onset of development of ODS steels and NFAs, the prevailing hypothesis has suggested irradiation will influence the long-term stability of the nanoclusters in these alloys. Several efforts have been made over the past few decades to apply a calculation model describing the evolution of nanoclusters as a result of varying irradiation conditions. Irradiation parameters such as dose rate, temperature, and irradiation particle will all potentially influence the nanocluster evolution. Ideally, a calculation model would capture the influence of each of these parameters and their relative effect on the long-term stability of the nanoclusters.

One of the earlier models was developed by Nelson, et al. [57]. Within this model, the authors isolate the ballistic effects on nanoparticle dissolution (recoil and

disordering), while overlaying simultaneous growth of nanoclusters via radiation-enhanced diffusion. First, the volumetric growth rate of nanoclusters due to concentration of solutes in the matrix, *c*, is written as:

$$\frac{dV}{dt} = \frac{3(D+D\prime)cr}{p} \tag{2.16}$$

in which *p* is the atomic fraction of solute atoms in the cluster phase, *r* is the radius of the nanocluster, and *(D+D')* represents the radiation-enhanced diffusion rate of the solutes. At the same time, total concentration of solute atoms (*C*) in the system is maintained as:

$$C = \frac{4}{3}p\pi r^3 n + c \tag{2.17}$$

where *n* is the number density of clusters per unit volume. The net result are equations for the rate of change in the radius of a nanocluster (*dr/dt*), written as follows:

$$\frac{dr}{dt} = -\frac{\phi}{N} + \frac{3(D+D\prime)C}{4\pi pr} - (D + D')r^2 n \qquad \text{(recoil dissolution)} \tag{2.18}$$

$$\frac{dr}{dt} = -\psi K + \frac{3(D+D\prime)C}{4\pi pr} - (D + D')r^2 n \qquad \text{(disorder dissolution)} \tag{2.19}$$

In these equations, both the second and third terms are identical and represent the growth rate of the nanoclusters applying Eqs. 2.16 and 2.17. The first terms in Eq. 2.18 and 2.19 each represent the recoil dissolution or disordering dissolution influence, respectively. For recoil dissolution, ϕ is the estimated flux of solute atoms ejected from existing nanoclusters, estimated as $\phi = 10^{14} \cdot K\ (cm^{-2}s^{-1})$ with *K* as the dose rate (in dpa/s), and *N* as the density of target atoms per unit volume. For the disordering dissolution term in Eq. 2.19, ψ represents the disordering parameter and is estimated as $\psi = lf$, where *l* is the estimated size of a damage cascade and *f* is the fraction of solutes that dissolve as a result of disordering. Application of either Eq. 2.18 or 2.19 will result in a solution similar to the one shown in Figure 2.12. These curves each indicate smaller precipitates

will exhibit a positive *dr/dt* (i.e. growth), while larger precipitates exhibit a negative *dr/dt* (i.e. shrinkage). The net result is an equilibrium radius, represented by the point at which each curve crosses the horizontal axis in Figure 2.12. Similarly, a plot of the precipitate radius evolution over increasing dose in illustrated in Figure 2.13 for two different dose rates. In both cases, large and small precipitates evolve to converge on an equilibrium size, and this evolution is generally completed within the first 5 dpa of irradiation. Within this model, Nelson et al. [57] acknowledge the least understood variable in Eq. 2.19 is the disordering parameter, ψ. The authors therefore suggest that this parameter may be fitted to existing experimental data to determine the estimated value for different irradiation conditions.

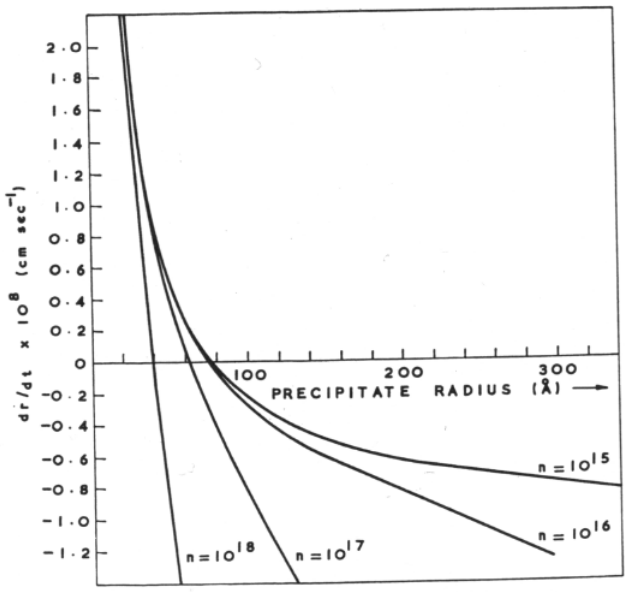

Figure 2.12. Solutions to Eq. 2.19 using values of $K = 10^{-2} dpa/s$, $D' = 6x10^{-14} cm^2/s$, $\psi = 10^{-6} cm$, and $C = 0.135$ and different values for n, from [57]**.**

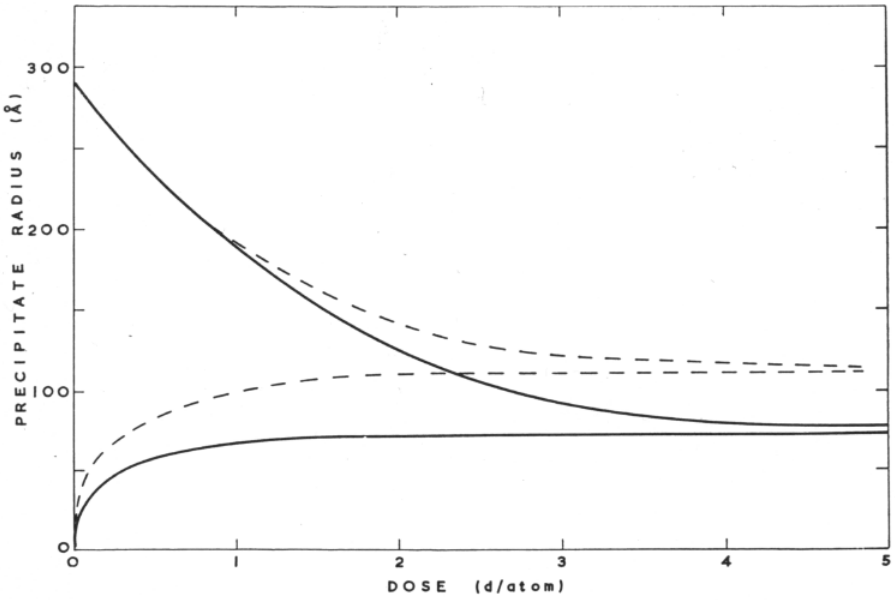

Figure 2.13. Change in precipitate radius with dose with values of $K = 10^{-2} dpa/s$ (solid lines) and $K = 10^{-6} dpa/s$ (dashed lines), from [57]**.**

Another approach to modeling cluster evolution is developed by Martin [60]. The basis of this model is a steady-state solution to the diffusion equations, which produce an equilibrium concentration profile around clustering solid solutions. Details of the derivation are more complex than the relatively elegant Nelson, et al. solution, and are detailed elsewhere [60]. One of the key conclusions developed through this model is the ballistic effects of irradiation will lead to an increase in configurational entropy of the system. This entropy increase is essentially the same as a rise in temperature of the system. The resulting equivalent temperature (T') is written as [60]:

$$T' = T(1 + \Delta) \tag{2.20}$$

where Δ is the temperature dilation factor and is influenced by both the irradiation flux and temperature (T), and can estimated as:

$$\Delta = \Delta_o e^{\left(\frac{E_\Delta}{k_B T}\right)} \tag{2.21}$$

The activation energy, E_Δ, in Eq. 2.21 is estimated as:

$$E_\Delta = E_D - E_F - \frac{E_m}{2} \cong \frac{E_m}{2} \tag{2.22}$$

where E_D, E_F, and E_m are the activation energies for solute diffusion, vacancy formation, and vacancy migration, respectively. An important feature to note in Eq. 2.21, which exhibits arrhenius behavior, is the dilation factor will be reduced at higher temperature. The implication of this temperature dilation is the potential shift in the solubility limits of the solutes in the surrounding matrix, per examples illustrated in Fig. 2.14. Depending on the equilibrium phase diagram of the system, irradiation ballistic effects may potentially induce dissolution of nanoscale phases, or it may facilitate phase separation from solid solution to two (or more) separate phases. In the case of the Martin model, Δ_0 is the least understood parameter, but the opportunity exists to apply this model to existing experimental data and deduce the values of Δ_0 for various irradiation conditions.

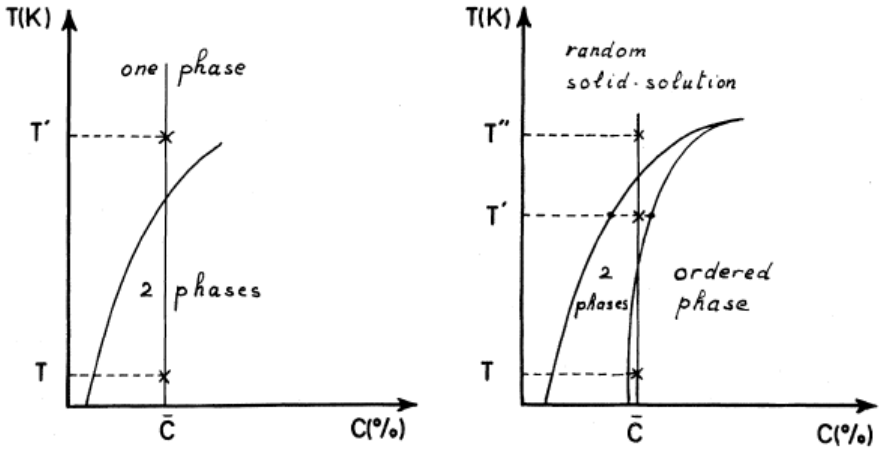

Figure 2.14. Possible alloy behaviors as a result of ballistic effects of irradiation, a) precipitate dissolution, or b) unmixing (at T') or complete disordering (at T''), from [60]**.**

More recently, Chen, et al. [79] has advanced a model originally introduced by Wagner [80] which couples the Gibbs-Thomson model of Ostwald ripening with ballistic dissolution. The model is based on the same competing mechanisms, in which the

diffusion-driven growth evolution of clusters is influenced by the interface coherency between the clusters and the surrounding matrix. They find that fine and coherent clusters (with low interface energy) experience the least dramatic change in size, while incoherent clusters (i.e. high interface energy) more readily dissolve, particularly at lower temperatures. Similarly to the Nelson, et al. solution [57], this model also predicts an equilibrium size of clusters will be reached over time. This equilibrium state is written as [79]:

$$\frac{dr}{dt} = \frac{D}{r} \cdot \frac{c - c_r}{c_p - c_r} - K\psi = 0 \tag{2.23}$$

in which D is the solute diffusion rate, r is the cluster radius, c is the solute matrix concentration, c_p is the solute cluster concentration, and c_r is the solute concentration at the interface with the matrix, given by:

$$c_r = c_\infty exp\left(\frac{2\gamma_i v_{at}}{kTr}\right) \tag{2.24}$$

where c_∞ is the concentration of solutes at a flat interface of the two phases, γ_i is the interface energy, v_{at} is the atomic volume within the cluster, T is the temperature, and k is the Boltzmann constant. The solution space for Eq. 2.23 is illustrated Figure 2.15, in which a finite region of interface energies and cluster radii will lead to cluster growth, while the remaining regions dictate cluster shrinkage.

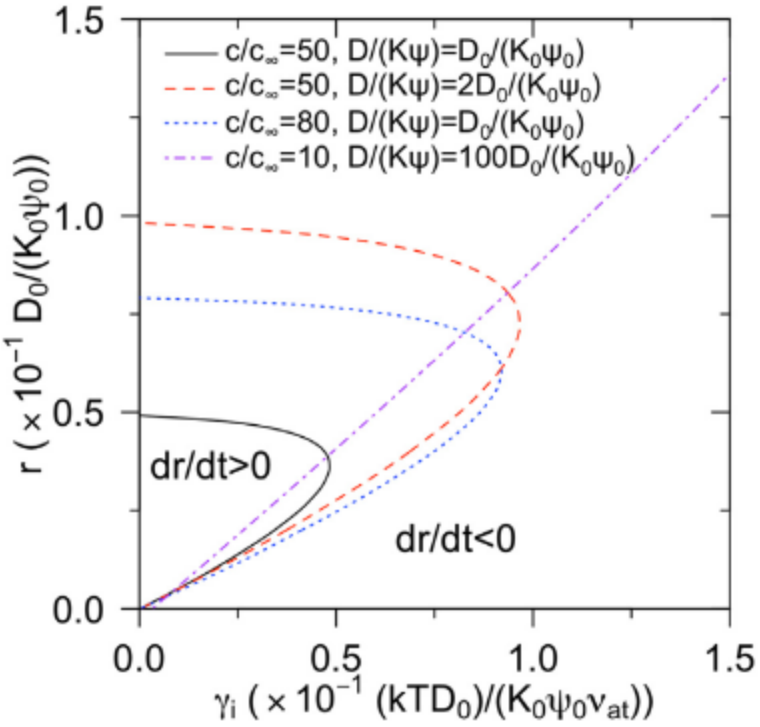

Figure 2.15. Solution space for Eq. 2.23 under various conditions, from [79]**.**

Finally, a relatively new study by Xu, et al. [35] evaluates a binary Fe-Cu alloy, correlating an atomistically based continuum model to experimental data. The model incorporates thermal and radiation-enhanced diffusion, clustering of Cu precipitates, thermal dissociation and cascade-induced redissolution effects. The model predicts a concentration (i.e. number density) gradient of clusters over time written as [35]:

$$\frac{dC_n}{dt} = k_{n-1}^{+}C_1C_{n-1} + k_{n+1}^{-}C_{n+1} - k_n^{+}C_1C_n - k_n^{-}C_n \tag{2.25}$$

where *C* is the concentration (i.e. number density) of n-Cu clusters, and with k_n^+ and k_n^- as the rate constants for capture and emission of Cu atoms, respectively. The capturing rate is written as:

$$k_n^{+} = 4\pi(r_1 + r_n)(D_1 + D_n) \tag{2.26}$$

where r is the radius, either of a Cu atom (r_1) or Cu cluster (r_n). Likewise, D is the diffusivity of a Cu atom (D_1) or for a Cu cluster (D_n). In this model, D_n is assumed to be zero. The rate of solute emission is then written as:

$$k_n^- = 4\pi(r_1 + r_{n-1})(D_1 + D_{n-1})C_0 \exp\left(-\frac{E_n^B}{k_B T}\right) + SICRD \cdot \frac{4\pi}{3}(r_n + a_0)^3 \cdot \phi \cdot \frac{\delta^2 N_{PKA \geq 1keV}}{\delta l \, \delta N_{ion}} \quad (2.27)$$

In this expression, C_0 is the matrix atomic number density, E_n^B is the binding energy of a Cu atom to the Cu-rich cluster. The SICRD represents the "size-independent cascade re-dissolution parameter" (~1 per PKA), a_0 is the lattice parameter of the Fe-matrix, ϕ is the ion flux, and the final derivative term represents the number of PKAs with energy above 1 keV generated per ion per unit depth, which may be calculated using SRIM and the "COLLISION.txt" output file [44]. In this study, Xu et al. initially anneal the sample to induce Cu precipitation as a starting point for all subsequent experiments. Upon incorporating irradiation at either -20°C or 300°C, the model predicts contrasting evolution of the cluster size distribution as shown in Figure 2.16. In this study, Xu et al. conduct physical experiments corresponding to the simulated irradiation conditions and demonstrate a strong correlation between the model and physical results. It is important to recognize that this calculation is for a binary Fe-Cu system, and may become incrementally much more cumbersome if attempted on a multi-component system such as ODS or F-M alloys.

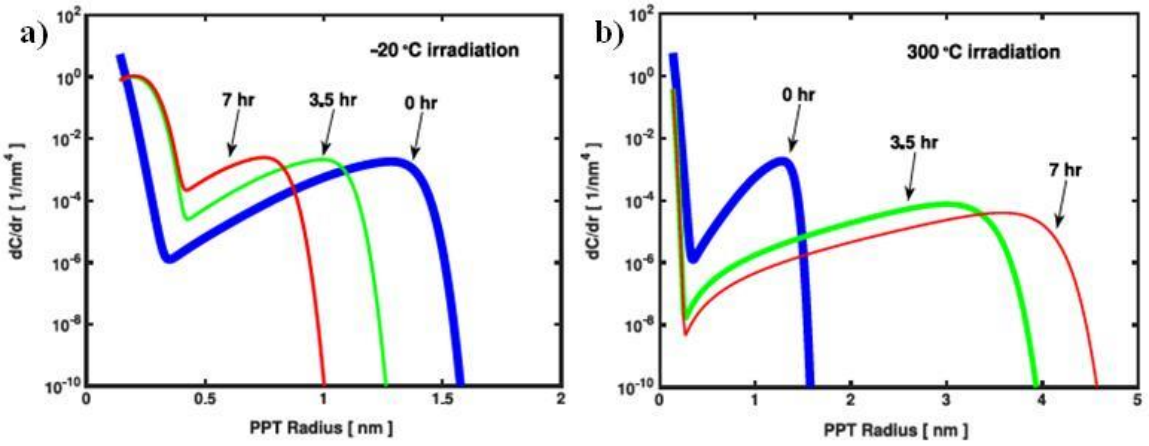

Figure 2.16. Model predicted cluster size distributions resulting from irradiation at a) -20°C, and b) 300°C, from [35]

Although each of these calculation models approach the simulation with unique methodology, the foundational theory of multiple active mechanisms persists throughout. Strong evidence is available to suggest the hypothesis of ballistic effects and diffusion-driven growth of clusters are competing upon irradiation. However, a comprehensive and universal solution for predicting the evolution of multi-component solute clusters in b.c.c. Fe-based alloys upon a range of irradiation conditions continues to remain elusive.

2.5 Cluster Evolution Experiments on ODS Alloys

Oxide dispersion strengthened alloys contain nanoclusters rich in Y-Ti-O atoms in the "as-manufactured" condition. These clusters have been shown to exhibit excellent strength and creep resistance, even at higher temperatures, and are expected to provide resistance to irradiation damage, particularly void and bubble growth [52,54–56]. Consequently, any alteration of these clusters as a result of irradiation would have implications on the mechanical properties and long-term irradiation resistance of components manufactured with these alloys. As a result, it is important to have a clear understanding of the evolution of these nanoclusters upon irradiation in order to predict the long-term durability and useful life of potential reactor structural components.

To date, several studies have observed irradiation-induced changes to nanocluster size, number density, chemistry, and/or crystal structure. However, the results from these studies are yet inconclusive, for a variety of reasons. Each experiment is typically conducted under unique conditions including: 1) ODS alloys with varying composition, fabrication processing, and heat treatment, 2) alloys with varying nanocluster composition and morphology, and 3) irradiation conditions with varying particle type and energy, dose, dose rate, and temperature. Each of these variables has the potential to significantly influence experimental results, thus making it difficult to make side-by-side comparisons between one study and another. To complicate matters, each study attempting to evaluate "stability" of the oxide nanoclusters defines "stability" slightly differently, which further obscures the development of a comprehensive conclusion.

A summary of all studies evaluating irradiation evolution of ODS nanoclusters are provided in Table 2.3. From the information, it can be seen that every possible result of irradiation-induced evolution has been observed. On the surface, there are no distinct trends, but one could ascertain that cluster morphology (i.e. size and number density), chemistry, and crystal structure are all highly relevant to defining the irradiation evolution of the oxide nanoclusters. In the following sections, each of these attributes of the nanoclusters will be further discussed in relation to observed irradiation-induced evolution available in literature.

Table 2.3 Summary of previous studies of oxide nanoparticle evolution in ODS alloys, from open literature (alloy type F = ferritic, M = martensitic, F-M = ferritic-martensitic.

Material	Type	Irrad. Particle	Irrad. Temp. (°C)	Irrad. Dose (dpa)	Dose Rate (dpa/s)	Method	Structure	Chemistry	Size	Number Density	Ref
F94	F	Fast n	400-530	2.5-15		TEM	n.s.	n.s.	Stable	Stable	[81]
MA957	F	Fast n	325	6		TEM, SANS	n.s.	n.s.	Stable	n.s.	[82]
9Cr ODS	M	Ni^{+}	500- 700	5, 50, 150	1.4×10^{-3}	HR-TEM	n.s.	n.s.	Decrease	Increase	[83,84]
MA957	F	He^{+} + Ni^{+}	450, 650	150	2×10^{-3}	TEM	n.s.	n.s.	Stable	Stable	[85]
MA957	F	Fast n	412-670	109-113		APT	n.s.	Stable	Stable	Stable	[86]
9Cr ODS	F	H^{+}	525	1	5×10^{-6}	APT, EFTEM	n.s.	Stable	Decrease	Decrease	[6]
14YWT	F	H^{+}	400	1, 3	5×10^{-6}	EFTEM	n.s.	n.s.	Increase	Increase	[5]
14YWT	F	Ni^{2+}	–75-600	5, 50, 100	2×10^{-3}	APT	n.s.	n.s.	Decrease at T_{irr}< 600°C; else stable	Stable	[5]
14YWT	F	Ni^{2+}	–75-600	5, 50, 100	2×10^{-3}	EFTEM	n.s.	n.s.	Increase	Decrease for $T_{irr} \leq$ 300°C; else increase	[5]
14YWT	F	Fast n	500	3	1×10^{-7}	APT, EFTEM	n.s.	n.s.	Decrease	Increase	[5]
12Cr ODS	F-M	Fe^{2+}	325-625	100, 200	n.s.	HRTEM	Larger phases lose coherency	n.s.	Decrease	Decrease	[79]

12Cr ODS	F-M	Fe^{8+} + He^{+} + H^{+}	21	4.4		EFTEM	n.s.	Stable	Stable	Stable	[87]
DY	F	Fast n	400-580	81		TEM	Halo; irregular O/M interfaces	Ti, Al loss	Decrease	Decrease	[88]
14YT	F	Fe^{3+}	700	50		APT	n.s.	Y:Ti decrease	Increase	Increase	[89]
14YWT	F	Ni^{2+}	300-600	100	1.39×10^{-2}	APT	n.s.	Y:Ti increase at 300°C	Decrease	Decrease	[8]
9Cr ODS	F	H^{+}	400	3.7	0.5×10^{-5}	APT	n.s.	Y:Ti increase	Increase	Decrease	[9]
MA957	F	He^{+} + Ni^{+}, C^{-}	475- 625	200	$3.0\text{-}14 \times 10^{-3}$	TEM	n.s.	n.s.	Stable	Stable	[90]
9Cr, 12Cr ODS	M, F	Fast n	420-835	28-51		TEM	n.s.	n.s.	Stable	Stable	[91]
MA957	F	Fe^{+}	25	18		TEM	Amorphize	n.s.	Stable	n.s.	[92]
MA957	F	Kr^{+}	500	200		TEM	Stable	n.s.	Stable	n.s.	[92]
K6	F	n.s. ion	300-700	20	9.9×10^{-5}	HRTEM	n.s.	n.s.	Stable	Stable	[93]
K1, K4	F	Fe^{3+}	500-700	20, 150	1×10^{-3}	STEM	n.s.	n.s.	Stable	Stable	[94]
SOC-1	F	Fe^{3+}	650	60	5×10^{-4}	STEM	n.s.	Stable	Stable	Stable	[95]
18Cr ODS	F	Fe^{+}	500	4-45		EFTEM	Interfaces become irregular		Stable	Stable	[96]
18Cr ODS	F	Fe^{+}	500	150		APT, EFTEM	n.s.	Approaches $Y_2Ti_2O_7$ stoich.	Increase	Decrease	[59]
18Cr ODS	F	Au^{2+}	RT	156		APT, EFTEM	Amorphization	n.s.	Dissolution	Dissolution	[59]
9Cr-2W ODS	M	e^{-}	400			TEM	Amorphization	n.s.	Decrease	Decrease	[97]
DY	F	Cr^{6+} + He^{+}	475	50	3.0×10^{-4}	TEM	Complex oxides not observed	n.s.	Stable	n.s.	[98]

F82H, 16Cr ODS	F	Fe^{3+}	380	20	1.1 x 10^{-3}	HRTEM	n.s.	n.s.	Decrease	Decrease	[12]
14Cr ODS	F	Fe^{3+}	Cryo - 700	15	3 x 10^{-3}	GIXRD	Stable	n.s.	Dissolution at cryo; else decrease or stable	Dissolution at cryo; else decrease or stable	[99]
MA957	F	Therm. n	325	2.0, 5.5	2.9 x 10^{-7}	TEM, SANS	Stable	n.s.	Stable	Stable	[100]
DY	F	Fast n	400-480	75.4		XAFS, TEM	Disordering	n.s.	Decrease (larger oxides)	Not Specified	[101]
MA957	F	Fast n	600	3	3.7 x 10^{-7}	APT	n.s.	Y:Ti decrease	Stable	Stable	[102]
DY	F	Kr^{18+}	RT			STEM	Amorphize		Stable	Stable	[103]
EM10 ODS	F	e^{-}	300-500	100	3-6 x 10^{-3}	HRTEM	n.s.	Stable	Decrease	n.s.	[72]
DY, EM10 ODS	F	He^{+}	400	0.05		HRTEM	n.s.	Stable	Stable	Stable	[104]
DY, EM10 ODS	F	Ar^{+}	400	33		HRTEM	Amorphize	n.s.	Decrease	Decrease	[104]
DY	F	Fast n	400-580	≤81		HRTEM	Halo	Al, Ti loss < 70 dpa; else stable	Decrease > 70 dpa	Decrease >70 dpa	[104]
DY, EM10 ODS	F	e^{-}	300-550	33	3-6 x 10^{-3}	HRTEM	n.s.	Stable	Decrease	Decrease	[104]
12YWT	F	Fe^{+}	300	0.7	1.9 x 10^{-4}	APT	n.s.	Stable	n.s.	Stable	[105]
12Cr, 14Cr ODS	F	Fe^{5+} + He^{+} + H^{+}	RT, 600	10-30	1 x 10^{-3}	PAS	Vacancy cluster-Cr complexes	n.s.	Stable	n.s.	[106]
14LMT	F	Fe^{2+}	30	10-100		APT, EFTEM	n.s.	Stable	Stable	n.s.	[107]
14LMT	F	Fe^{2+}	500	10-100		APT, EFTEM	n.s.	Cr, La pickup	Decrease	Stable	[107]
Eurofer 97 ODS	F-M	H^{+}	40	0.3, 1, 2		TEM	Amorphize particles <20 nm	n.s.	n.s.	Stable	[108]

18Cr ODS	F	Xe^{+}	27, 500	2.5		TEM	Amorphize at T_{irr}=27°C	n.s.	Increase at T_{irr}=27°C; else stable	n.s.	[109]
MA957	F	Fe^{+}	500	150	6.5×10^{-4}	HRTEM, EFTEM	Stable	n.s.	Increase	Decrease	[69]
MA957	F	Fast n	412, 430	50, 75	1.3×10^{-7}	HRTEM, EFTEM	Stable	n.s.	Stable at T_{irr}=412°C; else increase	Stable at T_{irr}=412°C; else decrease	[69,110,111]
14Cr ODS	F	Fe^{+}	500	150		EFTEM	n.s.	Stable non-stoich.	Increase	Decrease	[112]
Fe-Y_2O_3 ODS	F	Fe^{+} with/out He^{+}	500, 600	100		TEM, SANS	n.s.	n.s.	Stable at T_{irr}=500°C; else increase	Stable	[113]
Eurofer 97 ODS	F	Fast n	330	32		APT, TEM	n.s.	V loss, Y pickup	Dissolution (of particles > 10 nm)	Increase	[67,114]
Eurofer 97 ODS	F	Fe^{+}, Fe^{2+}, Fe^{3+}	RT	32		APT, TEM	n.s.	V, N Loss	Dissolution	Stable	[115]
Eurofer 97 ODS	F	Fe^{2+} and Ti^{2+}	RT	0.8-0.9		APT, TEM	n.s.	Y, O, Mn pickup	Decrease	Increase	[116]
13.5Cr ODS	F-M	Ti^{2+}	RT, 300	0.8-2.4		APT, TEM	n.s.	O pickup; Y:Ti decrease	Stable	Increase	[116]
13Cr ODS	F	e^{-}	400, 500	12	2.2×10^{-3}	TEM	n.s.	n.s.	Difficult to discern	Difficult to discern	[117]
14Cr ODS	F	Fe^{5+} + He^{+} + H^{+}	600	30		EFTEM	n.s.	Stable	Increase	Stable	[118]

Eurofer 97 ODS	M	H^+	40, 350	0.3-2.0		TEM	n.s.	n.s.	Stable	Stable	[119]
Cr16 ODS, EP450	F	Bi^+, Xe^+	350-650			HRTEM	Amorphous ion tracks	n.s.	Decrease for T_{irr}>600°C	Stable	[120]
EP450	F	Xe^+, Kr^+, Ar^+	RT			HRTEM	Amorphous ion tracks	n.s.	n.s.	n.s.	[121]
Eurofer 97 ODS	M	Fe^{2+}	400	2	~1 x 10^{-4}	APT	n.s.	Stable	Stable	Stable	[122]
1DS	M	Fast n	450-560	10.5-21		TEM	n.s.	n.s.	Decrease	Decrease	[123]
1DK	F	Fast n	450-560	10.5-21		TEM	n.s.	Y:Ti decrease	Increase	Decrease	[123]
F95	F	Fast n	400-530	2.5-15		HRTEM	Stable	Y:Ti decrease for $T_{irr}\geq$500°C	Stable	Stable	[81,124]
M93	M	Fast n	400-530	2.5-15		HRTEM	Stable	Y:Ti decrease	Stable	Stable	[81,124]
MA957	F	Fast n	500, 700	100	1.2 x 10^{-6}	TEM	n.s.	n.s.	Increase	Decrease	[125]
16Cr ODS	F	e^-	500	10		TEM	Stable	n.s.	Decrease	Stable	[126]
K3	F	Fe^{3+}	300, 500	1-10	1 x 10^{-3}	TEM	n.s.	n.s.	Stable	Stable	[127]
12.5Cr ODS	F	$e^- + H^+$	350-550	15	2 x 10^{-3}	TEM	O/M interface becomes irregular	n.s.	Stable	Stable	[128]
PM2000	F	Fast n, He^+	500	21		EFTEM	Amoprhization; faceted shape becomes spherical	Cr-rich shells	n.s.	n.s.	[129]

2.5.1 Size, Number Density, and Volume Fraction

Changes in size of the clusters is the most widely reported feature of irradiation-induced evolution, and it is important to understand the long-term evolution of cluster size over a range of doses. However, few studies report data of cluster size evolution over a dose range. The results of these studies are illustrated in Figure 2.17. From this comparison, the results are inconsistent, with no common direction or convergence as dose increases, making it impossible to interpret in a broad context. Similarly, the data in literature also presents contradictory results with respect to irradiation temperature.

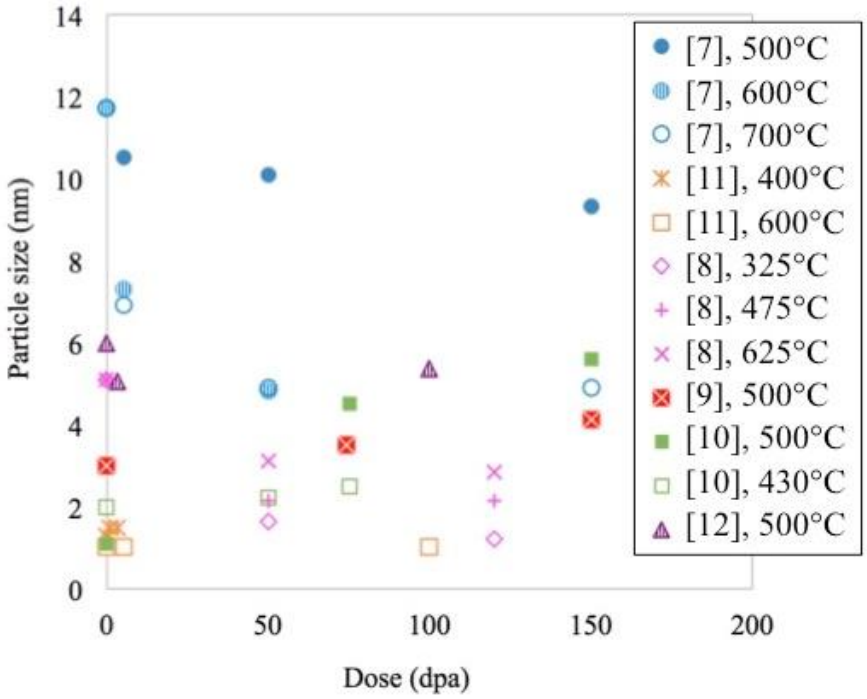

Figure 2.17. Nanocluster size evolution with increasing irradiation dose.

Figure 2.18 plots the results from literature (when available) with indication of direction of change respective to: a) nanoparticle size, b) number density, and c) volume fraction. For simplicity, the results from each study are classified directionally as increases, stable, or decreases to evaluate any potential trends. Based on these plots, no

clear trend or threshold is apparent within the range of doses or temperatures evaluated for nanocluster size or number density. The volume fraction plot (Figure 2.18c) potentially indicates a pattern suggesting decreasing volume fraction at temperatures >600°C, while increasing at temperatures <600°C. However, with so few data points available, this cannot be concluded with certainty.

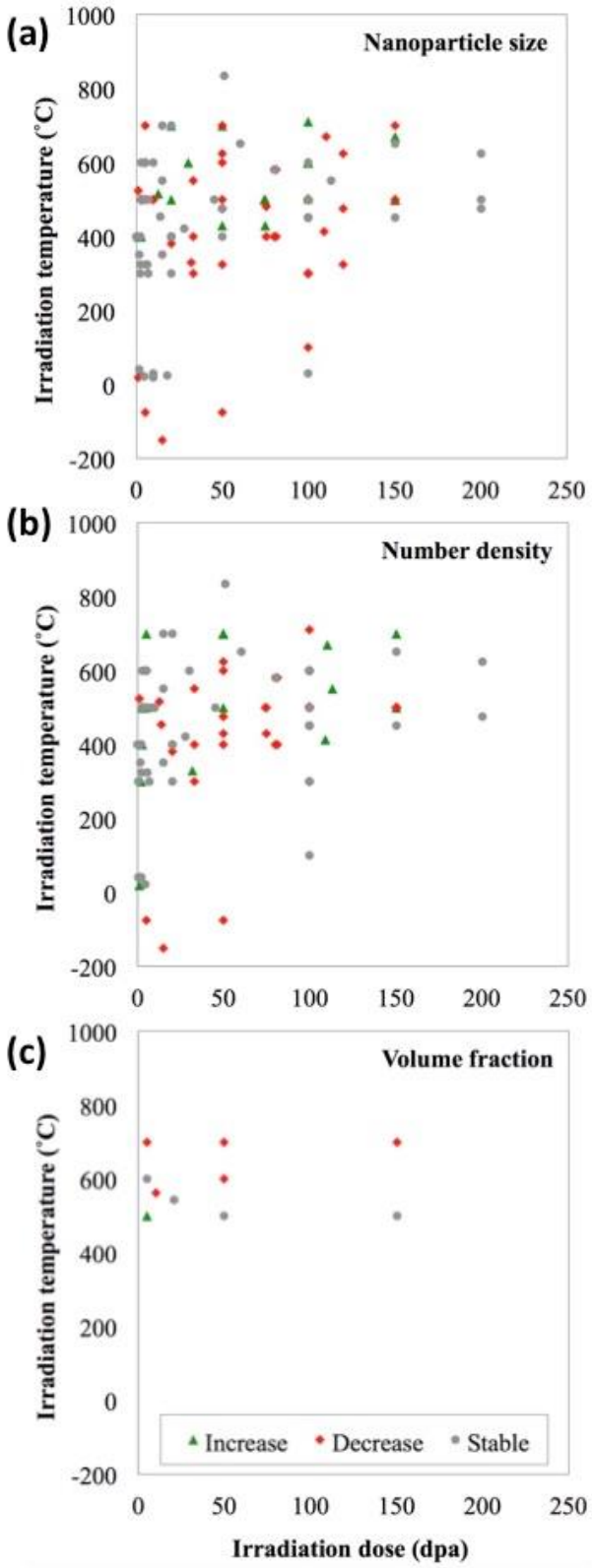

Figure 2.18. Results from literature indicating direction of irradiation-induced evolution of a) nanocluster size, b) number density, and c) volume fraction.

2.5.2 Chemistry

Historically, the chemistry of nanoclusters has been characterized using transmission electron microscopy (TEM) with electron energy loss spectroscopy (EELS) or energy filtered TEM (EFTEM) techniques. More recently, with the increased utilization of atom probe tomography (APT), the characterization of chemistry of clusters has become more precise, enabling the relative comparison of irradiation-induced chemistry evolution between specimens. Most commonly, irradiation-induced changes in oxide nanocluster chemistry are quantified in terms of the Y:Ti ratio and the (Y+Ti):O ratio, which give insight to the stoichiometry of the clusters and any changes in one solute element relative to the other. The Y:Ti ratio has been observed to both increase in some studies [8,9,59,67,88,104,114,116], and decrease in others [81,89,102,116,123,124], while the (T+Ti):O ratio is typically observed to remain the same [8,9,116]. A summary of literature data providing evolution information for these two ratios is provided in Figure 2.19. Studies observing a decrease in Y:Ti ratio tend to have temperatures above 500°C, while studies with increasing Y:Ti ratio are generally below 500°C. On the other hand, there is no apparent temperature dependence on the (Y+Ti):O ratio. Although changes in this ratio are observed at doses of 100-150 dpa, few data points exist, making it difficult to draw any conclusions about dose dependence. In addition to the oxide solute ratios, other studies have also observed such phenomena as Cr enrichment at the interface of nanoclusters [107,112], or depletion of Al from nanoclusters [88,104]. Enrichment of Cr is usually attributed to radiation-induced segregation of Cr to sinks such as the oxide nanoclusters [112,122].

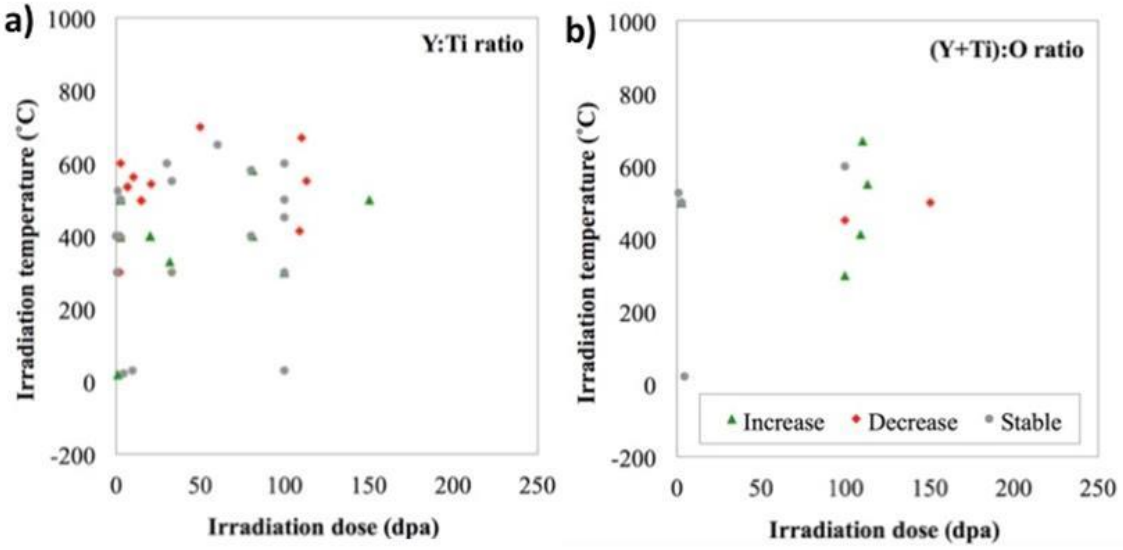

Figure 2.19. Results from literature indicating direction of irradiation-induced evolution of a) Y:Ti ratio, b) (Y+Ti):O ratio.

2.5.3 Crystal Structure

The coherency between the oxide nanocluster and matrix interface is considered a critical attribute of nanoclusters, as this will directly influence the effectiveness of the interface as a sink for defects [101,110,111,125]. Using high resolution transmission electron microscopy (HRTEM), several studies have found oxides to generally be coherent with the matrix [69,79,88,96,128]. Observations in literature also suggest that coherency may be closely related to the size of clusters, with smaller oxides trending towards non-stoichiometric chemistry with Y:Ti ratio ~0.50 [9,13], while larger oxides trend towards a Y:Ti ~1.3 [9,13] with a pyrochlore $Y_2Ti_2O_7$ or orthorhombic Y_2TiO_5 structure [124,130–134].

Oxide nanoclusters have been observed to amorphize to varying degrees upon irradiation [59,92,97,101,103,104,108,109,135]. The extent of amorphization is attributed to three factors: 1) the structure of the oxides, 2) irradiation dose, and 3) irradiation temperature [109,135]. Of these three influences, the effect of irradiation dose and the

structure of the oxides are the least understood, while a critical amorphization temperature may be determined for any given system and irradiation condition [135].

2.6 Cluster Evolution Experiments on F-M Alloys

Ferritic-martensitic alloys do not contain any nanoclusters in the "as-manufactured" condition. However, several species of nanoclusters have been found to nucleate in F-M alloys under irradiation. As such, these clusters have a similar potential to offer beneficial side-effects similar to those of oxides in ODS alloys. On the other hand, these phases have been shown to cause undesirable consequences, most notably embrittlement. Consequently, any nucleation and growth of these clusters as a result of irradiation will also have implications on the mechanical properties and long-term irradiation resistance of components manufactured with F-M alloys. As a result, it is important to have a clear understanding of the nucleation behavior and long-term stability of these nanoclusters upon irradiation in order to predict the durability of any structural components in reactor applications.

To date, several studies have observed irradiation-induced nucleation and growth of various nanoclusters in F-M alloys including: a) G-phase precipitates, which are rich in Si, Mn, and Ni, b) Cu-rich nanoclusters, often alongside the G-phases, and c) Cr-rich α' phases. A summary of the studies evaluating irradiation evolution of nanoclusters in F-M alloys are provided in Table 2.4. As with ODS steels, however, experimental evidence is somewhat limited, precluding any definitive conclusions regarding the role of temperature and damage cascades in F-M alloy microstructure evolution. In the following sections, each type of nanoclusters species will be further discussed in relation to the observed irradiation-induced evolution available in literature.

Table 2.4 Summary of previous studies with nanoparticle evolution in F-M alloys, from open literature.

Experiment Details						G-phase		Cu-rich		Cr-rich (α' phase)		Reference
Material	**Irrad. Particle**	**Irrad. Temp. (°C)**	**Irrad. Dose (dpa)**	**Dose Rate (dpa/s)**	**Charact. Method**	**Diam. (nm)**	**Number Density (x 10^{21} m^{-3})**	**Diam. (nm)**	**Number Density (x 10^{21} m^{-3})**	**Diam. (nm)**	**Number Density (x 10^{21} m^{-3})**	
HT9	Fast n	380	20	-	TEM	11.3	9.3	-	-	7.8	72	[20]
HT9	Fast n	410	100	-	TEM	16.0	3.2	-	-	8.8	22	[20]
HT9	Fast n	440	155	-	TEM	26.5	1.1	-	-	9.6	1.1	[20]
HT9	Fast n	466	92	-	TEM	-	-	-	-	-	-	[20]
HT9	Fast n	505	2	-	TEM	-	-	-	-	-	-	[20]
HT9	5 MeV Fe^{2+}	460	75	0.6-1.2 x 10^{-3}	TEM	7.9	0.24	-	-	-	-	[30]
HT9	5 MeV Fe^{2+}	460	130	0.6-1.2 x 10^{-3}	TEM	7.2	0.25	-	-	-	-	[30]
HT9	5 MeV Fe^{2+}	460	188	0.6-1.2 x 10^{-3}	TEM	11.0	0.79	-	-	-	-	[30]
HT9	5 MeV Fe^{2+}	460	250	0.6-1.2 x 10^{-3}	TEM	13.2	0.105	-	-	-	-	[30]
HT9	5 MeV Fe^{2+}	460	350	0.6-1.2 x 10^{-3}	TEM	12.3	0.74	-	-	-	-	[30]
HT9	5 MeV Fe^{2+}	460	450	0.6-1.2 x 10^{-3}	TEM	12.0	0.82	-	-	-	-	[30]
HT9	5 MeV Fe^{2+}	460	550	0.6-1.2 x 10^{-3}	TEM	15.3	0.99	-	-	-	-	[30]
HT9	5 MeV Fe^{2+}	460	650	0.6-1.2 x 10^{-3}	TEM	19.4	0.66	-	-	-	-	[30]
T91	5 MeV Fe^{2+}	460	350	0.6-1.2 x 10^{-3}	TEM	24.8	0.8	-	-	-	-	[30]
T92	5 MeV Fe^{2+}	460	350	0.6-1.2 x 10^{-3}	TEM	29.8	0.7	-	-	-	-	[30]
T91	2 MeV p^{+}	400	7	1.3 x 10^{-5}	APT	4.0	74	3.1	56	-	-	[23]
T91	2 MeV p^{+}	400	7	~10^{-5}	APT	4.4	127	4.0	74	-	-	[25]
T91	2 MeV p^{+}	500	7	~10^{-5}	APT	8.0	14	5.0	17	-	-	[25]
HCM12A	2 MeV p^{+}	400	7	~10^{-5}	APT	4.6	269	4.0	296	3.6	460	[25]
HCM12A	2 MeV p^{+}	500	7	~10^{-5}	APT	7.2	43	6.6	37	-	-	[25]
HCM12A	5 MeV Fe^{2+}	500	100	~10^{-3}	APT	7.8	8	6.2	29	-	-	[25]

HT9	2 MeV p^+	400	7	~10^{-5}	APT	4.6	180	-	-	3.8	1340	[25]
HCM12A	2 MeV p^+	400	3	~10^{-5}	APT	4.2	232	3.4	427	3.0	152	[24]
HCM12A	2 MeV p^+	400	7	~10^{-5}	APT	5.0	271	3.8	239	-	-	[24]
HCM12A	5 MeV Fe^{2+}	500	500	~10^{-3}	APT	7.4	7	-	-	20.2	10	[24]
Fe-2.5%Cr model	n	300	0.6	-	APT	3.6	130	-	-	-	-	[33]
Fe-5%Cr model	n	300	0.6	-	APT	4.4	130	-	-	-	-	[33]
Fe-9%Cr model	n	300	0.6	-	APT	3.3	240	-	-	2.2	210	[33]
Fe-12%Cr model	n	300	0.6	-	APT	3.2	110	-	-	2.2	5000	[33]
HT9	Fast n	443	155	-	TEM	22.0	1	-	-	-	-	[18]
HT9	Fast n	505	4	-	TEM	-	-	-	-	-	-	[18]
HT9	Fast n	384	28	-	TEM	8.5	4.5	-	-	-	-	[18]
Fe-3%Cr model	Fast n	290	1.82	-	APT	-	-	-	-	-	-	[31]
Fe-6%Cr model	Fast n	290	1.82	-	APT	-	-	-	-	-	-	[31]
Fe-9%Cr model	Fast n	290	1.82	-	APT	-	-	-	-	4.8	85	[31]
Fe-12%Cr model	Fast n	290	1.82	-	APT	-	-	-	-	3.0	950	[31]
Fe-15%Cr model	Fast n	290	1.82	-	APT	-	-	-	-	2.6	3200	[31]
Fe-18%Cr model	Fast n	290	1.82	-	APT	-	-	-	-	2.4	5300	[31]

2.6.1 G-phase Clusters

The irradiation-induced formation of G-phase, a complex silicide ($Mn_6Ni_{16}Si_7$), has been commonly observed in F-M alloys upon multiple irradiation conditions. Several studies report the morphology (size and density) of G-phase clusters at a given irradiation temperature and dose. However, few studies report data of cluster size evolution over a range of doses. A bubble chart summarizing the relative cluster sizes of each study is provided in Figure 2.20. From this comparison, the size of the clusters tend to be larger at higher doses and elevated temperatures. This trend may suggest that more advanced coarsening occurs at these conditions, which is consistent with lower number densities also observed at higher dose and temperature (Table 2.4). It is important to note that APT will enable much finer detectability of nanoscale phase, thus typically yielding smaller average clusters sizes (at higher density) as more of the smaller nanoclusters may be detected.

One study by Anderoglu, et al. [20] has suggested that phase precipitation is more sensitive to temperature than dose, which would suggest their formation and growth is a diffusion-driven process, but this has not been proven. Another study by Allen, et al. [16] observed a potential difference in the incubation period of G-phase nucleation, noting that clusters are observed between 1 and 3 dpa upon proton irradiation at 400°C, but are not present until ~7 dpa upon Fe^{2+} irradiation at the same temperature.

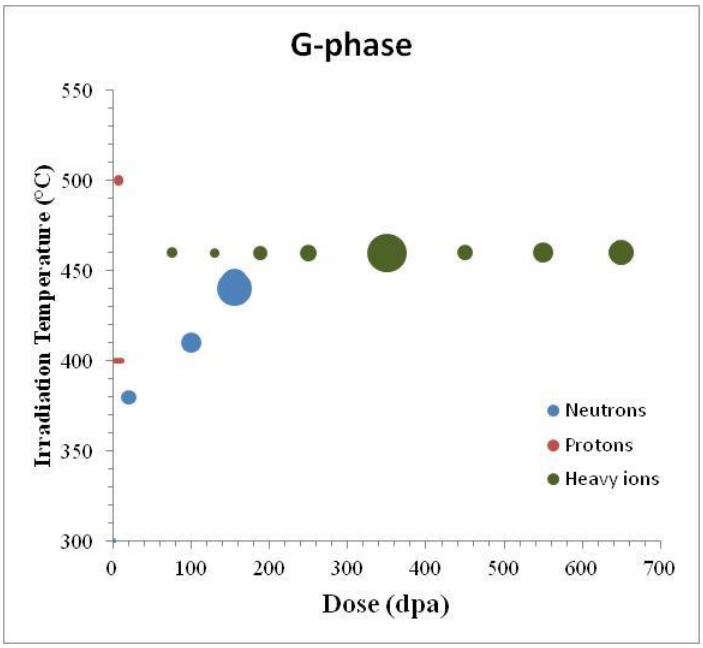

Figure 2.20. Results from literature indicating average size of irradiation-induced G-phase clusters. Size of bubbles represent relative size of clusters.

2.6.2 Cu-rich Clusters

The nucleation and growth of Cu-rich phases have also been observed by a number of studies. Clusters are commonly observed alongside G-phases [16,23–25], although their formation is typically attributed to the low solubility limits of Cu in b.c.c. Fe. To date, it is not clear whether G-phase or Cu precipitates first. A bubble chart summarizing the relative cluster sizes of each study is provided in Figure 2.21. Once again, the sizes of clusters tend to indicate coarsening at higher doses and elevated temperatures. However, very little data is available to draw any firm conclusions.

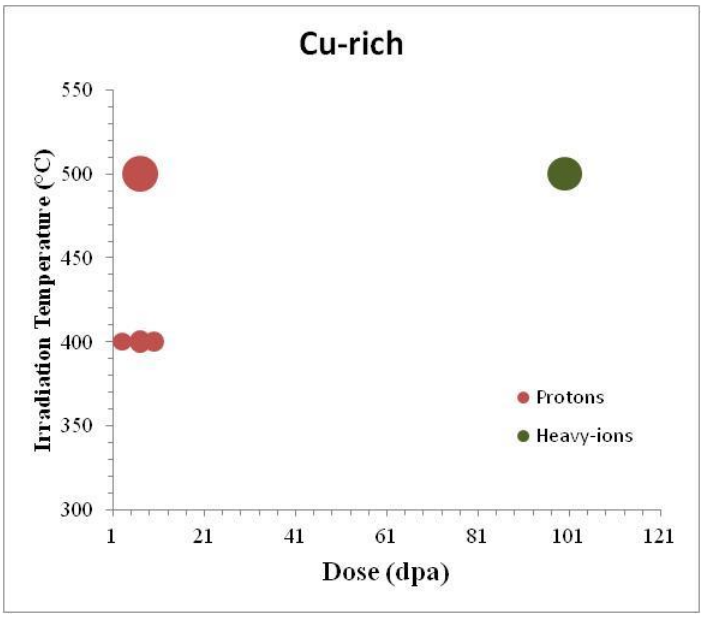

Figure 2.21. Results from literature indicating average size of irradiation-induced Cu-rich clusters. Size of bubbles represent relative size of clusters.

2.6.3 Cr-rich (α') Clusters

Another common phase observed to nucleate and grow in F-M alloys is the Cr-rich α' phase. A bubble chart summarizing the relative cluster sizes of each study is provided in Figure 2.22. Once again, the sizes of clusters tend to indicate coarsening at higher doses and elevated temperatures. Generally, phase separation of α-Fe and α' are only observed in alloys with Cr composition ≥ 9 at% Cr. As a result, this threshold corresponds to the approximate solubility limit of Cr in b.c.c. Fe. Several experiments and models have attempted to quantify the solubility limit of Cr upon irradiation, a summary of which is provide in Figure 2.24 [20]. Although some disagreement between the models and experiments persists, the observed solubility limit of 9 at% Cr appears to be a good approximation at temperatures below ~500°C.

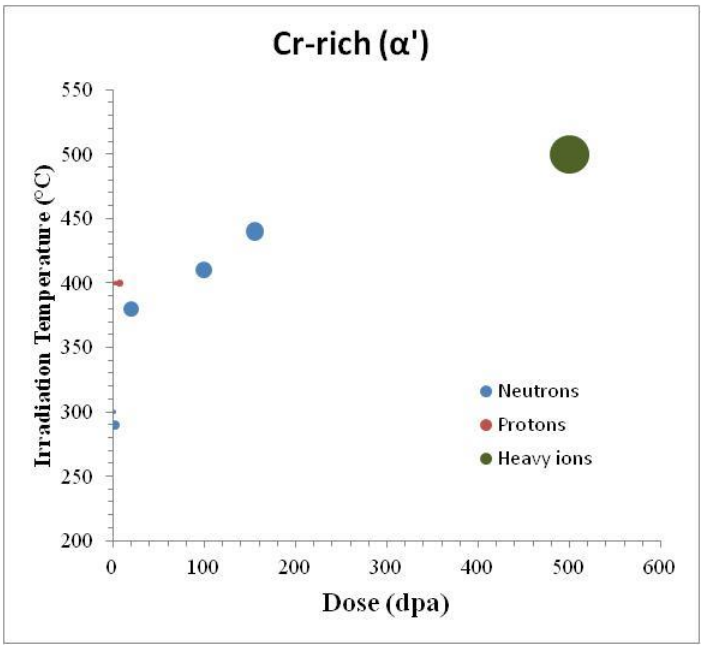

Figure 2.22. Results from literature indicating average size of irradiation-induced Cr-rich (α') clusters. Size of bubbles represent relative size of clusters.

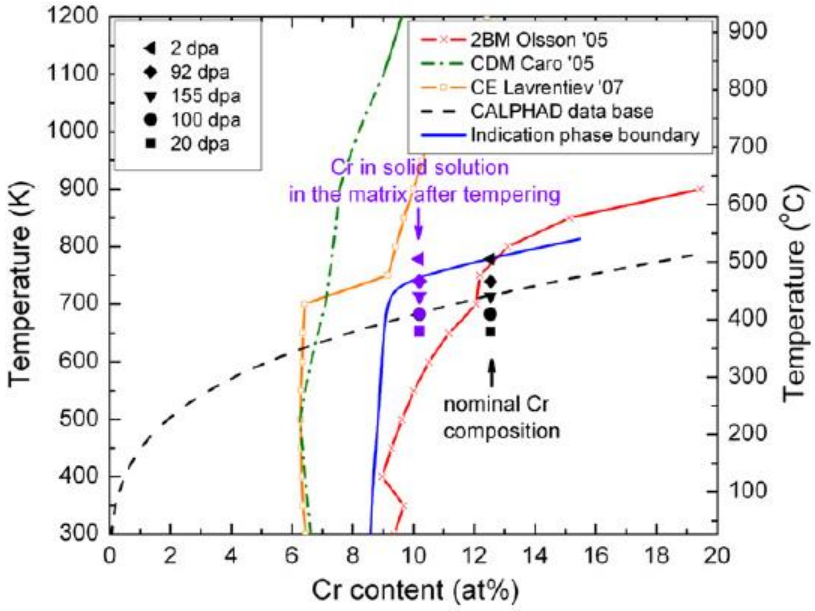

Figure 2.23. Models and experiments predicting α-α' phase separation, along with the irradiation temperatures of HT9 in ref. [20]**.**

2.7 Irradiation effects on Microstructure

In additional to irradiation-induced phase separation, the microstructure of the target alloy may also be considerably altered through the formation of irradiation-induced defect clusters. These changes in the microstructure may also influence the macroscopic mechanical properties of the material, potentially impacting the long-term durability of components. As a result, it is important to develop a clear understanding of the mechanisms of defect cluster formation and growth as a result of irradiation. This section will review the different types of defect clusters typically observed in F-M and ODS alloys upon irradiation including dislocation loops and voids, while connecting all microstructural changes to the resultant hardening of the alloy.

2.7.1 Dislocation Loops

Dislocation loops are irradiation-induced features formed as vacancy or interstitial defects cluster to form a mixed dislocation that alternates from edge to screw type dislocation as it wraps around in a ring-shape. Dislocation loops are most favorable on high density habit planes (i.e. {001} and {111} in b.c.c. Fe. Due to the higher mobility of interstitial defects, interstitial dislocation loops are vastly more common than vacancy dislocation loops, although the latter are theoretically possible. Dislocation loops typically range in size from a few nm up to tens of nanometers.

Upon irradiation, dislocation loops will nucleate and grow. It has been hypothesized that defect clusters such as loops will eventually approach a saturation value, as modeled by Whapham and Makin [136]. In this model, the number density (N) of defect clusters increases with dose by the following relationship [136,137]:

$$N = N_s \left[1 - exp\left(-\frac{\phi}{\phi_0}\right)\right] \tag{2.28}$$

in which N_s is the saturation density, ϕ is the irradiation dose, and ϕ_0 is the scaling dose which is used to characterize how fast saturation is approached. This model has also been corroborated by experimental observation, in which dislocation loop morphology appears to approach a saturation point at higher dose [16,23,138].

2.7.2 Voids

Over the past several decades, much effort has been spent in the nuclear materials research community to understand the mechanisms of void swelling and the development of materials more resistant to void nucleation and growth upon irradiation. One of the key attributes that make F-M and ODS alloys strong candidates for nuclear reactor applications is their improved resistance to void swelling. The mechanism of nucleation for defect clusters such as voids is essentially the same as that for solute phase separation. Vacancies cluster within the matrix, forming embryo whose fate is governed by the free energy barrier to formation for a void. If the void embryo grows beyond the critical radius, growth of the void is favored by thermodynamics.

2.7.3 Dispersed Barrier Hardening

It is well known that irradiation-induced microstructural features such as voids and dislocation loops increase the strength of a material by acting as obstacles to impede dislocation motion during deformation. Likewise, the oxide nanoclusters in ODS and the irradiation-induced phases in F-M alloys also serve as dislocation pinning points, contributing to hardening and increased yield strength of the alloys. The most common method for relating discrete microstructural features to the yield strength is the simplified dispersed barrier hardening model [139], written as:

$$\Delta\sigma_{y,i} = \alpha_i M \mu b \sqrt{N_i d_i} \tag{2.29}$$

In this equation, M is the Taylor factor (3.06 for b.c.c. Fe-Cr alloys such as the F-M alloys of interest [42]), μ is the shear modulus, b is the Burger's vector (0.248 nm for b.c.c. Fe [140]), N_i is the number density of feature type i, and d_i is the average diameter of feature i. The factor α_i represents the barrier strength of feature i and should be a coefficient valued between 0 and 1. A feature with a low α is considered a weak obstacle that more readily allows dislocations to bypass or shear through them, while features with α approaching a value of 1 are considered to be stronger inhibitors to dislocation motion. Equation 2.29 may be written for each type of feature present, then superimposed upon each other to calculate an overall net increase in yield strength from a network of microstructural features [42,141,142].

Over the years, studies have provided guidelines to directly estimate α_i [42,143]. But it is expected that α_i values are influenced by many sample-specific characteristics such as nanocluster composition and coherency, void faceting, and dislocation loop habit planes [144]. As a result, the values for each α_i will likely vary from sample to sample. To attain sample-specific α_i values, some studies have calculated the relative obstacle strengths necessary to mathematically relate the microstructure to the measured mechanical behavior (via indentation or tensile testing techniques) [144–146]. Adding to the complexity, additional studies have suggested that the strength of each obstacle is also dependent upon the size and/or number density of the obstacles in the matrix of the material [10,147–149].

More recently, Tan and Busby developed size- and density-dependent expressions for α of the obstacles of interest to F-M alloys [147]:

Incoherent Precipitates $$\alpha_{nc}^{incoh} = \frac{0.135}{(1-\nu)^{1/2}\left(1-0.816\boldsymbol{d}\sqrt{\boldsymbol{Nd}}\right)} ln\left(\frac{0.816\boldsymbol{d}}{r_0}\right) \quad (2.30)$$

Voids/Cavities $$\alpha_v = \frac{0.383}{(1-\nu)^{1/2}\left(1-0.816\boldsymbol{d}\sqrt{\boldsymbol{Nd}}\right)} ln\left[\frac{0.247\boldsymbol{d}}{r_0}\left(1-0.816\boldsymbol{d}\sqrt{\boldsymbol{Nd}}\right)\right] \quad (2.31)$$

Loops (thin plates) $$\alpha_l = \frac{0.271\boldsymbol{A}}{(1-\nu)^{1/2}\sqrt{\boldsymbol{Nd}}(16-\pi t\boldsymbol{A})} ln\left(\frac{0.637\boldsymbol{d}}{r_0}\right) \quad (2.32)$$

or, for coherent precipitates:

$$\alpha_{nc}^{coh} = \frac{0.816\gamma_{nc}\boldsymbol{d}}{\mu b^2\left(1-0.816\boldsymbol{d}\sqrt{\boldsymbol{Nd}}\right)} + 1.7\left(\frac{\boldsymbol{d}}{b}\right)^{1.5}\varepsilon^{1.5} + 0.0054\left(\frac{\boldsymbol{d}}{b}\right)^{0.275}\left(\frac{\Delta\mu}{\mu}\right)^{1.5} \quad (2.33)$$

where ν is Poisson's ratio (~0.33 [131,149–151]), $A = \sqrt{16\pi Nd} + 4Nd^2 - \pi^2 Ndt$, and t is the loop thickness (0.165 nm for {111} loops in b.c.c. Fe). The dislocation core radii, r_0, are not well known but often approximated as $r_0 \sim b$.

Once the contribution of each microstructure feature is determined, the next challenge is superimposing their respective effects to determine a combined influence on strength and hardening. Two methods are typically employed: 1) linear superposition, and 2) root-sum-square superposition. Linear superposition is generically written as [42]:

$$\Delta\sigma_{y,l} = \sum_i \Delta\sigma_{y,i} \quad (2.34)$$

and is considered more applicable when the obstacles have widely differing strengths. Root-sum-square superposition is written as [42]:

$$\Delta\sigma_{y,r} = \sqrt{\sum_i (\Delta\sigma_{y,i})^2} \quad (2.35)$$

and is considered more accurate when the obstacles have similar strengths. A mixed approach, introduced by Odette and Lucas [141], uses a weighting parameter S based on the relative strengths of the strongest and weakest barriers as:

$$\Delta\sigma_y = S\left(\Delta\sigma_{y,l} - \Delta\sigma_{y,r}\right) + \Delta\sigma_{y,r} \quad (2.36)$$

$$S = \alpha_s - 5\alpha_w + 3.3\alpha_s\alpha_w \quad (2.37)$$

where α_s is the strength of the strongest obstacle and α_w is the strength of the weakest obstacle. The difficulty in applying this mixed approach is that the α_i values for each obstacle type must be known in order to identify the strongest and weakest barriers.

2.7.4 Solid Solution Strengthening

Individual solutes within the matrix are also capable of inhibiting dislocation motion upon deformation of the material. A common method for modeling solid solution strengthening for a b.c.c. Fe matrix is [152,153]:

$$\Delta\sigma_{ss,i} = K_i C_i \tag{2.38}$$

in which $\Delta\sigma_{ss,i}$ is the resultant change in yield strength due to solid solution strengthening, K_i is the strengthening coefficient of the solute element, and C_i is the composition of the solutes in the matrix. Equation 2.38 may be applied for each solute element, then the overall solid solution strengthening effect may be calculated using [152]:

$$\Delta\sigma_{ss} = \sum_i \Delta\sigma_{ss,i} \tag{2.39}$$

Estimated values of K_i from prior studies of F-M and ODS alloys are tabulated in Table 5 from Refs. [152–155] for solutes in b.c.c. Fe. One particular observation is that interstitial solute species such as C and N have a strengthening factor K that is 2 to 3 orders of magnitude greater (~1000 MPa/at%) than K factors for solutes that occupy substitutional positions [153]. Unfortunately, limited data is available for the K factors of O, W, and Y in b.c.c. Fe, but they would be expected to have similar orders of magnitude as other interstitial solutes (for O) or other substitutional solutes (for W and Y).

Table 2.5 Solid solution strengthening coefficients for solute elements at room temperature (in MPa / at%), from Refs. [152–155]**.**

Element	**Substitutional or Interstitial**	**Ref.** [154]	**Ref.** [153]	**Ref.** [155]	**Ref.** [152]
C	Interstitial	-	~1050	-	1103.45
N	Interstitial	-	~1050	-	1103.45
O	Interstitial	-	-	-	-
Si	Substitutional	49-55	45	-	25.8
Mn	Substitutional	35-40	33	-	16.9
Ni	Substitutional	35-41	2.9	-	19.2
Cr	Substitutional	5-9	-	2.5-3.5	2.6
W	Substitutional	-	-	-	-
Ti	Substitutional	-	-	-	17.9
Y	Substitutional	-	-	-	-
Mo	Substitutional	-	-	-	15.9
Al	Substitutional	-	-	-	9.0
Co	Substitutional	-	-	-	2.1
V	Substitutional	-	-	-	2

CHAPTER THREE: OBJECTIVE

The objective of this dissertation is to determine the mechanism of radiation-induced nanocluster evolution in oxide dispersion strengthened and ferritic-martensitic alloys. Accomplishing this objective will incorporate a two-pronged approach: 1) experimentation to measure cluster evolution as a result of irradiation, and 2) modeling efforts to mathematically describe cluster evolution and provide an empirically-benchmarked tool for future alloy development. The activities of this thesis will be applied to alloys with different compositions, giving way to varying solute clustering behavior, and will be evaluated across multiple irradiating particles and a range of doses.

Prior modeling efforts in literature have incorporated a combination of influences from the competing effects of ballistic impacts (leading to nanocluster dissolution) and radiation-enhanced diffusion (leading to diffusion-driven growth). Each model has attempted to overlay each of these effects into an over-arching equation that describes the evolution of clusters in the presence of variable irradiation conditions [35,57,60,74]. To date, these models have demonstrated success in describing isolated experiments, but a comprehensive solution for predicting the evolution of multi-component solute clusters in b.c.c. Fe-based alloys upon a range of irradiation conditions continues to remain elusive.

Irradiation experiments are conducted on a model Fe-9%Cr ODS alloy and two commercial ferritic-martensitic alloys (HCM12A and HT9). Following each irradiation, the microstructure is characterized via TEM and APT to measure the average size and number density of grains, dislocations, carbide precipitates, dislocation loops, voids (if

present), and any nanoclusters present. The following experimental variable dependencies will be evaluated:

- *Composition dependence:* Fe-9%Cr ODS alloy contain solute clusters rich in Y, Ti, and O. HCM12A have demonstrated clustering of Si-Mn-Ni, Cu-rich clusters, and Cr-rich clusters in literature. HT9 is similar to HCM12A, but generally lacks Cu-rich clusters due to lower Cu content.
- *Irradiation particle and dose rate dependence:* Irradiations with Fe^{2+} ions (dose rate ~10^{-4} dpa/s), protons (~ 10^{-5} dpa/s) and neutrons (~ 10^{-7} dpa/s).
- *Dose dependence:* Irradiation doses with Fe^{2+} ions to 1, 3, and 100 dpa, with protons to 1, 3, and 7 dpa, and with neutrons to 3 dpa.

Direct measurement of the average size, number density and compositions of all nanoclusters from each specimen provides statistically relevant data that will be applied to modeling efforts for verification. The measurement of other microstructural features (grains, carbides, loops, voids, etc.) provides context as to the relative sink strengths of each alloy and the sink strength evolution in response to irradiation. Furthermore, the mechanisms of the irradiation evolution of loops and voids is well-known as compared to those of nanoclusters; measuring all of these features and contrasting their behaviors helps inform the lesser-known mechanisms of irradiation evolution of nanoclusters.

Modeling of the cluster evolution, in the form of change in cluster morphology over time (i.e. dose), will initially be conducted using the Nelson, Hudson, and Mazey (NHM) calculation approach [57]. Composition data measured via APT provide the necessary inputs required to successfully conduct the calculations progressively. Systematic development of the model will proceed through the following progression:

1) Application to the ODS alloy results, fitting the model to experimental cluster measurements to estimate the relative damage cascade disordering efficiencies (f) of each irradiation particle.
2) Division of ODS cluster measurements by individual solutes, fitting the model to measurements to estimate f_i for each solute. Identify any trends that contribute to species-specific f_i values.
3) Application to the HCM12A results, confirming particle-specific f values along with species-specific f_i values and the respective solute diffusion rates toward existing clusters.
4) Produce model-driven predictions for cluster evolution in HT9. Evaluation of predictions and reconfirmation of f_i and solute mobilities (as needed).
5) Comparison of model-predicted and measured clustering behavior as observed in literature on various F-M and ODS alloys.

With the convergence of the NHM modeling parameters, efforts move to evaluate the Martin theory [60] and the potential for a downward temperature shift to emulate solute cluster evolution using higher dose irradiations in place of lower dose irradiations.

Finally, using both the NHM and Martin calculation model results, the merit of charged particle irradiations as a surrogate for neutron irradiation is evaluated with respect to nanocluster evolution behavior. The potential for a downward temperature shift, as proposed by Martin [60], is analyzed and compared to prior reports in literature. The long-term goal of this work is to provide a predictive tool for the clustering response of b.c.c. Fe-based alloys, informing future development and optimization of alloys for advanced nuclear reactor applications.

CHAPTER FOUR: EXPERIMENTS

This chapter will detail the techniques and procedures used in conducting experimental measurements for this dissertation. The experiments are divided into sub-sections representing each major stage of development: 1) alloys and sample preparation, 2) irradiations, 3) post-irradiation sample preparation, 4) microstructure examination, and 5) cluster identification and analysis.

4.1 Alloys and Sample Preparation

In order to investigate the microstructural evolution of ferritic-martensitic and ODS alloys upon irradiation, three separate alloys were selected for study: a) a model ferritic Fe-9%Cr ODS alloy, which contains Y-Ti-O rich oxide nanoclusters in its "as-received" condition, b) commercial F-M alloy HCM12A, which contains Si, Mn, Ni, Cu solutes and ~11%Cr, and c) commercial F-M alloy HT9, which contains Si, Mn, Ni solutes and ~12%Cr, but, by contrast, contains only trace amounts of Cu. Previous studies of HCM12A and HT9 have demonstrated clustering of these solutes [24,25], making them of particular interest to irradiation-resistant alloy development.

4.1.1 Alloys and Processing

A rod of ferritic Fe-9%Cr ODS steel material was provided by the Japan Nuclear Cycle Development Institute (now known as the Japan Atomic Energy Agency). Alloyed ferritic steel was mechanically mixed with Y_2O_3 powders that were hot extruded at 1150°C. Finally, the rod was austenitized at 1050°C for 1 hour, air cooled, then tempered

at 800°C with subsequent air cooling. Additional details regarding the mechanical alloying and fabrication of the sample rod may be found in [156].

Alloy HCM12A, nominally 12Cr-MoVNbWCu, exhibits a two-phase microstructure comprised of martensite laths and δ-ferrite needles, both on the order of 0.9 μm wide and 6.1 μm long. Its final heat treatment involved austenitizing at 1050°C for 60 minutes followed by air cooling, and subsequent tempering at 770°C for 45 minutes followed by air cooling. Alloy HT9, nominally 12Cr-MoVW, exhibits a three-phase microstructure of martensite (laths are 0.4 μm wide and 14.6 μm long), δ-ferrite, and retained austenite. Its final heat treatment involved austenitizing at 1040°C for 30 minutes followed by air cooling, and subsequent tempering at 760°C for 60 minutes followed by air cooling. The complete alloy compositions for all three alloys are provided in Table 4.1.

Table 4.1 Chemical composition of Fe-9%Cr ODS, HCM12A, HT9, in wt%.

Element	Fe-9%Cr ODS	HCM12A	HT9
Cr	8.60	10.83	11.63
Mo	-	0.3	1
Mn	0.05	0.64	0.52
Ni	0.06	0.39	0.5
V	-	0.19	0.3
Cu	-	1.02	0.04
W	1.95	1.89	0.52
Si	0.048	0.27	0.22
Nb	-	0.054	-
C	0.14	0.11	0.2
N	0.017	0.063	0.047
Al	-	0.001	<0.01
P	<0.005	0.016	0.02
S	0.003	0.002	0.006
Ti	0.23	-	0.002
Y	0.27	-	-
O	0.14	-	0.013
Ar	0.004	-	-
Fe	Bal.	Bal.	Bal.

4.1.2 Sample Preparation

Specimens of each alloy for neutron irradiation were cut into transmission electron microscopic (TEM) discs, 3 mm in diameter, and approximately 150-200 μm thick. Prior to irradiation, the discs were also mechanically polished through 4000 grit SiC paper, followed by electropolishing at -30°C in 10% perchloric acid + 90% methanol at the Idaho National Laboratory (INL). The fabrication of neutron-irradiated specimens

was done prior to this study, as is not specifically part of this thesis. Charged particle irradiation specimens of each alloy were fabricated into separate rectangular rods for each irradiation. Each rod was cut by electrical discharge machining into 1.5-2 mm x 1.5 mm x 16-20 mm bars (Figure 4.1) to a quantity of: a) seven bars of Fe-9%Cr ODS, b) four bars of HCM12A, and c) four bars of HT9.

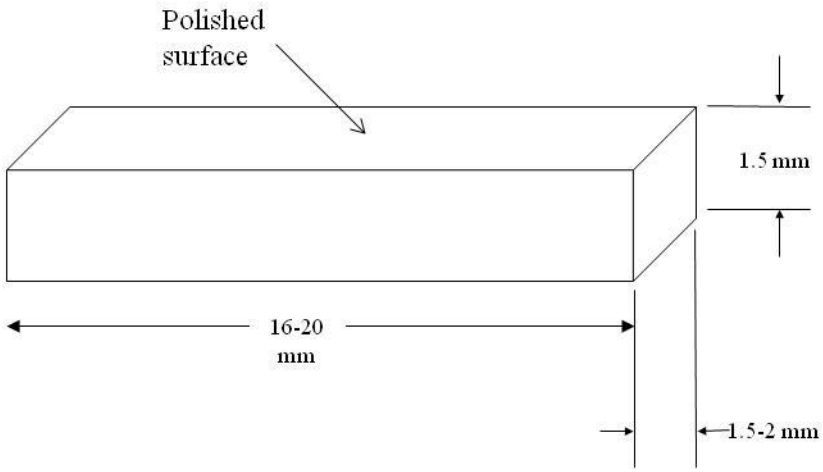

Figure 4.1 Geometry of charged particle irradiation specimens.

The collection of bar samples for each irradiation were assembled "side-by-side" onto a glass slide and mounted with wax. Each sample assembly was mechanically polished with SiC grit paper starting with 240 grit paper and gradually increasing to 4000 grit until a mirror finish was achieved with minimal scratches visible upon imaging with an optical microscope. The samples were then removed from the glass slide by soaking in a ultrasonic bath of acetone and then stored and labeled in sample tubes for transport to the Michigan Ion Beam Laboratory (MIBL). In order to remove any plastic deformation introduced by mechanical polishing, the samples were electropolished at MIBL for 20 seconds in a 10% perchloric acid + 90% methanol solution maintained at -40°C, with a 35 V applied potential between the specimen (anode) and platinum mesh cathode.

Separately, a specimen of the as-received Fe-9%Cr ODS was cut into a specimen ~5 mm x 5 mm x 1.5 mm thick and polished in the same manner. This specimen was not irradiated, but received the same microstructural examination as the irradiated samples in order to characterize the ODS microstructure and clusters prior to irradiation.

4.2 Irradiations

The irradiation conditions investigated for this dissertation are summarized in Table 4.2. All charged particle irradiations were conducted at the Michigan Ion Beam Laboratory at the University of Michigan, while the neutron irradiations were completed in the Advanced Test Reactor (ATR) at INL. The following sections will outline the unique considerations specific to each type of irradiations.

Table 4.2 Summary of irradiation conditions studied.

Irradiating Particle	Dose Rate (dpa/s)	Temperature (°C)	Dose (dpa)	Fe-9%Cr ODS	HCM12A	HT9
Neutron (ATR)	~ 10^{-7}	500	3	✓	✓	✓
2 MeV Proton	1.2 x 10^{-5}	500	1	✓	✓	✓
		500	3	✓	✓	✓
		500	7	✓	-	-
5 MeV Fe^{2+} Ion	2.2 x 10^{-4}	500	1	✓	-	-
		500	3	✓	✓	✓
		500	100	✓	✓	✓
		400	50	✓	-	-

4.2.1 Neutron Irradiations

Neutron irradiation began in September 2008 as part of the University of Wisconsin Pilot Project at the Advanced Test Reactor (ATR) National Scientific User Facility. Each of the sample discs were irradiated in a fast neutron spectrum (dose rate

~10^{-7} dpa/sec) in the ATR. The irradiation temperature of 500°C was determined with SiC electrical resistivity samples placed in experiment capsules; thermal models, in which the gas-gap distance was adjusted, correlated the SiC experimental data [157].

4.2.2 Proton Irradiations

For each proton irradiation experiment, the collection of alloy samples were re-assembled in the same sequence and orientation (including the guide bars) as when they were polished (Section 4.2.1). The sample assembly was mounted onto a copper irradiation stage with a shim filled with liquid indium sandwiched between the specimens and stage to provide efficient heat application or removal from the specimens. A hold-down plate was installed with four screws to ensure samples could not slip during installation or irradiation, and to prevent against liquid indium leakage. Finally, thermocouples were spot-welded onto the specimen to monitor and calibrate the initial temperature. An image of a typical stage assembly is provided in Figure 4.2.

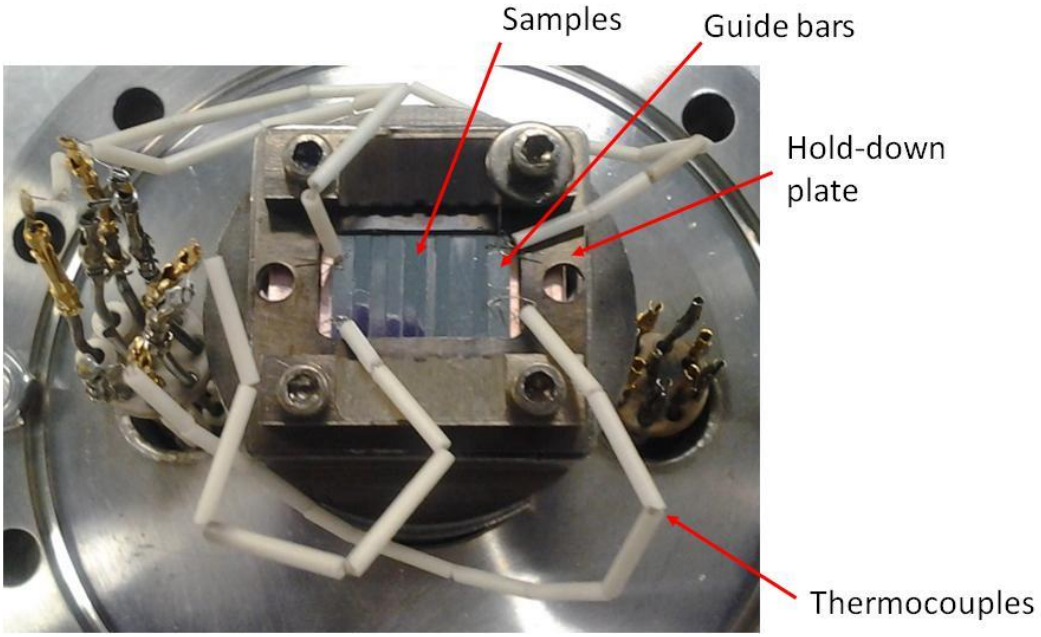

Figure 4.2 Typical sample stage assembly for charged particle irradiation at MIBL.

With the accelerator beam line inactive, the irradiation stage was installed at the end of the beamline chamber, with the stage electrically isolated from the accelerator beamline, to allow for accurate charge collection (Figure 4.3a). Pressure in the chamber was pumped down and maintained at pressures below 1.3 x 10^{-5} Pa (10^{-7} torr) throughout the experiment. Prior to commencement of irradiation, the size of the focused proton beam was measured in a beam profile monitor and was found to have a FWHM of no more than 3 mm. In order to define the target irradiation surface area, tantalum aperture plates were aligned such that the irradiation area fully overlapped each target sample and partially overlapped the guide bars on each side (Figure 4.3b and Figure 4.4).

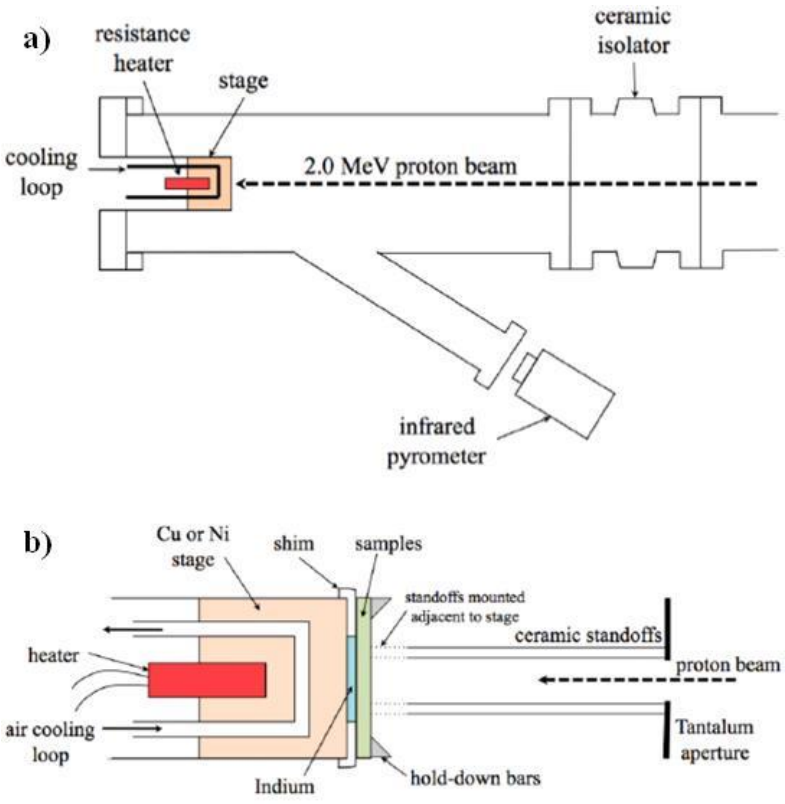

Figure 4.3 Irradiation stage mounting at end of beamline, from [158]**.**

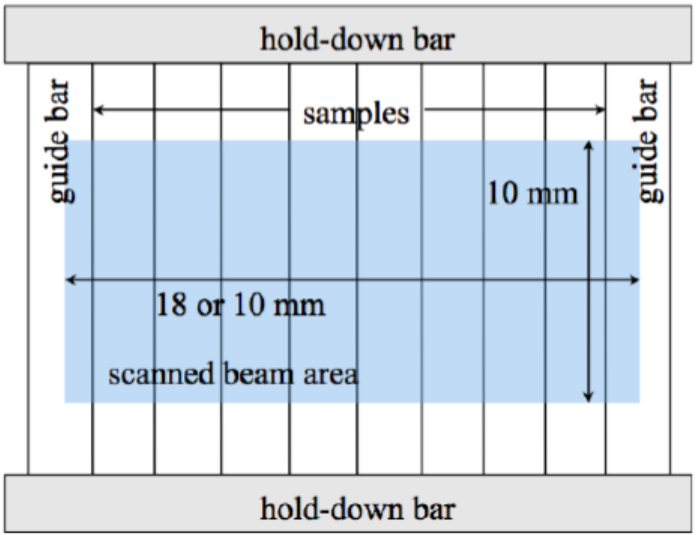

Figure 4.4 Typical irradiation region (i.e. scanned beam area), as defined by aperture plates with beam area fully covering samples and partially overlapping guide bars on each side, from [158]**.**

As a final step before irradiation commences, the installed thermocouples are used to calibrate a 2D infrared thermal pyrometer (Figure 4.3a), which records the temperatures of three areas of interest on the specimen at 0.1 Hz throughout the experiment. An example of the 2D thermal infrared pyrometer image is illustrated in Figure 4.5. Throughout the irradiation, a combination of resistance heating and air cooling were used to maintain the irradiation temperature at 500±10°C.

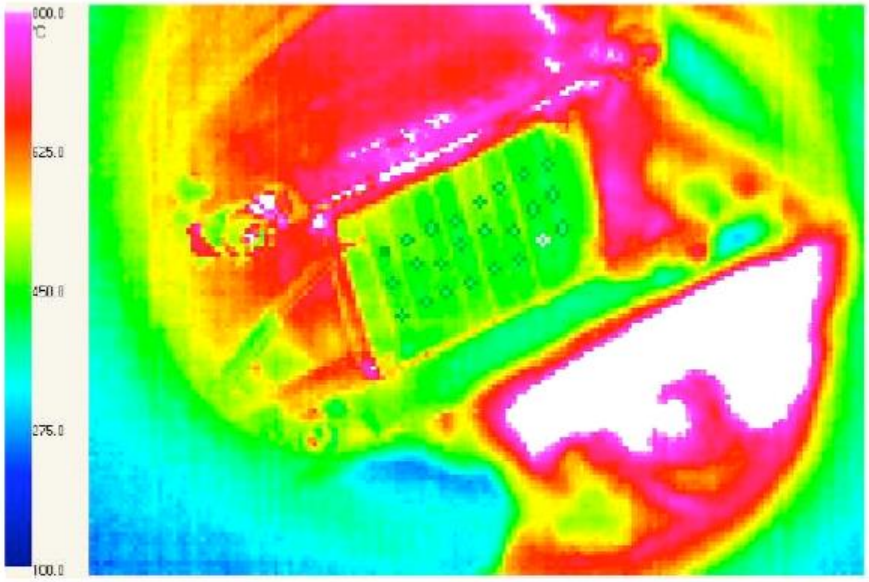

Figure 4.5 Typical 2D thermal infrared pyrometer image from a 500° irradiation, from [158]**.**

The specimens were then irradiated with 2.0 MeV protons in a 1.7 MV General Ionex Tandetron accelerator. During irradiation, the focused proton beam was raster-scanned across samples at a frequency of 2061 Hz in the vertical direction and 255 Hz in the horizontal direction. The duration of one scanning cycle in the vertical direction is 0.48 ms, and 3.9 ms in the horizontal direction. The ratio of these two scanning cycles is a non-integer number, which ensures that the beam path is offset from the previous scan cycle, which provides good spatial uniformity of the scanned beam area. Figure 4.6 illustrates this scanning pattern overlaid onto the alignment apertures. The resulting beam current density was ~22 $\mu A/cm^2$, yielding a dose rate of ~1.2 x 10^{-5} dpa/sec (Table 4.2).

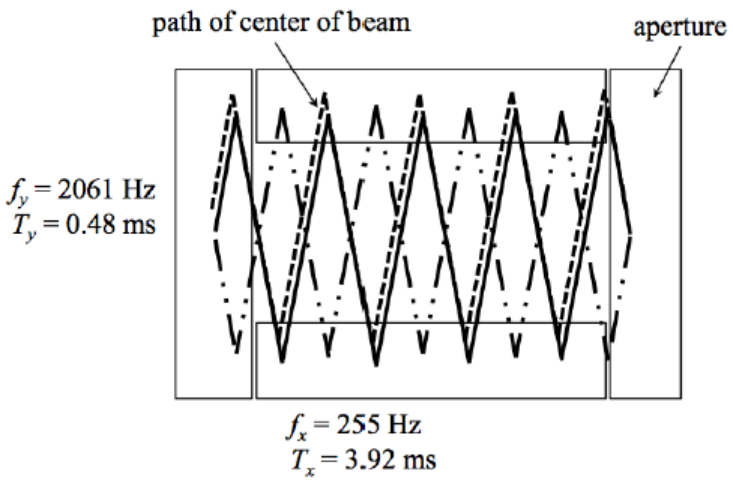

Figure 4.6 Pattern of raster-scanned beam during proton (and Fe2+ ion) irradiations, from [158].

Calculation of the displacement damage of 2 MeV protons incident on a nominal Fe-9%Cr alloy are calculated using the Stopping and Range of Ions in Matter (SRIM) software program. Damage was calculated through the simulation of 1,000,000 incident ions to enable high statistical confidence and a more finely distributed damage profile. The displacement energy for both the Fe and Cr target atoms is set to 40 eV [159]. The specific proton irradiation conducted to 3 dpa on the ODS, HCM12A, and HT9 alloys was conducted by Dr. Janelle Wharry [158] at MIBL in ~2010. At the time of that irradiation, the displacement damage of 3 dpa and the damage depth profile were calculated with the SRIM-2006 version [160] in "Detailed Calculation" mode and the displacements were obtained from the vacancy.txt file. A flux of 2.0 MeV protons normal to Fe-9%Cr produces a relatively uniform damage profile between 1 μm and 10 μm, with a damage peak at ~19 (Figure 2.2). Therefore, target irradiation dose is calculated at a depth of 9.5 μm from the surface, which avoids both the surface sink and the large damage peak. Subsequently, in 2013, Stoller, et al. demonstrated that SRIM calculations are more accurate when conducted in "Quick Calculation" (K-P) mode and the energy

partition results are used to obtain the estimate for displacements per ion [159]. With this recommended calculation method, and at these analysis depths, the accumulated dose would be ~2.1 dpa. For all other proton irradiations for this thesis (1 dpa and 7 dpa), the displacement damage was calculated with the SRIM-2013 software [44] in "Quick Calculation (K-P)" mode. The displacement damage calculated by SRIM is ~3 x 10^{-5} displacements/Å-ion.

The irradiation dose accumulation is in direct correlation with the flux of irradiating ions onto the target samples. Given that each irradiating proton carries a single unit charge (1.6 x 10^{-19} C/p^{+}), it is possible to monitor the flux of protons by measuring the beam current incident on the samples. At each measurement, the beam current is integrated over the amount of time passed to calculate the accumulated dose (in dpa) by the following equation:

$$Dose\ (dpa) = \frac{t \cdot I_{av} \cdot R_D}{N_{at} \cdot q \cdot A_{irr}} \tag{4.1}$$

where t is the total elapsed time of irradiation, I_{av} is the average current measured over the total elapsed time, R_D is the displacement rate (as calculated by SRIM), N_{at} is the atomic density of the target (~83.4 atoms/nm^3), q is the electronic charge (1.6 x 10^{-19} C), and A_{irr} is the irradiated region (as defined by the location of the Ta aperture plates). In this manner, the accumulated dose may be closely monitored. Once the target dose is achieved, the stage heating mechanism is disabled, allowing the temperature of the stage to decline to ~350°C before the irradiation flux is discontinued. The purpose of reducing the temperature prior to turning off the ion beam is to minimize any annealing of the target samples that may occur if the samples were held at 500°C at the time the beam is discontinued (even if only for a few minutes).

4.2.3 Fe^{2+} Irradiations

For each irradiation with Fe^{2+} ions at MIBL, the procedures for sample fabrication, polishing, stage assembly, beam alignment, and temperature monitoring were identical to those used for proton irradiation. However, for each irradiation, the specimens were irradiated with 5.0 MeV Fe^{2+} ions in the same 1.7 MV General Ionex Tandetron accelerator. As with proton irradiation, the focused beam was raster-scanned across samples at a frequency of 2061 Hz in the vertical direction and 255 Hz in the horizontal direction, yielding the same scanning cycle (Figure 4.6). The resulting beam current density was ~0.13 - 0.24 μA/cm^2, yielding a dose rate of ~2 x 10^{-4} dpa/sec (Table 4.2).

In the same manner as the proton irradiations, calculation of the displacement damage of 5 MeV Fe^{2+} ions incident on a nominal Fe-9%Cr alloy are calculated using the SRIM-2013 software program in "Quick Calculation (K-P)" mode. The damage profile (Figure 2.2) exhibits a steep gradient between the surface and the damage peak, which is located approximately 1.2 μm from the surface. Therefore, target irradiation dose is calculated at a depth of 600 nm from the surface, which avoids both the surface sink and the Fe implantation peak. The displacement damage calculate by SRIM is ~0.34 displacements/Å-ion.

As with proton irradiation, the irradiation dose accumulation is in direct correlation with the flux of irradiating ions onto the target samples. However, for heavier ions, measurement is accomplished by temporarily inserting a faraday cup in front of the samples and measuring the beam current. It is important to do this quickly, since irradiation is momentarily interrupted when the faraday cup is in place. Throughout the

irradiation, this current measurement is taken every ~20 minutes, or as needed depending on the stability of the beam current and the target dose. The accumulation of dose is monitored in the same manner and calculated using the following:

$$Dose\ (dpa) = \frac{t \cdot I_{av} \cdot R_D}{N_{at} \cdot q^2 \cdot A_{irr}} \quad (4.2)$$

where Eq. 4.2 only differs from Eq. 4.1 by the power of q in the denominator. For Fe^{2+} irradiation, q is squared due to the 2^+ charge of the incident ions.

4.3 Post-irradiation Sample Preparation

After each respective irradiation, the microstructure of each specimen was characterized to evaluate any irradiation-induced evolution of grains, dislocation density, and carbide phases, or any irradiation-induced dislocation loops or voids. Transmission electron microscopy (TEM) is the primary technique to conduct this analysis. In addition to the above features, characterization of the microstructure also entailed evaluating the evolution of the oxide nanocluster in the ODS, or any irradiation-induced solute clustering in the F-M alloys. Imaging of these nanoclusters is possible in TEM, particularly in areas of the lamellae having low dislocation contrast, allowing the z-contrast of the clusters to be more visibly prominent. However, this technique has limited detectability of nanoclusters <2 nm in diameter [6,161]. Thus, APT analysis complements the TEM work by identifying the <2 nm nanoclusters, providing results that more accurately quantify the average nanocluster size, number density, and composition. The following sections provide a summary of how samples from each specimen were fabricated for both TEM and APT analysis. These samples were created for each irradiation condition identified in Table 4.2, and for the as-received specimen of the model Fe-9%Cr ODS alloy.

4.3.1 TEM lamellae

TEM lamellae were prepared for all specimen conditions using the focused ion beam (FIB) lift-out technique on an FEI Quanta 3D FEG FIB at the Center for Advanced Energy Studies (CAES). TEM lamellae were cut and lifted perpendicular to the surface of the bulk material. In the case of proton and Fe^{2+} irradiation, this orientation provided a cross-section of the damage profile within the depth of the TEM film. Prior to milling, all specimen surfaces were protected with a 3 µm platinum deposit, which ensured the original irradiated surfaces were retained for reference. For each sample, a liftout ~2 µm in thickness was removed from the bulk via a series of trenching and cleaning steps to separate the sample from the bulk. Once the sample was removed, it was mounted onto a copper grid and attached using platinum deposit. Each sample was milled on both sides at 30 kV to an estimated thickness of ~100 nm, width of ~15 µm, and depth of ~7 µm (Figure 4.7). The samples were subsequently milled at 5 kV to an estimated thickness of 50-100 nm, followed by cleaning at 2 kV for approximately 1 minute on each side. The purpose of the cleaning process was to reduce any surface damage to the sample caused by the milling.

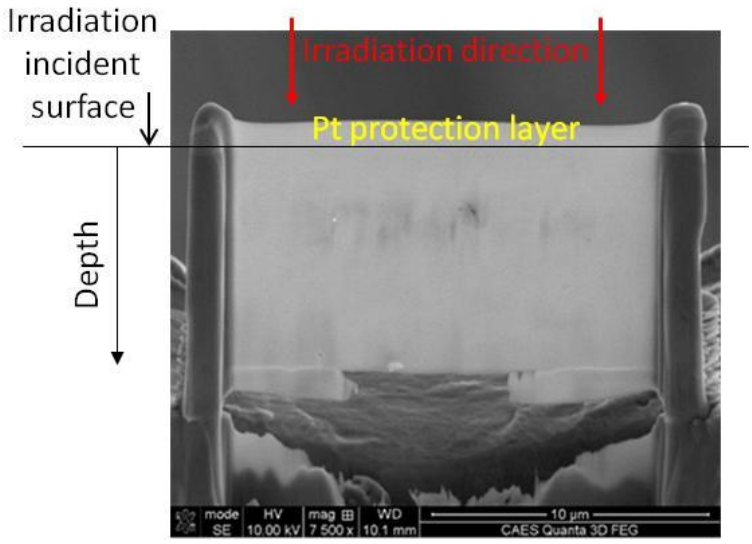

Figure 4.7 Typical sample geometry of TEM lamellae, imaged via SEM in the FIB, irradiation direction is specified for proton and Fe2+ irradiations only.

4.3.2 APT needles

APT needles were fabricated using the same FEI Quanta 3D FEG FIB at CAES. For the as-received, Fe^{2+} irradiated, and neutron-irradiated specimens, sample wedges ~2 µm wide and ~3 µm deep were cut and lifted in a direction perpendicular to the surface of the material (Figure 4.8a). The wedges were subsequently mounted onto the silicon posts (with platinum deposit) of a standard coupon and partitioned, resulting in 6-10 APT tips for each liftout (Figure 4.8b). Each tip was then milled using progressively smaller annular ring patterns to shape them into needles with a tip radius ≤ 50 nm [162], as shown in Figure 4.9. The needle was sharpened such that the tip of the needle was positioned just below the irradiated bulk surface. For proton-irradiated specimens, it is desired to position the needle tip ~1 µm below the irradiated surface in order to ensure sampling of the flat portion of the damage profile illustrated in Figure 2.2. Consequently, larger wedges ~3 µm wide and ~4.5 µm deep were cut and lifted from each proton-irradiated specimen. For these samples, attachment and annular milling was conducted in

the same manner, except the sharpening process was extended to remove the top 1 µm of material to position the tip of the sample accordingly.

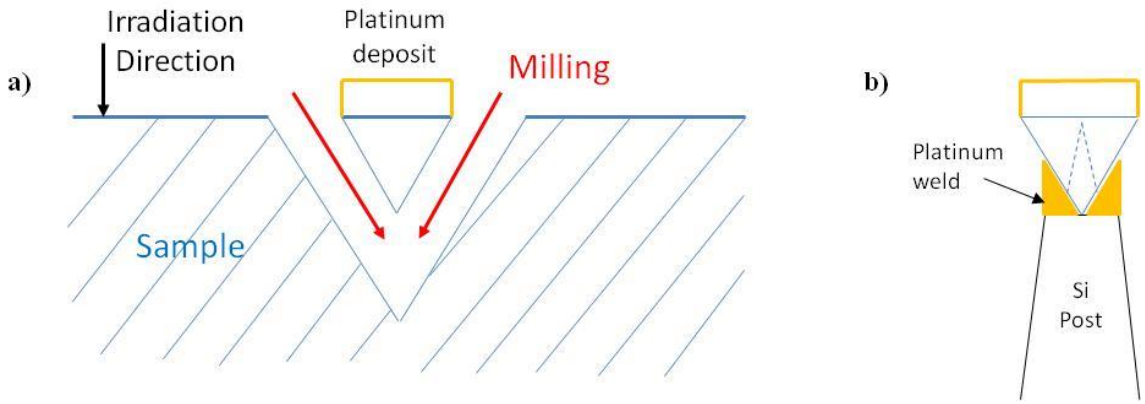

Figure 4.8 Typical sample preparation of APT needle: a) trenching to shape sample wedge, and b) mounting sample wedge onto Si posts of LEAP coupon.

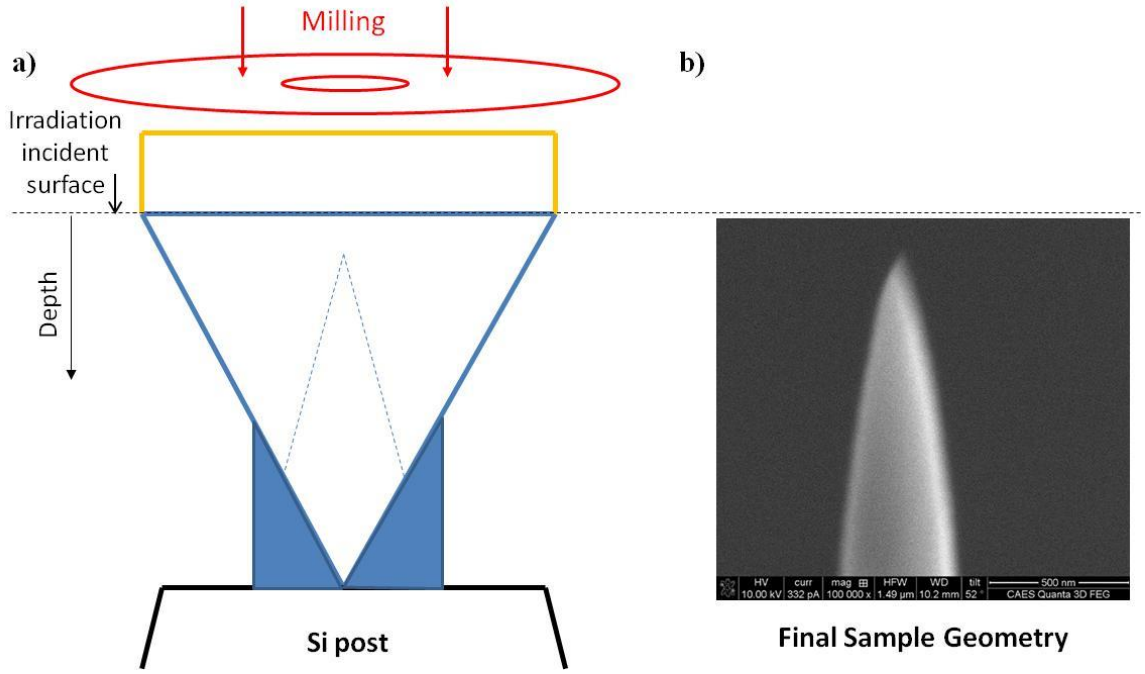

Figure 4.9 Illustration of needle shaping process showing a) annular ring milling, and b) typical final sample geometry imaged via SEM in the FIB.

4.4 Microstructure Examination

TEM specimens were analyzed using an FEI Tecnai TF30-FEG scanning transmission electron microscope (STEM) at CAES. This TEM features a field emission gun (FEG) source that operates at 300 keV and several attached analysis capabilities including scanning transmission electron microscopy (STEM) and electron energy loss spectroscopy (EELS), among many others. The following sections will describe the techniques used for imaging and characterization of the microstructure of each respective specimen in this study using TEM.

4.4.1 Bright Field Imaging

With the TEM lamellae thinned to 50-100 nm in thickness, bright field imaging is quiet effective at creating sufficient contrast to differentiate a multitude of features within the microstructure. As a result, bright field imaging is the first technique used to achieve an overall sense of the microstructure and evaluate any potential changes due to irradiation. For the as-received, proton- and neutron-irradiated specimens, the entire TEM lamellae is available for imaging of the microstructure. However, it is important to recognize that only the first ~1 um depth of the Fe^{2+} irradiated lamellae are influenced by irradiation. Furthermore, within this depth, the target analysis region resides at a depth of only 400-600 nm, which provides a relatively narrow area of sample which has experienced the target irradiation dose of each experiment and thus may be investigated. Image collection is conducted using Digital Micrograph software, while post-imaging analysis was conducted using ImageJ software.

The grain and lath structure of the alloys are typically imaged at a magnification of 5900x. Images are captured in succession while scanning across the analysis region of

the sample. Identification of grain and latch boundaries is accomplished through looking for continuously dark contrast lines, evidence of dislocation pile-up, and carbide phases, which typical reside on grain boundaries. For each grain that is identified, a measurement of its overall length (l_{gr}) and width (w_{gr}) is taken and the effective diameter (d_{gr}^{eff}) of each grain is calculated as:

$$d_{gr}^{eff} = \sqrt{l_{gr} \cdot w_{gr}} \tag{4.3}$$

An average effective diameter is also calculated for each specimen.

Carbide precipitates are typically imaged at a magnification of 12,000x and are identified primarily by their unique contrast with bright field imaging. Carbides typically display a darker, dislocation free contrast compared to the surrounding matrix, and are most often located on grain or lath boundaries. As with grains, the overall length (l_p) and width (w_p) of each carbide is measured and the effective carbide diameter (d_p^{eff}) is calculated as:

$$d_p^{eff} = \sqrt{l_p \cdot w_p} \tag{4.4}$$

An average carbide effective diameter is also calculated. Within each image, the relative analysis area in which the carbides were identified is measured. It is important to ensure that the analysis area of one image does not overlap with that of an adjacent image. The number density of carbide precipitates (N_p) is then calculated by:

$$N_p = \frac{n_p}{A_{tot} \cdot t_{av}} \tag{4.5}$$

where n_p is the total number of carbides identified, A_{tot} is the total image area analyzed, and t_{av} is the average measured thickness of the sample (see Section 4.4.3).

Dislocations are visible in bright field imaging as lines of dark contrast and are distributed throughout the microstructure. Depending on the orientation of each

individual grain, dislocations may be more or less visible, as typically Burgers vectors for the b.c.c. crystal structure are in the <111> family of directions [73]. In order to measure the dislocation density of an alloy, grains that exhibit the darkest contrast (and thus the highest density of dislocations) are selected for analysis. Within the selected grain, the areal density of dislocations is determined by measuring the linear density of dislocations for successively perpendicular measurements. A line of fixed length (l) is drawn within the grain and the number of intersecting dislocations across that line is counted (n_{disl}). Areal density of dislocations (N_{disl}) is then calculated for each line by:

$$N_{disl} = \left(\frac{n_{disl}}{l}\right)^2 \tag{4.6}$$

Finally, an overall average areal density of dislocations is calculated for each specimen.

After irradiation, it is possible for voids to be present in the microstructure of ODS and F-M alloys. If present, these voids are typically imaged via the through-focus technique in bright field TEM. It is generally easier to image voids in grains that exhibit low dislocation contrast, particularly if the voids are small. However, larger voids (>15 nm) are generally quite easy to identify anywhere within the sample. The through focus technique is conducted by first focusing the TEM onto a grain with low dislocation contrast. Next, the image is alternately under-focused and over-focused, respectively, to observe any changes in Fresnel contrast within the image. Spherical voids will typical exhibit a dark perimeter with a "hollow" bright center in the under-focus image, but will switch to exhibiting a bright perimeter with a "solid" dark center in the over-focus image. Smaller voids also tend to be invisible in the in-focused image. It is important to recognize that nanoscale phases (such as oxides) will also exhibit similar Fresnel contrast when imaged with the through-focus technique, although typically without a hollow

center in the over- or under-focused conditions. Larger oxides are also generally visible in the in-focused image. For each void identified, the diameter is measured, and an overall average diameter of voids (d_v), along with the standard deviation, is calculated. Similar to the carbides, a number density of voids (N_v) is determined as:

$$N_v = \frac{n_v}{A_{tot} \cdot t_{av}} \tag{4.7}$$

where n_v is the total number of voids identified, A_{tot} is the total image area analyzed, and t_{av} is the average measured thickness of the sample.

Upon irradiation, dislocation loops are a common side effect within the microstructure. Archival literature studies have commonly used techniques within bright field TEM imaging to image dislocation loops. The most common method is imaging with multiple two-beam conditions. This method is accomplished by the following steps: 1) locating a grain oriented on a low index zone axis (relative to the electron beam) such as [001], [011], and [111], 2) tilting the sample to achieve a two-beam condition in which ideally only one direction of beams are illuminated in the diffraction pattern, 3) capturing images of dislocation loops that have burgers vectors which are visible as a result of the respective two-beam condition, and then 4) tilting to another two-beam condition on the same grain and capturing more images. Although this technique is proven and effective, some inherent challenges with ODS and F-M alloys make this technique cumbersome and somewhat unreliable: a) the small grain structure makes it very difficult to tilt the sample without the image moving away from the particular grain in question, b) the high dislocation density of grains tilted onto low index zone axes floods the image, complicating the reliable distinguishing of loops from the rest of the dislocation forest. Due to these technical challenges in imaging dislocation loops, an alternate technique for

imaging dislocation loops via STEM was selected. The following section will outline the details of this relatively new method, which proved to be vastly more reliable.

4.4.2 STEM Imaging

Dislocation loops were imaged in STEM mode on the same instrument at CAES following a procedure outlined by Parish et al. [161]. Prior to imaging with STEM, the sample is imaged in TEM mode to locate a grain within the target analysis region that is oriented close to a low index zone axis such as [001], [011], or [111]. For the grain, the sample is tilted to align the electron beam of the microscope to as closely parallel to the zone axis as possible. Once this is accomplished, an image of the grain and the diffraction pattern for the grain is captured. Just before switching the microscope to STEM mode, the smallest condenser aperture at the top of the microscope is inserted and aligned with the source beam. The purpose of the small condenser aperture is to minimize the collection angle (β) of the beam interacting with the sample. Once the instrument is transitioned into STEM mode, the camera length for imaging is increased to its highest setting (4.5 m) to minimize the convergence (α) angles, which enables a STEM "bright field" image. This resulting image will reduce the amount of contrast due to the surrounding dislocation forest, while enabling all orientations of dislocation loops visible without any forbidden reflections (as is the case with two-beam conditions).

Identification of dislocation loops within the STEM images is aided by dislocation loops orientation maps developed by Yao, et al. [163] for b.c.c. Fe materials. Dislocation loops in b.c.c. Fe are known to commonly reside on the {001} and {111} habit planes. In this study by Yao, et al., the expected orientation and visibility of loops on each habit plane are identified (Figure 4.10). In order to use these maps, the diffraction

pattern acquired above is aligned with the map vectors, providing a prediction of each dislocation loop orientation and appearance within the image. In some cases, dislocation loops will appear as round circles, while loops with different orientation may appear as "edge-on". For loops imaged close to an “edge-on” condition, the longer dimension observed is taken to be the loop diameter [163]. For each loop identified, the diameter is measured, and an overall average diameter of loops (d_l), along with the standard deviation, is calculated. Similar to the carbides and voids, a number density of loops (N_l) is determined as:

$$N_l = \frac{n_l}{A_{tot} \cdot t_{av}} \tag{4.8}$$

where n_v is the total number of voids identified, A_{tot} is the total image area analyzed, and t_{av} is the average measured thickness of the sample.

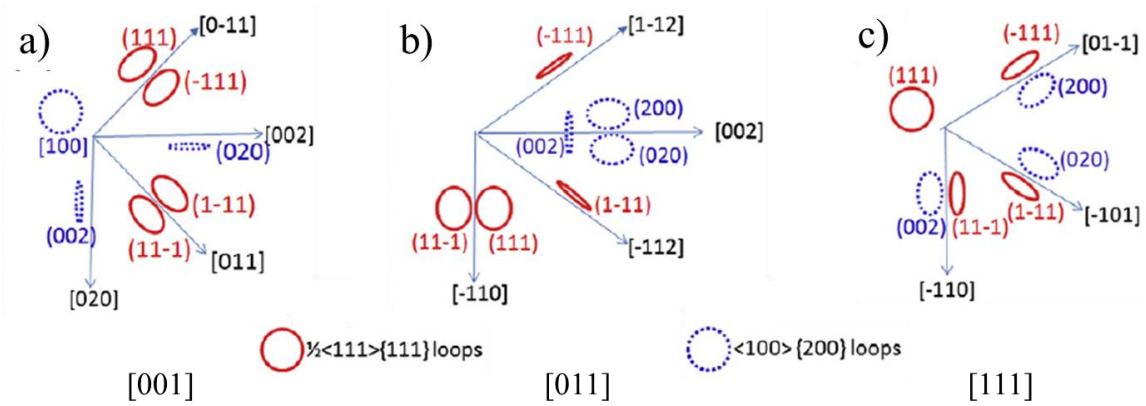

Figure 4.10 Dislocation loop orientation maps for the a) [001] zone axis, b) [011] zone axis, and c) [111] zone axis, from [163]**.**

It is important to note with the STEM imaging technique the visibility of loops is highly dependent upon the TEM lamella thickness. Lamellae less than 50 nm thick are generally more effective, but it is recognized this target thickness is difficult to

consistently achieve during sample fabrication. As a result, the loop visibility may vary with lamella thickness, which can lead to disparity in measured number densities.

4.4.3 Thickness Measurement

In order to measure the volumetric density of microstructure features such as carbides, voids and dislocation loops, a measurement of the sample thickness is required. This is accomplished using the electron energy loss spectroscopy (EELS) technique, which is an attached capability of the TEM at CAES. With EELS, a detector located below the sample collects electrons that translate through the sample based on their residual energy. The resulting measurement is a spectrum of energies (Figure 4.11), with a large, sharp peak at high energy which corresponds to electrons that have lost essentially zero energy as a result of passing through the sample. Using the Digital Micrograph software, an integration underneath the energy spectrum, not including the zero-loss peak, will provide an estimated thickness (t) at the location of the measurement. For this integration algorithm, it is key to provide the size of the respective condenser and objective apertures for the measurements. In the case of this study, the 100 nm condenser aperture and 50 nm objective aperture were used for each EELS thickness measurement. Multiple thickness measurements were conducted at a variety of locations within each sample and an average thickness (t_{av}) was calculated.

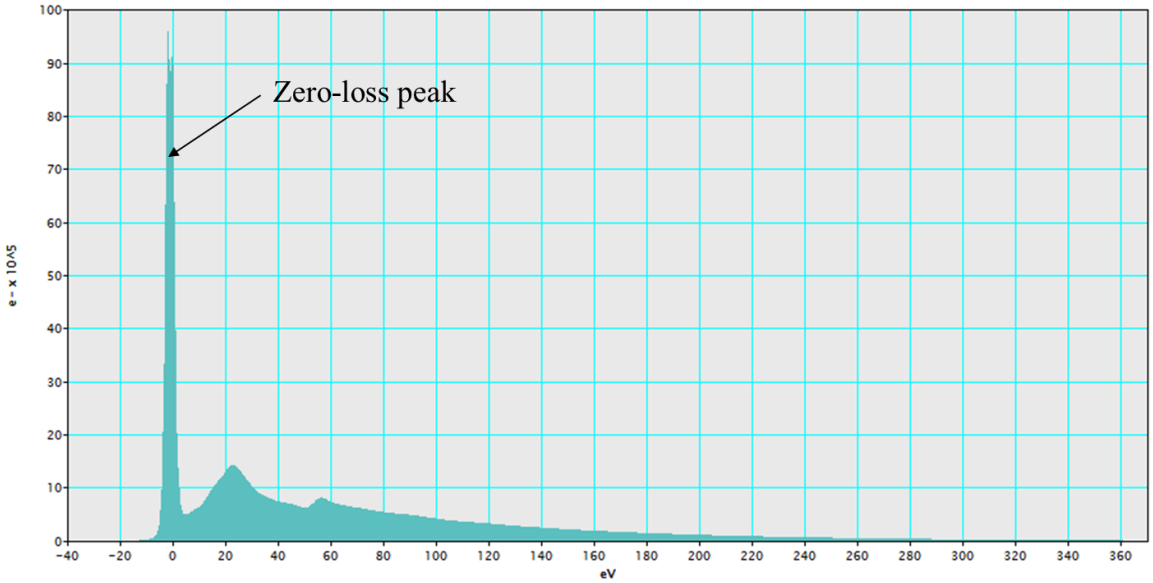

Figure 4.11 Example of EELS spectrum collected from a typical TEM lamella, collected using Digital Micrograph software.

4.4.4 TEM vs. APT Measurements

Throughout literature, a variety of characterization techniques are used to measurement the morphology of nanocluster and nanoscale phases in ODS and F-M alloys. Generally, these techniques fall into two primary categories of characterization: 1) TEM-based, and 2) APT-based. A few other techniques including x-ray absorption fine structure (XFAS) spectroscopy [101], glancing-incident angle x-ray diffraction (GIXRD) [99] and small angle neutron scattering (SANS) [82,100,164,165] are occasionally used as well. Characterization using TEM/STEM is often used as a combination of techniques aimed at conducting structural analysis with HRTEM [12,69,72,79,81,83,84,93,104,110,111,120,121,124], or compositional analysis with EFTEM [5,6,59,69,96,107,110–112,118,129,166] in addition to bright field TEM imaging.

For this thesis, the primary focus is the characterization of nanocluster morphology (size and number density) and its evolution as a result of irradiation. Bright

field images of the oxide clusters in Fe-9%Cr ODS were also obtained in TEM by reviewing areas having low dislocation contrast, allowing the z-contrast of the clusters to be more visibly prominent. For example, in the as-received specimen, the clusters appeared to be homogeneously distributed (Figure 4.12a). A similar distribution is observed in the specimen proton-irradiated to 3 dpa at 500°C (Figure 4.12b). On the other hand, in the specimen neutron-irradiated to 3 dpa at 500°C, the z-contrast of the clusters does not appear to be as prominent in the bright field images (Figure 4.12c). It is also important to recognize the local thickness of each sample for these images varies between 50 to 100 nm, so the perceived density of the clusters in each image cannot be directly compared. For all specimens, it becomes difficult to resolve any nanoclusters that are less than 2 nm in diameter [6,161]. As a result, atom probe tomography is believed to achieve a more objective determination of the oxide nanocluster average size and number density.

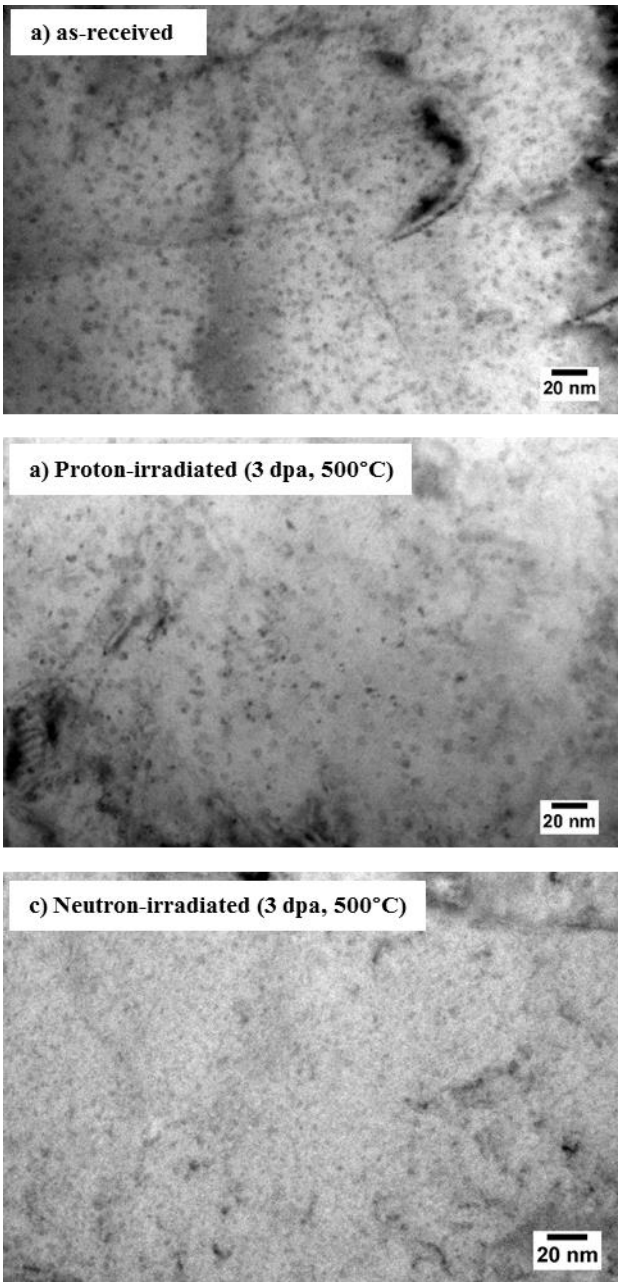

Figure 4.12 Bright field TEM images of oxide distributions for a) as-received, b) proton-irradiated (3 dpa, 500°C), and c) neutron-irradiated (3 dpa, 500°C) in Fe-9%Cr ODS.

4.5 Nanocluster Analysis

Atom probe tomography (APT) is increasingly being used to complement transmission electron microscopy (TEM) to characterize 3D chemical compositions and distributions at high spatial resolution, particularly for nanofeatured materials containing

phases below TEM resolution limits [6,8,9,24,25,40,59,86]. Local electrode atom probe (LEAP) tomographic cluster analysis algorithms provide an objective means to identify and measure the size and number density of these nanoscale phases [167]. The following sections will describe the techniques used for LEAP analysis, reconstruction, and cluster identification and analysis for each respective specimen in this study using APT.

4.5.1 LEAP Data Collection

For each specimen, a series of sample needles were fabricated according to the procedure outlined in Section 4.2. Each needle was analyzed one at a time using a Cameca LEAP 4000X HR at CAES. Within the LEAP, a high frequency voltage (or a pulsed laser) is applied to the needle-shaped sample. The thermal spike resulting from the voltage (or laser) ionizes and evaporates atoms from the surface, which are then accelerated towards a detector screen. The detector captures the location of incidence and the time-of-flight of the ion traveling from the pulse to impact with the detector (Figure 4.13). This process is continually repeated (up to several hours) to collect tens of millions of ions. The resulting data set includes the location of each incident ion and a spectrum of time-of-flight measurement peaks which may be translated into a mass-to-charge ratio for each ion, allowing elemental identification.

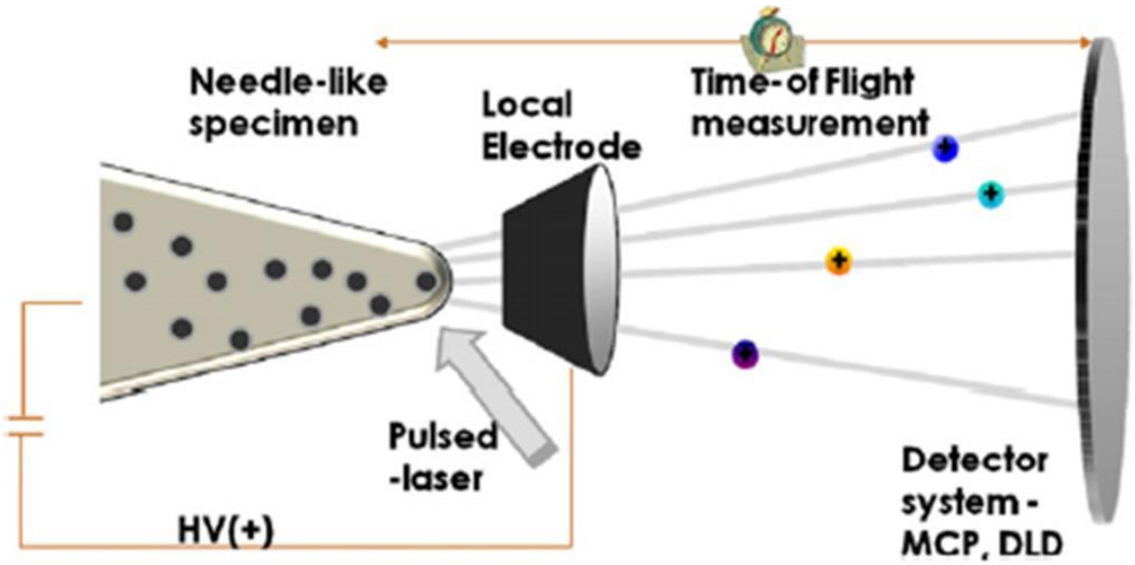

Figure 4.13 Schematic of atom probe tomography analysis technique, from [168].

For all of the specimens in this study, the LEAP was operated in laser pulsed mode with the samples held at 40 K. The sample is initially aligned manually with the electrode, followed by evaporation, which is largely an automated process. During evaporation, laser power ranged from 40-100 pJ, with a pulse repetition rate of 200 kHz. Evaporation may continue until the sample is exhausted (i.e. evaporation reaches the Si post), but most often ends when the sample eventually fractures due to thermal loading of the pulsing process. It is important to recognize the detector efficiency of the LEAP 4000X HR is only 36%. Even with this relatively low efficiency, the resulting data sets in this study ranged in size from <1 million ions up to ~60 million ion counts per needle. Once each sample has concluded evaporation, the data set is stored as a .RHIT file and is available for analysis offline using a separate software package (Section 4.5.2). A typical histogram of events seen by the detector for one needle is shown in Figure 4.14.

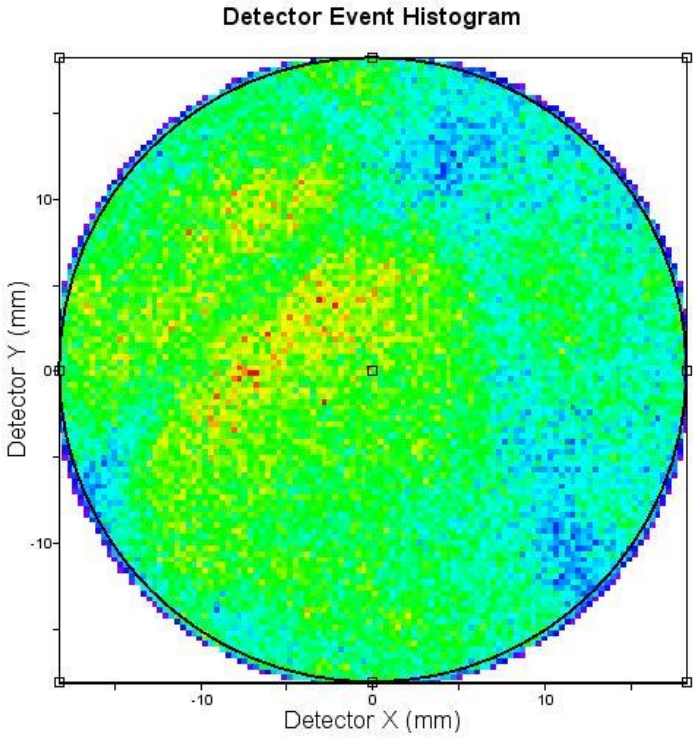

Figure 4.14 Typical detector event histogram from the field evaporation.

4.5.2 Reconstruction

The data analysis for each LEAP sample was conducted using the Integrated Visualization and Analysis Software (IVAS) Version 3.6.12. The IVAS software enables processing of the .RHIT file from the LEAP analysis to reconstruct the original sample "atom-by-atom" and is a versatile tool for interrogating the data via composition analysis, cluster identification and analysis, and many other techniques.

The first step of reconstruction is to establish the selected ions which will be used for virtually rebuilding the sample. This is accomplished via the voltage history of the LEAP ion evaporation, which is plotted against the sequence of ions collected by the detector. A typical voltage history from a single sample needle is given in Figure 4.15. In general, it is desirable to maximize the amount of ions from the voltage history used for reconstruction in order to maximize the analysis volume and counting statistics.

However, there are some areas in the curve that should be avoided. First, the ions collected at the very beginning of the analysis are collected as the LEAP process is being calibrated by the operator. These ions represent a very small volume and are difficult to accurately reconstruct. Second, it is beneficial to avoid any locations of the sample where a fracture of the sample has occurred. This would be evident in the voltage history by a large discontinuity in the history curve (example in Figure 4.16). Examples of the optimum selection of ions, as indicated by a highlighted box in both Figure 4.15 and Figure 4.16 is provided. Every sample will have its own unique voltage history. If it is unclear which ions in the history are best to select, it is suggested to iterate reconstruction with different sets of ions and evaluate which set yields the most reliable results.

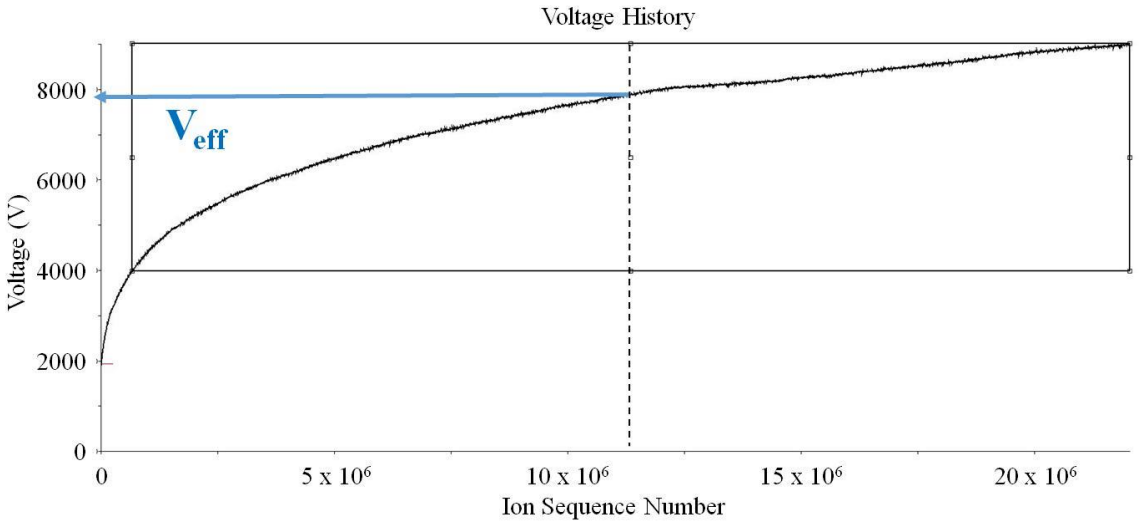

Figure 4.15 Typical voltage history from the LEAP evaporation process for a single sample needle. The highlight represents the selected ions for use in reconstruction.

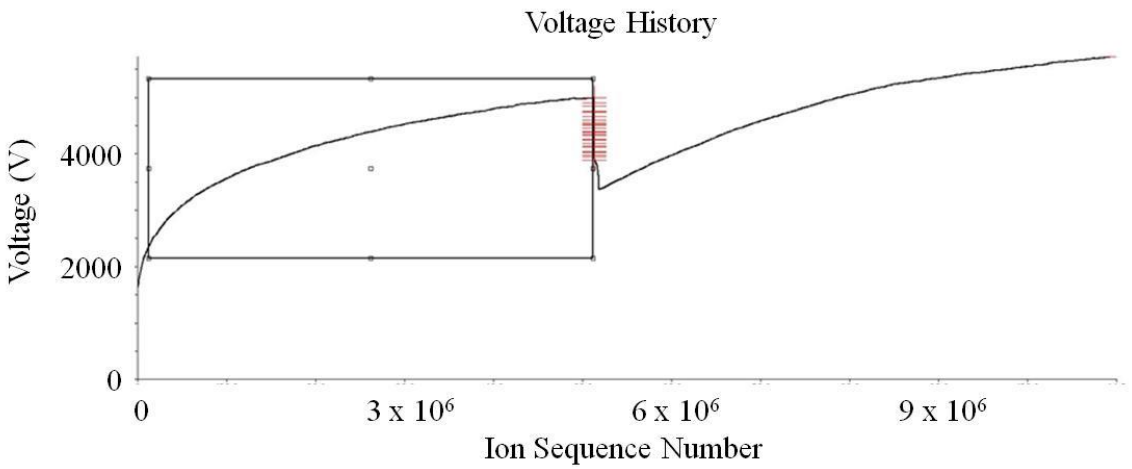

Figure 4.16 Example voltage history from the LEAP evaporation process which exhibits a fracture event during the collection process.

The next step in the reconstruction process is to initiate the time of flight (TOF) correction. This is an automated process within IVAS which translates the TOF information for each ion collected into a mass-to-charge ratio for each ion. The net result of this conversion is a distribution of counts for different mass-to-charge ratios from the sample, an example of which is illustrated in Figure 4.17. In this distribution, the user has an opportunity to identify the peaks highlighted in red. Knowledge of the material composition is particularly useful for this step, as well as the relative abundance of different elemental isotopes. Since Fe is by far the most prevalent element in the alloys of this study, it is helpful to identify these peaks first. Upon evaporation, the sample atoms are typically ionized to either a 1^+ or, more commonly, a 2^+ charge. It is also possible for higher charge ions, but less frequently. For Fe, the most abundant isotope is Fe^{56}. If these atoms are ionized to a 2^+ charge, the corresponding mass-to-charge ratio would equal 56 / 2 = 28. As a result, the largest peak, which is closest to a mass-to-charge value of 28, may be positively identified as the $^{2+}Fe^{56}$ isotope. The same logic may be applied to all other isotopes of Fe, as well as all of the other elements that make up the composition of the

studied alloy. It is important to recognize that some isotope peaks overlap, such as those of $^{58}Fe^{2+}$ and $^{58}Ni^{2+}$ at a mass-to-charge ratio of 29. For situations such as this, the peak should be identified as the elemental isotope which will be in most abundance given the alloy composition. In this example, the peak at 29 is identified to be $^{58}Fe^{2+}$ because the bulk concentration of Fe is ~1500 times that of Ni, although it is probable that a minority of these ions are $^{58}Ni^{2+}$. At this stage, it is not possible to deconvolute this peak into two separate elements.

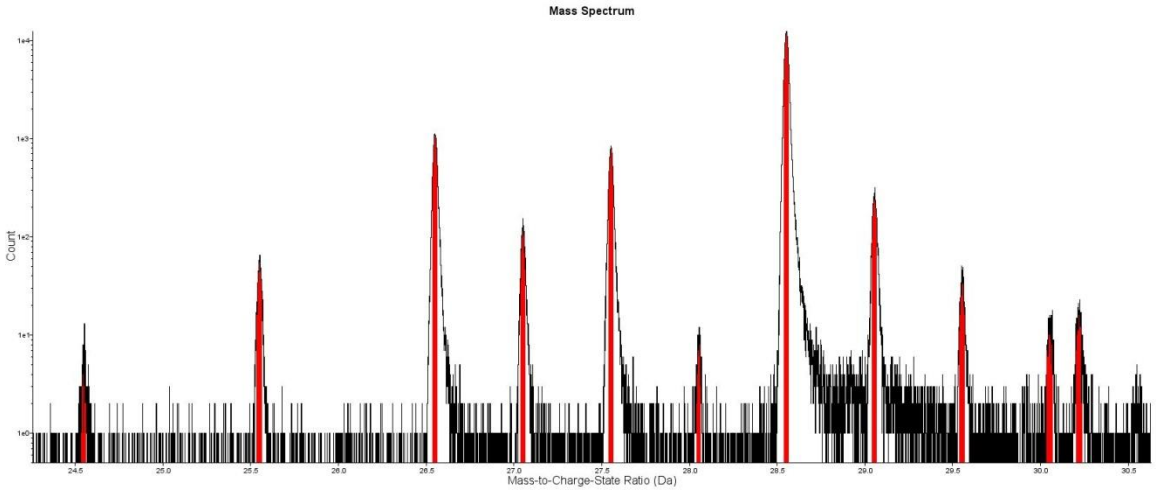

Figure 4.17 Example mass-to-charge ratio distribution prior to final calibration for the Fe-9%Cr ODS alloy. Peaks highlighted in red may be identified by the user to calibrate the mass spectrum.

On occasion, sample ions will evaporate together as a compound and impact the detector simultaneously. As a result, their time of flight will correspond to a higher mass equal to the combined masses of the respective atoms. Examples of this seen in the ODS alloy are oxide compounds such as FeO, CrO, YO, and TiO. Consequently, these peaks will correspond to "combined mass"-to-charge ratio values. Unfortunately, it is not possible to identify these peaks at this calibration step, but it is be possible to identify these compounds at a later time. Once all of the possible peaks have been identified, the

IVAS software will calibrate the full mass-to-charge spectrum, locating the identified peaks onto their known mass-to-charge ratios and locating all remaining peaks at the best "fit" to the spectrum as possible.

Once the mass spectrum has been calibrated, the analyst has an opportunity to "range" the peaks within the mass-to-charge ratio spectrum. In the same manner as above, each peak is identified based on it mass-to-charge ratio and its relative isotope abundance. IVAS provides several analysis tools to assist this process. Once a peak has been positively identified, a "range" of mass-to-charge ratio within the spectrum is selected to assign the ion counts within the peak to an element or compound. Within the APT community, some debate exists about where to start and end each range within the peak. Some argue that the range should start at the full-width half maximum (FWHM) front edge of the peak, and end at the FWHM back edge of the peak. Alternatively, and for all experiments in this study, the range is defined at edges located at the base of the peak, where the peak begins to rise above the background. Following this approach enables the maximum amount of atoms to be identified within the data set, increasing confidence in the reconstruction. Examples of peaks ranged at FWHM and at full width are given in Figure 4.18. The process is repeated, assigning and ranging each peak for their respective element or compound. For small data sets, many of the peaks may be difficult to differentiate from the background level in the mass-to-charge spectrum. As a result, only data sets containing > 2 million ions were used for APT analysis. Once all of the peaks have ranged, the next step is to define the tip profile for reconstruction.

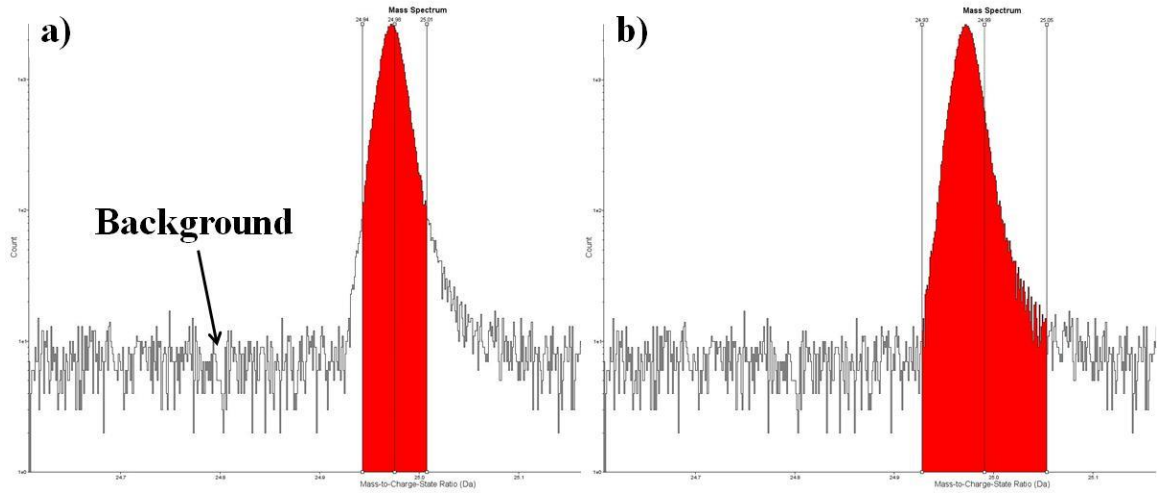

Figure 4.18 Example peaks ranged at a) full-width half maximum (FWHM), and b) full-width. The approach in b) was used for all peaks in this study.

The primary goal in reconstructing the data set is to approximate the original geometry and morphology of the sample needle as closely as possible. In order to accomplish this, the value of several parameters must first be identified and entered into IVAS including: a) the image compression factor (ICF), b) the k-factor (k), and c) the evaporation field (F). The most influential of these factors is the ICF, which may be estimated based on the voltage history of the evaporation (Figure 4.15). The ICF provides information about the amount of "compression" the trajectory of ions has experienced en route to the detector. As ions are evaporated and accelerated towards the detector, their flight path will follow a arced trajectory due to the accelerating voltage narrowing their flight path and resulting in a compression in their detector impact location, as illustrated in Figure 4.19. This image compression factor (ξ or ICF) is strongly correlated to the voltage and Prosa, et al. [169] have shown them to be related by the curve in Figure 4.20. Within the IVAS software, the default value for the ICF is 1.65, which is most accurate for a collection voltage of ~2800 V. But this voltage is typically well below the collection voltage history of all of the samples collected in this study. Since the ICF varies as a

function of collection voltage (Figure 4.20) [169], it would be ideal to collect data sets with a relatively constant voltage history. However, accomplishing this requires APT needles with a shank angle close to zero [169], which may not be practical for all materials and users, as was the case in this study. As a result, an "effective" voltage, V_{eff}, was estimated for each data set by selecting the collection voltage at the mid-point of the data history (Figure 4.15). Using the specific V_{eff} from each data set, an "effective" ICF_{eff} was then selected (Figure 4.20).

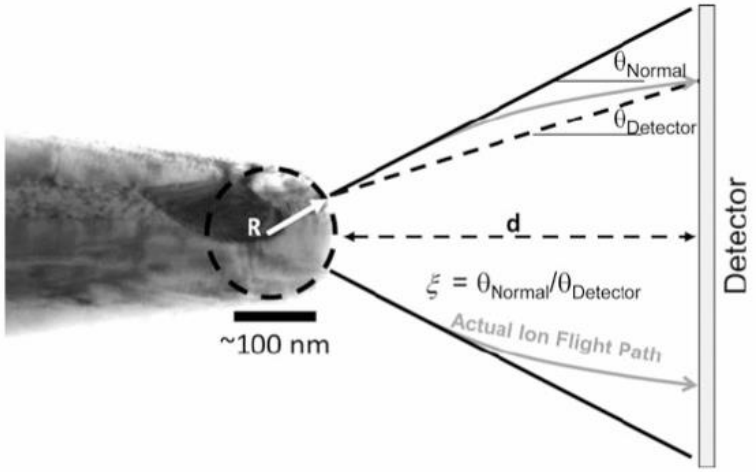

Figure 4.19 Illustration of image compression factor (ξ) and its influence on detector impact location, from [170].

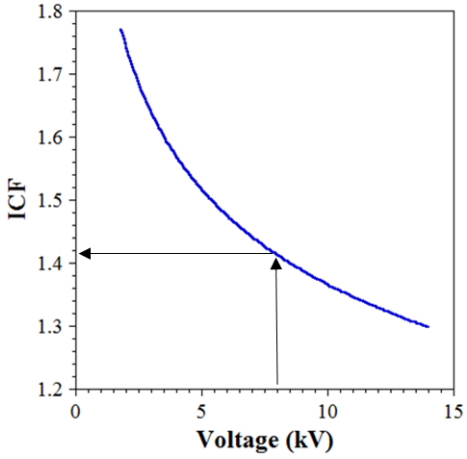

Figure 4.20 Relationship between collection voltage (V) and image compression factor (ICF), from [169].

The *k*-factor is also an important geometric factor that influences the reconstruction geometry. It is dependent on the tip radius of the sample, the shank angle and the relative proximity to the electrode during the LEAP process. In this experiment, each sample was fabricated following the same process, and LEAP was consistently conducted with the samples ~40 μm from the electrode. Based on these consistencies, the *k*-factor was consistent for each data set reconstruction at a value of 3.30.

Finally, the evaporation field, *F*, is dependent on the material analyzed. Each element will require a slightly different field value for evaporation. Given that each alloy is this study is predominantly Fe-based, the known field for Fe (33.00 V/nm) was used for each reconstruction. It is important to recognize that the evaporation of solutes within the samples is influenced by this field. As a result, localized concentrations of solutes, such as nanoclusters, may evaporate more readily or less readily depending on the elemental composition of the nanoclusters. This fluctuation in evaporation rate can have a small influence on the resulting density and measured size of the nanoclusters. Unfortunately, there is not any practical solution to this, but it is an important artifact for the analyst to be aware of. An example of the interface in IVAS for entering reconstruction parameters is shown in Figure 4.21. Before reconstruction, it's also critical to confirm the primary element (e.g. Fe in this study) is selected.

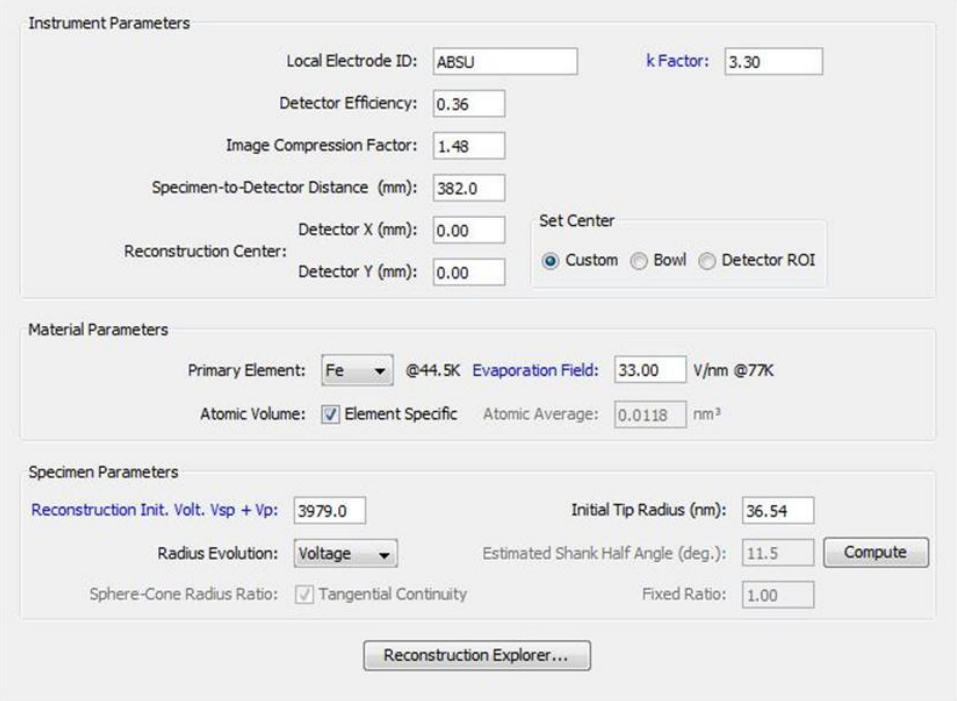

Figure 4.21 Typical interface in IVAS version 3.6.12 for entering parameters that define the reconstruction and data set geometry.

Within IVAS, there are three different possible methods for defining the tip profile of the data set, which will prescribe the corresponding shape of the reconstruction: 1) "Voltage" mode, 2) "Shank" mode, and 3) "Tip profile" mode. The voltage (V) at the time of ion evaporation is related to the tip radius of the sample (R_0), which can be written as [170]:

$$R_0 = \frac{V}{kF} \tag{4.9}$$

in which k is the geometric k-factor (3.30), and F is the evaporation field of the material sampled (33.00 V/nm for Fe). These values are taken as constants for the materials and sampling procedures used in this study. Consequently, the sample radius is essentially proportional to the collection voltage, which means the voltage history provides useful data for reconstructing the evolution of the sample radius during the LEAP analysis. For

all three reconstruction modes, the initial voltage is used to calculate the initial sample radius.

For reconstruction in "Voltage" mode, IVAS will simply use the entire voltage history (e.g. Figure 4.15) to calculate the tip radius throughout the entire evaporation history. The net result is a reconstructed tip radius which increases proportionally with the voltage increase and the sample. This methodology is generally the simplest and most accurate means for reconstruction as long as the voltage history is continuous. Conversely, if the voltage is discontinuous (e.g. Figure 4.16) the net result of reconstruction in this mode will be a sample that also contains this discontinuity, which is not representative of the original sample geometry. As a result, for data sets with discontinuous voltage history, reconstruction in Shank mode or Tip profile mode are likely to be more effective.

For reconstruction in Shank mode, it is required to predefine the shank angle of the original sample (i.e. the angle between the slope of the sample sides and the vertical axis of the tip). IVAS will estimate this angle based on the voltage history of the LEAP analysis, so it is possible to use this estimated value or manually enter a unique value. Typically, it is beneficial to generate "Preview" reconstructions with multiple angles and select the one which appears to reconstruct the data set in the most representative manner. The net result will be a reconstruction with an initial tip radius calculated from the initial voltage and then a linear side slope of the sample according to the defined shank angle. This mode succeeds at eliminating any profile discontinuities that would come from a discontinuous voltage profile, but accuracy of the evolving tip radius is also partially compromised.

For reconstruction in Tip Profile mode, it is possible to manually define the evolution of the tip radius. This is accomplished by importing an image of the sample tip (as taken via the SEM microscope in the FIB) prior to the LEAP analysis. Using this image, the corresponding tip radius of the sample is measured at a range of depths, enabling the construction of a tip radius profile. IVAS will then use this tip profile to define the resulting geometry of the reconstructed data set. This mode is most useful for very large data sets (i.e. > 30 million ions) to help ensure the radius evolution is consistent with the original sample.

Once the reconstruction parameters are set, the next step is to generate a "Preview" reconstruction (Figure 4.22). This provides an opportunity to review the resulting shape and cluster morphology of the data set. If this is satisfactory, the analyst may "Save Reconstruction" and proceed with generating the full reconstruction. IVAS will position each atom based on its relative detector position, the ICF, and the sequence in which it impacted the detector. Inevitably, these inputs may not perfectly converge on the precise location of every original sample atom. As a result, the algorithm will attempt to consider each input and locate each atom at is best "fit" location. As a result, the reconstruction will often exhibit localized fluctuations in atomic density to enable this best "fit". Although this is undesirable, it is also unavoidable due to the limitations in requiring ICF and the k-factor to be constant for the entire reconstruction and the estimations used in the tip profile generation. The procedures outline above are designed to minimize this effect and maximize the integrity of the resulting reconstruction.

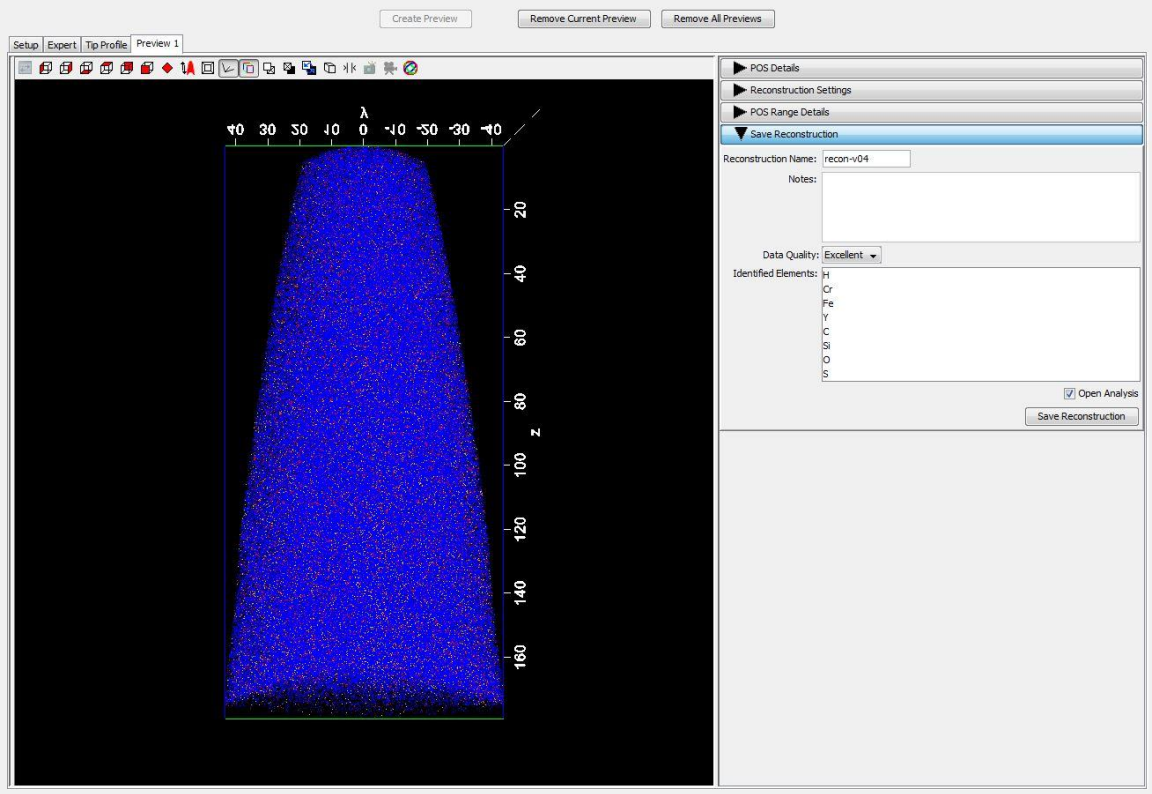

Figure 4.22 Typical "Preview" reconstruction in IVAS version 3.6.12.

Once the final reconstruction is completed, two more activities are critical for the accuracy of the reconstruction. First, it is recommended to review and update the mass spectrum ranging once again. It is at this stage that the analyst will have the most resolution of the spectrum, and can define all ions and compounds accordingly. Finally, the analyst should inspect the solute distribution for each element in the reconstruction, confirming any unique morphology or clustering is consistent with expectations. In the case of ODS and F-M alloys, the nanoclusters typically appear spherical when observed in the TEM. Therefore, it is expected that any ODS oxide nanoclusters (Y-Ti-O-rich) and F-M nanoclusters (Si-Mn-Ni-rich, Cu-rich, or Cr-rich) should appear as approximately spherical in the 3D reconstruction. If they instead appear to be consistently "stretched" in the horizontal or vertical directions, it would suggest the accuracy of the reconstruction is

not optimum, in which case an iterative process for reconstruction should be pursued until the solute morphology is the most representative.

Once satisfied with the reconstruction, a systematic analysis of the cluster morphology and composition may proceed. The following section provides detailed descriptions of the procedures followed to analyze nanoclusters in the ODS and F-M alloys used in this study.

4.5.3 Cluster Identification and Analysis

With a complete reconstruction of each data set, the IVAS software enables the identification and analysis of solute clusters using multiple techniques. For the work in this thesis, two complimentary techniques are used to maximize confidence in the objective identification of clusters: 1) construction of isosurfaces (i.e. iso-concentrations), and 2) the maximum separation method. Each technique is executed independently and the results are compared to ideally accomplish similar results, thus yielding confidence in the analysis parameters.

With the completed reconstruction, the isosurfaces method is used first for the clustered solutes in the studied specimen. In the case of Fe-9%Cr ODS, these solutes are Y, Ti, and O. For the HCM12A and HT9, solutes of Si, Mn, Ni, and P are studied. In addition, for HCM12A and HT9, separate isosurfaces and cluster analysis are conducted for Cu and Cr solutes if there is visible evidence of clustering of these elements in the data set. Isosurfaces are created in IVAS by "right-clicking" on the "3D Grid" in the Analysis menu for the data set. Initially, the solutes of interest are selected, as identified above (Figure 4.23a). Next, the user identifies the concentration threshold (in at.%) for the isosurfaces to be constructed (Figure 4.23b). For this study, a threshold of 6 at.% was

used for all of the studied alloys and elements, which consistently produced concentration profiles that most closely matched the size of clusters visible in the data set. On occasion, it is helpful to vary this threshold to perceive the influence of this parameter and/or adjust it as necessary. Once a concentration threshold is established, the isosurfaces are finalized (Figure 4.23b). The IVAS software measures the local concentrations of each set of solutes and constructis surfaces across the concentration gradients at the threshold identified. Referring back to the Analysis menu, an itemized list of the clusters is now available. With this list, the number of clusters is counted. For smaller samples in which each cluster is visually distinguishable, the number of clusters generated via isosurfaces is compared to the visual number of clusters. Ideally, these two number are a close match, suggesting the isosurfaces do an adequate job at distinguishing each individual cluster. If the numbers are not consistent, it is recommended for the user to reiterate the analysis using varying concentration thresholds.

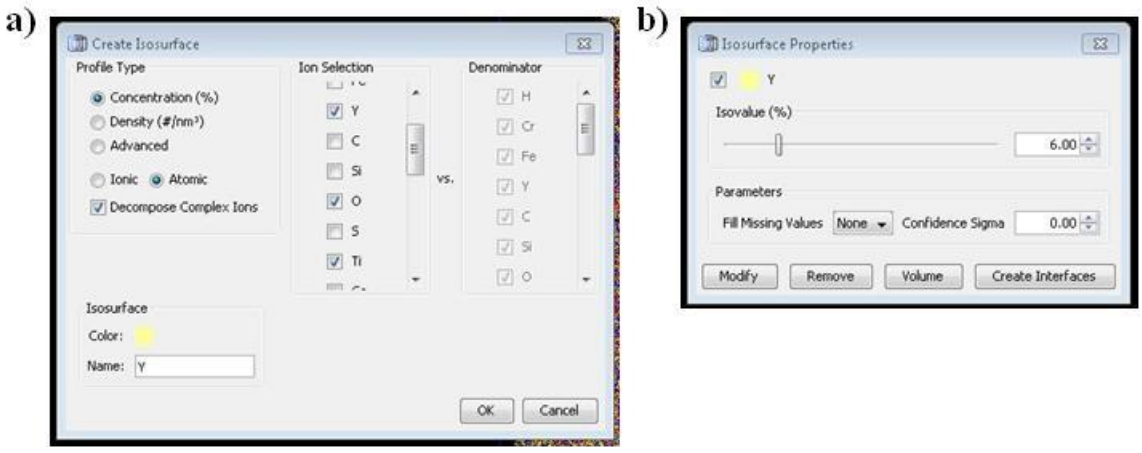

Figure 4.23 Entry points within IVAS for construction of solute iso-concentration surfaces: a) solute selection, and b) concentration threshold (i.e. Isovalue). Once the parameters are set, the user clicks on "Create Interfaces" to finalize.

Next, the maximum separation method is used to conduct a detailed analysis of the clusters present using a completely different algorithm. The accuracy of the

maximum separation method is highly dependent upon the input parameters selected for the algorithm [171]. The primary parameters to be defined are (Figure 4.24):

- d_{max} - the maximum distance between solute atoms for them to be identified as "clustered"
- N_{min} - the minimum number of "clustered" solute atoms required for a group of solutes to be formally identified as an individual "cluster"
- L - the maximum distance for adjacent non-solute atoms to be included in the cluster
- E - the maximum distance of atoms near the matrix interface to be removed (erosion distance)

The analysis is most sensitive to the selection of d_{max} and N_{min}, which depend upon the amount of solute concentration in the alloy and the relative distribution of the solutes within the matrix [172,173]. Since other authors have observed composition changes of nanoclusters under irradiation [8,9,13,59,104,124,174], it is considered likely that the d_{max} and N_{min} values may also differ for each specimen. As a result, both parameters are determined independently for each specimen and each individual data set.

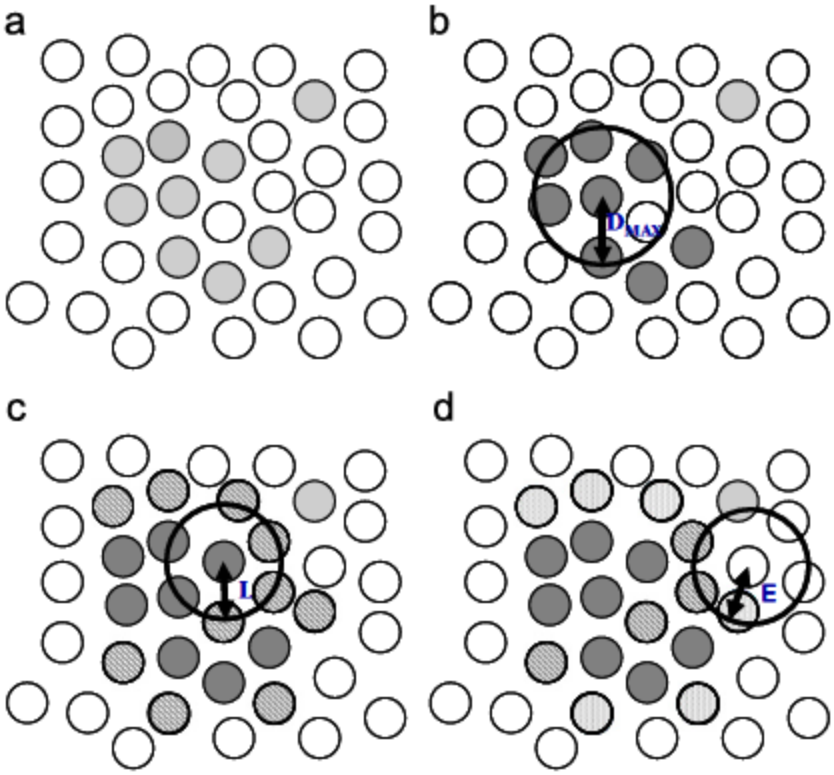

Figure 4.24 Schematic illustrating the maximum separation method: a) solute atoms shaded, b) solute atoms (core atoms) shaded darker if within DMAX, c) non-solute atoms (hatched) with L distance from the core atoms, and d) atoms within distance E from the matrix atoms are removed via erosion, from [171].

Selection of the analysis parameters for the maximum separation method is typically an iterative process using several different analysis tools within IVAS. The following is the approach utilized for this study. Within each data, the first tool used is a "Nearest Neighbor Distribution", which will confirm if significant clustering is present and assist with the initial estimation of the d_{max} parameter. With this algorithm, the user identifies the solute elements of interest, the range of atom-to-atom distances (d-pair) for consideration (usually up to 1.0-1.5 nm), and the sampling intervals (typically 0.05-0.1 nm to balance resolution and relative computing time). This algorithm is performing two separate calculations. First, it is measuring the amount of occurrences in which two solutes atoms fall within the d-pair distance, generating a histogram of this distribution.

Second, the algorithm calculates what this histogram would look like if all of the solute elements were randomly distributed throughout the sample. Therefore, if the sample truly has random distribution of solutes, these two histograms will be virtually identical. On the other hand, if these two histograms are grossly different, there is evidence of solute clustering. In which case, a point of reference is the cross-over point between these two curves (shown in Figure 4.25), which serves as the initial estimate of d_{max}.

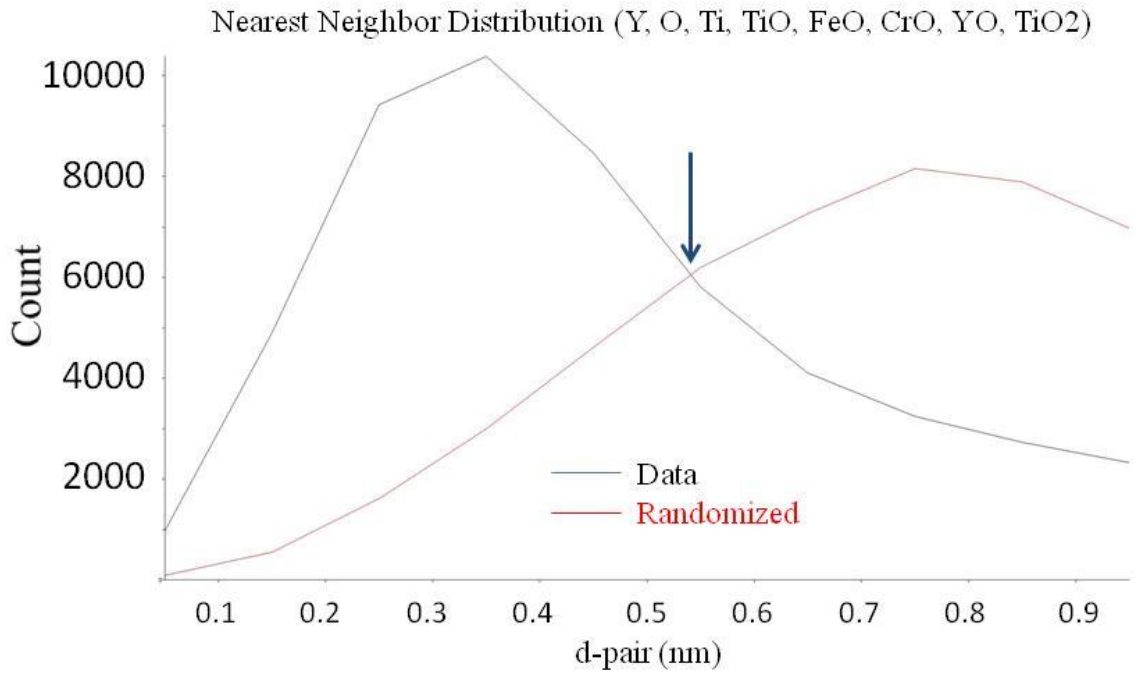

Figure 4.25 Typical results of a "Nearest Neighbor Distribution" for a data set exhibiting solute clustering. The cross-over point is highlighted with a blue arrow.

The next tool used is a "Cluster Size Distribution Analysis", which is used to estimate the value of the N_{min} parameter. For this calculation, the user once again identifies the solute elements of interest, and makes an initial estimate of d_{max} (in nm). Once again, the algorithm is performing two separate calculations. First, it applies the initial value for d_{max} across the data set to identify each cluster and plot a histogram of the size of each cluster. It is important to recognize this is an estimate, as the parameters L

and E are not considered at this time. Second, the algorithm estimates the distribution of cluster size as if the solutes were randomly distributed within the data set. Typical distributions of cluster sizes for both the data set and for a random distribution are illustrated in Figure 4.26. In the random calculation (red), it is expected that a few small "clusters" would still be identified as random solutes are coincidentally located near each other. The same effect is also observed for the calculation based on the actually data. One of the main goals of this step in the process is to filter out any of these random clustering events. As a result, the best approach is to iteratively choose different estimates of d_{max} until the low-end slopes of each of these curves closely match and converge on a common point on the x-axis. The point at which these slopes intersect the x-axis (Cluster Size) then provides a good estimate for the N_{min} parameter. With this approach, any clusters that are smaller in size are eliminated from consideration, thus ruling out any clusters that only occur randomly.

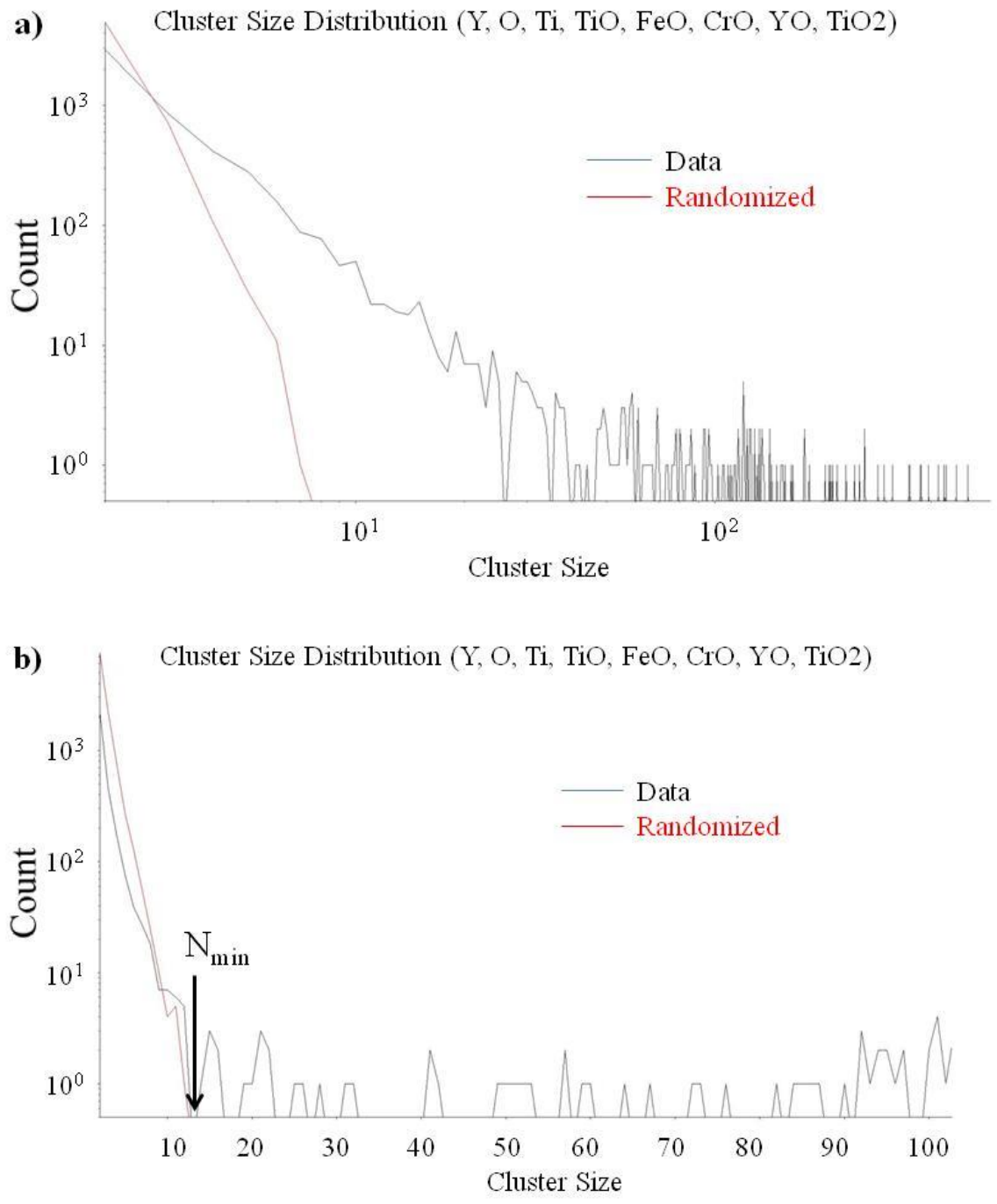

Figure 4.26 Typical results of a "Cluster Size Distribution Analysis" with a) the dmax estimate is too small, and b) dmax is more appropriately estimated and an initial Nmin is identified.

The next tool used is the "Cluster Count Distribution Analysis" which is used to finalize the value of d_{max}. Once again, the user identifies the solute elements of interest, the maximum of d_{max} distances to consider (usually up to 1.0-1.5 nm), and the sampling

intervals (typically 0.05-0.1 nm to balance resolution and relative computing time). The user defines the estimated N_{min} value from the prior step. The algorithm is once again performing two separate calculations, one against the existing data in the data set, the other for a random distribution of solutes, and plots histograms of the number of clusters identified based on the d_{max} parameter used for calculation. Typically, the random distribution results in a single mode distribution at higher d_{max} values. Conversely, the data set distribution will often have a single mode distribution at lower d_{max} values (Figure 4.27a), or a bimodal distribution with peaks at lower d_{max} values and at higher d_{max} values (Figure 4.27b). In the former situation, selection of d_{max} is a little more subjective. Typically, it is best to look for values in the region where the data-driven and random histograms cross-over (Figure 4.27a). However, in cases where a bimodal distribution is present, appropriate d_{max} values were selected for each condition following the approach proposed by Kolli and Seidman [175] and further refined by Williams, et al. [173], in which the selected d_{max} yielded a minimum number of counted clusters by the analysis (Figure 4.27b). When d_{max} values were too small, a “cluster of clusters” effect was present in which the software identified a single cluster as a group of smaller clusters clumped together. This effect overinflated the number density of clusters, while under-estimating their average size. Conversely, when d_{max} values were too large, additional clusters were spuriously generated and counted, which also overinflated the number density. In all cases, the best approach is to iterate between the "Cluster Size Distribution" and "Cluster Count Distribution" analyses until both d_{max} and N_{min} each converge onto the same values for both analyses. It is also helpful to compare the estimated number of clusters (y-axis) to the total number of clusters identified using

isosurfaces (via procedure above). Ideally, these values should be close (within ± 10%) to increase confidence in the selected parameters.

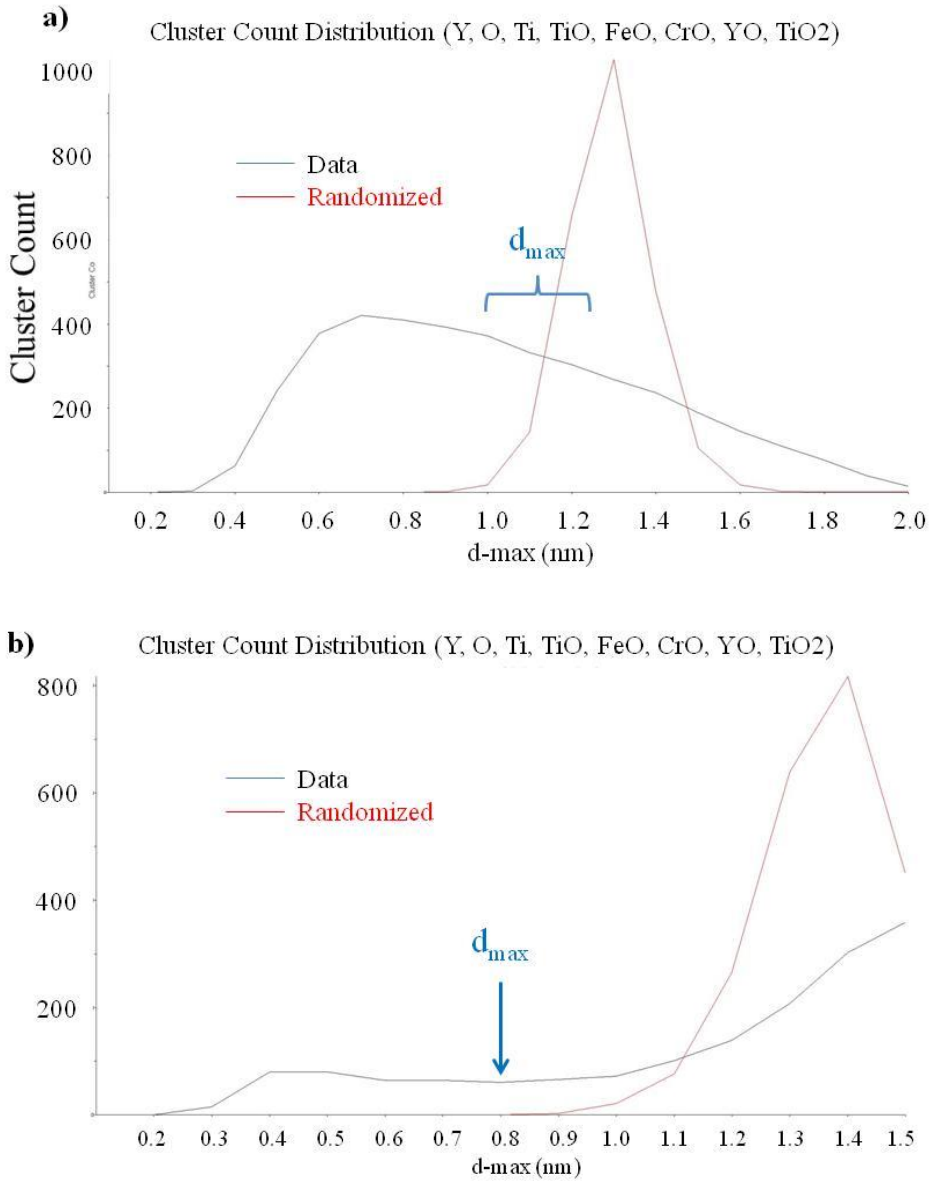

Figure 4.27 Typical results of a "Cluster Count Distribution Analysis" with a) a single mode distribution with the data set calculation, and b) a bimodal distribution with the data set calculation.

Finally, the parameter values for L and E must be selected. The value of L defines a maximum distance from cluster atoms identified in the analysis. Any matrix atom that

falls within this distance is also included in the cluster. The purpose of this addition is to ensure the measured cluster is not hollow. Typically, values for L are less than or equal to d_{max}. For this study, the value of L was defined as 0.5 nm for every data set, and no hollow clusters were ever observed in any of the samples. The value of E defines the erosion of the cluster at the interface with the matrix. Any matrix atoms that fall within this distance from an adjacent matrix atom at the interface is thus removed from the cluster. In this study, the value of E was consistently defined as 0.2 nm for every data set.

Once all of the input parameters have been defined, the formal cluster analysis is initiated. At the conclusion of this calculation, two major data outputs are available: a) a data table containing detailed information and measurements for each cluster, and b) an exportable Cluster .POS file. The latter can be used to reconstruct the data set as a 3D rendering with each cluster identified in a unique color (Figure 4.28). This is valuable for visual comparison with the isosurfaces created earlier in the original reconstruction, and also enables inspection for any evidence of a "clustering-of-clusters" effect, which is undesirable. Ideally, each cluster is distinct and closely matches those identified via isosurfaces. Once the user is satisfied with the integrity of the cluster analysis, the data table may be exported as a .CSV file, which may be opened in Microsoft Excel and used for subsequent analysis offline.

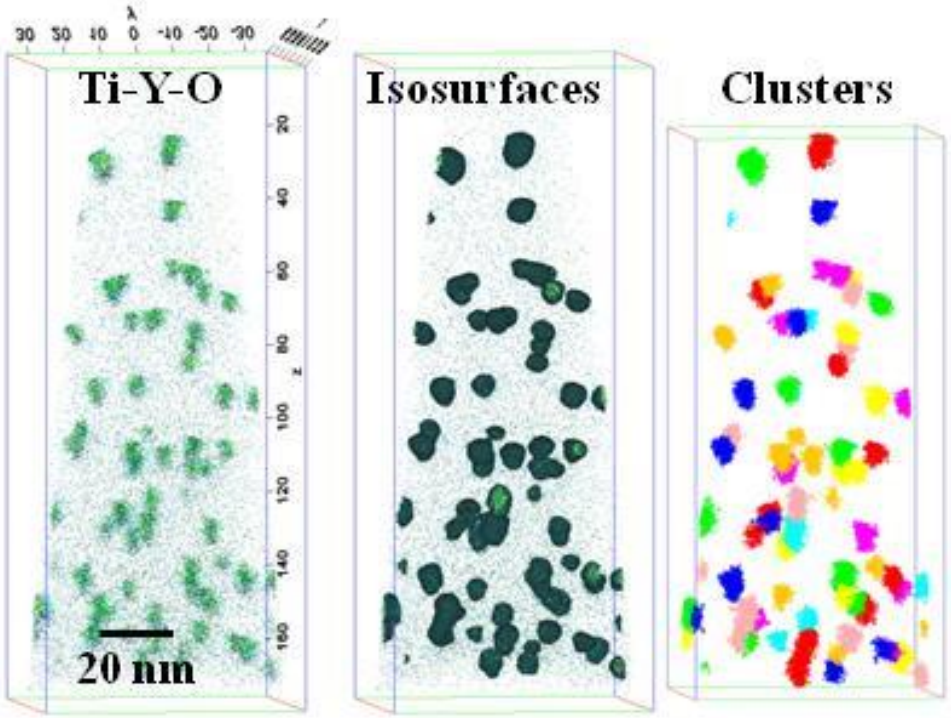

Figure 4.28 Typical 3D reconstructions of clusters in an ODS data set.

Finally, in IVAS, the bulk volume of the data set is estimated using the "Radial Distribution Function" calculation. For this calculation, any solute elements may be selected. The bulk volume is found as part of the "Properties" of this calculation and may be later used to calculate the overall number density of the clusters.

The IVAS cluster analysis output file (.CSV) provides values for R_{gx}, R_{gy} and R_{gz} for each cluster, which is taken to be the respective radius of gyration in each coordinate direction. An overall radius of gyration (R_g) for each cluster is calculated by [167]:

$$R_g = \sqrt{R_{gx}^2 + R_{gy}^2 + R_{gz}^2} \tag{4.10}$$

and the Guinier diameter (D_G) for each cluster is determined using [167,176]:

$$D_G = 2\sqrt{\frac{5}{3}}R_g \tag{4.11}$$

The average and standard deviation is calculated across all clusters measured and the error propagation formula is used to calculate an overall standard deviation for the

Guinier diameter. The standard deviation of the mean is also calculated to evaluate the relative certainty of the mean diameter. The cluster number density (N_{nc}) is determined by:

$$N_{nc} = \frac{\sum N_c}{\sum V_T} \tag{4.12}$$

where ΣN_c is the total number of clusters identified in all tips from a given condition and ΣV_T is the total analyzed volume in all tips from that condition. The volume fraction of clusters (f_v) is calculated using:

$$f_v = \frac{\sum N_{cl}}{N_{tot}} \tag{4.13}$$

where ΣN_{cl} is the total number of atoms within the measured clusters and N_{tot} is the total number of atoms within the combined reconstructed volumes from all sample tips [31].

Additional IVAS cluster analysis output data includes the elemental composition of each cluster identified, along with the composition of the matrix surrounding the clusters. Using this data, the average composition in at% is calculated for each cluster. Note that the measured amounts of Fe and Cr may be overinflated within the clusters due to trajectory aberrations [173,177]. Additional calculations enabled by the cluster analysis output data are conducted. The percentage of each element contained within clusters (f_{cl}^i) is found using:

$$f_{cl}^i = \frac{\sum N_{cl}^i}{N_{tot}^i} \tag{4.14}$$

where $\sum N_{cl}^i$ is the number of total number of species atoms within the clusters and N_{tot}^i is the total number of species atoms within the combined reconstruction volumes. Finally, the ratio of Y:Ti atoms and the (Y+Ti):O ratio are calculated for each cluster and

averaged. These additional calculations provide insight into the irradiation evolution of the composition of the oxide nanoclusters [9,13] and other irradiation-induced phases.

CHAPTER FIVE: RESULTS

The experimental work in this dissertation aims to characterize the microstructure of three separate alloys following a variety of irradiation conditions and doses. As outlined in chapter 4, two primary techniques are utilized to measure the microstructural morphology for a host of different features: a) transmission electron microscopy to study overall microstructure (grains, dislocations, carbide precipitates) and defect clusters (dislocation loops and voids), and b) atom probe tomography to study and measure any nanoclusters present. The following sections of this chapter will outline the results of microstructural measurements following each technique, respectively, for the alloys of interest in this thesis: 1) Fe-9%Cr ODS, 2) HCM12A, and 3) HT9.

5.1 Microstructure and Defect Cluster Morphology Results

A combination of TEM and STEM imaging is used to characterize the overall microstructure and defect cluster morphology for each specimen in this thesis. Bright field TEM imaging at a variety of magnifications enables the measurement of grain sizes, dislocation density, carbide precipitate size and number density, and the size and density of any voids that may be present in the specimen. Meanwhile, imaging and measurement of dislocation loops is carried out using STEM imaging on low-index zone axes. The following sections will detail the resulting measurements for each alloy studied.

5.1.1 Microstructure Results in Fe-9%Cr ODS

A comprehensive comparison of TEM microstructure results are provided in Table 5.1, enabling the comparison of microstructure evolution across a range of doses

for Fe^{2+}, proton, and neutron irradiation. For each specimen, approximately 100 grains and the carbide precipitates contained within them and along their boundaries, are measured. Grains and carbides exhibit little change with irradiation, having diameters ranging 0.23–0.41 µm and 0.07–0.11 µm, respectively. All diameter variations fall within the standard deviation of the measurements. Similarly, the dislocation line density in the as-received and all irradiated samples varies over 17.6–22.6 x 10^{14} m^{-2} with a standard deviation up to 7.6 x 10^{14} m^{-2}. Based on the range and standard deviations of these grain, carbide, and dislocation line measurements, there is no evidence to suggest that these features dramatically evolve in response to any irradiation condition. The typical microstructure of Fe-9%Cr ODS illustrating grains, carbides, and dislocation forest is shown in Figure 5.1.

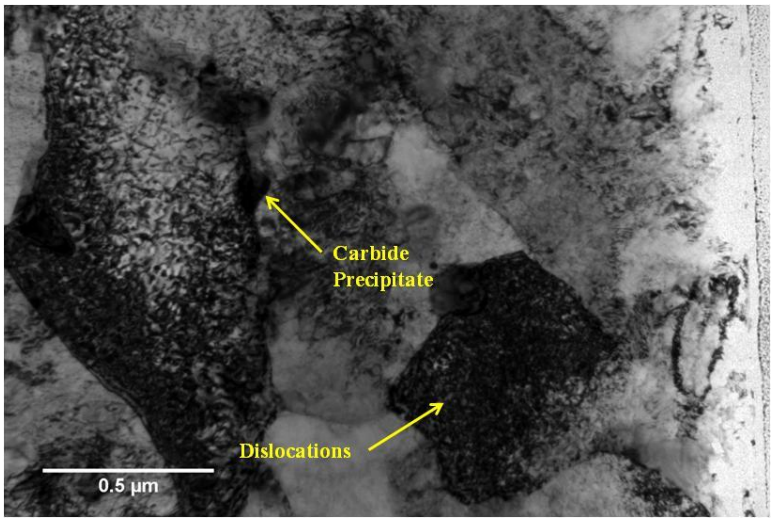

Figure 5.1 Representative microstructure of grains, carbides and dislocations in Fe-9%Cr ODS.

Table 5.1 Summary of microstructural measurements of Fe-9%Cr ODS using TEM/STEM.

Feature	Measurement	As Received	Fe^{2+} ion-irradiated (400°C) 50 dpa	Fe^{2+} ion-irradiated (500°C)			Proton-irradiated (500°C)			Neutron-irradiated (500°C) 3 dpa
				1 dpa	3 dpa	100 dpa	1 dpa	3 dpa	7 dpa	
Grains/ Laths	# of grains measured	104	105	101	104	105	104	104	104	104
	Effective diameter (x 10^{-6} m)	0.23 ± 0.12	0.28 ± 0.10	0.34 ± 0.08	0.28 ± 0.08	0.37 ± 0.19	0.36 ± 0.12	0.31 ± 0.11	0.41 ± 0.14	0.31 ± 0.09
Dislocation lines	# of measurements	17	27	18	21	35	26	46	26	39
	Density (x 10^{14} m^{-2})	19.1 ± 3.8	20.4 ± 8.8	21.1 ± 6.1	22.6 ± 4.8	18.4 ± 6.9	19.4 ± 4.1	17.6 ± 5.3	21.8 ± 7.6	18.5 ± 4.8
Carbide Precipitates	# of carbides measured	36	45	32	48	34	37	51	39	68
	Effective diameter (x 10^{-6} m)	0.11 ± 0.07	0.09 ± 0.05	0.08 ± 0.04	0.08 ± 0.04	0.08 ± 0.03	0.08 ± 0.02	0.07 ± 0.03	0.07 ± 0.03	0.10 ± 0.06
	Density (x 10^{20} m^{-3})	0.20	0.17	0.45	0.29	0.76	0.60	0.46	0.30	0.47
Voids	# of voids measured	0	63	0	0	0	0	8	1	22
	Diameter (x 10^{-9} m)	-	7.46 ± 2.69	-	-	-	-	4.00 ± 1.51	-	3.64 ± 1.14
	Density (x 10^{21} m^{-3})	-	0.46 ± 0.27	-	-	-	-	0.34 ± 0.44	-	0.24 ± 0.12
Dislocation loops	# of loops measured	0	97	51	48	136	79	688	77	182
	Diameter (x 10^{-9} m)	-	9.8 ± 3.4	8.5 ± 2.7	8.5 ± 2.2	10.7 ± 4.2	6.6 ± 1.2	8.4 ± 1.7	9.2 ± 3.6	8.9 ± 2.0
	Density (x 10^{21} m^{-3})	-	1.9 ± 0.5	2.8 ± 0.1	2.1 ± 0.1	4.3 ± 0.8	1.6 ± 0.2	10.2 ± 8.0	1.4 ± 0.02	2.7 ± 0.7

Small irradiation-induced voids are difficult to distinguish from the oxide nanoclusters in bright-field imaging, as both create similar Fresnel contrast when imaging using the through-focus technique. The majority of this contrast is attributed to the high density of oxide nanoclusters and not as voids. In some conditions, a small fraction of these features exhibit more distinct contrast with a solid bright center in the under-focused condition, a solid dark center in the over-focused condition, and are invisible when the sample is in-focus. These latter features are identified as likely voids. However, these voids are scarce and sparsely distributed, or indistinguishable throughout the specimens. No voids are positively identified in any of the Fe^{2+} irradiated specimens at 500°C, nor in the specimen proton-irradiated to 1 dpa. However, several voids are observed in the Fe^{2+} irradiated ODS to 50 dpa at 400°C (Figure 5.2), and a few features are identified in the specimens neutron-irradiated to 3 dpa (Figure 5.2) and proton-irradiated to 3 dpa and 7 dpa (Figure 5.3).

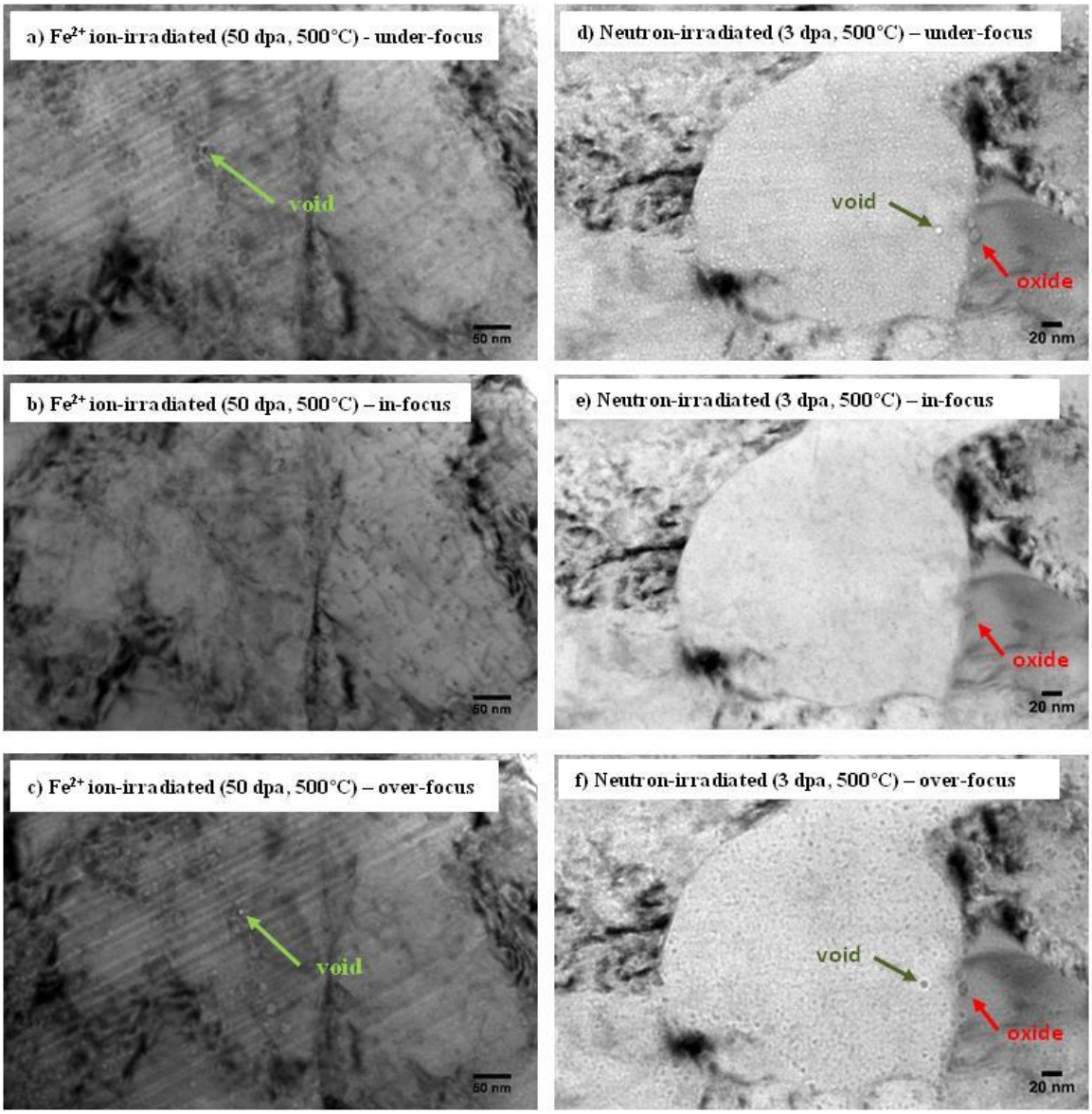

Figure 5.2 Representative images of voids in Fe-9%Cr ODS following: a-c) Fe2+ ion irradiation to 50 dpa at 400°C, and d-f) neutron irradiation to 3 dpa at 500°C.

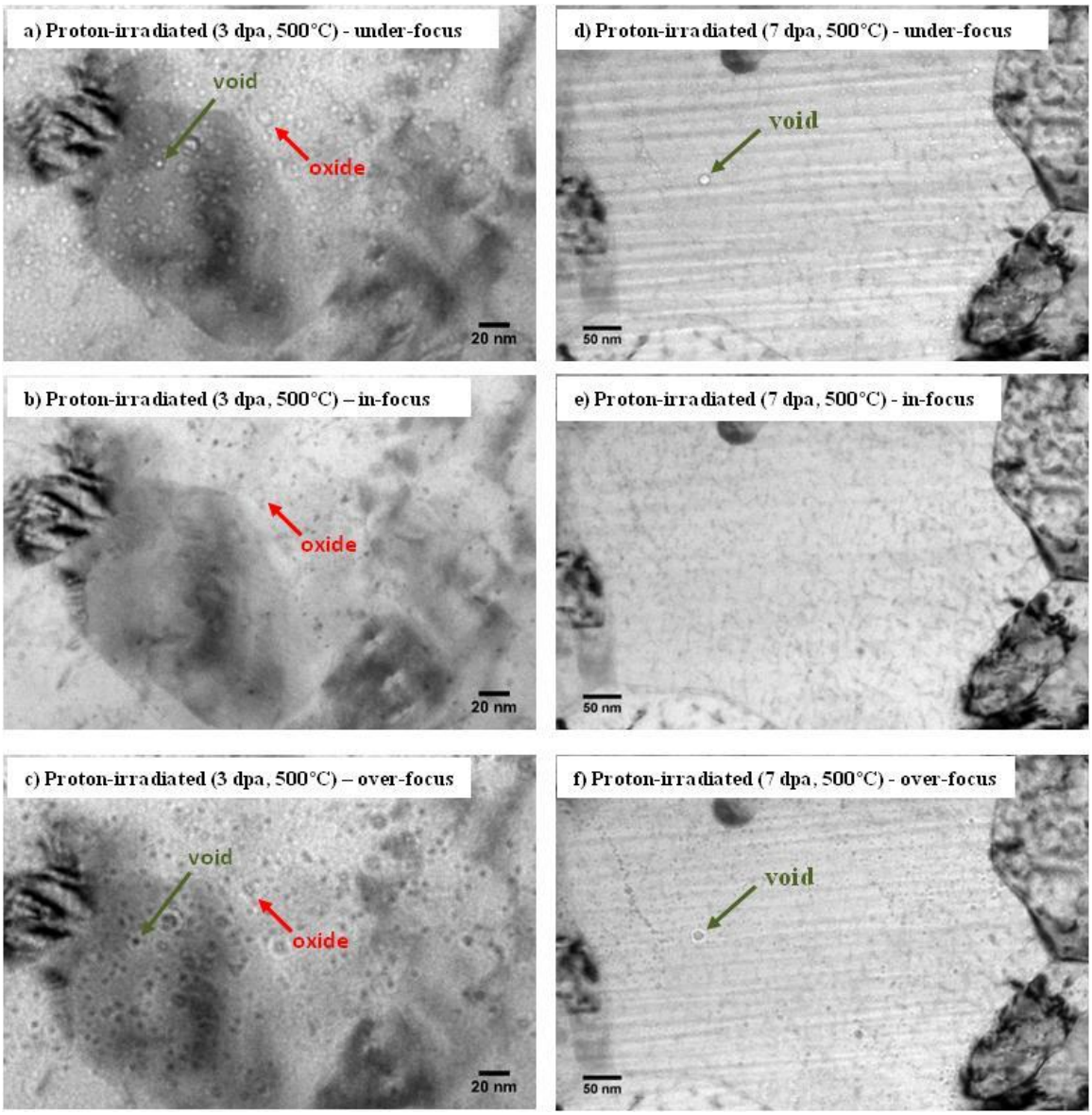

Figure 5.3 Representative images of voids in Fe-9%Cr ODS following: a-c) proton irradiation to 3 dpa, and d-f) proton irradiation to 7 dpa, both at 500°C.

Dislocation loops are imaged in STEM mode at the [011] and [111] zone axes. For each zone axis imaged, dislocation loop orientation maps generated by Yao, et al. [163] were used to determine that the loops commonly reside on the {111} or {001} habit planes. Following Fe^{2+} irradiation to 1 dpa, dislocation loops have an average diameter of 8.5 ± 2.7 nm and number density of 2.8 ± 0.1 x 10^{21} m^{-3}, which is nearly identical to the morphologies found after 3 dpa Fe^{2+} (diameter of 8.5 ± 2.2 nm and number density of 2.1

± 0.1 x 10^{21} m^{-3}). Loop size and number densities are higher, though not outside error bands, after 100 dpa Fe^{2+} irradiation, at 10.7 ± 4.2 nm and 4.3 ± 0.8 x 10^{21} m^{-3}, respectively. After the Fe^{2+} irradiation at 400°C to 50 dpa, loop size and number density are also similar at 9.8 ± 3.4 nm and 1.9 ± 0.5 x 10^{21} m^{-3}, respectively. With proton irradiation, dislocation loops grow from 6.6 ± 1.2 nm at 1 dpa, to 8.4 ± 1.7 nm at 3 dpa, and to 9.2 ± 3.6 nm after 7 dpa. Proton-irradiated loop number density remains unchanged between 1 and 7 dpa, at 1.6 ± 0.2 x 10^{21} m^{-3} and 1.4 ± 0.02 x 10^{21} m^{-3}, respectively. It is important to note with the STEM imaging technique the visibility of loops is highly dependent upon the TEM lamella thickness. Lamellae less than 50 nm thick are generally more effective, but the author recognizes this target thickness is difficult to consistently achieve during sample fabrication. As a result, the loop visibility varies with lamella thickness, which can lead to disparity in measured number densities. It is believed this is the primary reason for the inflated number density measurement in the proton-irradiated specimen to 3 dpa (10.2 ± 8.0 x 10^{21} m^{-3}), in which the FIB lift-out sample produced the highest quality image, enhancing visibility of the loops. Following neutron irradiation to 3 dpa at 500°C, the loop size and density are 8.9 ± 2.0 nm and 2.7 ± 0.7 x 10^{21} m^{-3}, respectively. STEM micrographs of representative distributions of dislocation loops following each proton irradiation and neutron irradiation are illustrated in Figure 5.4, while micrographs of loops following each Fe^{2+} ion irradiation are shown in Figure 5.5. Finally, trends in the dislocation loop morphology are plotted in Figure 5.6.

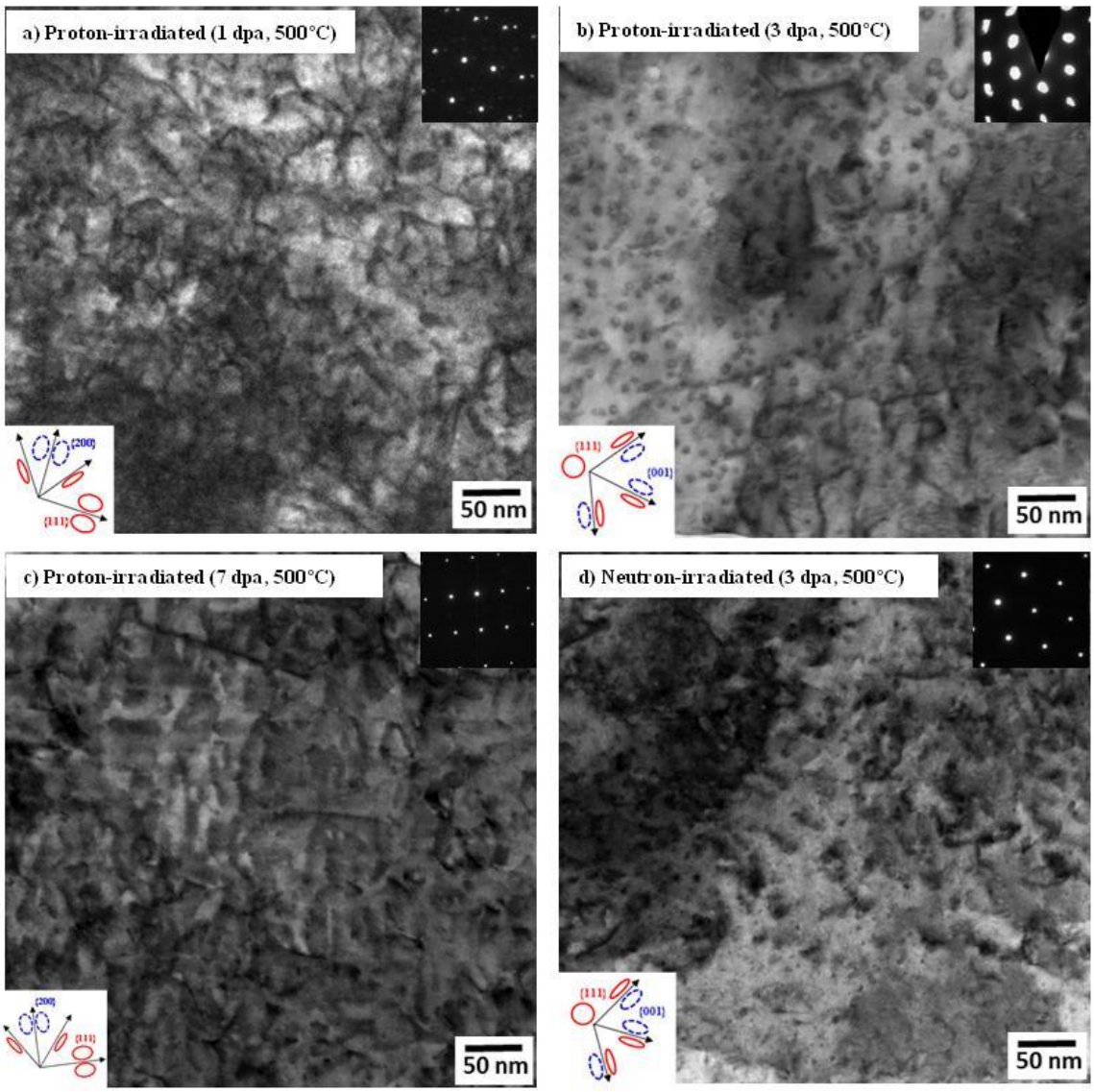

Figure 5.4 Representative images of dislocation loops in Fe-9%Cr ODS following proton irradiation to a) 1 dpa, b) 3 dpa, and c) 7 dpa and d) neutron irradiation to 3 dpa, all at 500°C.

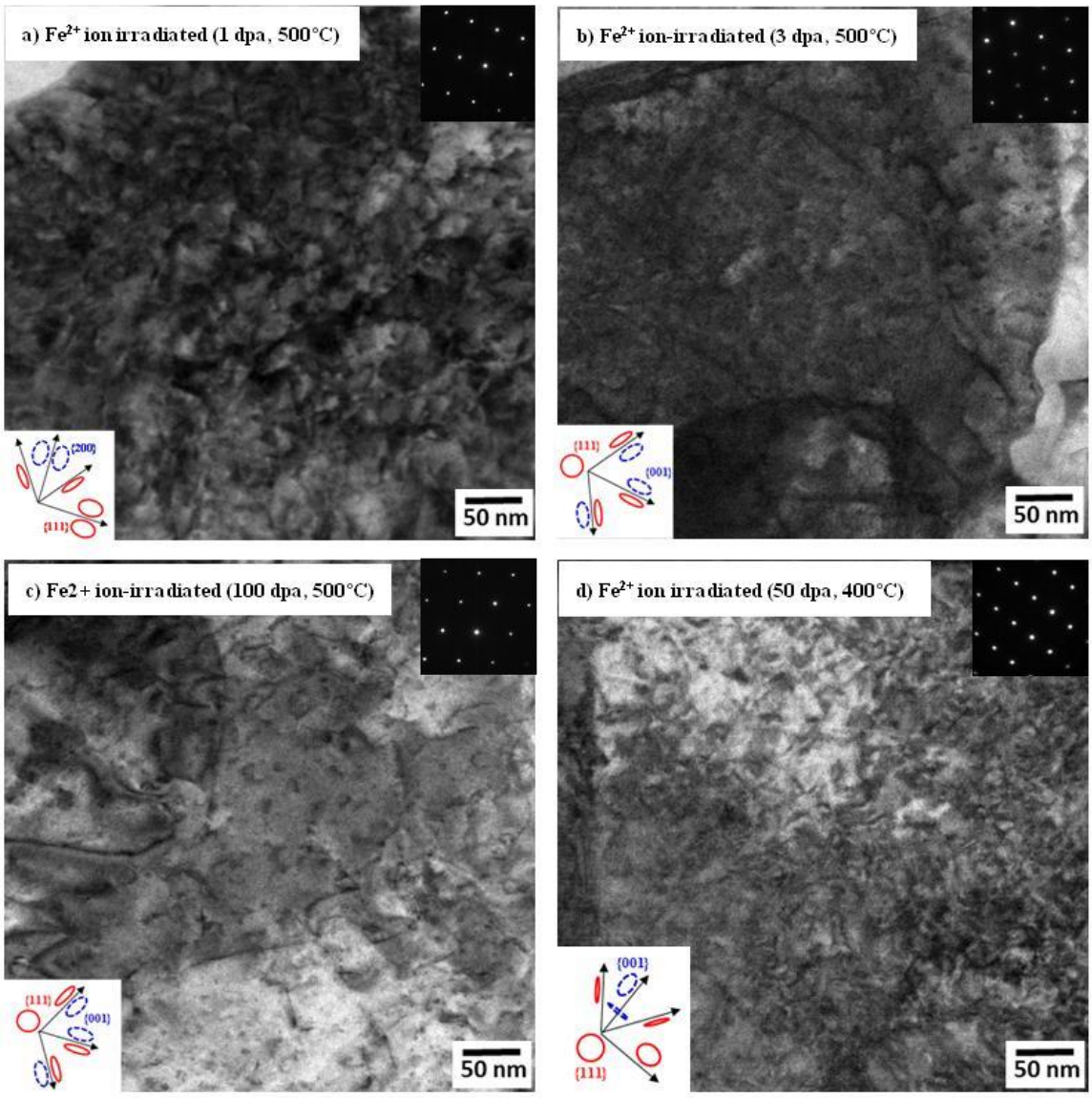

Figure 5.5 Representative images of dislocation loops in Fe-9%Cr ODS following Fe2+ ion irradiation following a) 1 dpa, b) 3 dpa, and c) 100 dpa at 500°C, and d) 50 dpa at 400°C.

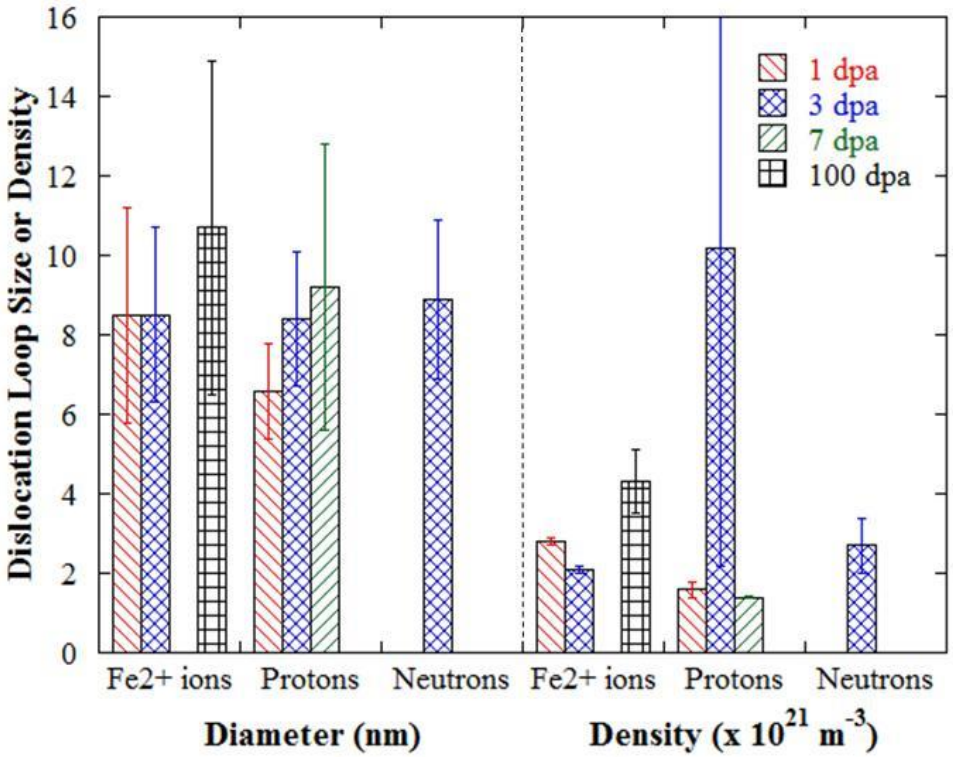

Figure 5.6 Summary of dislocation loop morphologies (average diameter and number density) after each irradiation at 500°C.

Bright field images of the oxide nanoclusters are obtained in areas of the lamellae having low dislocation contrast, which allows the z-contrast of the clusters to be more visibly prominent. However, this technique has limited detectability of nanoclusters, especially those <2 nm in diameter [4,5]. Thus, APT analysis complements the TEM work by identifying the <2 nm nanoclusters, providing results that more accurately quantify the oxide average nanocluster size, number density, and composition. A representative TEM image of the oxide nanoclusters in the as-received condition is shown in Figure 5.7, illustrating the challenge of quantifying nanoclusters using TEM.

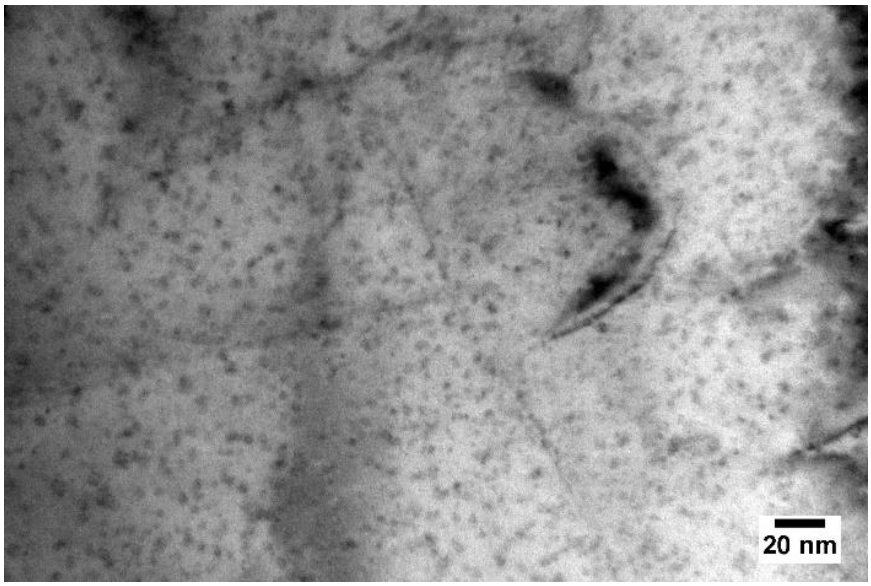

Figure 5.7 Bright field TEM images of the oxide distributions for the as-received Fe-9%Cr ODS.

5.1.2 Microstructure Results in HCM12A

Quantitative TEM microstructure results are provided in Table 5.2 for all HCM12A specimen conditions, enabling the comparison of microstructure evolution across of range of doses for proton and Fe^{2+} ion irradiation and across each particle irradiation at otherwise common conditions (3 dpa at 500°). Between 40 and 105 grains and the carbide precipitates contained within them and along grain boundaries, were measured. Grains and carbides exhibit little change with irradiation, having diameters ranging 0.61–0.63 μm and 0.07–0.11 μm, respectively. All diameter variations fall within the standard deviation of the measurements. Similarly, the dislocation line density varies over 12.1–14.6 x 10^{14} m^{-2} with a standard deviation up to 8.1 x 10^{14} m^{-2}. Based on these relatively narrow bands of size and density measurements, and their corresponding wide standard deviations, there is no statistically significant evidence to suggest that these features have dramatically evolved in response to either irradiation condition. The typical

microstructure of HCM12A illustrating grains, carbides, and dislocation forest is shown in Figure 5.8.

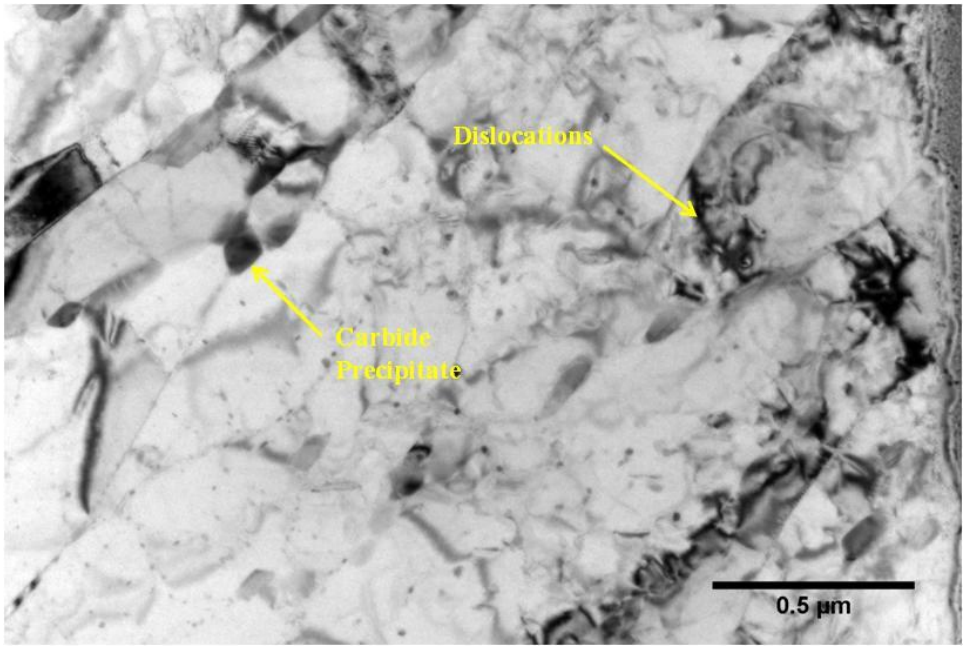

Figure 5.8 Representative microstructure of grains, carbides and dislocations in HCM12A.

Table 5.2 Summary of microstructural measurements of HCM12A using TEM/STEM.

Feature	Measurement	Fe^{2+} ion-irradiated (500°C)		Proton-irradiated (500°C)		Neutron-irradiated (500°C)
		3 dpa	100 dpa	1 dpa	3 dpa	3 dpa
Grains/Laths	# of grains measured	86	40	101	71	105
	Effective diameter (x 10^{-6} m)	0.63 ± 0.22	0.61 ± 0.18	0.62 ± 0.21	0.61 ± 0.26	0.66 ± 0.36
Dislocation lines	# of measurements	16	13	31	30	30
	Density (x 10^{14} m^{-2})	13.3 ± 4.4	14.6 ± 1.9	13.9 ± 8.1	12.1 ± 4.2	13.6 ± 3.6
Carbide Precipitates	# of carbides measured	32	33	41	58	35
	Effective diameter (x 10^{-6} m)	0.09 ± 0.04	0.11 ± 0.06	0.10 ± 0.04	0.11 ± 0.05	0.07 ± 0.03
	Density (x 10^{20} m^{-3})	0.35 ± 0.10	0.22 ± 0.17	0.15 ± 0.07	0.53 ± 0.28	0.97 ± 0.47
Voids	# of voids measured	0	75	0	0	0
	Diameter (x 10^{-9} m)	-	6.1 ± 5.4	-	-	-
	Density (x 10^{21} m^{-3})	-	0.17 ± 0.02	-	-	-
Dislocation loops	# of loops measured	84	234	105	136	101
	Diameter (x 10^{-9} m)	7.7 ± 02.4	12.0 ± 4.5	7.6 ± 2.1	7.6 ± 2.4	7.5 ± 2.2
	Density (x 10^{21} m^{-3})	2.2 ± 0.3	1.0 ± 0.2	1.6 ± 0.3	4.4 ± 1.1	4.0 ± 0.9

Irradiation-induced voids are only observed in the specimen irradiated with Fe^{2+} ions to 100 dpa (Figure 5.9), with sizes varying from 3-19 nm and a number density of $0.17 \pm 0.02 \times 10^{21}$ m^{-3}.

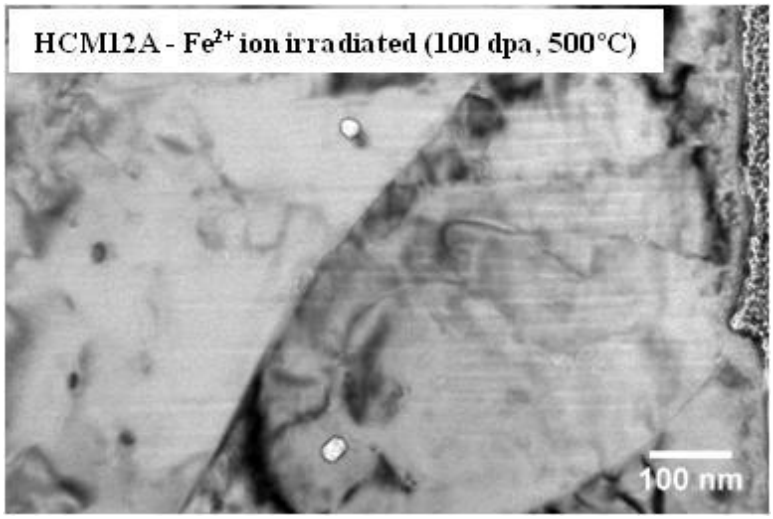

Figure 5.9 Representative voids in HCM12A following Fe2+ irradiation to 100 at 500°C.

Dislocation loops were imaged in STEM mode at the [001] and [111] zone axes. For each zone axis imaged, dislocation loop orientation maps generated by Yao, et al. [163] were used to determine that the loops commonly resided on the {111} or {001} habit planes [163]. Upon proton irradiation, dislocation loops were consistent in size following 1 dpa and 3 dpa, at 7.6 ± 2.1 nm 7.6 ± 2.4 nm, respectively, while number density increased from $1.6 \pm 0.3 \times 10^{21}$ m^{-3} to $4.4 \pm 1.1 \times 10^{21}$. On the other hand, upon Fe^{2+} ion irradiation, dislocation loops increased in size between 3 dpa (7.7 ± 2.4 nm) and 100 dpa (12.0 ± 4.5 nm) while the density potentially decreased slightly from $2.2 \pm 0.3 \times 10^{21}$ m^{-3} to $1.0 \pm 0.2 \times 10^{21}$, respectively. Finally, comparing Fe^{2+}, proton, and neutron irradiated specimens at common conditions of 3 dpa at 500°C, the morphology of dislocation loops is generally consistent, with average loops sizes ranging 7.6-7.7 nm and

densities ranging 2.2-4.4 x 10^{21} m^{-3}. STEM micrographs of typical dislocation loops in HCM12A are shown in Figure 5.10.

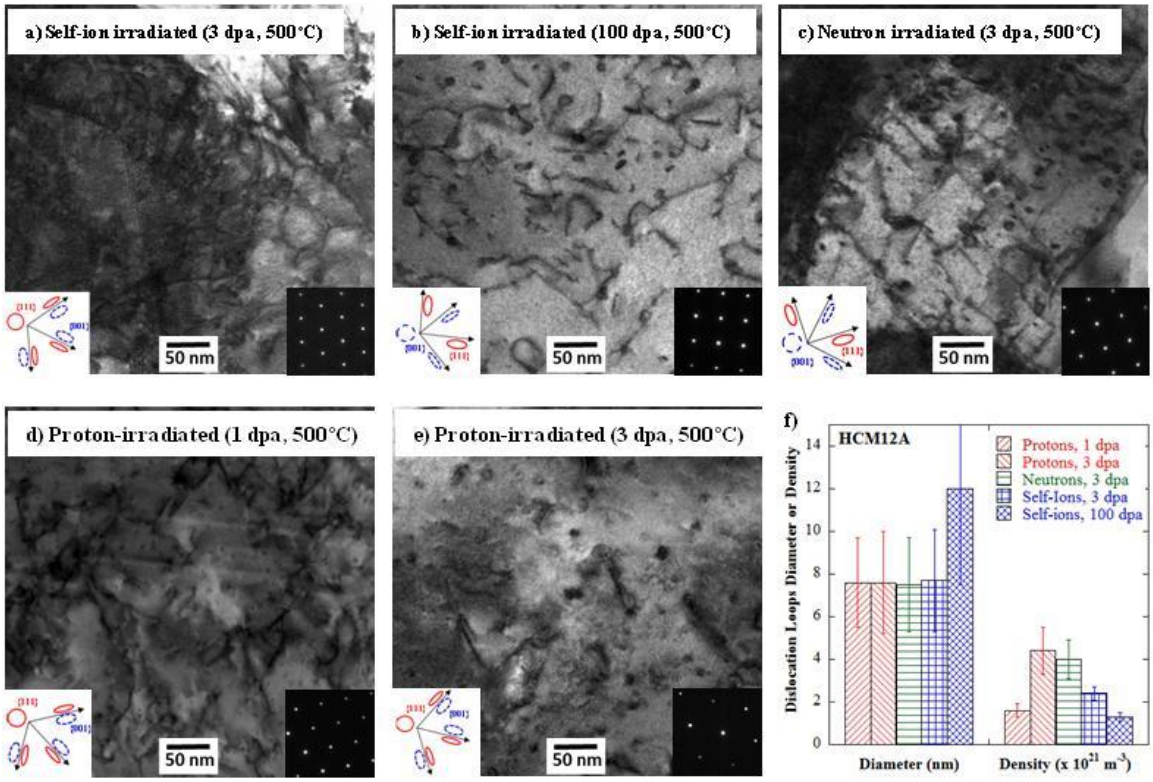

Figure 5.10 Representative dislocation loops in HCM12A imaged along the [111] or [001] zone axis following a) Fe2+ irradiation to 3 dpa, b) Fe2+ irradiation to 100 dpa, c) neutron irradiation to 3 dpa, d) proton irradiated to 1 dpa, and e) proton irradiated to 3 dpa, plus f) comparison of loops diameters and density for each condition.

5.1.3 Microstructure Results in HT9

Quantitative TEM microstructure results are provided in Table 5.3 for all HT9 specimen conditions, enabling the comparison of microstructure evolution across a range of doses for proton and Fe^{2+} ion irradiation and across each particle irradiation at otherwise common conditions (3 dpa at 500°). Approximately 100 grains and the carbide precipitates contained within them and along grain boundaries, were measured for each specimen. Grains and carbides exhibit little change with irradiation, having diameters ranging 0.30–0.41 μm and 0.06–0.08 μm, respectively. All diameter variations fall within

the standard deviation of the measurements. Similarly, the dislocation line density varies over 10.1–14.5 x 10^{14} m^{-2} with a standard deviation up to 12.6 x 10^{14} m^{-2}. Based on these relatively narrow bands of size and density measurements, and their corresponding wide standard deviations, there is no evidence to suggest that these features have dramatically evolved in response to any of the irradiations. The typical microstructure of HT9 illustrating grains, carbides, and dislocation forest is shown in Figure 5.11.

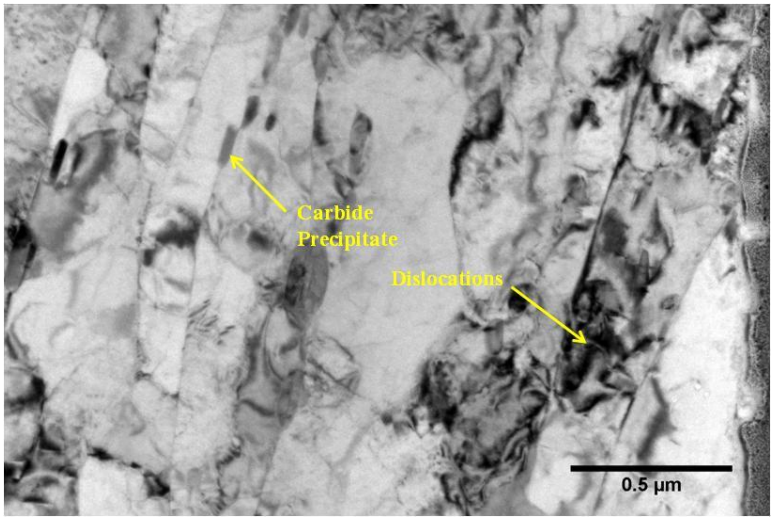

Figure 5.11 Representative microstructure of grains, carbides and dislocations in HT9.

Table 5.3 Summary of microstructural measurements of HT9 using TEM/STEM.

Feature	Measurement	Fe^{2+} ion-irradiated (500°C)		Proton-irradiated (500°C)		Neutron-irradiated (500°C)
		3 dpa	100 dpa	1 dpa	3 dpa	3 dpa
Grains/Laths	# of grains measured	101	93	104	105	105
	Effective diameter (x 10^{-6} m)	0.41 ± 0.16	0.38 ± 0.12	0.37 ± 0.10	0.31 ± 0.12	0.30 ± 0.10
Dislocation lines	# of measurements	23	10	22	43	33
	Density (x 10^{14} m^{-2})	13.6 ± 12.6	10.1 ± 3.8	14.5 ± 2.4	14.1 ± 4.0	13.8 ± 4.3
Carbide Precipitates	# of carbides measured	88	51	93	195	163
	Effective diameter (x 10^{-6} m)	0.07 ± 0.03	0.07 ± 0.02	0.08 ± 0.03	0.07 ± 0.03	0.06 ± 0.03
	Density (x 10^{20} m^{-3})	0.62 ± 0.28	0.46 ± 0.20	0.69 ± 0.34	0.62 ± 0.33	0.71 ± 0.41
Voids	# of voids measured	0	42	0	0	0
	Diameter (x 10^{-9} m)	-	12.0 ± 5.8	-	-	-
	Density (x 10^{21} m^{-3})	-	0.15 ± 0.14	-	-	-
Dislocation loops	# of loops measured	169	78	30	98	114
	Diameter (x 10^{-9} m)	7.6 ± 2.3	9.4 ± 3.6	7.3 ± 2.2	7.5 ± 2.1	7.6 ± 2.2
	Density (x 10^{21} m^{-3})	2.0 ± 0.3	1.2 ± 0.1	1.9 ± 0.2	2.4 ± 0.5	2.4 ± 0.5

As with HCM12A, irradiation-induced voids are only observed in the specimen irradiated with Fe^{2+} ions to 100 dpa (Figure 5.12), with sizes varying from 4-20 nm and a number density of 0.15 ± 0.14 x 10^{21} m^{-3}.

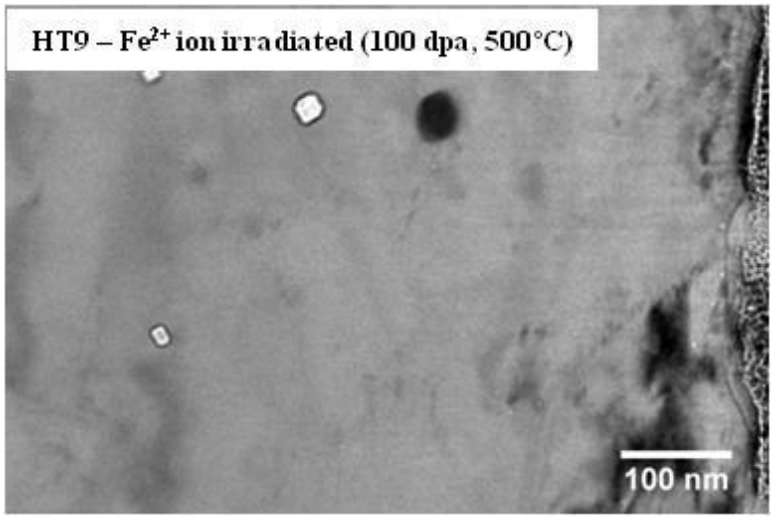

Figure 5.12 Representative voids in HT9 following Fe2+ irradiation to 100 at 500°C.

Dislocation loops were imaged in STEM mode on the [001] and [111] zone axes. Upon proton irradiation, dislocation loops were consistent in size following 1 dpa and 3 dpa, at 7.3 ± 2.2 nm 7.5 ± 2.1 nm, respectively, with a number density ranging 1.9 ± 0.2 x 10^{21} m^{-3} to 2.4 ± 0.5 x 10^{21}. On the other hand, upon Fe^{2+} ion irradiation, dislocation loops increased in average size between 3 dpa (7.6 ± 2.3 nm) and 100 dpa (9.6 ± 3.6 nm) while the densities are relatively consistent at 2.0 ± 0.3 x 10^{21} m^{-3} and 1.2 ± 0.1 x 10^{21}, respectively. Finally, comparing Fe^{2+}, proton, and neutron irradiated specimens at common conditions of 3 dpa at 500°C, the morphology of dislocation loops is generally consistent, with average loops sizes ranging 7.5-7.6 nm and densities ranging 2.0-2.4 x 10^{21} m^{-3}. STEM micrographs of typical dislocation loops in HT9 are shown in Figure 5.13.

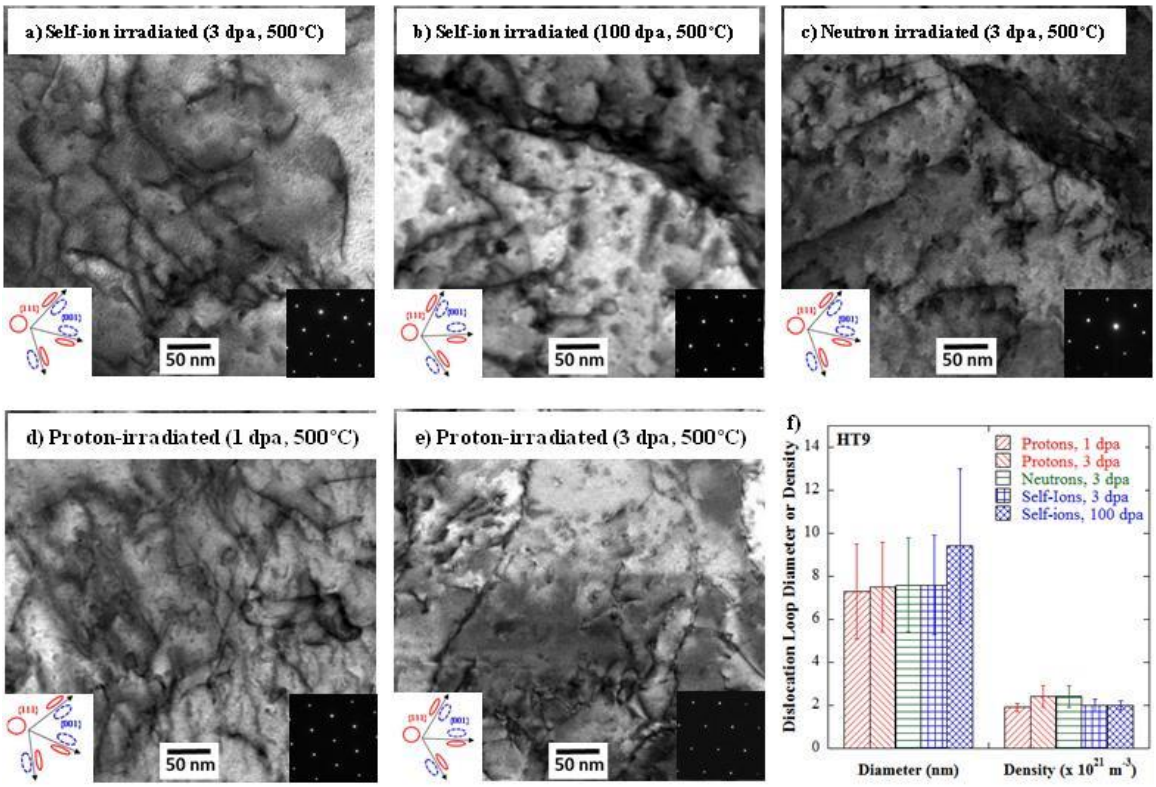

Figure 5.13 Representative dislocation loops in HT9 imaged along the [111] or [001] zone axis following a) Fe2+ irradiation to 3 dpa, b) Fe2+ irradiation to 100 dpa, c) neutron irradiation to 3 dpa, d) proton irradiated to 1 dpa, and e) proton irradiated to 3 dpa, plus f) comparison of loops diameters and density for each condition.

5.2 Nanocluster Morphology Results

The atom-by-atom detection capabilities of APT with IVAS cluster analysis enables high-fidelity spatial and compositional characterization of the nanoclusters in each specimen. The following sections will detail the resulting characterization the nanoclusters present for each alloy studied.

5.2.1 Clustering Results in Fe-9%Cr ODS

The 3D reconstructions of each of the ODS specimens exhibit clustering of Ti, O and Y atoms along with TiO, YO, FeO, and CrO compounds all at coincident locations in the matrix. For this reason, these atoms/compounds are chosen for the oxide cluster analysis in each condition. Oxide nanoclusters can be visualized and analyzed using three

separate imaging approaches: 1) 3D atom reconstruction with filtering to display the clustered elements (Ti, Y, and O atoms, and TiO and YO compounds), 2) isosurface construction with a concentration threshold of 6 at.% Y-Ti-O, and 3) cluster reconstruction. Representative APT tips are shown with clusters identified by each of these three approaches in Figures 5.14 (as-received and Fe^{2+} ion-irradiated to 50 dpa at 400°C), Figure 5.15 (Fe^{2+} ion-irradiated at 500°C), Figure 5.16 (proton-irradiated), and Figure 5.17 (neutron-irradiated).

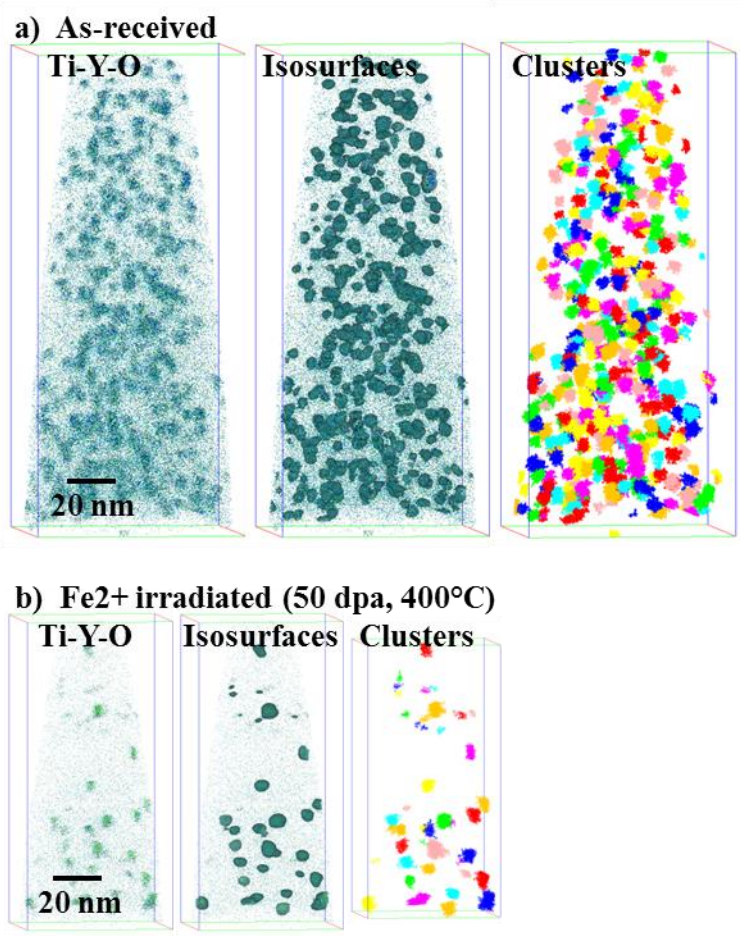

Figure 5.14 Representative atom distribution maps of oxide nanoclusters in a) as-received Fe-9%Cr ODS, and b) Fe2+ ions to 50 dpa at 400°C.

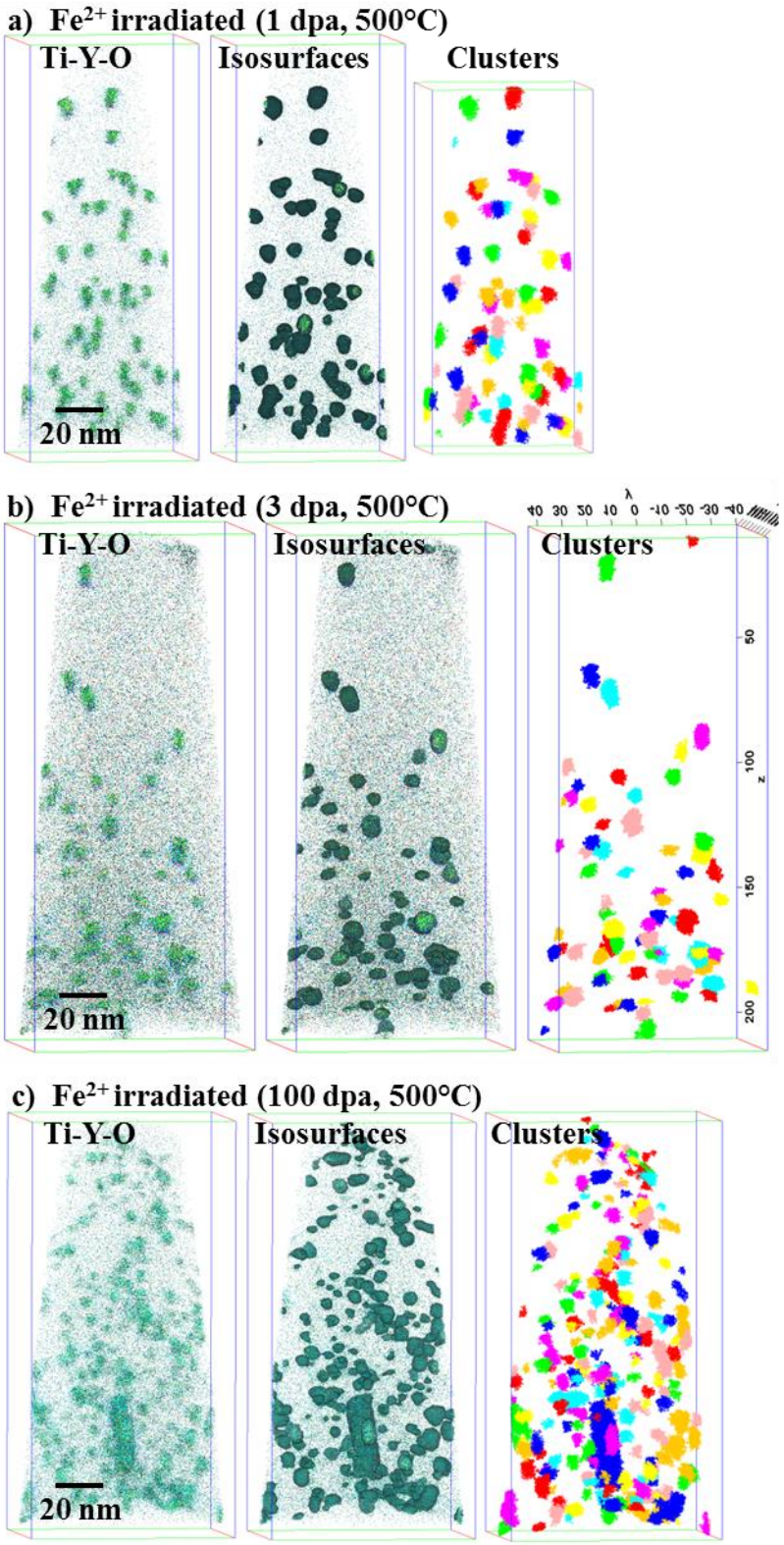

Figure 5.15 Atom distribution maps of oxide nanoclusters in Fe-9%Cr ODS irradiated with Fe2+ ions to a) 1 dpa, b) 3 dpa, and c) 100 dpa, all at 500°C.

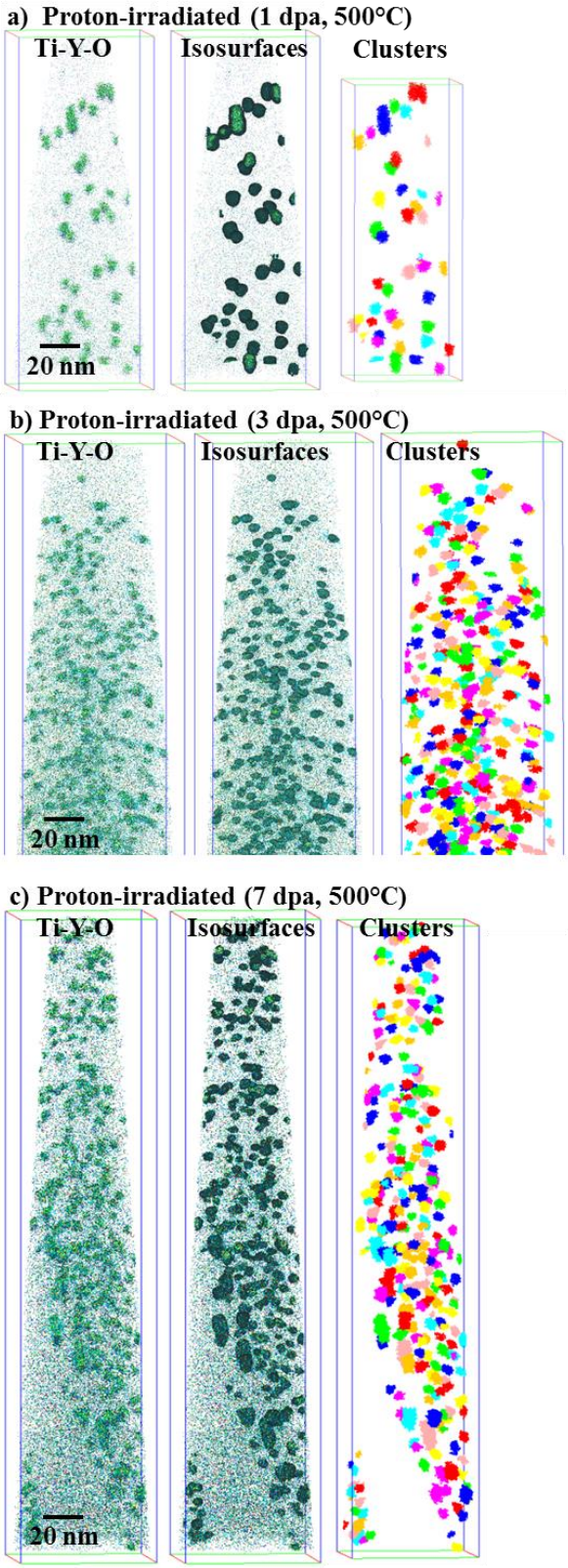

Figure 5.16 Atom distribution maps of oxide nanoclusters in Fe-9%Cr ODS irradiated with protons to a) 1 dpa, b) 3 dpa, and c) 7 dpa, all at 500°C.

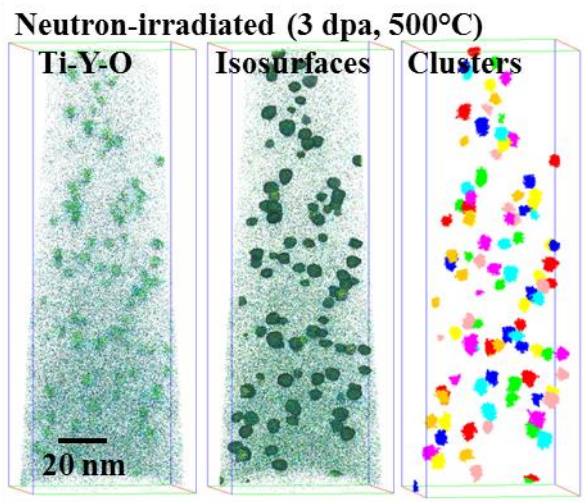

Figure 5.17 Atom distribution maps of oxide nanoclusters in Fe-9%Cr ODS irradiated with neutrons to 3 dpa at 500°C.

Within the irradiated specimens of Fe-9%Cr ODS, there is also visual evidence of clustering among the Si, Mn, and Ni atoms at coincident locations as the oxides. Some specimens exhibit this clustering more strongly than others. Some examples of this evidence are illustrated in Figure 5.18 (Fe^{2+} ion-irradiated to 100 dpa at 500°C), Figure 5.19 (proton-irradiated to 3 dpa at 500°C), and Figure 5.20 (neutron-irradiated to 3 dpa at 500°C).

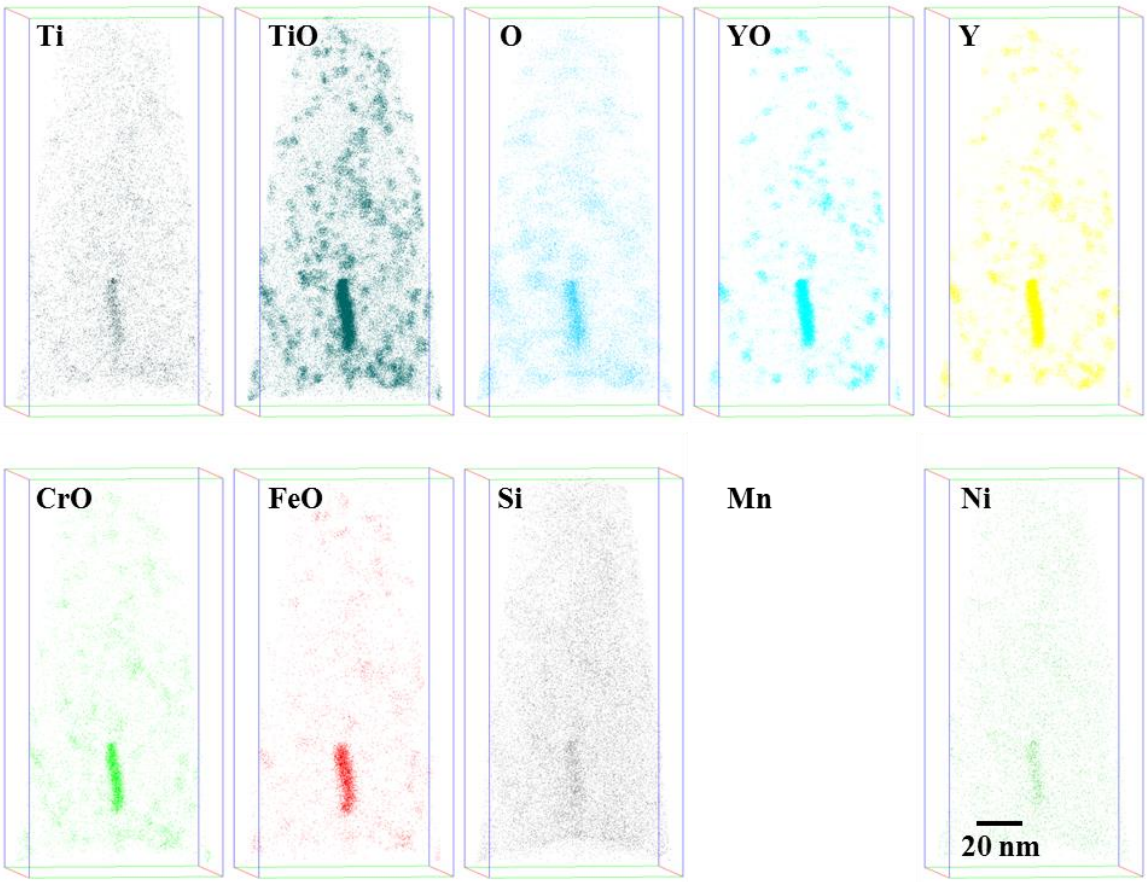

Figure 5.18 Atom distribution maps for each solute element in Fe-9%Cr ODS irradiated with Fe2+ ions to 100 dpa at 500°C.

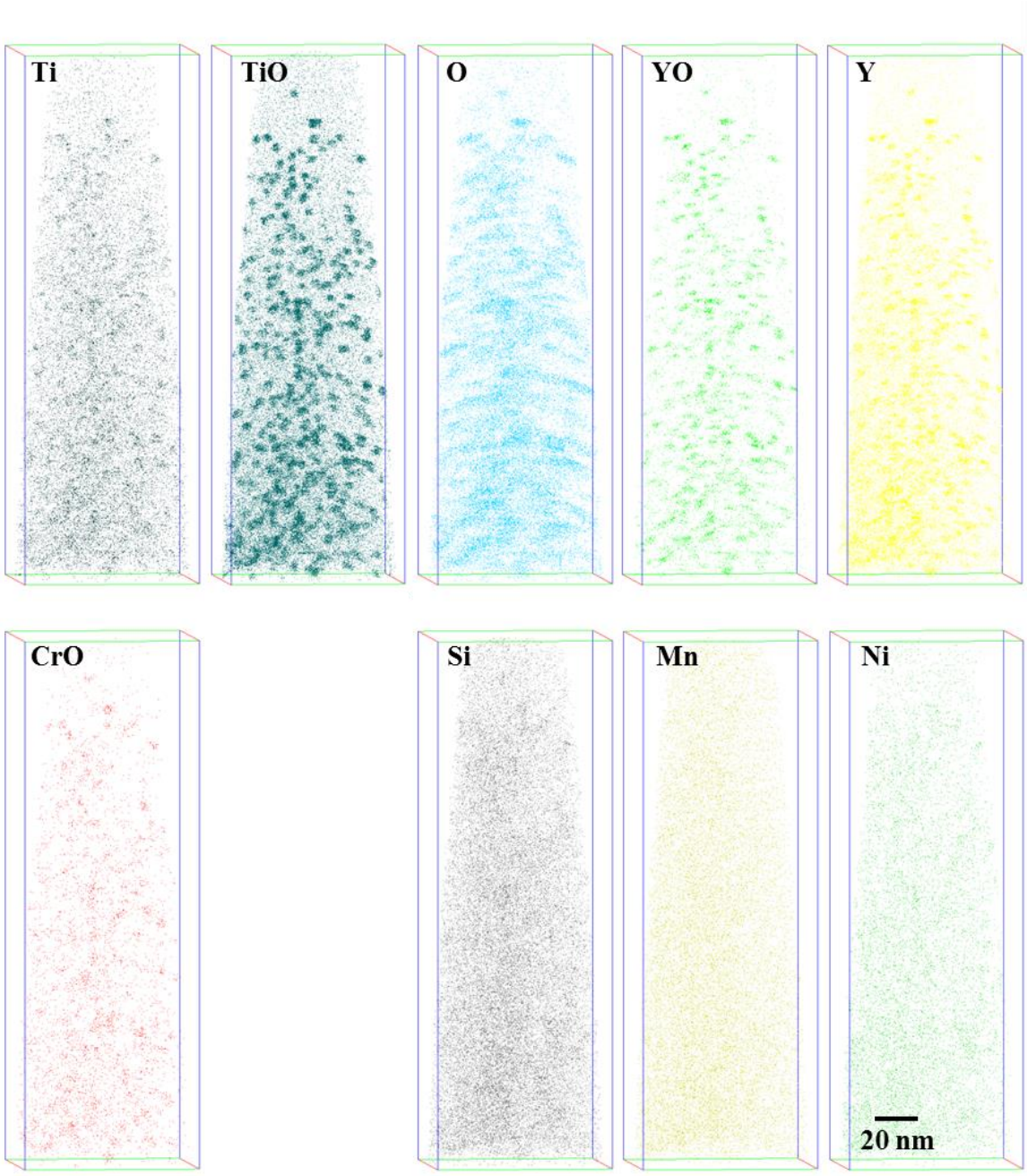

Figure 5.19 Atom distribution maps for each solute element in Fe-9%Cr ODS irradiated with protons to 3 dpa at 500°C.

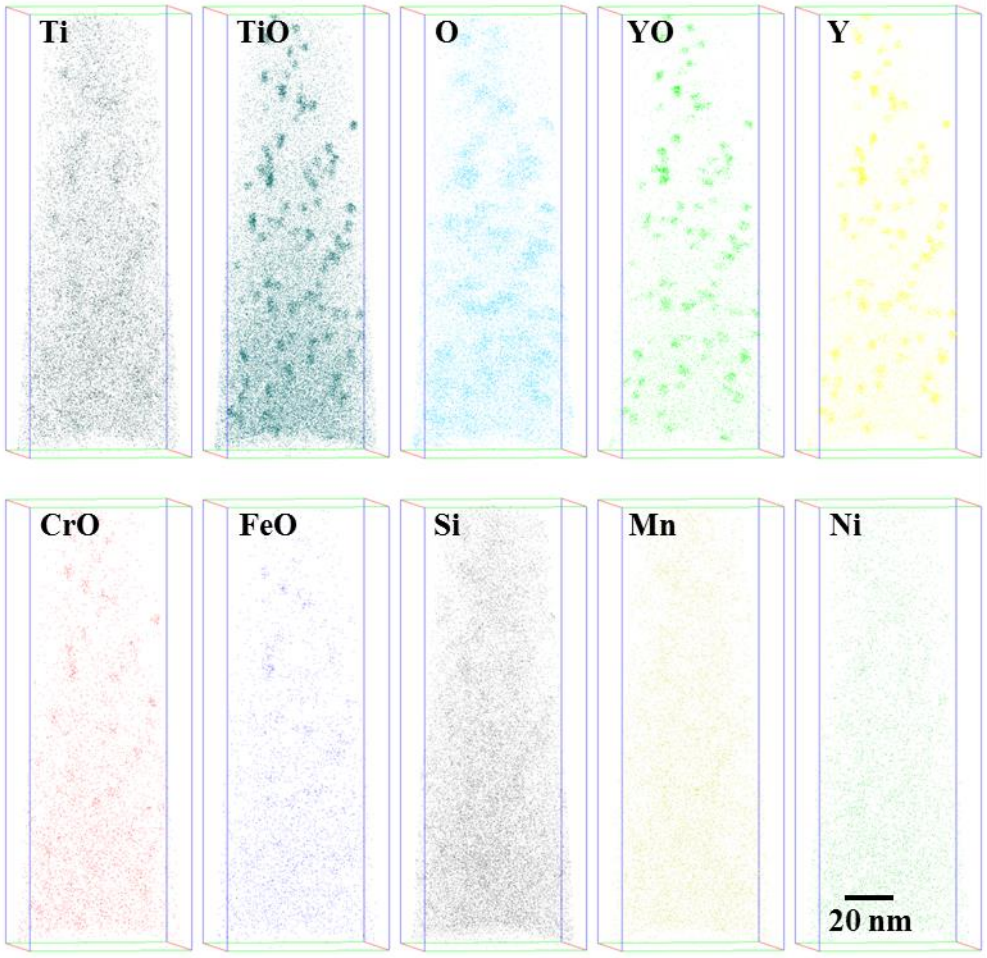

Figure 5.20 Atom distribution maps for each solute element in Fe-9%Cr ODS irradiated with neutrons to 3 dpa at 500°C.

Cluster analysis using the Integrated Visualization and Analysis Software (IVAS) Version 3.6.12 enables quantification of the oxide nanocluster sizes and number densities, along with specific chemical analysis of the clusters and the surrounding matrix. During cluster analysis for this thesis, it was observed that the cluster size is not independent of the data set size (i.e. number of collected and ranged ions). To further understand this relationship and its implications, the average nanocluster Guinier diameter was calculated for each data set from every specimen condition. The results of this exercise are shown in Figure 5.21 as a function of the total number of ranged ions in

each data set for the Fe-9%Cr ODS specimens. Linear trend lines are fitted to the data sets for each specimen, with a consistent slope (see trendlines in Figure 5.21) resulting for most specimens, particularly in those specimens for which a larger number of LEAP tips have been analyzed. This further emphasizes the value of collecting as many LEAP data sets as possible, including those with varying sizes of the data sets, to gain a higher confidence in this trend.

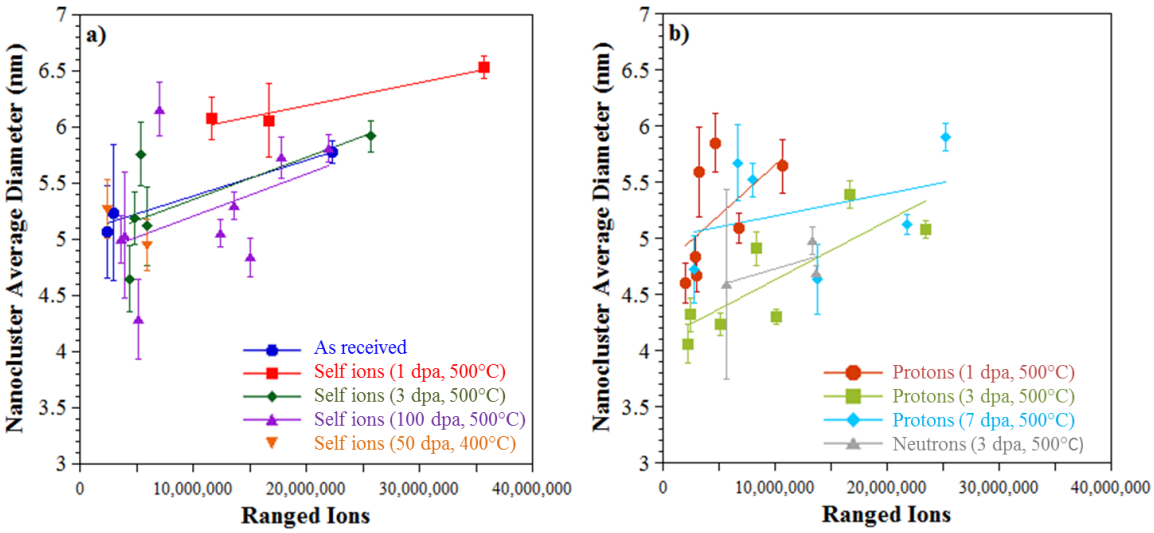

Figure 5.21 Average measured cluster Guinier diameter for each data set collected for each sample condition for Fe-9%Cr ODS for the a) as received and Fe2+ irradiated specimens, and b) proton- and neutron-irradiated specimens. Linear fits are applied for each sample condition showing a consistent trend of increasing diameter with increasing data set size (i.e. number of ranged ions).

As a result of these trends, it is helpful to normalize the data to create a more robust means to make an "apples-to-apples" comparison of average cluster size between different specimens. One such method is to project the average cluster size measurements for each specimen condition to a common data set size. This can be accomplished by using the slopes of the trend lines from Figure 5.21 and interpolating to a specified number of ranged ions. It is worth noting for each specimen, larger data sets including a larger number of clusters will provide a more statistically reliable measurement of the

average cluster size. Meanwhile, smaller data sets tend to contain fewer clusters and can therefore exhibit greater variation in cluster size. For instances in which only a few small data sets were collected, the cluster size measurements were used from either the largest data set, or a weighted average of the cluster sizes from the existing data sets. An average slope for cluster size vs. ranged ions is then be calculated from the other specimens available, and subsequently used to extrapolate the projected cluster size at a common data set size. Following this approach, all the cluster diameter data in this study is normalized to a common data set size of 20 million ions (Figure 5.22).

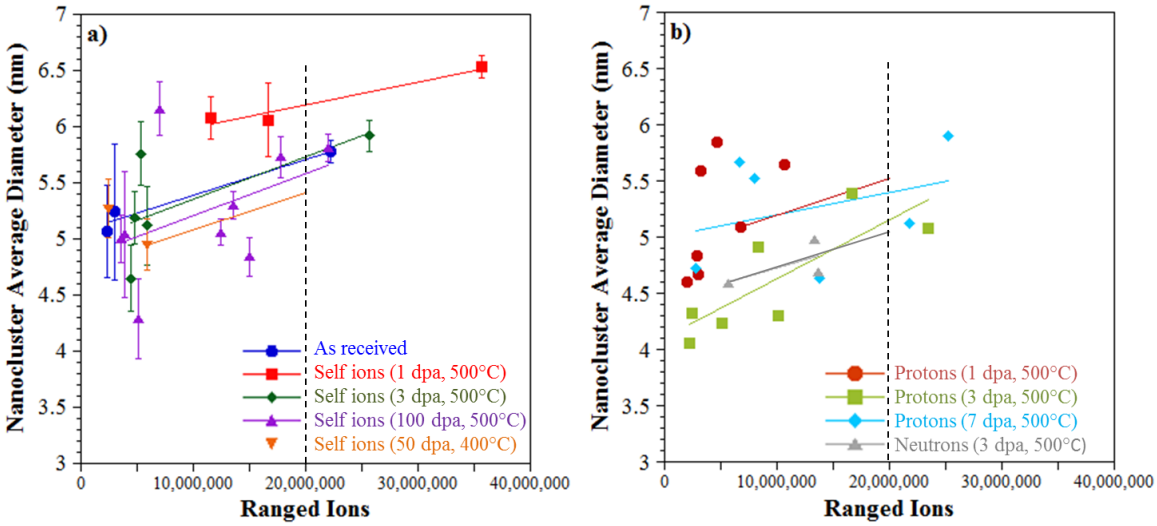

Figure 5.22 Normalized cluster Guinier diameter for each sample specimen of Fe-9%Cr ODS for the a) as received and Fe2+ irradiated specimens, and b) proton- and neutron-irradiated specimens. Linear fits are used to normalize the data comparison to a common data set size (e.g. 20 million ions).

The resulting measurements of average cluster size for each ODS specimen are tabulated in Table 5.4. Self-ion (Fe^{2+}) irradiation to 1 dpa causes the average nanocluster size to increase from 5.71 ± 1.92 nm to 6.20 ± 1.47 nm, but the clusters subsequently decrease in size to 5.73 ± 1.47 nm and 5.58 ± 2.30 nm after 3 dpa and 100 dpa, respectively. Proton irradiation, on the other hand, induces a continual decrease in

nanocluster size to 5.52 ± 1.66 after 1 dpa and further to 5.15 ± 1.40 nm and 5.40 ± 1.91 nm after 3 dpa and 7 dpa, respectively. Finally, irradiation with neutrons results in a decrease in nanocluster size to 5.03 ± 0.99 nm after 3 dpa.

Table 5.4 Summary of oxide nanocluster morphology and chemistry using APT, with normalized values for average cluster diameter.

Oxide nanoclusters	As Received	Fe^{2+} ion-irradiated (400°C) 50 dpa	Fe^{2+} ion-irradiated (500°C)			Proton-irradiated (500°C)			Neutron-irradiated (500°C) 3 dpa
			1 dpa	3 dpa	100 dpa	1 dpa	3 dpa[40,178][40,179][40,178]	7 dpa	
# of LEAP tips analyzed	3	3	3	5	9	7	7	6	3
# of clusters measured, ΣN_c	413	63	283	188	1474	176	975	652	169
Analysis Volume, ΣV_T (nm^3)	932,478	274,918	1,196,785	1,565,850	3,404,924	1,127,973	2,352,816	2,625,046	1,109,213
Average Diameter, D_G (nm)	5.71	5.41	6.20	5.73	5.58	5.52	5.15	5.40	5.03
Standard deviation for D_G	1.92	1.92	1.47	1.47	2.30	1.66	1.40	1.91	0.99
Std. dev. of the mean for D_G	0.09	0.24	0.09	0.11	0.06	0.13	0.04	0.07	0.08
Density, N_{nc} (x 10^{21} m^{-3})	443	229	131	120	433	156	414	226	152
Volume fraction, f_v	4.1%	2.5%	2.7%	1.8%	4.9%	1.8%	4.2%	2.1%	2.0%
$p_{Ti,Y}$	8.73%	10.97%	11.75%	10.54%	10.40%	15.18%	9.29%	10.53%	9.53%
$C_{Ti,Y}$	0.62%	0.23%	0.50%	0.43%	0.72%	0.39%	0.63%	0.37%	0.62%
Y:Ti	0.49 ± 0.14	0.48 ± 0.28	0.79 ± 0.20	0.92 ± 0.27	0.67 ± 0.34	0.81 ± 0.45	0.56 ± 0.16	0.55 ± 0.17	1.10 ± 0.35
(Y+Ti):O	1.25 ± 0.11	1.21 ± 0.14	1.20 ± 0.12	1.20 ± 0.17	1.16 ± 0.11	1.20 ± 0.13	1.21 ± 0.11	1.26 ± 0.15	1.24 ± 0.12
Matrix Composition, c_m^i (at%)									
Y	0.06%	0.05%	0.04%	0.06%	0.05%	0.02%	0.07%	0.04%	0.10%
Ti	0.21%	0.19%	0.14%	0.18%	0.18%	0.09%	0.18%	0.12%	0.34%

O	0.30%	0.27%	0.19%	0.22%	0.25%	0.12%	0.24%	0.16%	0.38%
Cr	8.45%	8.02%	8.35%	8.14%	7.35%	8.56%	8.29%	8.41%	8.14%
Si	0.16%	0.11%	0.13%	0.13%	0.10%	0.11%	0.13%	0.12%	0.14%
Mn	0.22%	0.05%	0.06%	0.08%	0.04%	0.08%	0.07%	0.06%	0.07%
Ni	0.04%	0.03%	0.04%	0.04%	0.03%	0.03%	0.03%	0.03%	0.05%
C	0.16%	0.20%	0.10%	0.12%	0.08%	0.09%	0.11%	0.07%	0.18%
W	0.63%	0.61%	0.60%	0.65%	0.60%	0.44%	0.61%	0.57%	0.67%
Trace amounts of P, S, N and H, Ga detected (balance is Fe)									

The number density and volume fraction of oxide nanoclusters is also calculated for each specimen and given in Table 5.4. However, the sampled APT analysis volume for each specimen, and hence the number density, is highly sensitive to a non-homogeneous distribution of nanoclusters within the matrix. An example is illustrated in Figure 5.15c and Figure 5.18, in which the lower portion of this APT needle exhibits localized absence of oxides. In this example, and others, the oxide-free region does not coincide with a Cr-Ti-C-rich carbide, nor is there any chemical evidence to suggest the presence of a grain boundary or other major precipitate or feature. This sort of non-homogeneous distribution is not observed in all specimens from an alloy/condition. Local inhomogeneities are also evident in the concentration of Ti and Y atoms in non-carbide regions of each specimen ($C_{Ti,Y}$), which fluctuates between 0.23% to 0.72% (Table 4). Comparing the nanocluster number density across specimens having such variable $C_{Ti,Y}$ values inhibits a "like-for-like" comparison – specimens having higher $C_{Ti,Y}$ values (i.e. more Ti and Y to begin with) will be biased toward higher nanocluster volume fractions. Instead, an adjusted volume fraction (f_v^{adj}) of nanoclusters is calculated to provide a more meaningful comparison. The adjusted volume fraction assumes the overall non-carbide Ti and Y concentration is consistent for all specimens (i.e. Ti and Y can only exist in the matrix or in clusters; they are neither lost nor gained to carbides and grain boundaries upon irradiation); this assumption is supported by the lack of evidence for segregation to grain boundaries and the observed balance between the composition of solutes in clusters and in the matrix (Section 3.2). The adjusted volume fraction is determined using:

$$f_v^{adj} = \frac{C_{Ti,Y} - c_{m,ar}^{Ti,Y}}{p_{Ti,Y}} \tag{5.1}$$

in which $c_{m,ar}^{Ti,Y}$ is the combined matrix composition of Ti and Y atoms in the as-received specimen and $p_{Ti,Y}$ is the fraction of all clustered atoms that are Ti and Y. Using f_v^{adj}, an adjusted nanocluster number density (N_{nc}^{adj}) is estimated using:

$$N_{nc}^{adj} = N_{nc} \cdot \frac{f_v^{adj}}{f_v} \tag{5.2}$$

The adjusted volume fractions and number densities provide more meaningful insight into the irradiation evolution of the nanoclusters; these adjusted volume fraction and number densities are tabulated in Table 5.5 and illustrated in Figure 5.23. Upon Fe^{2+} irradiation, the adjusted volume fraction decreases from 4.1% to 3.7% after 1 dpa, but then remains relatively consistent up to 100 dpa (3.8%). Meanwhile, the adjusted number density [from Fe^{2+}] drops sharply from 443 x 10^{21} m^{-3} to 180 x 10^{21} m^{-3} with 1 dpa, then increases to 240 x 10^{21} m^{-3} and 341 x 10^{21} m^{-3} after 3 dpa and 100 dpa, respectively. Under proton irradiation, both the volume fraction and the number density exhibit the trend of a rapid decrease between 0 and 1 dpa, followed by an increase from 1 to 3 to 7 dpa. Finally, after neutron irradiation to 3 dpa, the adjusted volume fraction and number density decrease to 2.0% and 149 x 10^{21} m^{-3}, respectively, which represents the most dramatic evidence of nanocluster dissolution of any of the irradiations to 3 dpa at 500°C. For comparison, the respective particle size distributions (in relative number density) of the as-received samples and following each irradiation are illustrated in Figure 5.24, while a plot of the average cluster size evolution relative to dose is provided in Figure 5.25.

Table 5.5 Adjusted volume fraction and number density values for oxide nanoclusters, using Eqs. (5.1) and (5.2), and

Oxide nanoclusters	As Received	Fe^{2+} ion-irradiated (400°C) 50 dpa	Fe^{2+} ion-irradiated (500°C)			Proton-irradiated (500°C)			Neutron-irradiated (500°C) 3 dpa
			1 dpa	3 dpa	100 dpa	1 dpa	3 dpa	7 dpa	
Adjusted volume fraction, f_v^{norm}	4.1%	3.5%	3.7%	3.6%	3.8%	3.3%	4.1%	4.4%	2.0%
Adjusted number density, N_{nc}^{norm} (x 10^{21} m^{-3})	443	323	180	240	341	282	402	488	149
Species enrichment in clusters, $f_{en}{}^{i}$ (above f_v^{norm})									
Y	63.0%	63.4%	75.1%	57.1%	80.1%	80.4%	66.9%	66.6%	49.8%
Ti	50.3%	45.9%	52.1%	32.1%	57.4%	59.9%	53.7%	49.6%	19.6%
O	46.6%	44.9%	55.6%	39.6%	62.0%	63.1%	54.8%	49.2%	28.0%
Cr*	0.8%	1.0%	0.1%	-1.1%	3.0%	-0.7%	2.0%	-1.6%	0.9%
Si	1.4%	2.3%	2.9%	0.9%	7.7%	1.5%	5.3%	-0.6%	5.3%
Mn	-2.4%	1.4%	0.2%	-1.2%	3.1%	-1.0%	1.5%	-2.0%	3.6%
Ni	1.6%	3.3%	5.2%	3.4%	13.0%	4.4%	10.2%	-0.1%	6.5%
C*	4.1%	4.0%	10.6%	1.3%	3.5%	8.8%	7.3%	2.7%	1.6%
W*	-0.2%	0.1%	-0.7%	-2.4%	-1.0%	-0.4%	-1.6%	-2.6%	-0.6%
*Does not include species clustering in carbide precipitates									

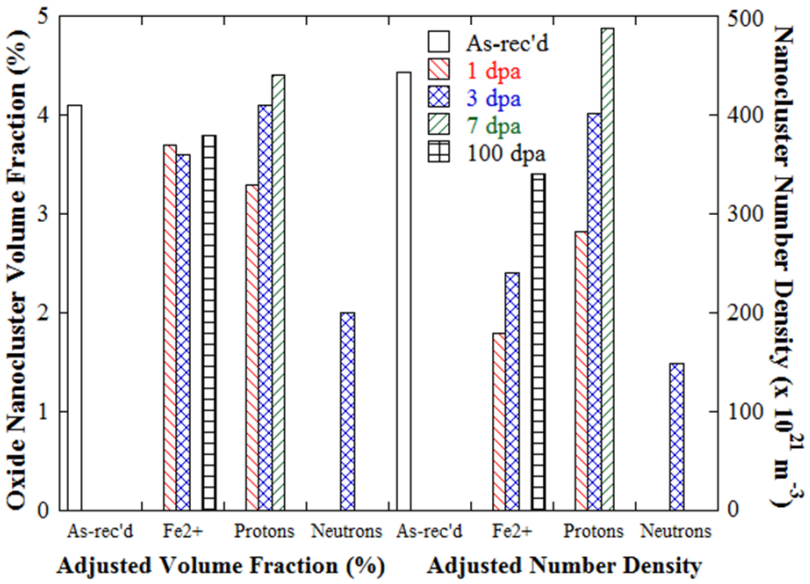

Figure 5.23 Evolution of oxide nanocluster adjusted volume fraction and number density following each irradiation at 500°C.

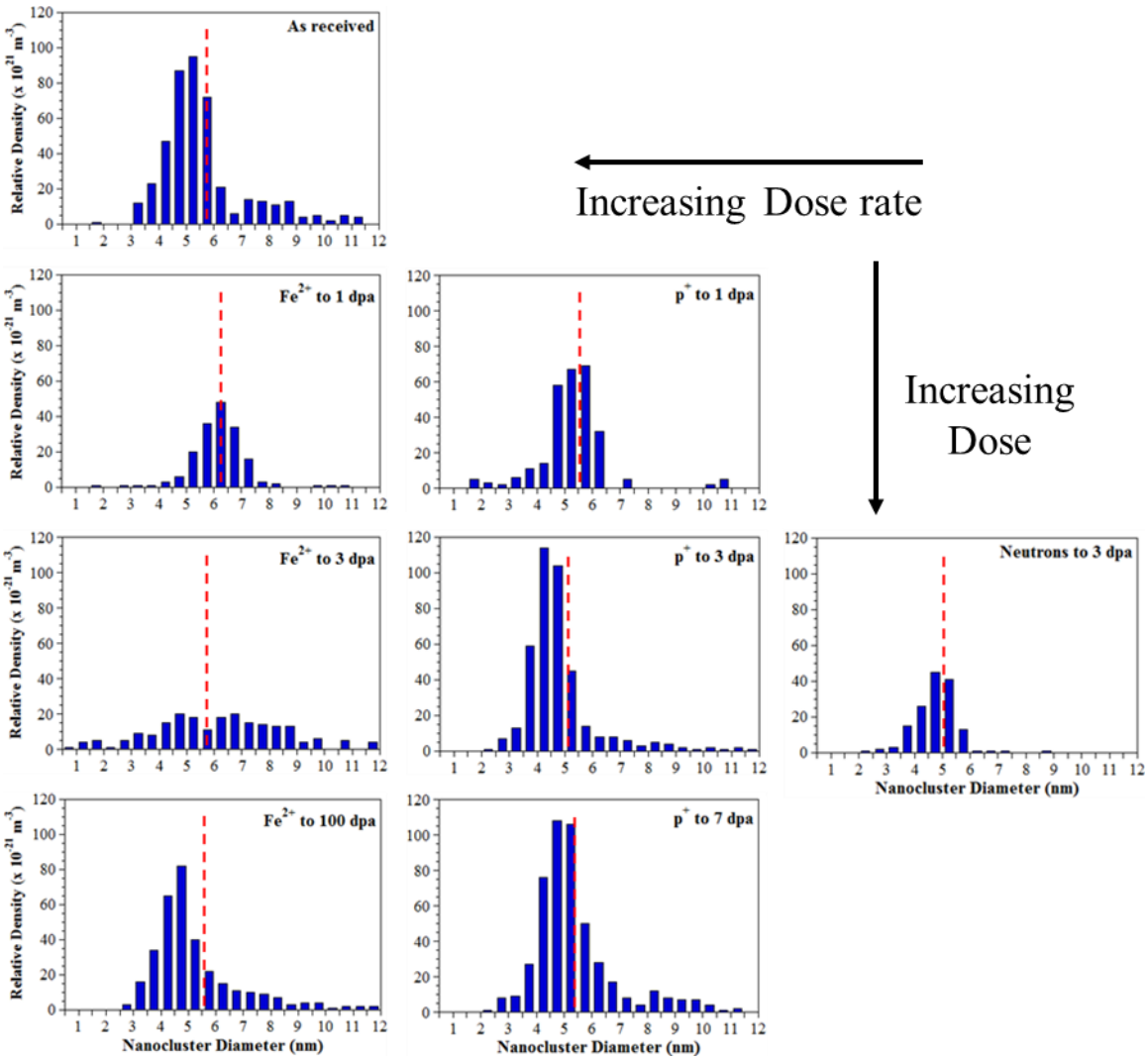

Figure 5.24 Nanocluster particle size distributions for each analyzed specimen, plotted as relative number density for size and overall number density comparison.

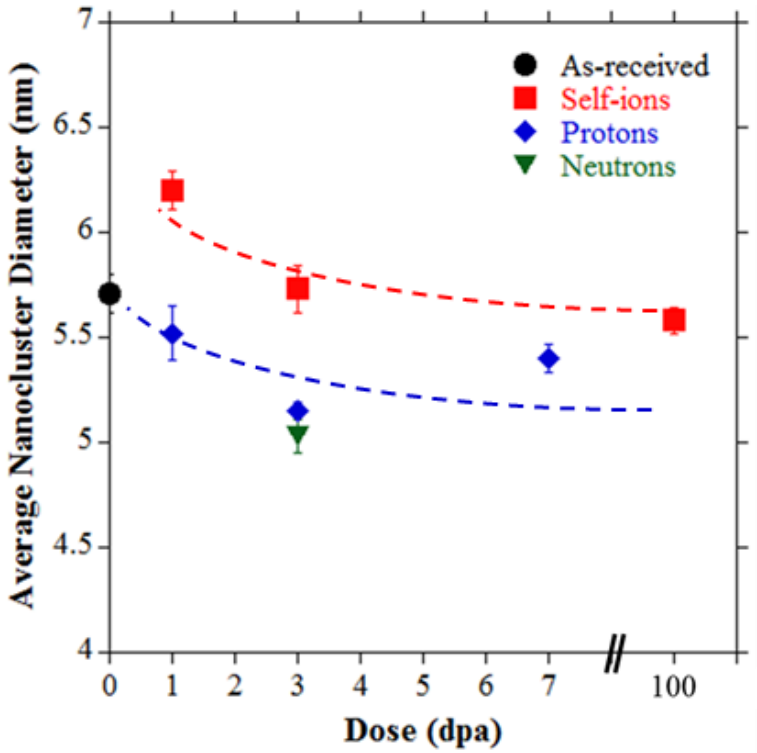

Figure 5.25 Oxide nanocluster average diameter evolution in Fe-9%Cr ODS following each irradiation.

The enrichment parameter f_{en}^{i} (Table 5.5), represents the percent of all collected ions of species *i*, above the normalized volume fraction, which is contained in the analyzed clusters. This is a key parameter from APT cluster analysis that enables one to understand the irradiation evolution of nanocluster chemistry. Upon Fe^{2+} irradiation, the f_{en}^{i} of Y, Ti, and O increases after 1 dpa, declines after 3 dpa, then increases again at 100 dpa. Upon proton irradiation, the f_{en}^{i} of Y, Ti, and O increases considerably at 1 dpa, then declines at 3 dpa, where it remains relatively consistent through 7 dpa at values that are slightly higher than in the as-received specimen. The most dramatic decrease in f_{en}^{Y}, f_{en}^{Ti}, and f_{en}^{O} is following neutron irradiation to 3 dpa. One of the most pivotal de-clustering species is measured for Ti; prior to irradiation, 50.3% of all Ti ions above the normalized volume fraction are clustered, compared to only 19.6% enrichment following neutron

irradiation. As expected, the matrix composition generally demonstrates an opposite trend as f_{en}^{i} values (Table 5.5). For elements that exhibit reduced enrichment in clusters upon irradiation (Y, Ti, and O) there is a corresponding increase in matrix concentration. For elements that exhibit increased enrichment upon irradiation (Si, Mn, and Ni), there is a corresponding decrease in matrix concentration.

A final method to evaluate the chemical evolution of nanoclusters is through measurement of the Y:Ti and (Y+Ti):O ratios. A summary of the Y:Ti ratio and (Y+Ti):O ratio evolution for each irradiation is illustrated in Figure 5.26. Upon Fe^{2+} irradiation, the Y:Ti ratio increases from 0.49 ± 0.14 to 0.79 ± 0.20 up to 1 dpa, increases further to 0.92 ± 0.27 at 3 dpa, then declines to 0.67 ± 0.34 after 100 dpa. Upon proton irradiation, the Y:Ti ratio increases to 0.81 ± 0.45 following 1 dpa, then declines to 0.56 ± 0.16 and 0.55 ± 0.17 after 3 dpa and 7 dpa, respectively. Again, the most dramatic change is observed after neutron irradiation to 3 dpa (Y:Ti = 1.10 ± 0.35). Regardless, each irradiation has resulted in an increase in Y:Ti ratio, which is consistent with other studies in literature [8,9], suggesting that Ti atoms are more readily displaced from nanoclusters than are Y atoms. Interestingly, the (Y+Ti):O ratio consistently falls in the range 1.16–1.25, statistically unaffected by any of the irradiations. This result implies that O atoms are displaced at the same rate as Ti atoms are ejected.

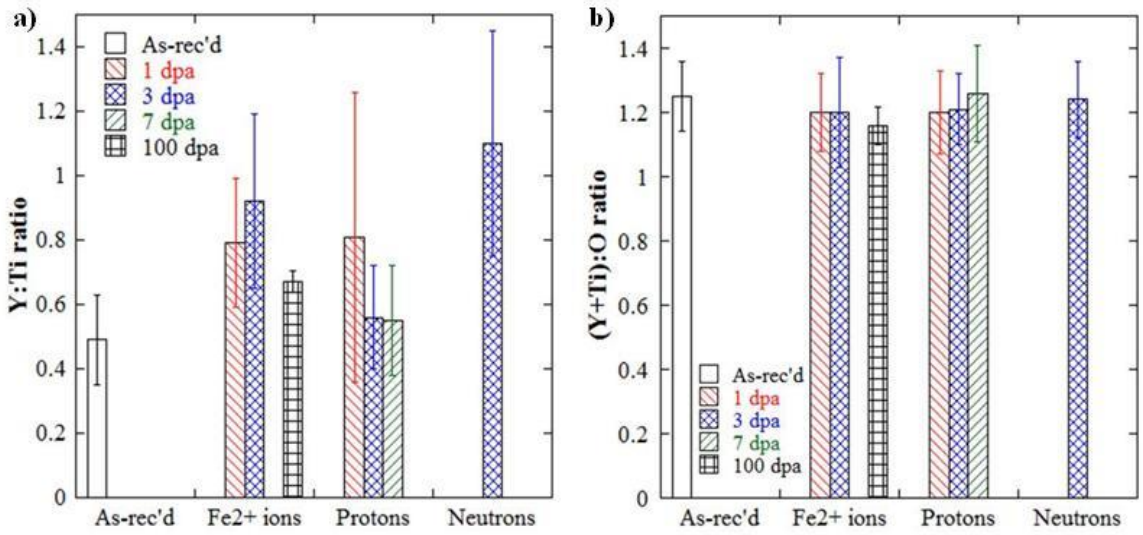

Figure 5.26 Summary of oxide nanocluster chemistry evolution following each irradiation at 500°C: a) Y:Ti ratio, and b) (Y+Ti):O ratio.

5.2.2 Clustering Results in HCM12A

The atomic-level resolution of APT with IVAS cluster analysis enabled the characterization of the nanoclusters after each irradiation condition. Each HCM12A specimen following Fe^{2+}, proton, and neutron irradiation at common conditions of 3 dpa at 500°C exhibit clustering of Si, Mn, Ni, P atoms (G-phase precipitates) along with Cu atom clusters at adjacent locations. However, a lower dose proton irradiation to 1 dpa exhibited only the Cu atoms clustering, without adjacent G-phases. In addition, no clusters were found after Fe^{2+} irradiation to 100 dpa. Clustering of Cr atoms (i.e. α' phase) was observed only after neutron-irradiation (3 dpa). Representative atom distribution maps of Si, Mn, Ni, P, Cu and separate maps for Cr are found in Figure 5.27. Out of the 6 total tips analyzed for the specimen irradiated with Fe^{2+} ions to 100 dpa, no clusters were found. In one of the tips, shown in Figure 5.27e, clear evidence of grain boundary segregation is evident. The significance of this is further discussed in Section 7.4.2.2.

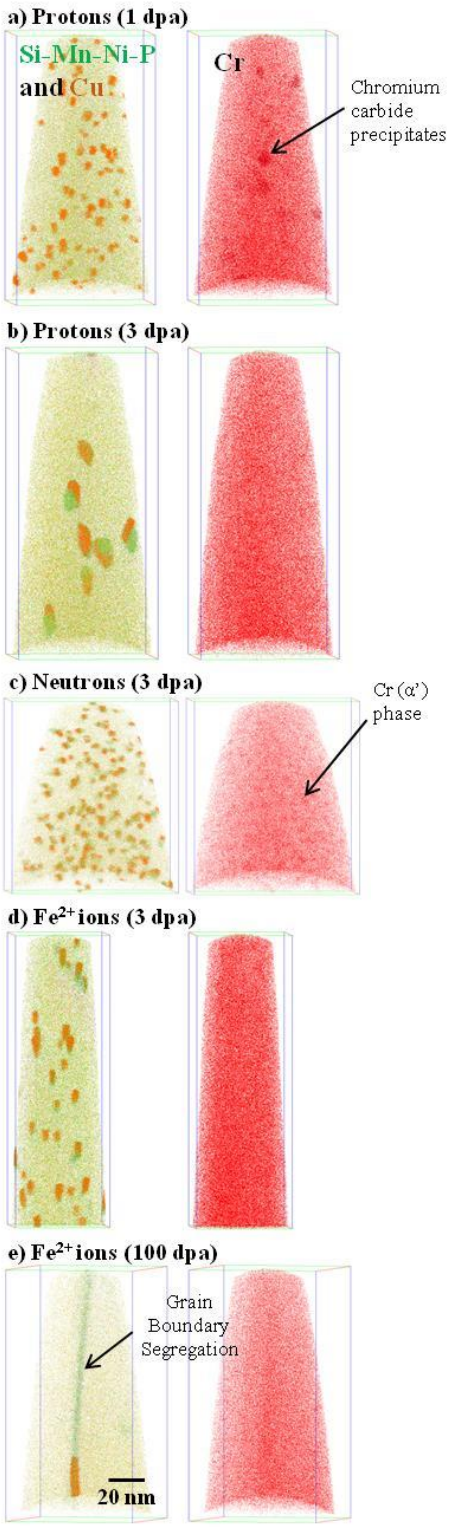

Figure 5.27 Atom probe distribution maps of Si-Mn-Ni-P, Cu, and Cr atom distribution in HCM12A following a) proton irradiation to 1 dpa, b) proton irradiation to 3 dpa, c) neutron irradiation to 3 dpa, d) Fe2+ ion irradiation to 3 dpa, and e) Fe2+ ion irradiation to 100 dpa.

As with the Fe-9%Cr ODS, the average nanocluster Guinier diameter was calculated for each data set from every specimen condition. The results of this exercise are shown in Figure 5.28 as a function of the total number of ranged ions in each data set for the HCM12A specimens. Linear trend lines are fitted to the data sets for each specimen, with a consistent slope resulting for most specimens, particularly in those specimens for which a larger number of LEAP tips have been analyzed (i.e. a larger statistical sample size is available). Following the approach as with the Fe-9%Cr ODS, all the cluster diameter data in this study is normalized to a common data set size of 20 million ions (Figure 5.29). Quantitative cluster analysis results are provided in Table 5.6, enabling the comparison of cluster evolution across of range of doses for proton and self-ion irradiation and across each particle irradiation at otherwise common conditions (3 dpa at 500°).

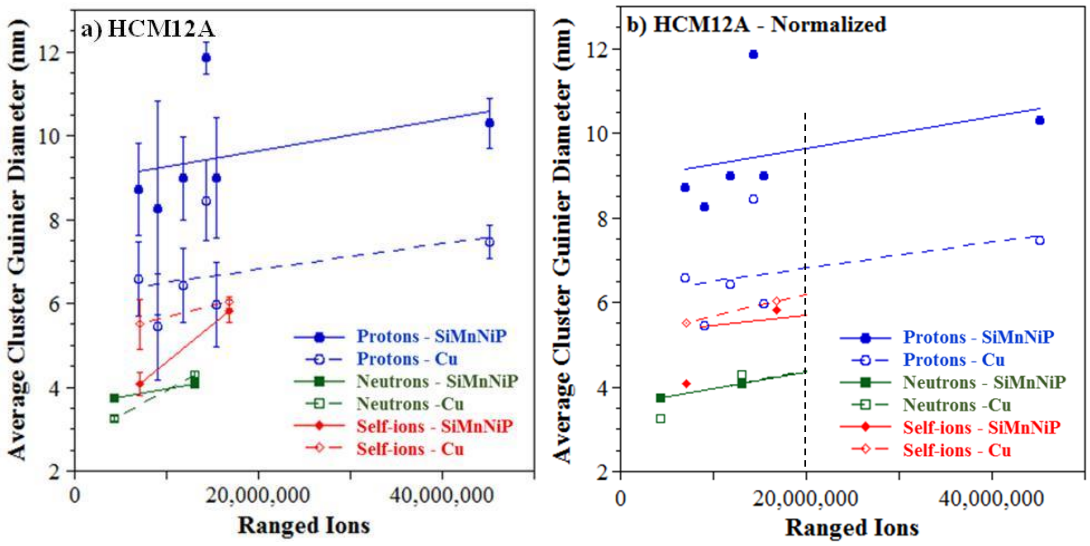

Figure 5.28 Average measured cluster Guinier diameter for each data set collected for each sample condition in HCM12A for a) as measured, and b) normalized to 20 million ions). Linear fits are used to normalize the data comparison to a common data set size (e.g. 20 million ions in this study).

Table 5.6 Summary of cluster analysis of HCM12A for each irradiation condition using APT.

Nanocluster Analysis	Fe^{2+} ion-irradiated (500°C)		Proton-irradiated (500°C)		Neutron-irradiated (500°C)
	3 dpa	100 dpa	1 dpa	3 dpa	3 dpa
# of LEAP tips analyzed	2	6	5	6	2
Analysis Volume, V_T (nm^3)	811,282	1,536,885	1,383,130	3,426,840	572,186
Si-Mn-Ni-P rich clusters					
# of clusters measured, $\sum N_{nc}^{Si}$	75	0	0	66	228
Average Diameter, D_G^{Si} (nm)	5.95	-	-	9.63	4.36
Standard deviation for D_G^{Si}	2.01	-	-	3.49	0.80
Std. dev. of the mean for D_G^{Si}	0.23	-	-	0.43	0.05
Density, N_{nc}^{Si} (x 10^{21} m^{-3})	92	-	-	19	398
Volume fraction, f_v^{Si}	1.1%	-	-	1.9%	2.8%
Cu-rich clusters					
# of clusters measured, $\sum N_{nc}^{Cu}$	87	0	247	66	213
Average Diameter, D_G^{Cu} (nm)	6.18	-	5.03	6.82	4.59
Standard deviation for D_G^{Cu}	1.26	-	1.12	2.59	0.90
Std. dev. of the mean for D_G^{Cu}	0.13	-	0.07	0.32	0.06
Density, N_{nc}^{Cu} (x 10^{21} m^{-3})	107	-	179	19	372
Volume fraction, f_v^{Cu}	2.5%	-	2.6%	1.5%	3.1%

Cr-rich clusters					
# of clusters measured, $\sum N_{nc}^{Cr}$	0	0	0	0	203
Average Diameter, D_G^{Cr} (nm)	-	-	-	-	3.17
Standard deviation for D_G^{Cr}	-	-	-	-	0.49
Std. dev. of the mean for D_G^{Cr}	-	-	-	-	0.03
Density, N_{nc}^{Cr} (x 10^{21} m^{-3})	-	-	-	-	355
Volume fraction, f_v^{Cr}	-	-	-	-	0.57%

A total of 66, 75, and 228 Si-Mn-Ni-P-rich nanoclusters were identified and analyzed in the specimens of HCM12A irradiated with protons, Fe^{2+} ions, or neutrons to 3 dpa, respectively. Proton irradiation induced the largest average size of these nanoclusters at 9.63 ± 3.49 nm, while clusters following Fe^{2+} and neutron irradiation were 5.95 ± 2.01 nm and 4.36 ± 0.87 nm, respectively. Conversely, number density of Si-Mn-Ni-P-rich clusters was lowest following proton irradiation to 3 dpa (19 x 10^{21} m^{-3}) and increased to 92 x 10^{21} m^{-3} and 398 x 10^{21} m^{-3} following Fe^{2+} and neutron irradiation to 3 dpa, respectively. For the Cu-rich clusters in HCM12A, a total of 247, 66, 87, and 213 clusters were identified after proton irradiation to 1 dpa and 3 dpa, and after Fe^{2+} and neutron irradiation to 3 dpa, respectively. Upon proton irradiation, Cu clusters coarsened following doses of 1 dpa and 3 dpa, increased in size from 5.03 ± 1.12 nm to 6.82 ± 2.59, while decreasing in density from 179 x 10^{21} m^{-3} to 19 x 10^{21} $m^{-}3$, respectively. Similar to the Si-Mn-Ni-P clusters, neutron irradiation yielded the smallest average Cu-rich cluster size at 4.59 ± 0.90 nm, while clusters following Fe^{2+} irradiation were 6.18 ± 1.26 nm. Similar to the Si-Mn-Ni-P clusters, number density of Cu-rich clusters is highest following neutron irradiation to 3 dpa (372 x 10^{21} m^{-3}), while the density following Fe^{2+} irradiation is an intermediate value of 107 x 10^{21} m^{-3}. Finally, Cr-rich clusters found in the neutron-irradiated specimen averaged 3.17 ± 0.49 nm in diameter with a density of 355 x 10^{21} m^{-3}. A summary of average nanocluster diameter evolution upon each irradiation of HCM12A is illustrated in Fig. 5.29.

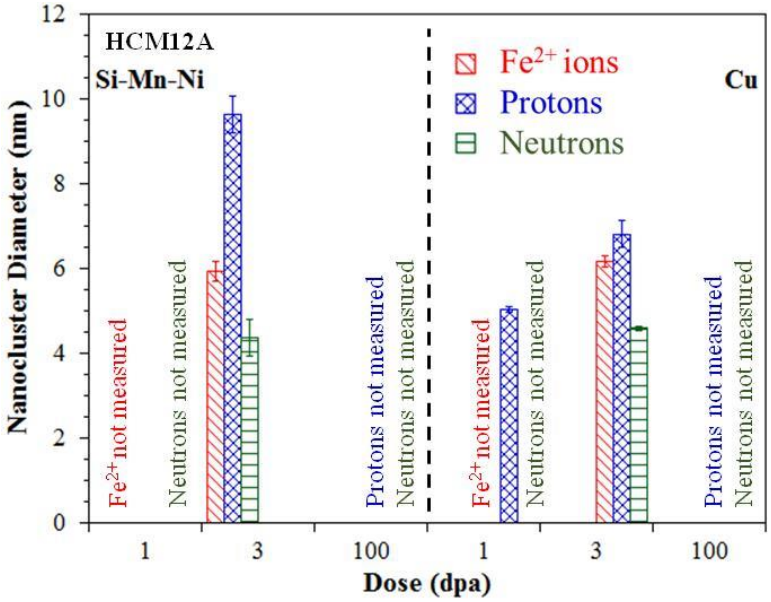

Figure 5.29 Nanocluster average diameter evolution in HCM12A for Si-Mn-Ni - rich and Cu-rich clusters.

5.2.3 Clustering Results in HT9

The HT9 specimens following proton and neutron irradiation at common conditions of 3 dpa at 500°C exhibit clustering of Si, Mn, Ni, P atoms, but do not display any clusters upon Fe^{2+} irradiation either to 3 dpa or 100 dpa. Similarly, after proton irradiation to only 1 dpa, no Si-Mn-Ni-P-rich clusters were found. Clustering of Cr atoms (i.e. α' phase) are present only after neutron-irradiation (3 dpa). Representative atom distribution maps of Si, Mn, Ni, and P and separate maps for Cr are found in Figure 5.30. Out of the 2 tips analyzed for the specimen irradiated with Fe^{2+} ions to 100 dpa, no clusters were found. In one of the tips, shown in Figure 5.29e, clear evidence of grain boundary segregation is evident. The significance of this is further discussed in Section 7.4.2.2.

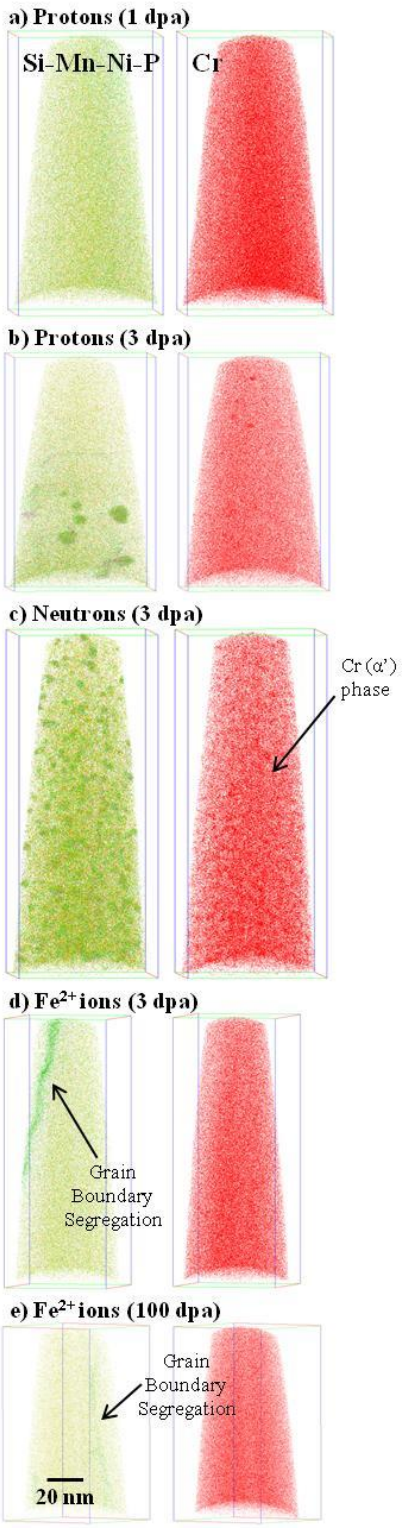

Figure 5.30 Atom probe distribution maps of Si-Mn-Ni-P and Cr atom distribution in HT9 following a) proton irradiation to 1 dpa, b) proton irradiation to 3 dpa, c) neutron irradiation to 3 dpa, d) Fe2+ ion irradiation to 3 dpa, and e) Fe2+ ion irradiation to 100 dpa.

As with the Fe-9%Cr ODS and HCM12A, the average nanocluster Guinier diameter is calculated for each data set from every specimen condition. The results of this exercise are shown in Figure 5.31 plotted against the total number of ranged ions in each data set for the HT9 specimens. Linear trend lines are fitted to the data sets for each specimen. With a limited number of samples and specimens, the trends are less clear, particularly for the small samples of the proton-irradiated specimen. Since the trendline slope for the larger neutron-irradiated specimen is very similar to those found in the ODS specimens, this same slope was used to normalize the proton-irradiated measurements. Furthermore, since the smallest proton-irradiated sample only contained 1 cluster, the trendline is extrapolated from the larger proton-irradiated sample (Figure 5.31b). Quantitative cluster analysis results are provided in Table 5.7, enabling the comparison of cluster evolution across a range of doses for proton and self-ion irradiation and across each particle irradiation at otherwise common conditions (3 dpa at 500°).

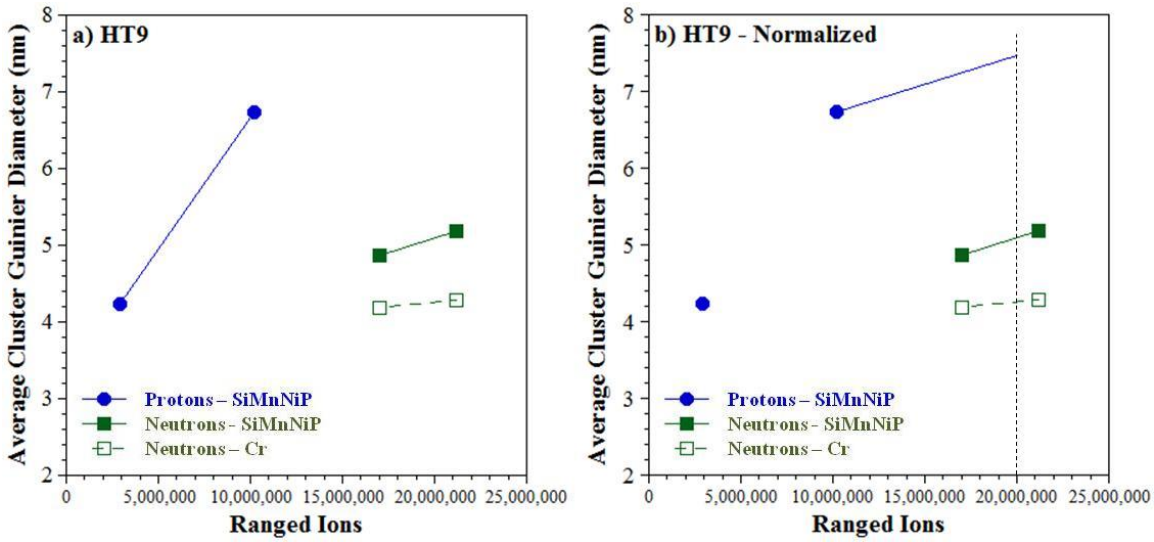

Figure 5.31 Average measured cluster Guinier diameter for each data set collected for each sample condition in HT9 for a) as measured, and b) normalized to 20 million ions). Linear fits are used to normalize the data comparison to a common data set size (e.g. 20 million ions in this study).

Table 5.7 Summary of cluster analysis of HT9 for each irradiation condition using APT.

Nanocluster Analysis	Fe^{2+} ion-irradiated (500°C)		Proton-irradiated (500°C)		Neutron-irradiated (500°C) 3 dpa
	3 dpa	100 dpa	1 dpa	3 dpa	
# of LEAP tips analyzed	2	3	5	2	2
Analysis Volume, V_T (nm^3)	643,426	584,088	1,330,673	449,677	1,275,897
Si-Mn-Ni-P rich clusters					
# of clusters measured, $\sum N_{nc}^{Si}$	0	0	0	13	515
Average Diameter, D_G^{Si} (nm)	-	-	-	7.47	5.09
Standard deviation for D_G^{Si}	-	-	-	3.21	4.19
Std. dev. of the mean for D_G^{Si}	-	-	-	0.89	0.18
Density, N_{nc}^{Si} (x 10^{21} m^{-3})	-	-	-	29	404
Volume fraction, f_v^{Si}	-	-	-	0.7%	3.8%
Cr-rich clusters					
# of clusters measured, $\sum N_{nc}^{Cr}$	0	0	0	0	1578
Average Diameter, D_G^{Cr} (nm)	-	-	-	-	4.27
Standard deviation for D_G^{Cr}	-	-	-	-	0.79
Std. dev. of the mean for D_G^{Cr}	-	-	-	-	0.02
Density, N_{nc}^{Cr} (x 10^{21} m^{-3})	-	-	-	-	1273
Volume fraction, f_v^{Cr}	-	-	-	-	5.7%

For the HT9 specimens, a total of 13 and 515 Si-Mn-Ni-P-rich nanoclusters were identified and analyzed in proton-irradiated (3 dpa), and neutron-irradiated (3 dpa) specimens, respectively. As with HCM12A, proton irradiation induced the coarsest distribution of nanoclusters, with an average diameter of 7.47 ± 2.92 nm and number density of 29 x 10^{21} m^{-3}, while clusters following neutron irradiation were 5.09 ± 1.63 nm with a density of 404 x 10^{21} m^{-3}. Cr-rich clusters found in the neutron-irradiated specimen averaged 4.27 ± 1.35 nm in diameter with a density of 1237 x 10^{21} m^{-3}. A summary of average nanocluster diameter evolution upon each irradiation of HT9 is illustrated in Figure 5.32.

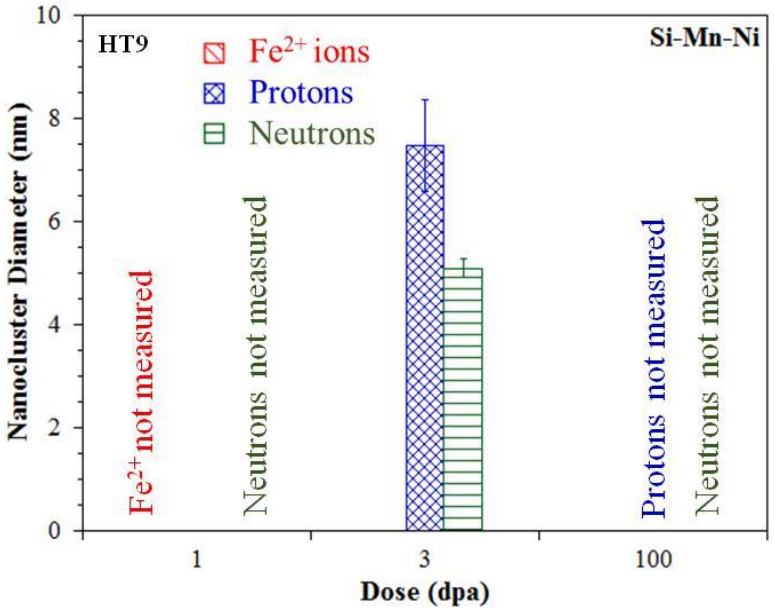

Figure 5.32 Nanocluster diameter evolution in HT9 for Si-Mn-Ni-rich clusters.

CHAPTER SIX: MODELING NANOCLUSTER EVOLUTION

This chapter contains the modeling work conducted in the context of this thesis to describe irradiation-induced nanocluster evolution. Through this effort, three primary objectives are accomplished: 1) provide context and understanding of the relative damage creation mechanisms of different irradiating particles, 2) determine whether an irradiation temperature shift is required to emulate nanocluster evolution with varying dose rate irradiations, and 3) provide the framework for developing an adaptive model applicable to any b.c.c. Fe-based alloy (and other systems) for predicting radiation-induced nanocluster evolution. The following sections will outline the modeling methodology used, its application to the Fe-9%Cr ODS, HCM12A, and HT9 alloys evaluated in this study, and summarize the consistent trends, key takeaways, and potential as a future predictive development tool.

6.1 Modeling Methodology

The modeling conducted for this thesis is primarily based on a calculation methodology development by Nelson, Hudson, and Mazey [57]. The basis of this model is the consideration of multiple radiation effects occurring simultaneously, and their combined influence on the relative size (i.e. radius) of the nanoclusters with the alloy matrix. The following sections will provide a more detailed overview of the Nelson-Hudson-Mazey model, the development and selection of the input parameters for the model, and its application. It will be shown how the model is first used to simulate the observed cluster evolution for the Fe-9%Cr ODS alloy (the richest set of data) by initially

fitting two unknown parameters. Next, using these fit parameters, the model is used to simulate the cluster evolution in HCM12A (which contains several common solutes to ODS) and to refine the fit of each parameter. Finally, the predictability of the model will be tested against the observed irradiation-induced cluster evolution of the HT9 alloy.

6.1.1 The Nelson-Hudson-Mazey Model

The Nelson-Hudson-Mazey (NHM) model is briefly introduced in Section 2.4.6 and is essentially a set of first-order differential equations describing the change in precipitate radius over a unit of time. For this thesis, the same equations are applied to describe nanoclusters in the alloys, which may not be true stoichiometric secondary phases. As discussed in Section 2.4.6, the NHM equation was derived to account for two separate alternative mechanisms for ballistic dissolution of nanocluster phases: a) recoil dissolution, and b) disordering dissolution. Given these mechanisms are theoretically mutually exclusive, the possibility is considered that each mechanism may both act simultaneously during the process of irradiation. As a result, the NHM equations (Eq. 2.15 and 2.16) for each respective mechanism are combined into a single governing equation written as:

$$\frac{dr}{dt} = -\frac{\phi}{N} - \psi K + \frac{3D^{irr}C}{4\pi pr} - D^{irr}r^2 n \qquad (6.1)$$

In this equation, the first two terms on the right hand side represent the effects of recoil and disordering dissolution, respectively. Each of these terms are preceded with a negative sign, representing the change in cluster radius resulting from these effects is a reduction. As outlined in Section 2.4.6, the third and fourth terms in Eq. 6.1 represent the balance of solute migration from the matrix to the nanocluster, resulting in a net growth in the cluster size. In its entirety, the calculation may result in either a positive change in

radius, or a negative change in radius over time, depending on the values used for each variable in the equation.

With the more recent development and improvement of atom probe tomography techniques, the ability to precisely measure many of the variables in Eq. 6.1 has been greatly enhanced, making application of the NHM model much more feasible. One of the fundamental challenges is the measurement of the parameters C and p in the third term. The value of C represents the total combined concentration of solutes that are included in both the existing nanoclusters and within the matrix of the material. This value may not be the same as the overall composition of solutes in the material, as some of the solute species may also reside within existing carbide precipitates, which are excluded from this analysis. Given that the carbide precipitate size and number density are observed to be stable upon irradiation (Section 5.1), it is assumed the solutes within the carbide precipitates are also stable. As a result, C represents the total amount of non-carbide solutes. Meanwhile, the value for p represents the relative percentage of clustered atoms, which are identified as solute atoms. Combining chemistry analysis with the objective cluster analysis techniques outlined in Section 4.5.3 allows one to statistically measure these values at high precision over the entire collection of data sets and clusters available for each studied specimen.

The NHM model for this thesis is executed using Microsoft Excel and structured as a series of inter-dependent workbooks. Each workbook represents a subroutine or individual variations of the calculation to enable comparison of dependencies such as irradiating particle dependence, temperature dependence, and solute species-specific dependence. The model is modularly designed, enabling the possibility to add calculation

variations as needed for sensitivity analysis of variables. It is also possible to add calculations utilizing data from different studies, such as those derived from the existing literature, for comparison of results. Finally, when attempting to apply the model to an alternative alloy system with differing species of clustering solutes, the model may be converted to a new file and all relative data inputs for the new system are adjusted accordingly. An overview of the model structure and logic is illustrated as a flowchart in Figure 6.1. The two primary subroutines of the model are: 1) estimation of the respective damage cascade effective diameter for each irradiating particle, and 2) estimation of the respective system parameters influencing the radiation-enhanced diffusion rates for each solute and respective irradiation. The logic and role for each of these subroutines are described in the following sections.

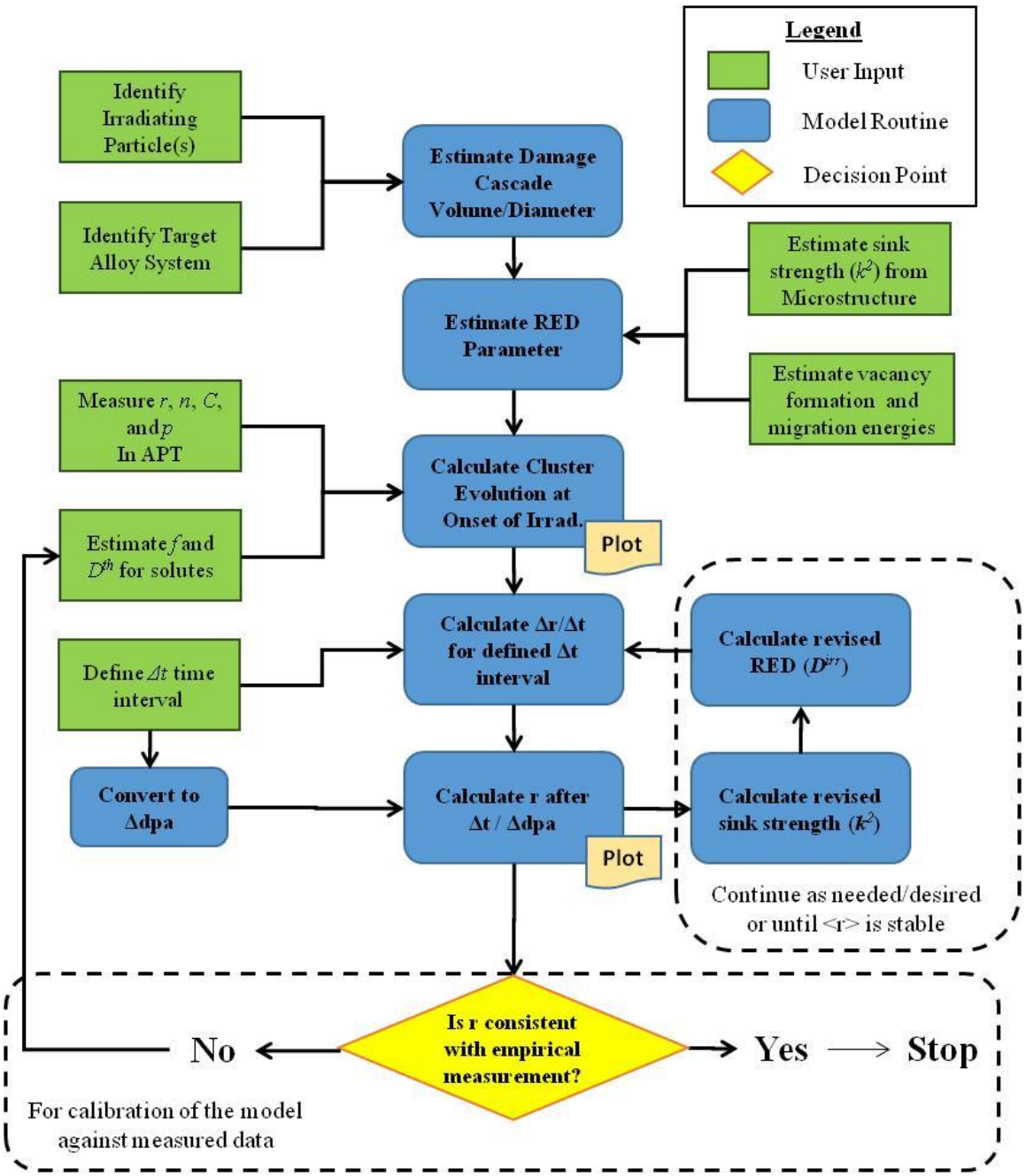

Figure 6.1 Flowchart of NHM model logic and approach for radiation-induced nanocluster evolution calculations.

6.1.1.1 Cascade Effective Diameter Estimation

Estimation of the respective volume for a damage cascade resulting from different irradiating particles is an important input to the model. Within the second term of Eq. 6.1 is the disordering parameter, ψ, which is defined as product between the cascade relative

size (i.e. effective diameter), *l*, and the disordering efficiency, *f*. In Section 2.1.2, the methodology for estimating the value of *l* for each type of irradiating particle is provided. Within the model, the user provides inputs/estimates for the average energy transferred to the primary knock-on atom (PKA) for each cascade, T, and the respective atomic number, Z, and atomic weight, A, for both the irradiating particle and the target alloy (i.e. Fe for this study). The values for T used for this study are tabulated in Table 2.1 in Section 2.1.2. It is important to recognize the value of *l* is not only dependent upon the irradiating particle, but also depends on the target alloy system (e.g. displacement energies, interatomic potentials, nearest neighbor species). For this thesis, each alloy studied is based on the b.c.c. Fe system. However, if the model is adapted for a different alloy system (e.g. Zr-based), the values for *l* will be influenced even if the irradiation conditions are otherwise kept consistent. For the purpose of this thesis, the respective values for *l* are estimated to be ~2.3 nm for proton irradiation, ~6.8 nm for Fe^{2+} irradiation, and ~10.4 nm for neutron irradiation.

6.1.1.2 Radiation-Enhanced Diffusion Parameters

As discussed in Section 2.1, one of the primary effects of irradiation on a target alloy is the non-equilibrium generation of vacancy and interstitial defects in the material, thus enhancing the mobility of diffusing solutes [42]. This radiation-enhanced diffusion (RED) rate of solutes is generally expressed as [42]:

$$D^{irr} = D_v C_v + D_i C_i \tag{6.2}$$

where C_v and C_i are concentrations of vacancies and interstitials, respectively, and D_v and D_i are the respective diffusion rates of vacancies and interstitials. In the context of solute atoms, Eq. 6.2 may be rewritten as:

$$D_{sol}^{irr} = D_{sol}^{v} C_{v}^{irr} + D_{sol}^{i} C_{i}^{sol} \quad (6.3)$$

in which D_{sol}^{irr}, is the total radiation-enhanced diffusion rate of the solute, while D_{sol}^{v} and D_{sol}^{i} are the solute diffusion rates via vacancies and interstitials, respectively. The term C_{v}^{irr} is the total number of irradiation-induced vacancies in the microstructure (not limited to any specific solute) and C_{i}^{sol} is the concentration of solutes that have been displaced to interstitial sites (predominantly due to irradiation). Since the total concentration of the solutes in F-M and ODS alloys in this study are low, the concentration of solutes displaced to interstitial sites upon irradiation will also be very low. By comparison, the concentration of vacancies (first term in Eq. 6.3) is not dependent on solute concentration. It follows the diffusion rate via vacancies will dominate for most solutes.

Two exceptions to this logic are relevant in this study. First, the solute concentration of Cr in each of the alloys in this study range 9-12%, suggesting the concentration of irradiation-induced solute interstitials is likely to be a more significant amount. Wharry has demonstrated there is a crossover temperature at which the dominant diffusion mechanism changes from vacancy diffusion to interstitial diffusion [179]. The other exception is with O in the Fe-9%Cr ODS alloys, which is known to predominantly reside on interstitial sites in equilibrium [154], and thus predominantly diffuse interstitially. Therefore, the mobility of O will be much higher than other solutes, and thus not a limiting factor to the overall cluster evolution [4,59]. The same approach of assuming vacancy diffusion as the dominant mechanism for all other solutes is also taken in [59,60], where the irradiation-induced mobility of solutes (D_{sol}^{irr}) is expressed as [59,60]:

$$D_{sol}^{irr} = \frac{C_v^{irr}}{C_v^{eq}} D_{sol}^{th} \tag{6.4}$$

in which C_v^{irr} is the non-equilibrium concentration of vacancies due to irradiation, while C_v^{eq} is the concentration of vacancies at thermal equilibrium when irradiation is not present. The value of C_v^{eq} may be estimated as [59]:

$$C_v^{eq} = exp\left(-\frac{E_v^f}{k_b T}\right) \tag{6.5}$$

in which E_v^f is the formation energy for a vacancy (estimated to be 2.2 eV [59]), k_b is the Boltzmann constant, and T is the temperature. Similarly, the thermal diffusion, D^{th}, may be written as:

$$D_{sol}^{th} = D_0 exp\left(-\frac{E_{sol}^m}{k_b T}\right) \tag{6.6}$$

where D_0 is the pre-exponential and E_{sol}^m is the migration energy. These values may be retrieved for each respective solute in literature. Finally, the value for C_v^{irr} may be estimated as [59]:

$$C_v^{irr} = K\tau \tag{6.7}$$

in which K is the dose rate of the irradiation (in dpa/s), and τ is the characteristic time required for these vacancy defects to migrate to a sink in the microstructure, and is calculated as [59]:

$$\tau = \frac{1}{k_{total}^2 D_v} \tag{6.8}$$

In Eq. 6.8, τ is dependent upon both the sink strength of the microstructure for the target alloy (k^2) and D_v, which is the diffusion coefficient for the vacancies.

The total sink strength for the microstructure of an alloy may be estimated as the cumulative sum of the respective sink strengths for each microstructural feature [42]:

$$k_{total}^2 = k_{gb}^2 + k_{disl}^2 + k_{carb}^2 + k_{nc}^2 + k_{loops}^2 + k_{voids}^2 \quad (6.9)$$

Furthermore, the sink strength contribution of each feature in the microstructure is calculated as follows:

Grain boundaries [180]: $k_{gb}^2 = \frac{\gamma}{R_g^2}$ (6.10)

where R_g is the mean effective radius of the grains, and γ is expressed as

$$\gamma = \frac{\frac{3}{2}\left\langle 3+4\beta-\frac{6\beta(\beta-1)}{\alpha^2}+\left\{\left[3+4\beta-\frac{6\beta(\beta-1)}{\alpha^2}\right]^2-4(\beta^2-\alpha^2)\left[2-\frac{3(\beta-1)}{\alpha^2}\right]^2\right\}^{\frac{1}{2}}\right\rangle}{\left[2-\frac{3(\beta-1)}{\alpha^2}\right]^2} \quad (6.11)$$

in which $\beta = \alpha\coth(\alpha)$ and $\alpha = k_{sb}R_g$, where k_{sb} is the sink strength of the bulk material (i.e. the microstructural features contained with the matrix of the material internal to the grains, including any nanoclusters, voids and dislocation loops). The value of k_{sb} is estimated as [42]:

$$k_{sb} = \sqrt{k_{nc}^2 + k_{voids}^2 + k_{loops}^2} \quad (6.12)$$

The estimates of the respective bulk microstructure features are calculated using:

Nanoclusters [180]: $k_{nc}^2 = 4\pi r_{nc}N_{nc}\left(1 + r_{nc}\sqrt{4\pi r_{nc}N_{nc}}\right)$ (6.13)

Voids [180]: $k_{voids}^2 = 4\pi r_{voids}N_{voids}\left(1 + r_{voids}\sqrt{4\pi r_{voids}N_{voids}}\right)$ (6.14)

where r_{nc} and r_{voids} are the average radius of the nanoclusters or voids, respectively, and N_{nc} and N_{voids} are the measured number density of nanoclusters or voids, respectively.

Dislocation loops [181]: $k_{loops}^2 = \frac{4\pi^2 N_{loops}\left(R_{loops}^2 - r_t^2\right)^{1/2}}{ln\left(\frac{8R_{loops}}{r_t}\right)}$ (6.15)

in which N_{loops} is the measured number density of the dislocation loops, R_{loops} is the average major radius of the toroid shape of the loops and r_t is the minor radius of the toroid and is estimated to be ~2x the lattice constant, a.

Once the bulk sink strength is calculated, the sink strength of the grain boundaries is determined. Next, the total sink strength is calculated via Eq. 6.9 by adding the respective sink strengths for the dislocations and carbide precipitates:

Dislocations [182]: $$k_{disl}^2 = \frac{2\pi\rho_d\left(1-\frac{R_D^2}{\mathcal{R}^2}\right)}{ln\left(\frac{\mathcal{R}}{R_D}\right)-\frac{3}{4}+\frac{R_D^2}{\mathcal{R}^2}\left(1-\frac{R_D^2}{4\mathcal{R}^2}\right)} \quad (6.16)$$

in which ρ_d is the density of dislocation lines, R_D is dislocation radius (~$2a$), and $\mathcal{R} = \sqrt{1/\pi\rho_d}$. Finally, the sink strength for carbides follows the formulism for incoherent precipitates:

Carbide precipitates [180]: $$k_{carb}^2 = 4\pi r_{carb} N_{carb}\left(1 + r_{carb}\sqrt{4\pi r_{carb} N_{carb}}\right) \quad (6.17)$$

where r_{carb} and N_{carb} are the average effective radius and number density of the carbides, respectively.

Once the total microstructure sink strength is determined, the other key factor required to identify the characteristic time (τ) for vacancies to migrate to sinks (Eq. 6.8) is the diffusion rate of the vacancies (D_v), which is estimated as:

$$D_v = \alpha a^2 v\, exp\left(-\frac{E_v^m}{k_b T}\right) \quad (6.18)$$

in which α is a geometric factor (equal to 1 [42] for a b.c.c. structure), a is once again the lattice constant (0.286 for the b.c.c. Fe system), v is the Debye frequency (10^{13} s^{-1}), and E_v^m is the migration energy for vacancies (estimated as 0.68 eV [183]). Once the value for τ is determined, the concentration of vacancies as a result of irradiation may be estimated (Eq. 6.7) and subsequently the radiation-enhanced diffusion rate of the solutes is estimated via Eq. 6.4.

6.1.1.3 Other Input Parameters

The remaining inputs into the model are more directly identified. The first term on the right hand side of Eq. 6.1 represents the recoil dissolution, where ϕ is the irradiation flux, which may be estimated as $\phi = K \cdot 10^{14}$[57]. Within both the recoil and disordering terms (1st and 2nd terms on right hand side of Eq. 6.1), the dose rate of irradiation is represented by the variable, *K*. This factor is dependent upon the irradiation experiment itself. For this study, the respective dose rates for the Fe^{2+}, proton, and neutron irradiation are given in Table 4.2. The dose rate for Fe^{2+} irradiation is 2.2 x 10^{-4} dpa/s, while the dose rates for proton and neutron irradiation are 1.2 x 10^{-5} dpa/s and ~10^{-7} dpa/s, respectively. Furthermore, in the first term on the right had side of Eq. 6.1, the variable *N* represents the atomic density of the target alloy. Using the atomic radius of Fe (0.124 nm) and the b.c.c. structure, the atomic density is estimated to be 85.2 atoms/nm^3.

Finally, the last two terms on the right hand side of Eq. 6.1 contain variables of *r*, *n*, *p*, and *C*. The value for the average cluster radius, *r*, is calculated as:

$$r = \frac{1}{2} D_G \tag{6.19}$$

where D_G is the average cluster Guinier diameter of the as-received alloy as defined by Eq. 4.11 and tabulated in Table 5.4 for the Fe-9%Cr ODS. Meanwhile, *n* represents the adjusted number density (as prescribed in Section 5.2.1) of the as-received alloy and is tabulated in Table 5.5 as N_{nc}^{adj} for the Fe-9%Cr ODS. The values for *p* and *C* are also acquired through the atom probe tomography analysis. From the composition data of the clusters, the value for *p* is calculated as:

$$p_{cl}^{i} = \frac{N_{cl}^{i}}{\sum N_{cl}} \tag{6.20}$$

in which N_{cl}^{i} is the total number of atoms of a specific species found in clusters and $\sum N_{cl}$ is the total number atoms found in the clusters. Finally, the value of *C* is equal to the total non-carbide composition of each of the clustering species and is tabulated in Table 5.4 for the Fe-9%Cr ODS. Since the HCM12A and HT9 alloys do not contain any pre-existing nanoclusters in the as-received condition, the values for *r*, *n*, and *p* are initially equal to 0, and the values for C are estimated as the bulk concentration of each clustering solute, as tabulated in Table 4.1.

At this point, the only remaining variable is the disordering efficiency, *f*, which is defined in Section 6.1.1.1. The value of this variable is accepted as unknown and will be used as the primary fitting parameter to calibrate the model against the measured data.

6.1.2 NHM Model Execution

Once all the input parameters are determined, the model is ready to proceed with a calculation to emulate the evolution of nanocluster size as a function of time (and dpa). Initially, Eq. 6.1 is applied to the as-received nanocluster morphology and the respective parameters of each irradiation (Fe^{2+}, proton, and neutron) separately. A value for *dr/dt* is calculated for each irradiation and is applied over a finite amount of time, Δt, after which a new resulting nanocluster radius is determined. Using this revised nanocluster radius, a revised total sink strength of the microstructure is calculated following Eqs. 6.13 and 6.9. Subsequently, the characteristic time, τ, the radiation-induced concentration of vacancies, C_v^{irr}, and the radiation-enhanced diffusion rate, D_{sol}^{irr}, are all updated accordingly. This stepwise calculation is repeated over the same finite time intervals, incrementally accumulating more "dose" over increasing time.

To initiate the calculation, an estimate for the disordering efficiency, *f*, and the thermal diffusion rate of the respective solutes is required. Typically, initial values of ~0.1 are a good starting estimate for the disordering efficiency. As the calculation is carried out to increasing dose, it will be shown how the predicted nanocluster evolution will approach and converge on a stable nanocluster size. Generally, the estimated value of *f* will influence the predicted stable nanocluster size, so this parameter is highly effective as a fitting parameter to enable the model calculation to predict nanocluster size evolution to match the empirically measured results.

Estimation of the initial thermal diffusion rate for the clustering solutes is also a non-trivial matter. The approach taken for this study is to initially calculate estimates for thermal diffusion for each of the individual clustering species (Y and Ti for Fe-9%Cr ODS, and Si, Mn, Ni, P, Cu, and Cr for HCM12A and HT9). Once the diffusion rate of each species is established, a combined thermal diffusion rate for solutes based on a weighted average of the matrix composition is calculated. A summary of the initial estimated thermal diffusion rates for each solute and groups of solutes are provided in Table 6.1.

Table 6.1 Initial estimates for thermal diffusion rates of solutes at 500°C.

Solute(s)	Pre-exponential, D_0 (cm^2/s)	Migration energy, E_{sol}^m (eV)	Calculated D_{sol}^{th} (cm^2/s)	Source
Y	0.1	3.1	6.24×10^{-22}	[10]
Ti	2100	3.04	3.29×10^{-17}	[184]
Y-Ti*	-	-	**1.33×10^{-18}**	-
Si	$0.735(1+0.124C_{Si})$	2.27	$\sim 1.2 \times 10^{-15}$	[185]
Mn	5.95	3.26	3.36×10^{-21}	[185]
Ni	0.56	0.70	1.54×10^{-5}	[185]
Si-Mn-Ni*	-	-	**1.53×10^{-17}**	-
Cu	6.1	2.78	4.63×10^{-18}	[185]
Cr	1.48	2.39	4.37×10^{-16}	[185]

*estimates based on weighted average of concentrations in Fe-9%Cr ODS (Table 6.2)

Table 6.2 Measured values for non-carbide solute concentrations in Fe-9%Cr ODS, from APT.

Solute Element	Non-carbide concentration, C_i
Y	0.0018
Ti	0.0043
Cr	0.0852
Si	0.0017
Mn	0.0022
Ni	0.0004

In the case of modeling nanocluster evolution of HCM12A and HT9, an additional challenge is present. In the as-received condition, these alloys do not contain any nanocluster morphology. As a result, the initial values for *r*, *n*, and *p* are all essentially equal to 0. Since the NHM model requires some inherent nanoclusters to be

present, the initial value of p is set to a small value of 0.001 and an artificial "nucleation" event is introduced by manually setting the value of r to ~1.0 nm. The timing at which this manual nucleation is introduced may depend on any empirical information available which provides information about the timing (i.e. approximate dose) at which cluster nucleation occurs. For example, in HCM12A, measured data after proton irradiation to 1 dpa indicates only Cu-rich clusters are present, suggesting that Cu-rich clusters nucleate prior to 1 dpa. However, after proton irradiation to 3 dpa, both Cu-rich clustering and Si-Mn-Ni-rich clusters are present, suggesting that Si-Mn-Ni-rich clusters nucleate sometime in between 1 and 3 dpa. As a result, Cu cluster nucleation is introduced in the model at approximately 0.5 dpa, while Si-Mn-Ni cluster nucleation is introduced at approximate 1.5 dpa. In the case when no such information is available, manual nucleation of clusters is initially introduced at approximately 1.5 dpa. It will be shown in subsequent sections of this thesis that after simultaneous model calibration to all three alloys, it is possible to deduce additional information about the nucleation point of different types of clusters and adjust accordingly.

6.2 Nanocluster Evolution in Fe-9%Cr ODS

The first system to be modeled is the Fe-9%Cr ODS alloy, which contains a high density of oxide nanoclusters in the as-received condition. A summary of the initial parameters used in modeling Fe-9%Cr ODS for each irradiation is provided in Table 6.3. The stepwise calculation is repeated over the same finite time intervals (Δt), incrementally accumulating more "dose" over increasing time. Each calculation is fitted to the experimental data as closely as possible. The following sections will review how the NHM model is informative with regards to: a) the relative disordering efficiencies of

each irradiating particle, b) whether a temperature shift is required to emulate nanocluster evolution using varying dose rate irradiations, and c) the relative clustering behavior of each solute species in the presence of irradiation.

Table 6.3 Initial parameters in the NHM model setup for Fe-9%Cr ODS.

Parameter	Fe^{2+} irradiation	Proton irradiation	Neutron irradiation	Source
$\phi = K \cdot 10^{14}$	2.23 x 10^{10}	1.20 x 10^{9}	1.00 x 10^{7}	K from Table 4.2
N (atoms/nm^3)	85.2			-
l (nm)	6.8	2.3	10.4	Table 2.1
f	fitted parameter	fitted parameter	fitted parameter	-
k^2 (cm^{-2})	2.70 x 10^{12}			Eq. 6.9
T (K)	773 K (500°C)			-
D_{sol}^{th} (cm^2/s)	1.33 x 10^{-18}			Table 6.1
E_v^f (eV)	2.2			[59]
E_v^m (eV)	0.68			[183]
Calculated D^{irr}(cm^2/s)	2.30 x 10^{-16}	1.24 x 10^{-17}	1.03 x 10^{-19}	Eq. 6.4
r (nm)	2.855			Table 5.4
n (m^{-3})	4.43 x 10^{23}			Table 5.5
$p_{Y,Ti}$	0.0873			Table 5.4
$C_{Y,Ti}$	0.0062			Table 5.4
Δt (s)	1200	14400	1440000	-

For illustration purposes, the process for fitting the disordering efficiency, f^p, against the Fe-9%Cr ODS alloy data after each proton irradiation will be shown. Using the initial parameters in Table 6.3 and an estimated $f^p = 0.1$, it is quickly found the model predicts very rapid growth of the clusters to a diameter of 6.72 nm (calculation **1** on Figure 6.2), which does not represent the experimental observations (d = 5.40 nm at 7

dpa). This result suggests either the estimated value for f^p is too low (i.e. not enough ballistic disordering), or the assumption for D_{sol}^{th} is too high (favoring growth). Since f^p is required to be a value between 0 and 1.0, the input for f^p into the model is maximized to 1.0. After this change, the model continues to predict very rapid growth of the clusters to a diameter of 6.63 nm (**2** on Figure 6.2). Next, keeping f^p = 1.0, the value for D_{sol}^{th} is adjusted to enable the calculation to more closely simulate the stable cluster sizes measured. Using a value of D_{sol}^{th} = 7.81 x 10^{-20} cm^2/s, the calculation predicts a stable cluster size of d = 5.38 nm within the first 0.26 dpa, which is reasonably close to the stable value at 7 dpa, but does not necessarily represent the cluster evolution sizes observed at 1 dpa and 3 dpa (**3** on Figure 6.2). For comparison of sensitivity, a value of f^p = 0.01 is input and the value for D_{sol}^{th} is adjusted to 4.43 x 10^{-22} cm2/s to enable the calculation to approximate the measured data (**4** on Figure 6.2). In this case, the predicted size is a reasonable fit to the measurements, but does not show any trend toward a stable size. As a result, it is deduced that an intermediate combination of values for both f^p and D_{sol}^{th} would likely provide a better fit to the full set of cluster size measurements from 1 to 7 dpa. Using values of f^p = 0.150 and D_{sol}^{th} = 3.88 x 10^{-21} cm^2/s provides a more representative fit to the data (**5** on Figure 6.2). Henceforth, both f and D_{sol}^{th} are treated as independent fitting parameters for the model. A different f value is fitted for each irradiating particle, while D_{sol}^{th} is kept common within each model iteration, since the relative solutes are consistent. Generally, revising the thermal diffusion rate, and thus the calculated RED of the solutes, will influence the rate of evolution of the nanocluster sizes. A higher diffusion rate will predict the nanoclusters to evolve towards a stable size more quickly, while a slower diffusion rate will predict nanoclusters to evolve towards

the stable size more slowly. By contrast, adjusting the value for f only influences the magnitude of the predicted stable size. As a result, using a combination of the fitting parameters, f and D_{sol}^{th}, enables the user to calibrate the NHM model against empirical data, particularly when three or more separate data points are available.

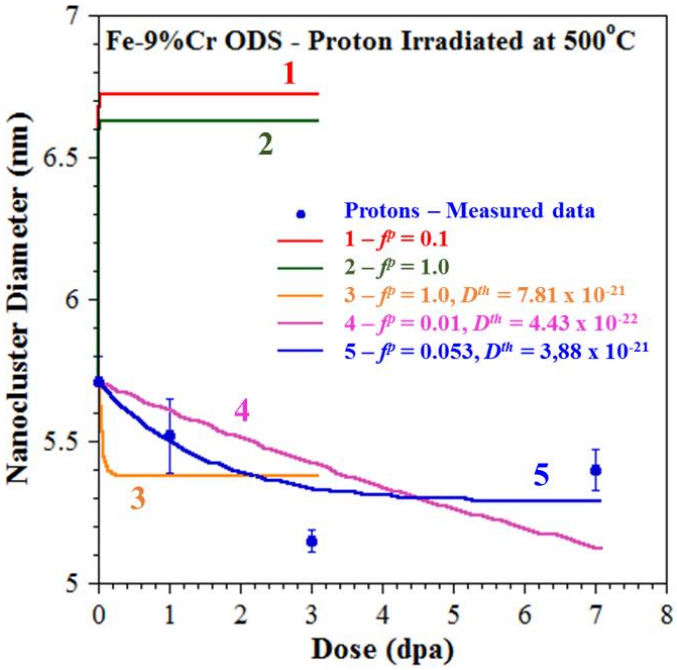

Figure 6.2 Calculations with the NHM model for proton-irradiated Fe-9%Cr illustrating the fitting method for fp and D_{sol}^{th} (measured data from Table 5.4).

6.2.1 Irradiating Particle Dependence

Using the fitting procedure described above, the NHM model parameters are fitted with predictions plotted as solid lines against the measured cluster sizes following each irradiation experiment in Figure 6.3. For all three irradiating particles, the average cluster size approaches a steady state within the first few dpa. Each calculation is fitted to the experimental data as closely as possible using disordering efficiencies of f^{Fe} = 0.039, f^p = 0.150, and f^n = 0.046, respectively, and a common value of D_{sol}^{th} = 3.88 x 10^{-21} cm^2/s.

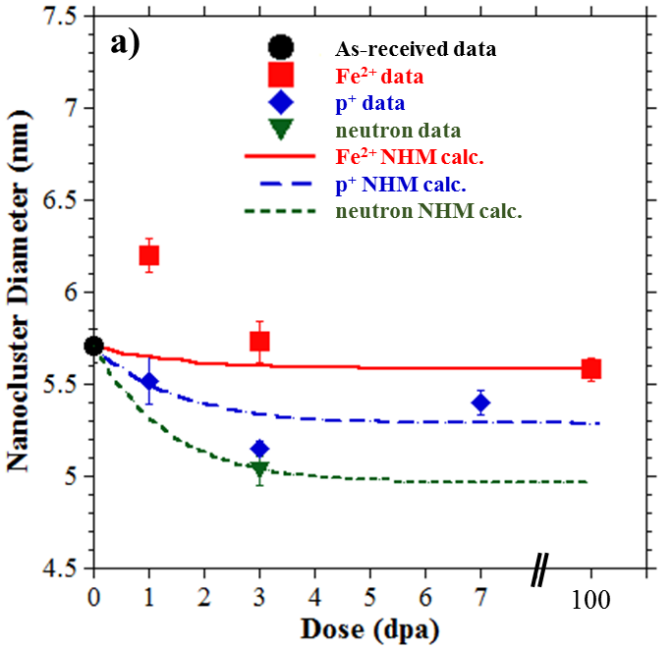

Figure 6.3 Stepwise calculations using the NHM model fitted against Fe-9%Cr ODS (measured data from 5.4).

6.2.2 Temperature Shift

To evaluate the sensitivity of this stepwise calculation, the input temperature is varied to determine the influence on the predicted stable cluster size. A lower irradiation temperature will directly reduce RED by lowering the equilibrium concentration of vacancies, increasing the time required for vacancy defects to migrate to sinks, and decreasing the thermal diffusion rate of the solutes. Keeping all other inputs into Eq. 6.1 the same, a revised stepwise NHM calculation for Fe^{2+} irradiation at 380°C predicts steady-state nanocluster size equivalent to that predicted (and measured) for neutron irradiation at 500°C (Figure 6.4). This suggests that a downward temperature shift of -120°C is required for Fe^{2+} irradiation to emulate the same cluster evolution as neutron irradiation at 500°C. The same approach is applied for proton irradiation, for which an irradiation temperature of 426°C (i.e. a temperature shift of -74°C) predicts the same stable cluster size as that of 500°C neutron irradiation.

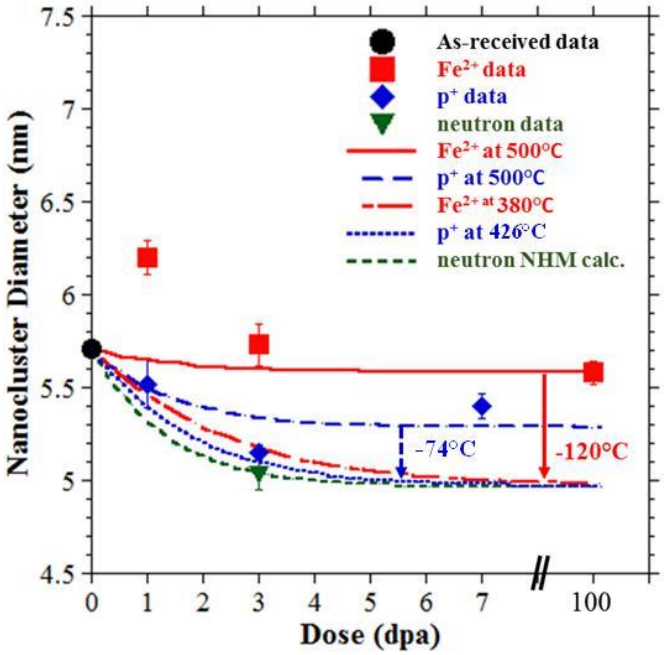

Figure 6.4 Stepwise calculations of Fe2+ irradiation and p+ irradiation with implemented temperature shifts to fit the measured neutron irradiation nanocluster evolution.

6.2.3 Solute Dependence

One of the key observations in Fe-9%Cr ODS following irradiation is the variation of clustering behavior of the different solute species. In Section 5.2.1, it was noted that Ti appears to more readily dissolve during irradiation, while Y appears to be more stable, as evidenced by the evolution of the Y:Ti ratio. Additionally, in Section 5.2.1, it was highlighted how additional solutes including Si, Mn, and Ni also exhibit enrichment at the oxide nanoclusters to varying degrees during irradiation. Because of this solute specific behavior, it is also informative to model the cluster evolution for each individual species independently.

With the measured average size of the clusters (Section 4.5.3) and the values for p_i of each solute, it is possible to derive the partial radius of the clusters, r_i, for a given species i. First, the clustering volume fraction for each clustering species (f_v^i) is:

$$f_v^i = f_v p_i \cdot \frac{V_{i,atom}}{V_{m,atom}} \tag{6.21}$$

Where f_v is the overall volume fraction of the clusters (Section 4.5.3, Eq. 4.13). Since p_i (Eq. 6.20) is only based on the relative count of solute atoms in the cluster (using APT data), the relative size contribution of each individual solute atom is must be considered. Therefore, in Eq. 6.21, $V_{i,atom}$ is the effective volume of a solute specie atom and $V_{m,atom}$ is the effective volume of a matrix atom in the bulk material (in this case, Fe). Since volume fraction may also be written as $f_v = \frac{4}{3}\pi r^3 n$, where n is the cluster number density, the partial volume fraction is also written as:

$$f_v^i = \frac{4}{3}\pi r^3 n p_i \frac{V_{i,atom}}{V_{m,at}} = \frac{4}{3}\pi r_i^3 n \tag{6.22}$$

Equation 6.22 may then be simplified to:

$$r^3 p_i \frac{r_{i,at}^3}{r_{m,at}^3} = r_i^3 \tag{6.23}$$

where $r_{i,at}$ is the atomic radius of the solute species (Table 6.4) and $r_{m,at}$ is the atomic radius of the matrix atoms (0.124 nm). Eq. 6.23 is rearranged to solve for the partial radius:

$$r_i = r \frac{r_{i,at}}{r_{m,at}} \sqrt[3]{p_i} \tag{6.24}$$

Finally, the partial diameter of the clusters for each species, d_i, is calculated as:

$$d_i = 2r_i. \tag{6.25}$$

Table 6.4 Atomic radius values used for solutes in this study, from [73]**.**

Solute Element	**Atomic radius, $r_{i,at}$ (nm)**
Y	0.180
Ti	0.145
Cr	0.125
Si	0.118

Mn	0.112
Ni	0.125
P	0.109
Cu	0.128

The partial diameter for each solute species is calculated using the APT measured data following each of the irradiation experiments (Table 6.5). Using these values, a separate NHM model calculation is executed for each solute species and each set of irradiation conditions. As before, each of these calculations are run to simulate the evolution of the overall oxide nanocluster radius over time/dose. However, in this case, the values for C_i and p_i are substituted for C and p, respectively in Eq. 6.1 for the as-received condition (i.e. at 0 dpa). As discussed in Section 6.2, the same approach is used for fitting the disordering efficiencies, f_i, and the thermal rate of diffusion, D_i^{th}, for each solute specie i. However, for solute specific cluster evolution, the circumstances for the model calculation are slightly different. Despite using the initial values for C_i and p_i, the model still calculates a prediction of the overall cluster size evolution (not the partial diameter) in order to maintain an updating estimate for the overall sink strength of the microstructure at each time interval. As a result, the model requires additional information about the evolution of p_i to make a continuing estimate of d_i according to Eq. 6.24 and 6.25. To accommodate this, the values for p_i are substituted at each data point for which a measurement is available, and the values for p_i at each intermediate iteration of the calculation are linearly interpolated. With this in place, it is possible to plot both the overall cluster size evolution, and the partial diameter size evolution, simultaneously.

Table 6.5 Summary of APT measurements of p_i and the resulting partial diameter, d_i, for clustering of individual solutes in Fe-9%Cr ODS.

Solute Element	As Received	Fe^{2+} ion-irradiated (400°C) 50 dpa	Fe^{2+} ion-irradiated (500°C)			Proton-irradiated (500°C)			Neutron-irradiated (500°C) 3 dpa
			1 dpa	3 dpa	100 dpa	1 dpa	3 dpa	7 dpa	
Measurement of p_i									
Y	0.0297	0.0402	0.0535	0.0518	0.0479	0.0671	0.0369	0.0407	0.0509
Ti	0.0576	0.0696	0.0640	0.0537	0.0561	0.0846	0.0560	0.0645	0.0444
Cr	0.1013	0.1152	0.1194	0.1145	0.1057	0.1253	0.1226	0.1112	0.1166
Si	0.0022	0.0022	0.0034	0.0033	0.0025	0.0031	0.0031	0.0022	0.0725
Mn	0.0009	0.0008	0.0009	0.0011	0.0006	0.0010	0.0009	0.0006	0.0367
Ni	0.0006	0.0006	0.0013	0.0016	0.0013	0.0013	0.0011	0.0006	0.0275
Calculation of partial diameter d_i (nm)									
Y	2.5652	2.6897	3.3884	3.0993	2.9409	3.2547	2.4867	2.6956	2.7045
Ti	2.5762	2.6023	2.8985	2.5274	2.4969	2.8324	2.3025	2.5313	2.0821
Cr	2.6810	2.6541	3.0758	2.8042	2.6587	2.7830	2.5767	2.6164	2.4761
Si	0.7065	0.6697	0.8861	0.8093	0.7165	0.7620	0.7166	0.6661	1.9955
Mn	0.4977	0.4537	0.5348	0.5279	0.4331	0.4979	0.4439	0.4199	1.5096
Ni	0.4771	0.4601	0.6785	0.6808	0.6186	0.6058	0.5427	0.4520	1.5298

The same initial parameters from Table 6.3 are used, with the exception of solute specific values for C_i (Table 6.2) and p_i (Table 6.5) and D_i^{th} (Table 6.1). As with the overall clusters, the initial diffusivity values for each of the solutes do not allow the model to fit the data, so each D_i^{th} is once again used as a fitting parameter. The fitting of f_i, and $D_i^{th}$is done in the same manner as before. However, the analyst has an additional reference with plots of both the overall cluster size prediction and the partial diameter cluster prediction. Therefore, higher confidence in the fitted parameters results when the predicted cluster evolution matches both sets of data points.

The NHM model predictions for each solute species are plotted as lines against the measured cluster sizes following each irradiation experiment in Figure 6.5 for Y and Ti, Figure 6.6 for Cr and Si, and Figure 6.7 for Mn and Ni. In each case, the partial diameter tends to track more closely to the measured values, due to entry of p_i. In all cases, the model provides a reasonable fit to the overall cluster evolution and the partial diameter size evolution.

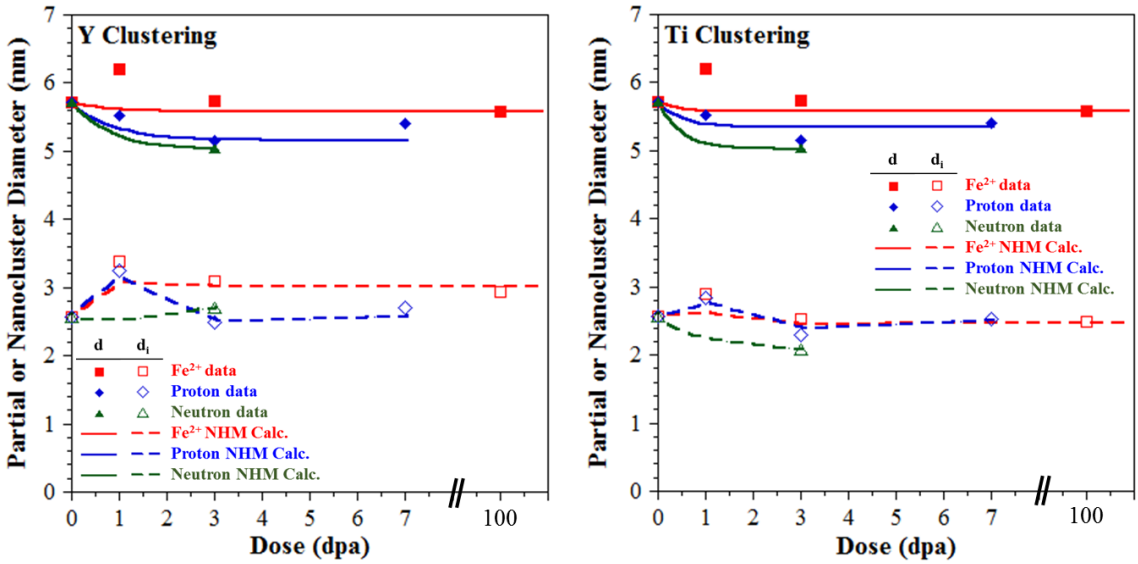

Figure 6.5 Calculations of NHM model fitted against Fe-9%Cr ODS clusters (d) and partial diameters (di) from Table 6.5 for a) Y solutes, and b) Ti solutes.

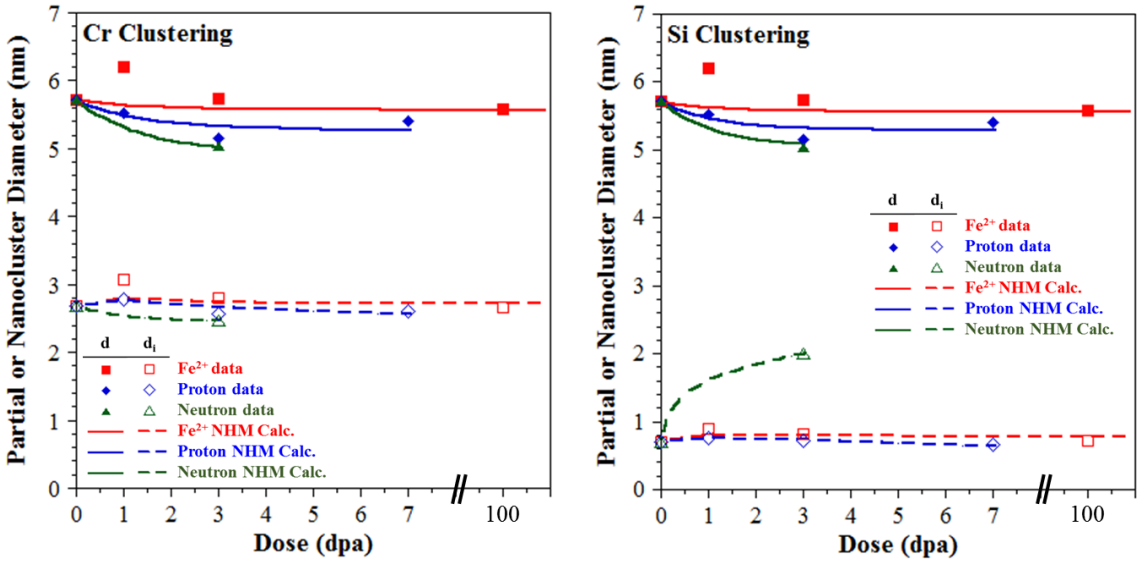

Figure 6.6 Calculations of NHM model fitted against Fe-9%Cr ODS clusters (d) and partial diameters (di) from Table 6.5 for a) Cr solutes, and b) Si solutes.

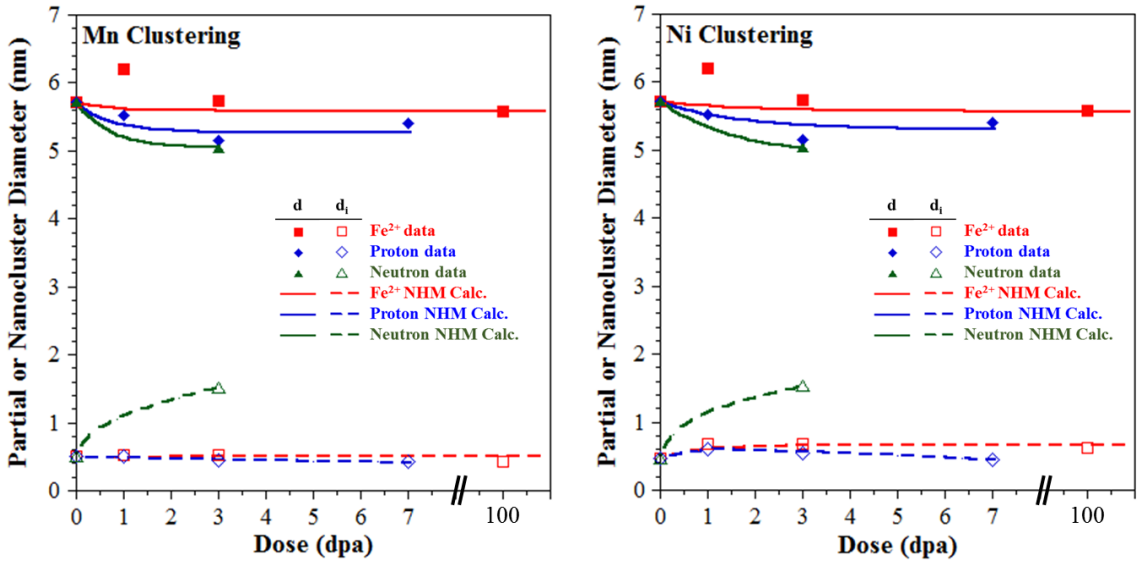

Figure 6.7 Calculations of NHM model fitted against Fe-9%Cr ODS clusters (d) and partial diameters (di) from Table 6.5 for a) Mn solutes, and b) Ni solutes.

For each solute species, unique values for f_i are fitted for each condition, while the fitted values for D_i^{th} are consistent across all irradiation conditions. The fitted values for each solute are provided in Table 6.6 for comparison. For all the solutes, the respective

f_i^{Fe} and f_i^n are similar and consistently the lowest, while the f_i^p are consistently the highest values. This result is consistent with the relative magnitudes of *f* fitted to the whole nanoclusters as reported in Section 6.2.1. Interestingly, the fitted thermal diffusion rates, D_i^{th}, are all lower values than those found in Table 6.1 (with the exception of Y). Therefore, additional mechanisms are likely influencing the rate of diffusion of the solutes towards the nanoclusters. This subject is discussed further in Section 6.5.3.

Table 6.6 Fitted values for f_i and D_i^{th} for each solute species in Fe-9%Cr ODS.

Solute Element	Fitted D_i^{th} (cm^2/s)	f_i^{Fe}	f_i^p	f_i^n
Y	6.86 x 10^{-21}	0.048	0.180	0.060
Ti	9.32 x 10^{-21}	0.112	0.394	0.118
Cr	3.88 x 10^{-22}	0.106	0.388	0.089
Si	5.31 x 10^{-22}	0.129	0.410	0.107
Mn	2.59 x 10^{-22}	0.209	0.668	0.171
Ni	3.88 x 10^{-22}	0.089	0.284	0.076

6.3 Nanocluster Evolution in HCM12A

The next system to be modeled is the HCM12A alloy, which does not contain any pre-existing nanoclusters in the as-received condition. A summary of the unique initial parameters used in modeling HCM12A for each irradiation is provided in Table 6.7. All other parameters are the same as provided in Table 6.3. As with the ODS calculations, the stepwise calculation is repeated over the same finite time intervals (Δt), incrementally accumulating more "dose" over increasing time. However, in the case for HCM12A, two separate model calculations are conducted to simulate nanocluster evolution for the Si-Mn-Ni-rich clusters and Cu-rich clusters. Also, since the initial values for cluster radius

are equal to zero at the onset of irradiation, a nucleation event is introduced into the calculation at a dose > 0 dpa via manually entry of a finite value for the radius.

The model thus commences with predicting nanocluster evolution following this nucleation event. Each calculation is fitted to the experimental data available from this study and from complimentary data in literature conducted on the same heat of HCM12A. The following sections will detail: a) the approach to simulate nucleation of the different clustering species, b) the additional experimental data available from literature, c) the relative disordering efficiencies of each irradiating particle, d) whether a temperature shift is required to emulate nanocluster evolution using varying dose rate irradiations, and e) the relative clustering behavior of each solute species in the presence of irradiation.

Table 6.7 Initial parameters in the NHM model setup for HCM12A.

Parameter	All irradiations	Source
k^2 (cm^{-2})	2.90 x 10^{11}	Eq. 6.9
r (nm)	0	-
n (m^{-3})	0	-
$p_{Si,Mn,Ni}$	0.001	-
$C_{Si,Mn,Ni}$	0.0212	APT data
p_{Cu}	0.001	-
C_{Cu}	0.0132	APT data

6.3.1 Nucleation

The nanocluster measurements following proton irradiation to 1 dpa and 3 dpa at 500°C provide some insight into the timing of nanocluster nucleation. After proton irradiation to 1 dpa, only Cu-rich clusters exist, while after 3 dpa both Cu-rich and Si-Mn-Ni-rich clusters are present. This information suggests that Cu-rich clusters nucleate

sometime between 0 and 1 dpa, while the Si-Mn-Ni-rich clusters nucleate between 1 and 3 dpa upon proton irradiation. In the case of Fe^{2+} and neutron irradiation, the only data available is at 3 dpa, in which both Cu-rich and Si-Mn-Ni-rich clusters are present, confirming both sets of clusters nucleate between 0 and 3 dpa under these conditions.

Based on this information available, nucleation events are manually introduced in the NHM calculation at differing points. For the Cu-rich clusters, an initial cluster radius of 1 nm is introduced for each calculation at an irradiation damage between 0.34 - 0.80 dpa. The initial radius value is arbitrary and is found to have negligible influence on the end result of the NHM calculation. For the Si-Mn-Ni-rich clusters, an initial cluster radius of 1 nm is introduced at doses between 1.15 - 1.34 dpa.

6.3.2 Consideration of Literature Data

For the purpose of calibrating the NHM calculation model, it is desirable to have as much experimental data as possible to most accurately fit the parameters f and D^{th}. Jiao, et al. have conducted prior experiments on the same production heat of alloy HCM12A as the one used for this thesis [24]. Several proton-irradiation experiments were conducted at both 400°C and 500°C to doses ranging from 3-10 dpa, and atom probe tomography is used to characterize the average size of the Si-Mn-Ni-rich, Cu-rich, and Cr-rich nanoclusters following each irradiation experiment. A summary of this data is provided in Table 6.8, and is considered to be complimentary to the data from this study (Table 5.6). As a result, the data from both studies will be used to provide a more complete picture of nanocluster evolution and enable a more complete analysis using the NHM calculation model.

Table 6.8 Summary of cluster analysis of HCM12A for each irradiation condition in Ref [24]**.**

Nanocluster Analysis	Proton-irradiation			
	(400°C)			(500°C)
	3 dpa	7 dpa	10 dpa	7 dpa
Si-Mn-Ni-P rich clusters				
Average Diameter, D_G^{Si}(nm)	4.2	4.6	5.0	7.2
Std. dev. of the mean for D_G^{Si}	0.2	0.2	0.4	0.4
Cu-rich clusters				
Average Diameter, D_G^{Cu}(nm)	3.4	4.0	3.8	6.6
Std. dev. of the mean for D_G^{Cu}	0.4	0.2	0.4	0.4
Cr-rich clusters				
Average Diameter, D_G^{Cr}(nm)	3.0	3.6	3.4	-
Std. dev. of the mean for D_G^{Cr}	0.2	0.2	0.4	-

6.3.3 Irradiating Particle Dependence

The NHM model predictions are plotted as lines against the measured cluster sizes following each irradiation experiment in Figure 6.8. For all three irradiating particles, the average size of Si-Mn-Ni-rich and Cu-rich clusters grow quickly after nucleation and evolve toward a steady state within the first few dpa. Each calculation is fitted to the experimental data point which represents the cluster size at the highest known dose. For the Si-Mn-Ni clusters, the fitted disordering efficiencies are f_{si}^{Fe} = 0.095, f_{si}^{p} = 0.342, and f_{Si}^{n}= 0.123, respectively, with $D_{Si,Mn,Ni}^{th} = 2.59\ x10^{-24} cm^2/s$. For the Cu-rich clusters, the disordering efficiencies are f_{Cu}^{Fe}= 0.220, f_{Cu}^{p}= 0.688, and f_{Cu}^{n}= 0.229, respectively, with $D_{Cu}^{th} = 6.76\ x10^{-24} cm^2/s$.

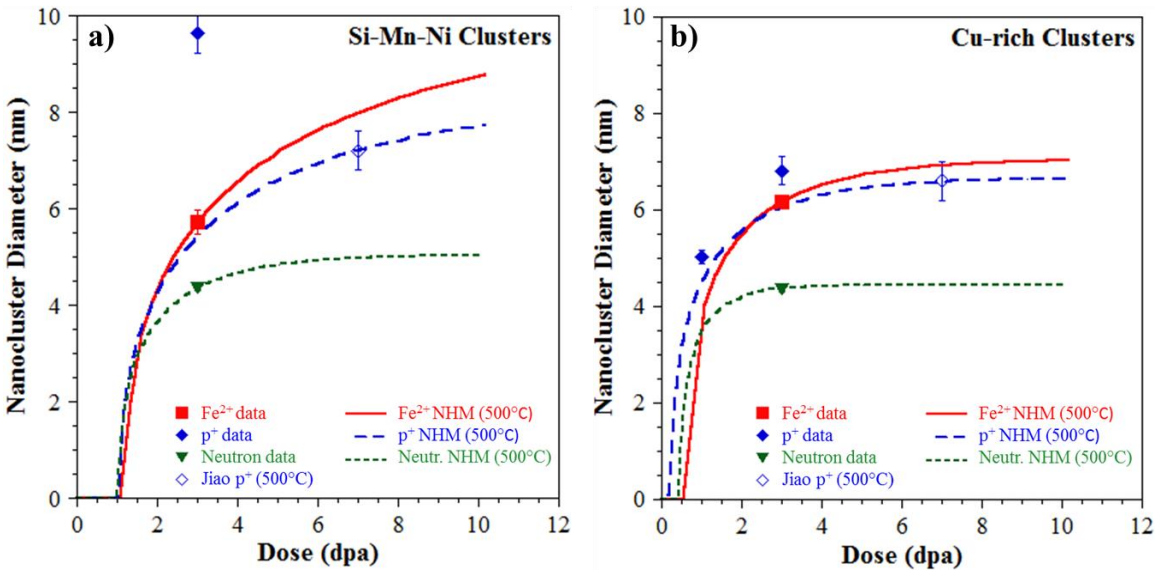

Figure 6.8 NHM model calculations fitted against HCM12A measured data from Table 5.6 and Table 6.8 for a) Si-Mn-Ni-rich clusters, and b) Cu-rich clusters.

6.3.4 Temperature Shift

As with the calculation for ODS, the sensitivity of the stepwise calculation for HCM12A is evaluated by varying the input temperature to determine the influence on the predicted stable cluster size. Keeping all other inputs into Eq. 6.1 the same, a revised stepwise NHM calculation for Fe^{2+} irradiation at 370°C predicts a steady-state Si-Mn-Ni-rich nanocluster size equivalent to that predicted (and measured) for neutron irradiation at 500°C (Figure 6.9a). This suggests that a downward temperature shift of -130°C is required for Fe^{2+} irradiation to emulate the same cluster evolution as neutron irradiation at 500°C for Si-Mn-Ni-rich clusters. The same approach is applied for proton irradiation, for which an irradiation temperature of 400°C (i.e. a temperature shift of -100°C) predicts the same stable Si-Mn-Ni-rich cluster size as that of 500°C neutron irradiation.

Similarly, a revised stepwise NHM calculation for Fe^{2+} irradiation at 400°C predicts a steady-state Cu-rich nanocluster size equivalent to that predicted (and measured) for neutron irradiation at 500°C (Figure 6.9b). This suggests that a downward

temperature shift of -100°C is required for Fe^{2+} irradiation to emulate the same cluster evolution as neutron irradiation at 500°C for Cu-rich clusters. The same approach is applied for proton irradiation, for which an irradiation temperature of 410°C (i.e. a temperature shift of -90°C) predicts the same stable Cu-rich cluster size as that of 500°C neutron irradiation. It can also be seen in Figure 6.9 how a temperature shift of -100°C (i.e. at 400°C) would also reasonably simulate the measured data from the Jiao, et al. study of nanoclusters after proton irradiation at 400°C [24].

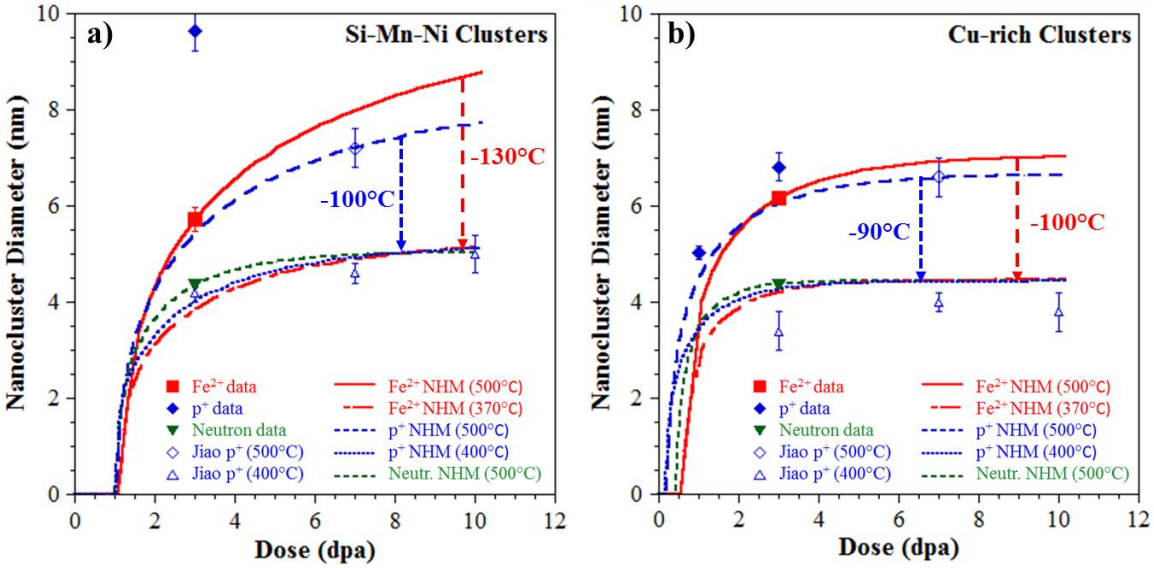

Figure 6.9 Calculations of Fe2+ irradiation and p+ irradiation with implemented temperature shifts to fit the measured neutron irradiation nanocluster evolution for a) Si-Mn-Ni-rich clusters, and b) Cu-rich clusters.

6.3.5 Solute Dependence

In the HCM12A alloy, irradiation-induced clustering has been observed for solutes of Si, Mn, Ni, P, Cu, and Cr. Using the atomic radius values provided in Table 6.4, the partial diameter for each of these species is calculated using the APT measured data following each of the irradiation experiments and provided in Table 6.9. With these values, a separate NHM model calculation is executed for each solute species, and each

set of irradiation conditions, to simulate the evolution of the overall nanocluster radius over time/dose.

Table 6.9 Summary of APT measurements of p_i and the resulting partial diameter, d_i, for clustering of individual solutes in HCM12A.

Nanocluster Analysis	Fe^{2+} ion-irradiated (500°C)		Proton-irradiated (500°C)		Neutron-irradiated (500°C) 3 dpa
	3 dpa	100 dpa	1 dpa	3 dpa	
Measurement of p_i					
Si	0.0186	-	-	0.0673	0.0579
Mn	0.0212	-	-	0.0520	0.0426
Ni	0.0450	-	-	0.0543	0.0292
P	0.0022	-	-	0.0033	0.0034
Cu	0.2060	-	0.2628	0.4448	0.1540
Cr	-	-	-	-	0.3542
Calculation of partial diameter d_i (nm)					
Si	1.4397	-	-	3.7274	1.6060
Mn	1.4278	-	-	3.2477	1.3765
Ni	2.0487	-	-	3.6776	1.3536
P	0.6553	-	-	1.2615	0.5762
Cu	3.7678	-	3.3228	5.3719	2.4169
Cr	-	-	-	-	2.2603

The long-term vision of the NHM model is for use as a predictive tool for the evolution of nanoclusters. In the case of the HCM12A alloy, there are three solute species which are common with the ODS alloy modeled in the prior section (Si, Mn, and Ni). Therefore, it is possible to use the same respective disordering efficiencies found in the ODS study and evaluate their effectiveness in modeling the solute clustering behavior in HCM12A. In the case of modeling these solutes in HCM12A, the same values for f_i are

used (Table 6.6) in the model, while continuing to allow D_i^{th} to be fitted for each species following the same approach as in Section 6.2.3. However, once a new D_i^{th} is fitted, it is kept consistent across all irradiation conditions. The remaining new species in HCM12A is P, for which unique values for f_i and D_i^{th} are fitted, with D_i^{th} once again kept consistent across all irradiations. The resulting NHM model predictions in HCM12A for each solute species are plotted as lines against the measured cluster sizes following each irradiation experiment in Figure 6.10 for Si and Mn, and Figure 6.11 for Ni and P.

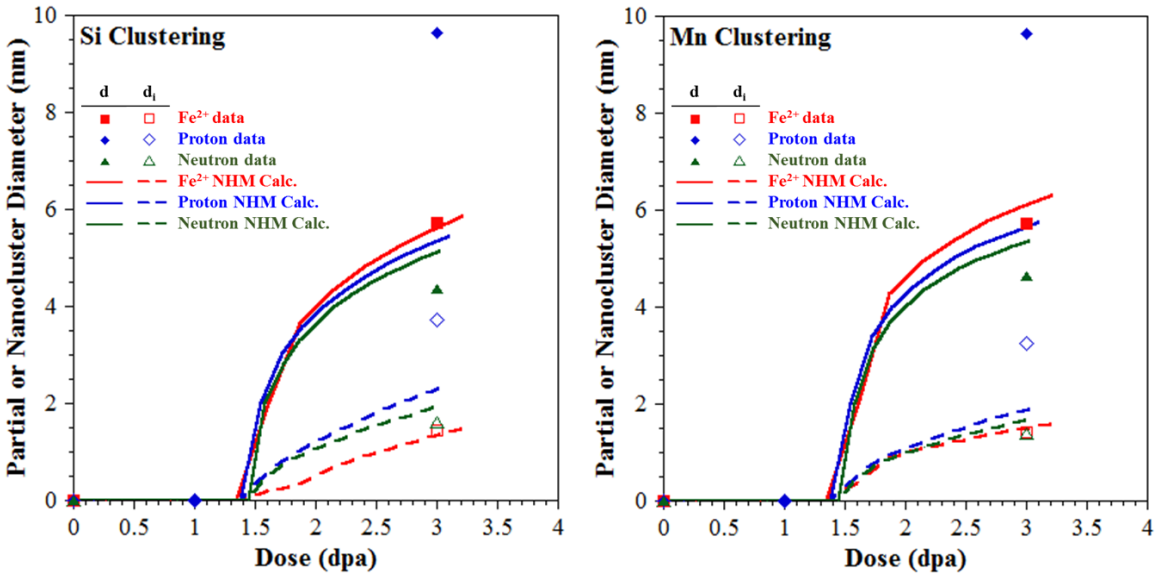

Figure 6.10 Calculations of NHM model fitted against HCM12A clusters (d) and partial diameters (di) from Table 6.9 for a) Si solutes, and b) Mn solutes.

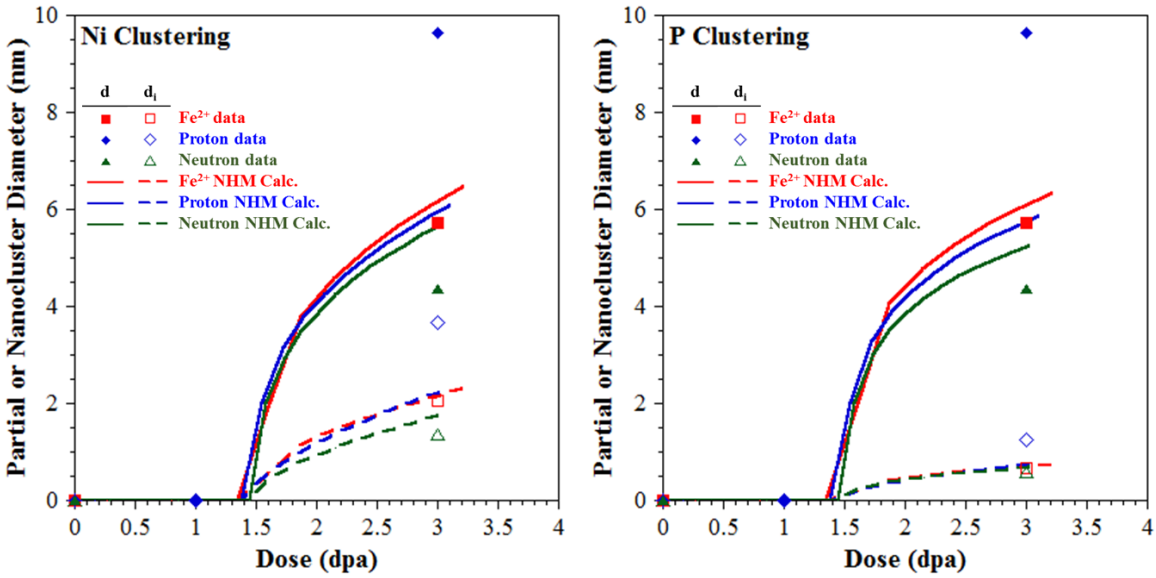

Figure 6.11 Calculations of NHM model fitted against HCM12A clusters (d) and partial diameters (di) from Table 6.9 for a) Ni solutes, and b) P solutes.

For all four solutes, nucleation is introduced at approximately 1.5 dpa, and the model predicts clustering of the solutes at 3 dpa, consistent with experimental observation. Although the predicted cluster sizes at 3 dpa are not a perfect match for all three irradiation conditions, the predictions are reasonable considering the constraints placed on the model: a) all the disordering efficiencies, f_i, for Si, Mn, and Ni are consistent with those found modeling ODS, and b) all of the thermal diffusion rates, D_i^{th}, are consistent across all irradiation conditions. With only minor adjustments to these values, the predictions may be brought into alignment with the measured values. It is also worth noting the clustering behavior measured at 3 dpa may not be indicative of the longer-term clustering behavior which would be present at higher doses. An example of this is illustrated in Figure 6.8 and Figure 6.9, in which the measured cluster size values at 3 dpa are much higher than those measured at 7 dpa. Unfortunately, solute specific data is not available for the irradiations conducted by Jiao, et al. to 7 dpa [25].

An overall summary of the fitted values for each solute are provided in Table 6.10 for comparison. As with the ODS alloy, the respective f_i^{Fe} are f_i^n are similar and the lowest, while the f_i^p are consistently the highest values. Once again, the fitted thermal diffusion rates, D_i^{th}, are all lower values than those found in Table 6.1.

Table 6.10 Fitted values for f_i and D_i^{th} for each solute species in HCM12A.

Solute Element	Fitted D_i^{th} (cm^2/s)	f_i^{Fe}	f_i^p	f_i^n
Si	1.11 x 10^{-23}	0.129	0.410	0.107
Mn	1.81 x 10^{-23}	0.209	0.668	0.171
Ni	6.76 x 10^{-24}	0.089	0.284	0.076
P	1.04 x 10^{-20}	0.180	0.180	0.220
Cu	6.76 x 10^{-24}	0.220	0.560	0.216

A unique set of circumstances exist for modeling of the Cr-rich clusters in HCM12A. In the Results section of this thesis (Sections 5.2.2), it was outlined how Cr-rich clusters were visually observed only after neutron irradiation to 3 dpa. Using the NHM model and the disordering efficiencies from Table 6.6, it is possible to fit a combination of f_{Cr}^n and D_{Cr}^{th} parameters to predict the clustering behavior of Cr upon neutron irradiation. However, by taking this same approach for modeling irradiation with Fe^{2+} ions or protons, the NHM model predicts Cr-rich clusters to evolve to sizes larger than those from neutron irradiation, which is not consistent with experimental observation. The explanation of this disconnect may reside in the relative phases in equilibrium, as predicted by thermodynamics, at the temperature of irradiation. At 500°C, The Fe-Cr phase diagram (Figure 6.12) predicts Cr to be fully soluble in Fe. With the addition of irradiation upon the system, the mobility of Cr solutes increases, thus

kinetically increasing the rate at which the system will evolve towards equilibrium (i.e. remain in dissolution). On the other hand, the irradiation durations for the self-ion, proton, and neutron irradiations are ~4 hours, ~3.5 days and ~1 year, respectively. Thus, Cr clustering only in the neutron-irradiated specimens may be largely influenced by thermal aging at 500°C over ~1 year. This topic will be further discussed in Section 7.4.3.

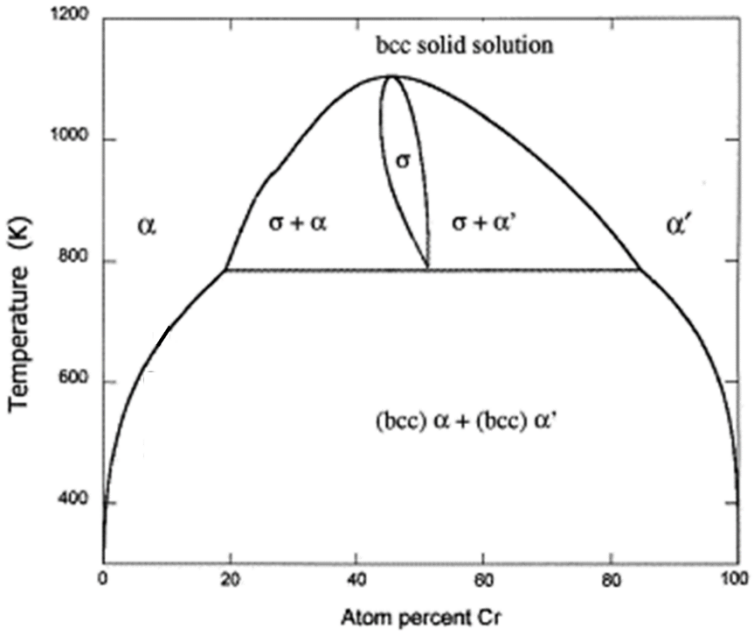

Figure 6.12 Phase Diagram for the Fe-Cr alloy system, from [186].

6.4 Nanocluster Evolution in HT9

The final system to be modeled is the HT9 alloy, which also does not contain any pre-existing nanoclusters in the as-received condition. The clustering solutes in HT9 are also Si, Mn, Ni, and P, similarly to both the ODS and HCM12A. Therefore, based on the common fitted values of f_i for each of these species and the values of D_i^{th} fitted with the HCM12A, it is possible to fully evaluate the NHM model as a predictive tool for the clustering behavior in the HT9 alloy. A summary of the unique initial parameters used in modeling HT9 for each irradiation is provided in Table 6.11. All other parameters are the

same as provided in Table 6.3. Once again, the stepwise calculation is repeated over the same finite time intervals (Δt), incrementally accumulating more "dose" over increasing time, and a nucleation event is introduced into the calculation at approximately 1.5 dpa via manual entry of a finite value for the radius. The model thus commences with predicting nanocluster evolution following this nucleation event. The following sections will detail: a) the additional experimental data available from literature, b) the resulting cluster evolution following each irradiation, c) whether a temperature shift is required to emulate nanocluster evolution using varying dose rate irradiations, and d) the relative clustering behavior of each solute species in the presence of irradiation.

Table 6.11 Initial parameters in the NHM model setup for HT9.

Parameter	All irradiations	Source
k^2 (cm^{-2})	3.28 x 10^{11}	Eq. 6.9
r (nm)	0	-
n (m^{-3})	0	-
$p_{Si,Mn,Ni}$	0.001	-
$C_{Si,Mn,Ni}$	0.0197	APT Data

6.4.1 Consideration of Literature Data

Several studies in literature have evaluated secondary phase evolution in HT9. However, most of these studies rely only on TEM/STEM techniques for characterization of the small nanoscale phases, which are limited in their ability to detect nanoclusters smaller than 5 nm. One study conducted by Jiao, et al. evaluated proton-irradiation to 7 dpa at 400°C on the same production heat of alloy HT9 as the one used for this thesis [25], and used atom probe tomography to characterize the average size of the Si-Mn-Ni-rich, and Cr-rich nanoclusters. A summary of this data is provided in Table 6.12, and is

considered to be complimentary to the data from this study (Table 5.7) for analysis using the NHM calculation model.

Table 6.12 Summary of cluster analysis of HT9 for each irradiation condition in Ref [25]**.**

Nanocluster Analysis	Proton irradiation (400°C) 7 dpa
Si-Mn-Ni-P rich clusters	
Average Diameter, D_G^{Si}(nm)	4.6
Std. dev. of the mean for D_G^{Si}	0.8
Cr-rich clusters	
Average Diameter, D_G^{Cr}(nm)	3.8
Std. dev. of the mean for D_G^{Cr}	0.8

6.4.2 Irradiating Particle Dependence

For the Si-Mn-Ni clusters, the values for the disordering efficiencies and thermal diffusion rates are the same as fitted with the HCM12A modeling effort, so no empirical fitting of these parameters is required. To recap, the disordering efficiencies for the Si-Mn-Ni-rich clusters are f_{si}^{Fe} = 0.095, f_{si}^{p} = 0.342, and f_{Si}^{n}= 0.123, respectively, with $D_{Si,Mn,Ni}^{t} = 2.59\,x10^{-24} cm^2/s$. The NHM model predictions are plotted as lines against the measured cluster sizes following each irradiation experiment at 500°C in Figure 6.13. Experimentally, no clusters were observed after Fe^{2+} irradiation, so only proton and neutron irradiation are modeled for comparison to the measured values. For each irradiating particle, the Si-Mn-Ni-rich clusters grow quickly after nucleation and evolve toward a steady state within the first few dpa. However, when compared to the measured data points at 3 dpa, the model predicts slightly smaller clusters than those measured.

But, this is also consistent with the model fits for HCM12A, in which the measured values after 3 dpa are also much larger than the model predicted values (Figure 6.8). In this case, more experimental data at higher doses would be helpful to understand the validity of this model prediction, but such information is not currently available. A data point from Jiao, et al. is available at 7 dpa at 400°C and is discussed in more detail in the next section.

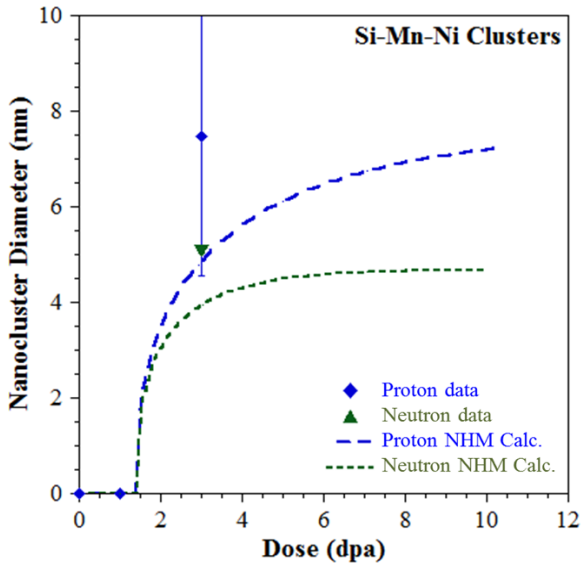

Figure 6.13 Predicted nanocluster evolution using the NHM model in HT9 compared to measured data from Table 5.7 for Si-Mn-Ni-rich clusters.

6.4.3 Temperature Shift

As with the other alloys, the sensitivity of the stepwise calculation for HT9 is evaluated by varying the input temperature to determine the influence on the predicted stable cluster size. Keeping all other inputs into Eq. 6.1 the same, a revised stepwise NHM calculation for proton irradiation at 400°C predicts a steady-state Si-Mn-Ni-rich nanocluster size to that predicted (and measured) for neutron irradiation at 500°C (Figure 6.14). This calculation is also a very good fit to the cluster measurements of Jiao, et al. [25] following 7 dpa irradiation with protons at 400°C.

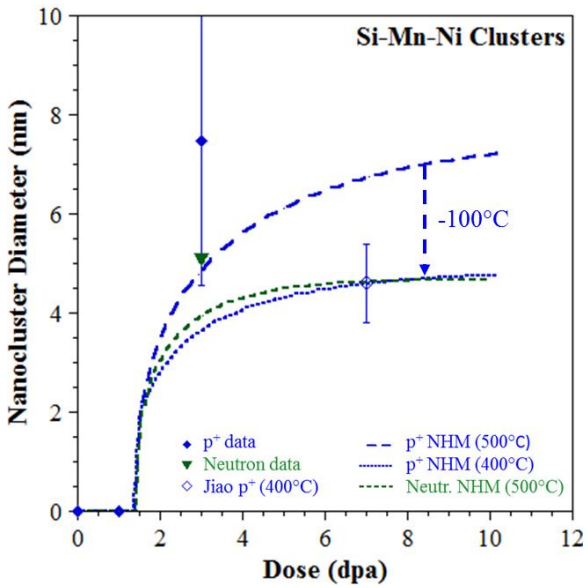

Figure 6.14 Calculations of p+ irradiation with temperature shift to fit the predicted neutron irradiation nanocluster evolution for Si-Mn-Ni-rich clusters.

6.4.4 Solute Dependence

In the HT9 alloy, irradiation-induced clustering has been observed for solutes of Si, Mn, Ni, and P, and Cr. Using the same atomic radius values provided in Table 6.4, the partial diameter for each of these species is calculated using the APT measured data following each of the irradiation experiments and provided in Table 6.13. With these values, a separate NHM model calculation is executed for each solute species upon proton and neutron irradiation to predict the evolution of the overall cluster partial diameter for each solute over time/dose.

Table 6.13 Summary of APT measurements of p_i and the resulting partial diameter, d_i, for clustering of individual solutes in HT9.

Nanocluster Analysis	Fe^{2+} ion-irradiated (500°C)		Proton-irradiated (500°C)		Neutron-irradiated (500°C)
	3 dpa	100 -dpa	1 dpa	3 dpa	3 dpa
Measurement of p_i					
Si	-	-	-	0.0776	0.0398
Mn	-	-	-	0.0578	0.0319
Ni	-	-	-	0.0752	0.0327
P	-	-	-	0.0206	0.0038
Cr	-	-	-	-	0.2281
Calculation of partial diameter d_i (nm)					
Si	-	-	-	3.0311	1.6537
Mn	-	-	-	2.6077	1.4572
Ni	-	-	-	3.1766	1.6407
P	-	-	-	1.7995	0.6998
Cr	-	-	-	-	2.6276

In the case of predicting the solute-specific behavior in HT9, the same values for f_i and D_i^{th} are used from HCM12A (Table 6.10) in the model for each species. And, as before, D_i^{th} is kept consistent across all irradiation conditions for each solute. As with ODS and HCM12A, the model will predict the overall cluster size evolution, but additional information is still required about the evolution of p_i to make a continuing estimate of d_i according to Eq. 6.24 and 6.25. For both ODS and HCM12A, the values for p_i are substituted at each data point for which a measurement is available, and the values for p_i at each intermediate iteration of the calculation are linearly interpolated. However, since the current interest is for the model to make a prediction of the solute clustering

without any prior knowledge, input of p_i is more challenging. It is important to acknowledge this limitation of the model when attempting to make individual predictions about the clustering behavior of individual solutes – some prior knowledge of the solute clustering behavior is still required.

Based on this limitation, two potential approaches are possible to move forward: 1) use the measured values for p_i measured at each data point for HT9 (interpolating values at intermediate time intervals), or 2) use the respective p_i values measured at each data point for HCM12A (with interpolated values). With option 1, the model is no longer a predictive calculation, but is rather a comparison of the model fit to the measured data. On the other hand, with option 2, the p_i values are estimated based on information known about another alloy, not the HT9 in question. The justification for using the same p_i values as HCM12A is based on the knowledge from literature that both alloys are known to form Si-Mn-Ni-rich clusters (G-phase) upon irradiated. Therefore, it is reasonable to hypothesize the resulting G-phase clusters will have similar composition, and thus similar p_i values. This is a not a perfect scenario, but provides a means to test the NHM model as a "predictive" tool for the solute behavior in HT9. Using this latter approach, the resulting NHM model predictions in HT9 for each solute species are plotted against the measured cluster sizes and solute partial diameters following each irradiation experiment in Figure 6.15 for Si and Mn, and Figure 6.16 for Ni and P.

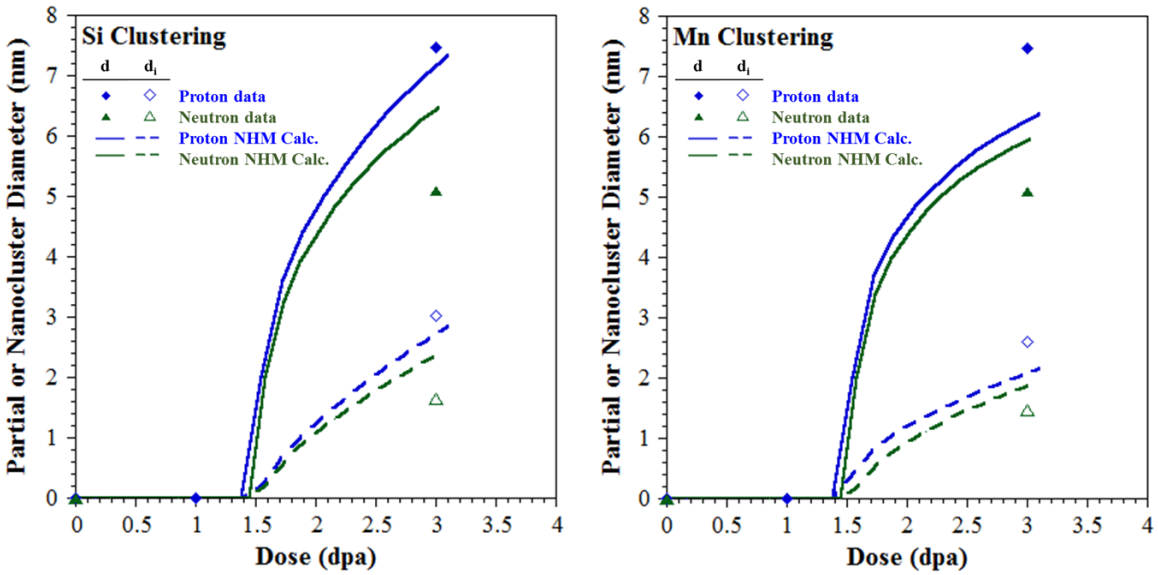

Figure 6.15 Predictions of NHM model fitted against HT9 clusters (d) and partial diameters (di) from Table 6.13 for a) Si solutes, and b) Mn solutes.

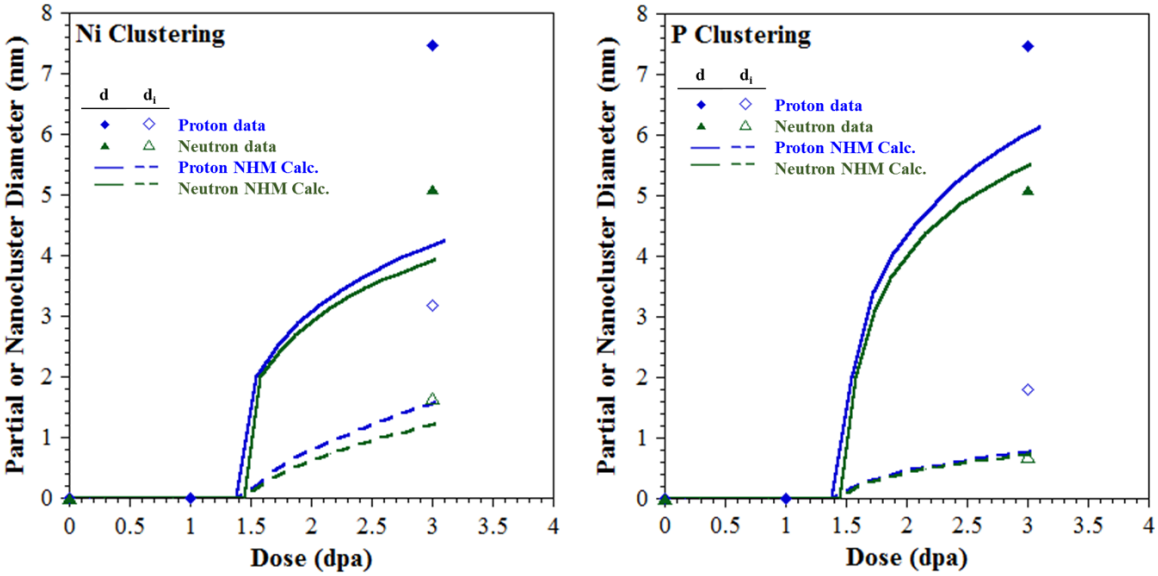

Figure 6.16 Predictions of NHM model fitted against HT9 clusters (d) and partial diameters (di) from Table 6.13 for a) Ni solutes, and b) P solutes.

For all four solutes, nucleation is introduced at approximately 1.5 dpa, and the model predicts clustering of the solutes at 3 dpa, consistent with experimental observation. The predicted cluster sizes at 3 dpa are not a perfect match for all three irradiation conditions, but are still reasonable considering no empirical fitting is conducted for these calculations. Plus, as with HCM12A, the clustering behavior

measured at 3 dpa may not be fully indicative of the longer-term clustering behavior at higher dose.

As was the case for HCM12A, the same set of circumstances apply for Cr-rich clustering in HT9. In the Results section of this thesis (Sections 5.2.3), Cr-rich clusters were only observed after neutron irradiation to 3 dpa. Using the NHM model and the disordering efficiencies from Table 6.6, it is possible to fit a combination of f_{Cr}^{n} and D_{Cr}^{th} parameters to emulate the clustering behavior of Cr upon neutron irradiation. However, taking this same approach for modeling irradiation with Fe^{2+} ions or protons as with HCM12A, the same disconnect between the model and empirical results persists. The same explanation provided in Section 6.3.5 is also applicable here.

6.5 Overall Summary of Trends

In the previous sections, the NHM model is applied systematically to simulate the nanocluster evolution in a model Fe-9%Cr ODS alloys and the commercial F-M alloys HCM12A and HT9, respectively. These modeling efforts are conducted sequentially to progressively gain insight into the influence of each set of irradiation conditions on the evolution of cluster size. Through this activity, new information about the mechanism of nanocluster evolution has been elucidated including: a) a need for a downward temperature shift when using higher dose rate irradiations to emulate low dose rate irradiation, b) the relative disordering efficiencies of each irradiating particle and their damage cascades, and for each individual solute species, and c) the rate at which solutes tend to migrate toward nanoclusters. The following sections will further discuss each of these trends observed in the modeling of each alloy.

6.5.1 Temperature Shift

For each alloy, the relative sensitivity of the model to the irradiation temperature was evaluated. In all cases, a downward temperature shift is required for higher dose rate irradiations to predict equivalent nanocluster evolution which matches the cluster evolution upon neutron irradiation for all nanocluster types (oxides, Si-Mn-Ni-rich, and Cu-rich). A summary of the temperature shifts determined are provided in Table 6.14. With Fe^{2+} irradiation, a negative temperature shift (i.e. temperature reduction) between 100-130°C is required to achieve comparable nanocluster evolution with neutron irradiation. Meanwhile, with proton irradiation, the reduction is between 74-100°C to get equivalent nanocluster evolution.

Table 6.14 Summary of temperature shifts required to enable calculations for Fe^{2+} and proton irradiation to simulate nanocluster evolution upon neutron irradiation.

Alloy	Cluster Type	Fe^{2+} → neutron irradiation Temperature shift	p^{+} → neutron irradiation Temperature shift
Fe-9%Cr ODS	Y-Ti-O-rich	-120°C	-74°C
HCM12A	Si-Mn-Ni-rich	-130°C	-100°C
HCM12A	Cu-rich	-100°C	-90°C
HT9	Si-Mn-Ni-rich	-	-100°C
Average Temperature Shift		**-117°C**	**-91°C**

The most important aspect of these calculated temperature shifts is the downward direction. The model suggests irradiation at higher dose rates (e.g. charged particle irradiations) need to be conducted at a lower temperature than the corresponding neutron irradiation to achieve comparable evolution of any nanoscale phases. As dose rate increases, the downward temperature shift must be greater in order to suppress radiation-

enhanced diffusion of the solutes leading to cluster growth and coarsening. This temperature shift is opposite that predicted by Mansur [187,188], which indicates increasing dose rate requires a simultaneous increase in irradiation temperature to emulate lower dose rate evolution of defect clusters (i.e. voids). The Mansur theory is discussed further in Section 7.6.2. For solute clusters, a negative temperature shift is also consistent with two other models, which will be reviewed in the following sub-sections. microstructures.

6.5.1.1 The Martin Model

It is possible to estimate the temperature shift using Martin's theories (see Section 2.4.6), which calculate the irradiation-induced dilated temperature (T') as [60]:

$$T' = T(1 + \Delta) \tag{6.24}$$

where T is actually irradiation temperature, and Δ is a temperature dilation factor, which can be estimated as [60]:

$$\Delta = \frac{C_v^0}{D^{th}} (\phi D_v)^{1/2} g \tag{6.25}$$

in which C_v^0 is the thermal concentration of vacancies (without irradiation), D^{th} is the thermal diffusion rate of solutes (without irradiation), ϕ is the irradiation flux, and D_v is the thermal diffusion rate of vacancies. Based on this dependency on the irradiation flux, higher dose rate irradiation will lead to a larger temperature dilation. The geometric factor, g, is written as [60]:

$$g = \sigma_r b^2 \left(\frac{4\pi r_c N_v}{\sigma_d}\right)^{1/2} \tag{6.26}$$

where σ_r, and σ_d are the replacement and displacement cross sections, respectively, b is the average length of each ballistic displacement, r_c is the recombination radius [$r_c = (3/4\pi N_{nc})^{1/3}$ = 8.1 nm] [42], and N_v is the atomic density of the target material (85.2

atoms/nm^3). Estimates for b are determined following a method outline by Heinig, et al. [58] in which a probability distribution function is fit against a SRIM calculation of atoms displaced from a flat oxide composition layer with a surrounding Fe matrix. Estimated values ranging from 0.25-0.35 are obtained for both Fe^{2+} and proton irradiation, and are consistent with those reported in Refs. [59] and [189] using the same methodology; an average value of 0.3 is used. One of the challenges with this calculation is the estimation of the cross-section terms, particularly σ_r, which is difficult to estimate for this system. However, another way Martin looked at the dilation factor is as [60]:

$$\Delta = \Delta_0 exp\left(\frac{E_\Delta}{k_b T}\right) \tag{6.27}$$

with $E_\Delta = E_d - E_f - E_m/2$, where E_d (0.31 eV [10]), E_f (2.2 eV [59]) and E_m (0.68 eV [183]) are the activation energies for solute diffusion, vacancy formation, and vacancy migration, respectively. Meanwhile, the Δ_0 is a function of $\phi^{1/2}g$, and k_b and T are the Boltzmann constant at the temperature, respectively. Because there are too many unknowns, we can instead carry out this calculation for Fe^{2+} irradiation at a shifted temperature of 383°C (based on the average temperature shift in Table 6.14) the dilation factor is estimated to be $\Delta^{Fe} = 0.206$, with $\Delta_0^{Fe} = 1.46\phi^{1/2}g$, yielding T' = 518°C. Next, we can estimate the pre-exponential of the dilation factor for neutron irradiation as:

$$\Delta_0^n = \Delta_0^{Fe}\frac{f^n}{f^{Fe}} \tag{6.28}$$

in which f^n and f^{Fe} are the disordering efficiencies of neutrons and Fe^{2+} ions, respectively (Section 6.2.1). The dilation factor for neutron irradiation at 500°C is estimated as $\Delta^n = 0.023$, and T' also becomes 518°C. Finally, following the same approach for proton irradiation to achieve the same T' = 518°C, the proton irradiation temperature T would need to be 388°C, which yields a $\Delta^p = 0.197$. This predicted proton irradiation

temperature (388°C) to yield comparable nanocluster evolution as neutron irradiation is reasonably close to the average temperature of 409°C estimated by the NHM model (Table 6.14).

6.5.1.2 The Wagner Model (via Chen)

Another model similar to the NHM model (developed by Wagner [80]) is advanced by Chen, et al. [79] to predict nanocluster cluster evolution in ODS alloys (Section 2.4.6). The governing equation for this model is:

$$\frac{dr}{dt} = -K\psi + \frac{D^{irr}}{r} \cdot \frac{c - c_r}{c_p - c_r} \tag{6.29}$$

in which the first term on the right hand side is identical to the second term on the right hand side of Eq. 6.1. The last term in Eq. 6.29 captures the growth of nanoclusters, in which c is concentrations of solutes in the matrix, and c_p is the solute concentration in the clusters. The term c_r is the concentration of solutes at the interface of the cluster and matrix and is expressed as [79]:

$$c_r = c_\infty exp\left(\frac{2\gamma_i v_{at}}{kTr}\right) \tag{6.30}$$

where c_∞ is the solubility limit of solutes at a flat interface between cluster and matrix, γ_i is the interfacial energy between the two phase (estimated as 0.016 J/m^2 [41]), v_{at} is the atomic volume of the target material ($v_{at} = \frac{1}{N} = 0.01174\ nm^3$), k is the Boltzmann constant, T is the temperature, and r is the radius of the nanocluster(s). The remaining variable, c_∞, is not readily available, but it may be used as a fitting parameter as was done for the disordering efficiency, f, in the NHM model. By the same justification as the NHM model, Eq. 6.29 is modified to account for possible recoil dissolution acting in parallel to disordering dissolution and is rewritten as:

$$\frac{dr}{dt} = -\frac{\phi}{N} - K\psi + \frac{D^{irr}}{r} \cdot \frac{c - c_r}{c_p - c_r} \tag{6.31}$$

which is formatted similarly to Eq. 6.1.

Using these parameters and the same disordering efficiencies fitted for Fe-9%Cr ODS (Section 6.2.1), the Chen, et al. model is applied to the Fe-9%Cr ODS system for each irradiation condition. In the same manner as the NHM model, the stepwise calculation is repeated over the same finite time intervals (Δt), incrementally accumulating more "dose" over increasing time. Each calculation is fitted to the experimental data as closely as possible using c_∞ as a fitting parameter. The Chen model predictions are plotted as solid lines against the measured cluster sizes following each irradiation experiment in Figure 6.17. For all three irradiating particles, the average cluster size approaches a steady state within the first few dpa. Each calculation is fitted to the experimental data as closely as possible using disordering efficiencies of $c_\infty^{Fe} = 0.0019$, $c_\infty^{p} = 0.0018$, and $c_\infty^{n} = 0.0018$, respectively.

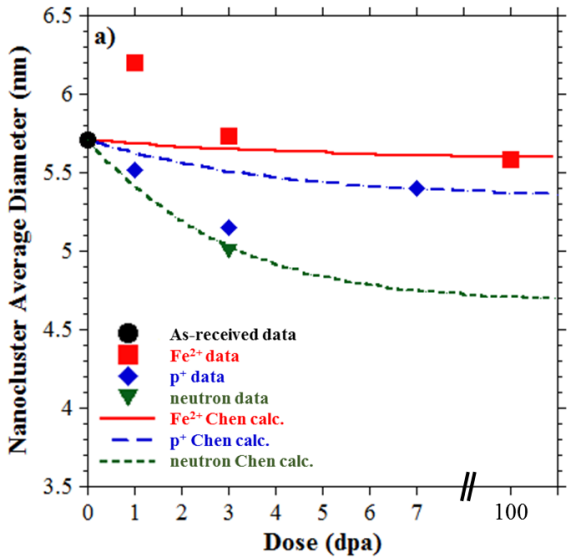

Figure 6.17 Stepwise calculations using the Chen, et al. model fitted against Fe-9%Cr ODS measured data from Table 5.4.

Once more, the sensitivity of the stepwise Chen model calculation for Fe-9%Cr ODS is evaluated by varying the input temperature to determine the influence on the predicted stable cluster size. Keeping all other inputs into Eq. 6.31 the same, a revised stepwise N calculation for Fe^{2+} irradiation at 383°C predicts steady-state oxide nanocluster size equivalent to that predicted (and measured) for neutron irradiation at 3 dpa and 500°C (Figure 6.18). Likewise, the same approach is applied for proton irradiation, for which an irradiation temperature of 409°C predicts cluster size which approaches that of 500°C neutron irradiation. These results are consistent with both the NHM and Martin theories in identifying the need for a downward temperature shift when using higher dose irradiations (i.e. charged particles) to emulate cluster evolution with lower dose irradiation (i.e. neutron irradiation).

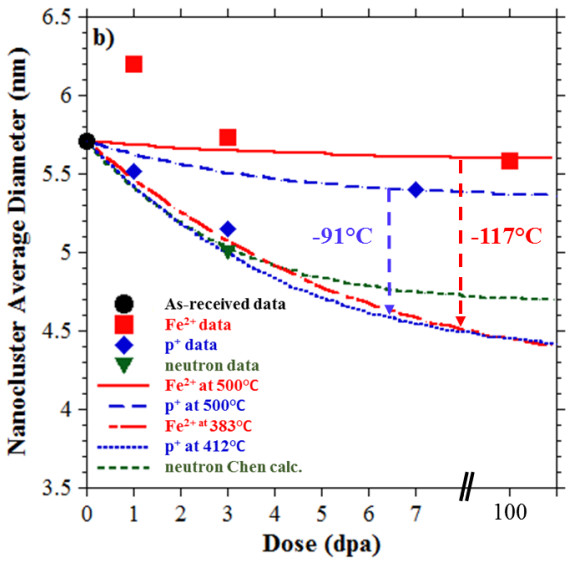

Figure 6.18 Stepwise calculations of Fe2+ irradiation and p+ irradiation with temperature shifts to emulate neutron irradiation nanocluster evolution.

6.5.2 Disordering Efficiency

In its original introduction, the authors of the NHM theory [57] acknowledge the disordering efficiency of the irradiation, *f*, is the most uncertain variable in the model.

However, by using this factor as a fitting parameter and comparing the results of several experiments to the theory, it is possible to deduce some useful information about this variable. For this thesis, the theoretical values of *f* for each irradiation condition on multiple alloys is evaluated, as well as the theoretical values for f_i for each of the clustering solute species within the alloys. A summary of the respective *f* values for each type of nanocluster is provided in Table 6.15 and each type of solute in Table 6.16. For all the clusters and solutes in this thesis, the disordering efficiencies are consistently lowest for Fe^{2+} and neutron irradiation and highest for proton irradiation. Interestingly, This relative pattern is also consistent with the estimated displacement efficiencies published in [42].

Table 6.15 Comparison of disordering efficiency (*f*) values fitted for each type of cluster and irradiating particle.

Irradiating Particle	**Fe-9%Cr ODS Y-Ti-O-rich**	**HT9 / HCM12A Si-Mn-Ni-rich**	**HCM12A Cu-rich**	**Displacement efficiency in** [42]
Fe^{2+} ions	0.039	0.095	0.220	0.04
Protons	0.150	0.342	0.688	0.25
Neutrons	0.046	0.123	0.229	0.02

Table 6.16 Fitted values for solute disordering efficiency (f_i) and displacement energy (E_d) for each solute species in this thesis.

Solute Element	**Disordering efficiency**			**Displacement energy**	
	f_i^{Fe}	f_i^{p}	f_i^{n}	**Reference**	**E_d (eV)**
Y	0.048	0.180	0.060	[190]	57
Ti	0.112	0.394	0.118	[191]	30
Cr	0.106	0.338	0.089	[191]	40
Si	0.129	0.410	0.107	-	-
Mn	0.209	0.668	0.171	[191]	40

Ni	0.089	0.284	0.076	[191]	40
P	0.180	0.180	0.220	-	-
Cu	0.220	0.560	0.216	[191]	30

The mechanism of disordering involves the localized disruption of the atomic structure of the target material (via irradiation damage), thus enabling solute atoms to more readily disassociate from their parent cluster (i.e. diffuse into the matrix) [57]. As such, it follows that substitutional solute atoms are displaced from their lattice positions (upon irradiation) when this localized disordering occurs. On this basis, the relative disordering efficiencies of each solute element are compared to the respective displacement energy, E_d, for each of the solute elements (Table 6.16) in Figure 6.19. These values for E_d are acknowledged to be only estimates [191], as the displacement energy is likely dependent upon the nature of the bonding with its surrounding species. Even so, a notable trend appears to exist for all three types of irradiating particles - solutes with higher displacement energy tend to have a lower cascade disordering efficiency. The identification of this trend itself may be informative for using the model as a predictive tool for systems with a variety of solutes. The potential usefulness of this will be discussed in more detail on Section 7.6.

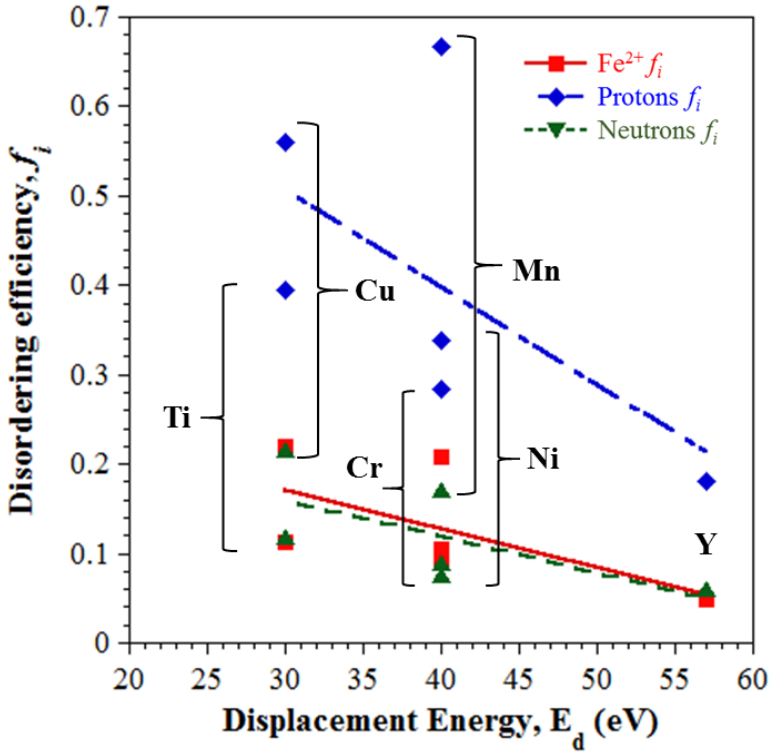

Figure 6.19 Comparison of fitted disordering efficiencies and literature values for solute displacement energies for each solute species. Linear trend lines fitted for each respective irradiating particle.

6.5.3 Solute Diffusion Rates

In the previous sections describing the NHM model and its application to individual solutes, the fitted values for the thermal diffusion, D_i^{th}, for each of the solutes are identified to be much lower than typical values found in archival literature (with the exception of Y) for diffusion in a b.c.c. Fe-matrix (Table 6.1). As a result, these fitted values (summarized in Table 6.17) likely only represent the rate of diffusion of the solutes *toward* the solute clusters, enabling the clusters to grow. Therefore, any solutes migrating toward clusters (which are already rich in the same solute) are diffusing against the solute concentration gradient. Considering this "uphill" migration, it is not surprising the fitted values for diffusion toward the clusters are consistently lower than traditional values for thermal diffusion, where solute flux is from higher to lower concentrations (i.e.

"downhill"). As a result, the magnitude of this fitted diffusion rate may reflect the relative "affinity" of each solute to the clusters of interest. This would explain why common solutes between the ODS and the F-M alloys have slightly different rates of diffusion toward different types of clusters (Y-Ti-O-rich oxides vs. G-phase).

Table 6.17 Solute thermal diffusion rates fitted using the NHM model.

Solute Element	Fe-9%Cr ODS	HCM12A / HT9
	Fitted D_i^{th} (cm^2/s)	Fitted D_i^{th} (cm^2/s)
Y	6.86×10^{-21}	-
Ti	9.32×10^{-21}	-
Cr	3.88×10^{-22}	-
Si	3.11×10^{-22}	1.11×10^{-23}
Mn	2.59×10^{-22}	1.81×10^{-23}
Ni	3.88×10^{-22}	6.76×10^{-24}
P	-	1.04×10^{-20}
Cu	-	6.76×10^{-24}

Furthermore, in comparing the fitted rates of the solutes within the ODS alloy, the solute element with the highest rate toward the oxide nanoclusters is Ti, followed by Y. Although these elements typically exhibit lower mobility in b.c.c. Fe than the other solutes, an additional thermodynamic driving force for clustering is likely present. Barnard et al. modeled the behavior of oxide precipitation in NFAs [192], concluding that precipitation is driven by strong thermodynamic driving forces and kinetics which favor rapid nucleation. Barnard et al. attribute this behavior to a large enthalpy of formation for the oxides phases and the low solubility of Y in the Fe-Cr matrix. This low solubility of Y may also explain why the fitted thermal diffusion rate of Y (Table 6.17) is actually

slightly higher than the literature value for thermal diffusion (Table 6.1). The Y atoms appear to have a high affinity for the oxide clusters, which may also explain why the fitted disordering efficiencies for Y are also the lowest of all of the solutes (Table 6.16)

The formation enthalpies for the several relevant oxide compounds may be compared (Table 6.18). The enthalpies of formation for Y_2O_3 and TiO_2 are -1907 kJ/mol and -889 kJ/mol, respectively [22] (Note: the exact structure of the nanoclusters may not be a simple mixture of Y_2O_3 and TiO_2), suggesting both will have a high affinity for oxygen. In addition, Ti and Y have a low solubility limit in b.c.c. Fe due to their larger atomic radius (Table 6.4), although Ti is less oversized and generally has a higher mobility [184]. It follows that Ti would likely have a slightly higher mobility overall, consistent with the fitted values (Table 6.17).

Table 6.18 Comparison of enthalpy of formation for various oxide phases, from [185]**.**

Element	**Oxide Composition**	**ΔH_f^{298} (kJ/mol)**
Fe	Fe_3O_4	-1118
Cr	Cr_2O_3	-1130
Y	Y_2O_3	-1907
Ti	TiO_2	-889
Si	SiO_2	-911
Mn	Mn_3O_4	-1388
Ni	NiO	-241
W	WO_3	-839

Meanwhile, the clustering of Si, Mn, and Ni elements are likely a result of radiation-induced segregation (RIS) in both the ODS and F-M alloys. Si, Mn, and Ni are known to segregate toward grain boundaries in commercial F-M and austenitic stainless

steels [23,193,194]. This also explains why clusters with these species are not present in the as-received condition. As a result, the mechanism of RIS is likely to be a weaker driving force for solute cluster than the formation of Y- and Ti-rich oxides.

CHAPTER SEVEN: DISCUSSION

Charged particle irradiations, including protons and heavier species have increasingly been utilized to emulate neutron irradiation effects in F-M and ODS alloys, especially at irradiation damage levels ≥100 dpa [30,36–39]. Ions can deliver high irradiation damage rates in short experimental time frames, at lower costs, and with little to no residual radioactivity, enabling a much quicker turnaround time for conducting verification experiments on candidate materials. However, questions remain about the ability of ions to comprehensively emulate the damage introduced by neutrons in a reactor environment.

With the advancement of the NHM model in this thesis, it is possible to create a baseline estimate for how nanoclusters will evolve under different irradiation conditions. With this information, the appropriate temperature shift required to simulate nanocluster evolution using higher dose rate, charged particle irradiations may be determined. Furthermore, with the capability to isolate the clustering behavior of individual solutes in a given alloy, the model may be used as an informative tool for the elemental tailoring of existing or new alloys to be more radiation-resistant.

In this chapter, Sections 7.1-7.3 will review the limitations of both TEM and APT techniques, and discuss the relevance of other nanocluster measurements found in archival literature. Sections 7.4 - 7.5 will review the analysis and interpretation of results to evaluate the ability of Fe^{2+} and proton irradiation to successfully emulate neutron irradiation in the context of: a) the overall microstructure and defect cluster evolution, b)

the evolution of various nanocluster types in ODS and F-M alloys, respectively. Finally, Section7.6 will review the advanced NHM model developed for this thesis and its potential for broader use as an informative and predictive tool to engineer radiation-resistant alloys for future nuclear reactor applications.

7.1 Limitations of TEM/STEM Measurements

Transmission electron microscopy (TEM) is a unique and powerful technique which is used ubiquitously in the field of nuclear materials. TEM enables microstructural imaging of small samples and is powerful enough to resolve features in the microstructure at or below 2 nm in size. As a result, it is fundamental for studying features which are highly relevant in the study of nuclear materials such as grain structure, carbide and other secondary phases, dislocation line density, and smaller nanoscale phases as well as irradiation-induced features including dislocation loops and voids or cavities. However, when reviewing published data resulting from TEM analysis, it is important to recognize the inherent challenges, limitations, and subjectivity involved with the technique. The following sections provide an overview of these considerations.

7.1.1 Image Quality

The quality (or resolvability) of the TEM images from one sample to the next are rarely exactly the same. The primary influence on the ability to resolve microstructural features in a given sample is the relative thickness of the TEM lamellae. Generally, the thickness of a lamellae needs to be less than 100 nm to achieve high quality images when using a TEM operating at 200-300 keV. For this thesis, a consistent focused ion beam (FIB) technique is used for fabrication of the TEM lamellae from each specimen; limitations of FIB will be discussed in the next section. In all cases, thinning of the

lamellae at 30 keV was conducted until the samples were measured to be less than 100 nm. Then, the samples are further thinned using lower energy ions (5 keV) until an opening in the lamellae is visually seen (see Section 4.3.1). With this technique, the entire sample is expected to be between 0 and 100 nm in thickness, enabling high quality imaging throughout.

Upon inspection of each sample in the TEM, the thickness is measured by electron energy loss spectroscopy (EELS) in several locations and an average thickness is calculated (Section 4.4.3). Despite utilizing a consistent approach in the FIB for fabricating each of the samples, the average thickness of the TEM lamellae for each sample ranges from 29 nm to 104 nm, with the majority of the sample thicknesses falling between 50-98 nm. The differences in sample thickness can influence the detectability of microstructural features within the samples, particularly in alloys such as the Fe-9%Cr ODS and F-M alloy in this thesis due to their relative small grain/lath sizes and high dislocation density. In particular, the detectability of dislocation loops in STEM is directly influenced by the sample thickness. Examples of this influence are evident in Figure 7.1. Both images utilize the same STEM imaging technique to image dislocation loops. The image in Figure 7.1a is taken from an irradiated ODS sample with an average thickness of 51 nm, while the image in Figure 7.1b is from an irradiated ODS sample with average thickness of 104 nm. In the former image, the contrast appears more distinct, thus making detectability of the dislocation loops clearer. It is believed this is the primary reason for the high number density measurement in the proton-irradiated specimen to 3 dpa ($10.2 \pm 8.0 \times 10^{21}$ m^{-3}), in which the FIB lift-out sample produced the highest quality image, enhancing the visibility of the loops.

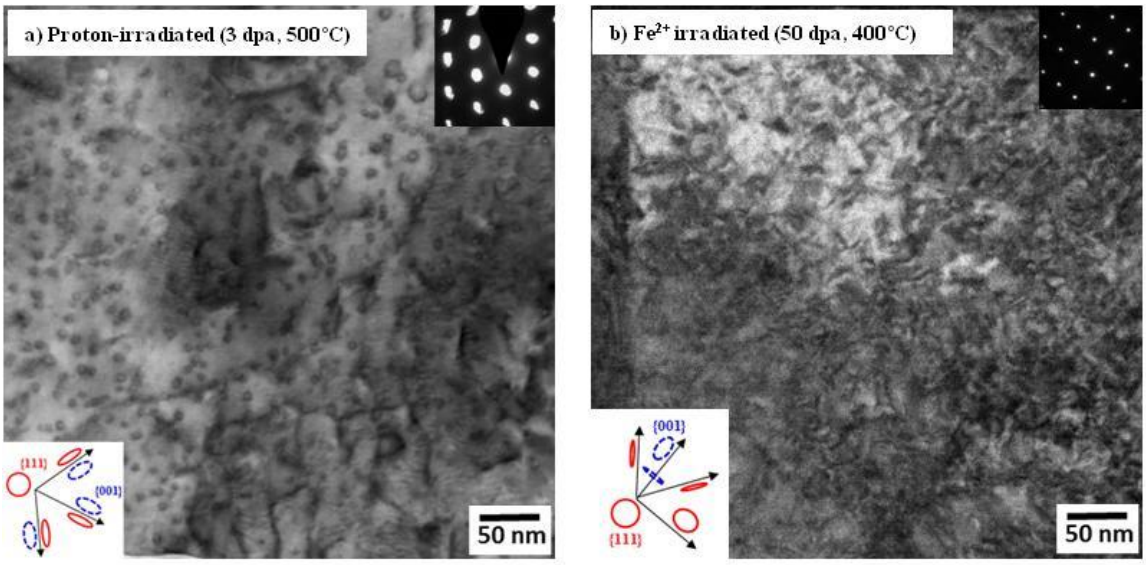

Figure 7.1 Representative STEM Images of dislocation loops in Fe-9%Cr ODS. The sample in a) is ~51 nm thick, while the sample is b) is ~104 nm thick.

7.1.2 FIB Damage

Fabrication of the TEM lamellae using the FIB technique is a versatile method for quickly creating a sample of an irradiated specimen without grossly disrupting the irradiated portion of the bulk material. In the case of Fe^{2+} irradiation, the damage layer is only ~1.2 μm deep, while with the proton irradiation, the damage layer is ~20 μm deep (Section 2.1.2). In both cases, it is imperative that the damage layer of the sample be preserved as much as possible during the fabrication process to enable the most representative analysis of the irradiated microstructure.

In the FIB process, material is removed from the sample via a beam of heavy Ga^{+} ions, which impact the surface atoms of the material, displacing them from the bulk. In a sense, this bombardment of Ga^{+} ions is essentially another form of irradiation upon the sample. As a result, care is taken during the sample preparation to minimize the amount of time the sample is exposed to the ion beam. Additionally, during the final thinning of the sample with the ion beam, the incident angles of the beam are minimized (typically

1.5°) to minimize the Ga^+ ion penetration into the sample. Even with these precautions in place, elimination of any damage caused by the milling process is very difficult. This damage can manifest in the TEM imaging as additional ion beam-induced defects [195], making accurate characterization of irradiation-induced defects more challenging. Examples of TEM micrographs of unirradiated HT9 are provided in Figure 7.2, comparing the imaging after sample preparation using electro-polishing (Figure 7.2a) and FIB lift-out (Figure 7.2b) [195].

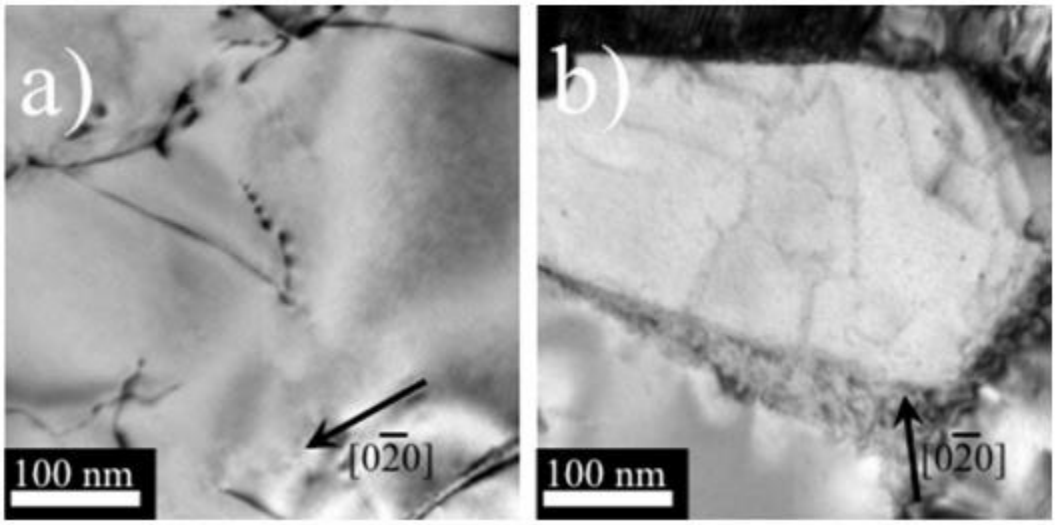

Figure 7.2 TEM micrographs of unirradiated HT9 following sample preparation using a) electro-polishing, and b) FIB fabrication [195].

Aitkaliyeva, et al. developed a post-FIB fabrication technique to reduce the amount of FIB damage present in the samples [195] using a Gatan PIPS-2 system or a Fischione NanoMill. These systems use a lower energy beam (<1000 eV) of Ar ions for final thinning and removal of the FIB damage layer from the sample. In their study, positive results in removing FIB beam damage in a Fe-12Cr alloy were realized using the PIPS-2 system and sample preparation recommendations using the PIPS-2 system are provided. In the case of this thesis, the post-FIB processing system available for use at

the Center for Advanced Energy Studies (CAES) is a Fischione Model 1040 NanoMill. This instrument was used for several of the TEM lamellae fabricated for this thesis. In each case, beam energy was set to 900 eV at 130 pA, with a incidence angle of only 9 degrees. The milling time was initially set for 20 minutes on each side of the TEM lamellae for the sample of Fe-9%Cr ODS irradiated with Fe^{2+} ions to 3 dpa at 500°C. The milling time was subsequently increased to 45 minutes on each side of the TEM lamellae for the sample of Fe-9%Cr ODS irradiated with Fe^{2+} ions to 100 dpa at 500°C and for subsequent samples of HCM12A and HT9 irradiated with Fe^{2+} ions to 3 dpa at 500°C each. In all cases, the post-FIB nanomilling process was successful in eroding the majority of the Pt deposit placed at the surface of the sample, but did not result in any noticeable improvement in reducing FIB damage in the bright field or STEM images.

Given the consideration for the presence of potential FIB damage, it is important for the analyst to utilize a consistent approach and threshold for how microstructural features are identified and measured within TEM images. The significance of this will be further discussed in the following section.

7.1.3 Subjectivity

Despite the best practices and precautions in place to systematically characterize microstructures using TEM imaging, some inherent subjectivity still remains. For the identification and measurement of each feature within the microstructure, each analyst may define their own thresholds for when to make a positive identification. For example, grain and lath boundaries are often difficult to differentiate from the “forest” of dislocations in the microstructure. In some cases, a survey of the surrounding microstructural context is required to deduce where grain boundaries are most likely

located. Therefore, each analyst may apply their own interpretation of the grain morphology. Similarly, identification of carbides and other secondary phases in TEM is largely accomplished by looking for areas of different Z-contrast, indicating localized variation is the material composition. Smaller areas of Z-contrast may be more difficult to positively identify, particularly in alloys which contain high dislocation density and imaging contrast as those evaluated in this study. It has also been previously highlighted that dislocation loop identification may be influenced by the sample thickness and the subjective differentiation of loops from the surrounding dislocation forest. Finally, the positive identification of small voids, particularly in the presence of nanoscale phases (such as ODS oxides) is also subjective using the through focus technique, as highlighted in Section 4.4.1.

Given the inherent subjectivity of microstructural characterization using TEM and STEM imaging, it is difficult to draw definitive conclusions when comparing the results of one study to those from a different study conducted by a different analyst. However, it is informative to evaluate the results measured by the same analyst, in which consistent interpretation and identification thresholds are applied for all specimens, as is the case for this study. As a result, in the context of microstructure characterization via TEM/STEM, the most useful information from this thesis is the comparison of microstructure within each specimen studied to evaluate the evolution trends and dependencies on different irradiation parameters such as dose rate, temperature, and irradiation damage (dpa).

7.1.4 Analysis Regions

For each form of irradiation (i.e. Fe^{2+} ions, protons, or neutrons) a different resulting damage profile results, as illustrated in Figure 2.2. For neutron irradiation, the

damage profile is essentially uniform throughout the irradiated specimen, suggesting that microstructural analysis may be conducted in any region of the sample. With proton irradiation, the damage profile peak is at a depth of ~19 μm (Figure 2.2), which is well in excess of the relative depth of the TEM lamellae fabricated for this study (~7 μm), and the target analysis region is located between ~1 - 10 μm. Therefore, the full lamellae, with the exception of the top ~1 um layer, may be analyzed for characterization of the microstructure (Figure 7.3a). On the other hand, with Fe^{2+} ion irradiation, the damage peak is ~1.0-1.2 μm deep into the bulk material (Figure 2.2), while the target analysis region is at ~400 - 600 nm in depth. Due to this limitation, characterization of the microstructure for Fe^{2+} irradiated samples much be conducted within this very narrow "band" on each lamella (Figure 7.3b). With smaller volumes available for analysis, it becomes more difficult to maximize counting statistics of microstructural features.

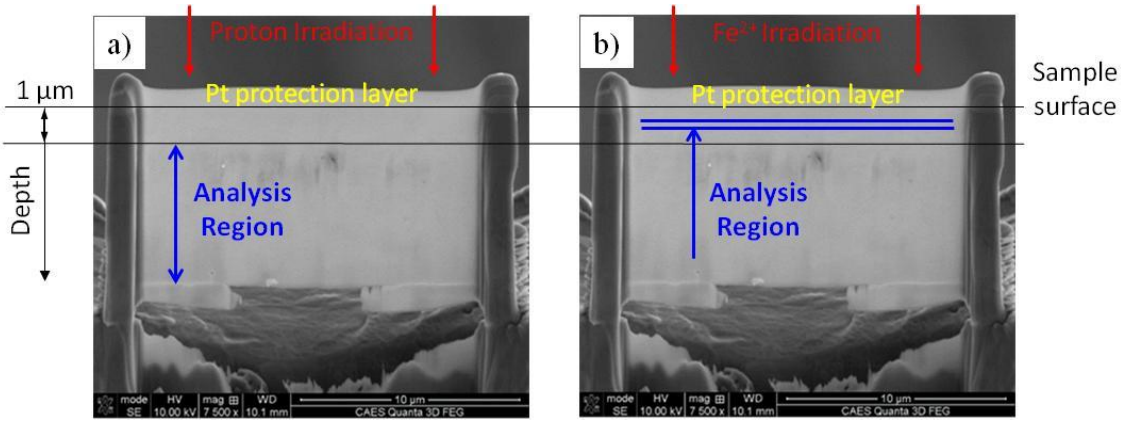

Figure 7.3 Representative FIB/SEM micrographs of TEM lamellae fabricated via FIB with indication of the relative analysis regions available for a) proton-irradiated samples, and b) Fe2+ irradiated samples.

7.1.5 Summary

Although TEM is a proven and productive technique for analyzing irradiated microstructures, the inherent limitations and subjectivity associated with TEM are real

and should always be considered. As a result, most studies employ a complimentary technique to analyze microstructures, reducing the subjectivity and increasing confidence in the measured results. Since the primary thrust of this thesis is the study of nanocluster evolution, the complimentary technique of atom probe tomography (APT) is used to obtain a more objective measurement of the nanocluster morphologies in each alloy. However, some inherent limitations and artifacts in APT also exist and should be taken into consideration when interpreting the results. Section 7.3 will review each of these considerations as well.

7.2 Microstructure and Defect Clusters using TEM

Historically, ion irradiation conditions have been selected to emulate a defined neutron irradiation condition based on the invariance theory [188], which purports that the accelerated irradiation damage rate from ions can be made up for with temperature adjustments, to produce equivalent void microstructures. Recent studies using modern computational techniques [196,197], have corroborated the invariance theory. But they have also found the development of an irradiation damage cascade to be a critical factor in the accumulation of local defect and defect cluster morphologies. Experimental evidence for the role of temperature and damage cascades specifically in F-M and ODS alloy microstructure evolution, is somewhat limited, however, because of the challenge of comparing neutron to ion irradiations on identical heats of archival alloys.

One of the seminal studies on this topic has been conducted by Was, et al. [36], who characterized F-M alloy HT9 under neutron and ion irradiation conditions. The irradiation temperatures were selected based on the invariance theory; neutron irradiations were carried out to 155 dpa at 443°C, while 5 MeV Fe^{2+} self-ion irradiations

were carried out to 188 dpa at 460°C. While Was, et al. [36] is able to obtain a relatively consistent void morphology between neutron and ion irradiations, the G-phase and dislocation loop morphologies are markedly different between neutron and ion irradiations. Ions produce smaller G-phases at a higher number density than do neutrons. The opposite is observed with dislocation loops: ions produce larger loops at a lower number density, although the resultant total loop line length is relatively constant between the irradiation types. These differing trends for loops and G-phases are consistent with the conclusions of Getto, et al. [198], which suggest that G-phases do not influence the evolution of loops.

In the next sections, the ability of charged particle irradiations to emulate neutron irradiation will be evaluated on the basis of the overall microstructure and defect cluster (i.e. voids and dislocation loops) evolution upon each irradiation.

7.2.1 Grains, Carbides, and Dislocation Lines

For all three alloys studied for this thesis, the morphology of grains, carbide precipitates, and dislocation line density are measured. After common irradiation conditions of 3 dpa dose at 500°C, these morphologies are found to be statistically invariant upon irradiation with Fe^{2+} ions, proton, and neutron irradiation. Additionally, the morphologies of grains, carbides and dislocations are also invariant with dose under Fe^{2+} and proton irradiation, including up to doses as high as 100 dpa with Fe^{2+} ions. These results are illustrated in Figure 7.4 for Fe-9%Cr ODS and Figure 7.5 for HCM12A and HT9 and suggest these features are stable upon irradiation.

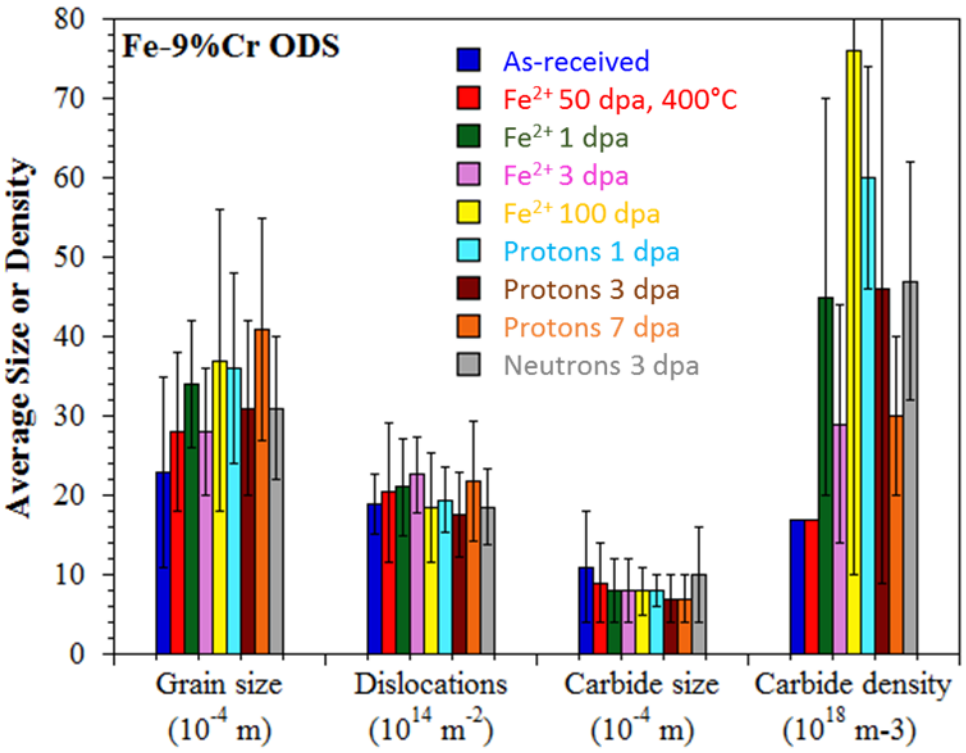

Figure 7.4 Comparison of microstructure measurements of grains, carbides, and dislocation lines in each specimen of Fe-9%Cr ODS.

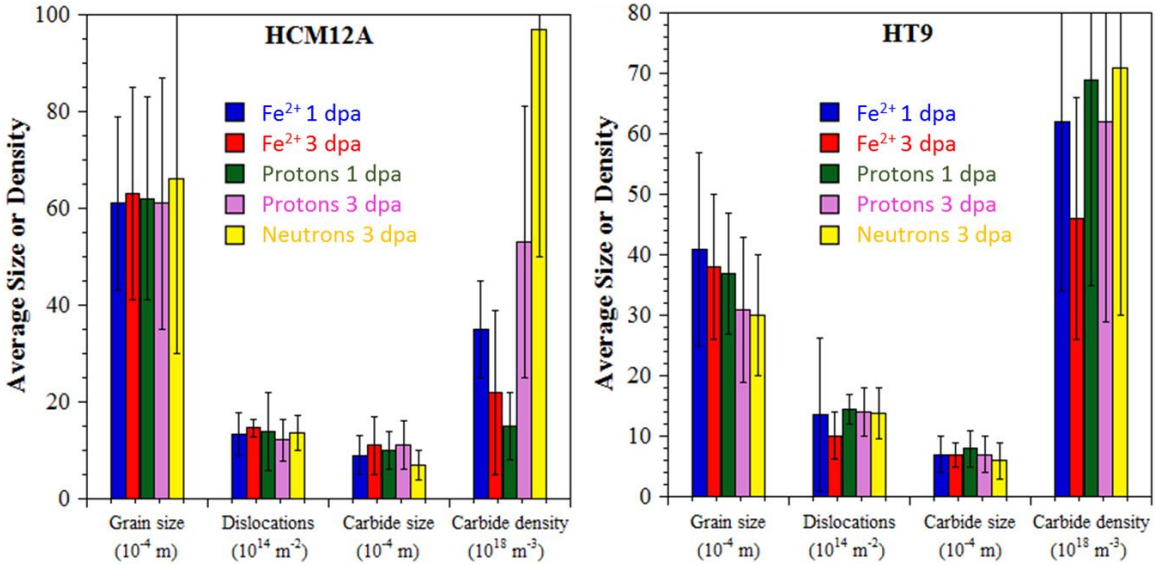

Figure 7.5 Comparison of microstructure measurements of grains, carbides, and dislocation lines in each specimen of a) HCM12A and b) HT9.

7.2.2 Voids

Some void nucleation and growth are detected in each of the alloys. In the Fe-9%Cr ODS alloy, any voids present in each of the specimens are scarce and relatively small (between 2.5 and 5.5 nm) making them difficult to positively identify. Most notably, no voids are identified upon any of the Fe^{2+} irradiation, including up to doses of 100 dpa at 500°C. This result suggests the ODS is likely successful at suppressing void swelling up to higher doses. Most literature studies of ODS alloys focus primarily on the nanocluster evolution upon irradiation. One study by He, et al. [9] briefly reports evolution of dislocation loops, but makes no mention of any observed voids after proton irradiation to 3.7 dpa at 400°C.

Similarly, in the HCM12A and HT9 alloys, voids are not detected in any of the irradiation conditions at lower doses of 1 to 3 dpa. However, larger faceted voids (up to ~20 nm) are clearly evident after Fe^{2+} irradiation up to 100 dpa in both alloys, although the number density remains relatively low. This result suggests the resistance of the HCM12A and HT9 to void swelling may be less effective than the ODS alloy at higher dose. Getto, et al. [199] have also shown how pre-implantation of He is needed to induce nucleation of voids at lower doses in HT9. Some prior evaluations of void evolution in HT9 are published in literature and plotted in Figure 7.6, along with the results herein. Getto, et al. [30] conducted irradiations with Fe^{2+} ions at 460°C up to doses ranging from 75-650 dpa. In this study, voids were characterized using STEM bright field and high-angle annular dark-field (HAADF) imaging. After 75 dpa, no voids were detected, but beginning at a dose of 130 dpa, voids were observed to increase in average diameter from 15 nm up to ~60 nm at 650 dpa, while number density slightly declined from ~14 x 10^{20}

m^{-3} to ~7 x 10^{20} m^{-3} in the same dose range, resulting in an approximately linear swelling rate observed in this range of doses. Sencer et al. [29] also observed voids in HT9 with an average diameter ~28 nm and number density of ~2.5 x 10^{20} m^{-3} after Fe^{2+} irradiation to 155 dpa at 443°C. Both of these results are reasonable and consistent with those found in this study after Fe^{2+} ion irradiation to 100 dpa at 500°C (average diameter of 12.8 nm and density of 2.4 x 10^{20} m^{-3}).

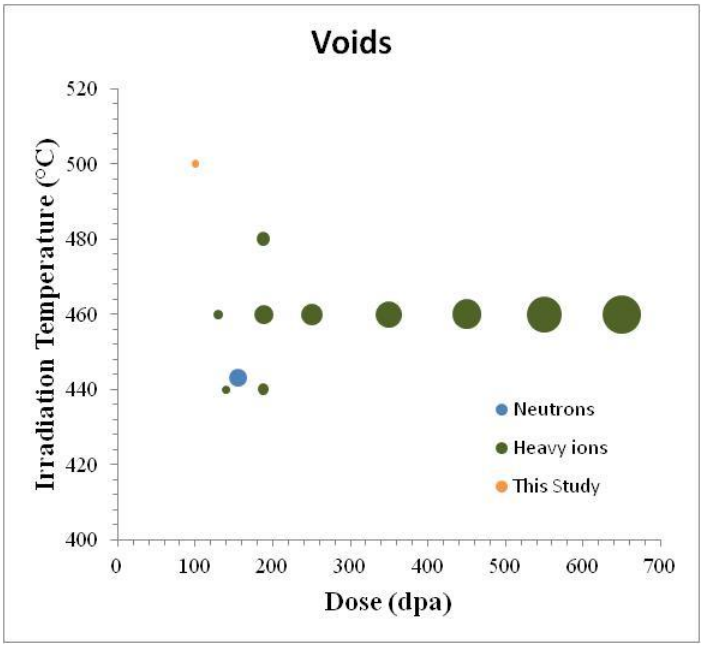

Figure 7.6 Results from literature indicating average size of irradiation-induced voids in F-M alloys. Size of bubbles represent relative size of voids.

7.2.3 Dislocation Loops

Using the STEM imaging technique, dislocation loops are readily visible and measurable. In the Fe-9%Cr ODS alloy, dislocation loops are present after 1 dpa upon irradiation with either Fe^{2+} ions or protons. In all specimens, dislocation loops were relatively small, generally measuring below 20 nm, with the majority of them between 6-10 nm. As dose increases, loops exhibit only marginal growth, suggesting the size of loops are largely stable up to higher doses. This result is consistent with loop growth

observations in various ferritic-martensitic alloys [16,23,138] and austenitic stainless steels [42], and it supports the theory of defect cluster saturation developed by Whapham and Makin [136,137]. It is also reasonably consistent with a study by He et al. [9] on the same ODS alloy, where dislocation loops averaged 15.4 nm after proton irradiation to 3.7 dpa at 400°C. The three irradiations to 3 dpa at 500°C have consistent dislocation loop sizes and number densities, suggesting that Fe^{2+}, protons, and neutrons can all produce comparable loop microstructures, at least up to a dose of 3 dpa. Similar trends are observed for both the HCM12A and HT9 alloys. Dislocation loops are present after 1 dpa of proton irradiation, yet exhibit minimal growth up to 3 dpa. Some prior evaluations of dislocation loop evolution in F-M alloys are published in literature and plotted in Figure 7.7, along with the results herein. At low dose, the average size of dislocation loops is consistently smaller than 20 nm, regardless of irradiation temperature. With doses increasing up to 200-300 dpa, the loops get much larger, but the size appears to plateau up until > 500 dpa, when the sizes get substantially larger again. The results also suggests defect cluster saturation, up to a point, or perhaps saturation plateaus. The reason for these potential plateaus is not clear, and would be worth further investigation to determine if an additional mechanism takes over, particularly at higher doses above >500 dpa.

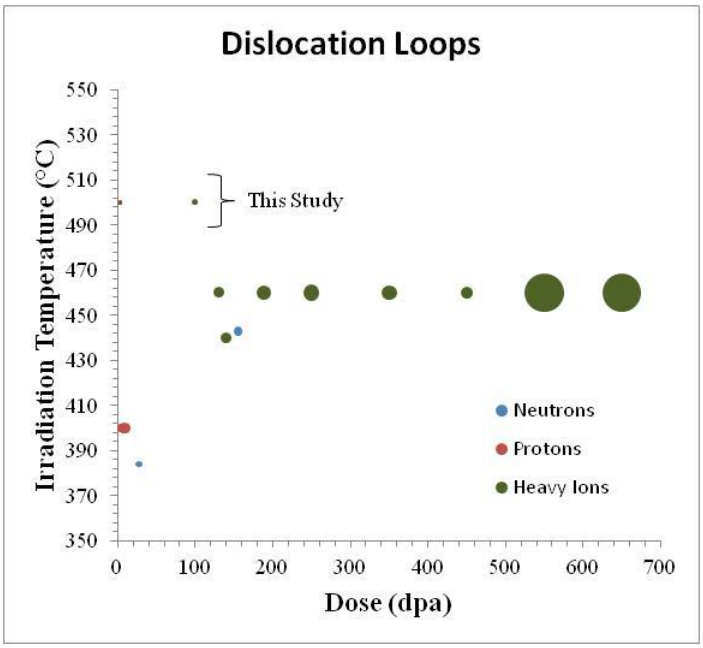

Figure 7.7 Results from literature indicating average size of irradiation-induced dislocation loops in F-M alloys. Size of bubbles represent relative size of loops.

7.2.4 Temperature Shift Theory for Defect Clusters

Mansur [187,188] theorized a temperature shift is necessary in order to produce consistent microstructures with respect to defect clusters when the irradiation dose rate increases. The desired microstructures are bound by two mechanisms of point defect loss: 1) mutual recombination in the matrix, and 2) diffusion to sinks. The temperature shift for recombination-dominant and diffusion-dominant regimes is calculated for a reference condition of 500°C at 10^{-7} dpa/sec (Figure 7.8), conditions comparable to the neutron irradiation experiment in the present study. The vacancy migration and formation energies are taken to be 0.68 eV and 2.2 eV, respectively, for a b.c.c. Fe-9%Cr steel [179]. But since the temperature is fixed at both dose rates in the present irradiation experiments, the temperature shift curve must have a slope ~0 in order for the Fe^{2+} ion-, proton-, and neutron-irradiated void and dislocation loop microstructures to be consistent with one another, as observed in this work. It thus follows that void and loop nucleation

and growth are recombination-driven processes (red line, Figure 7.8), so their evolution will be relatively independent of dose rate at a fixed temperature. Overall, Proton and Fe^{2+} irradiation provide a meaningful simulation of the recombination-driven microstructural processes, such as dislocation loop and void nucleation and growth, resulting from neutron irradiation at a fixed dose and temperature.

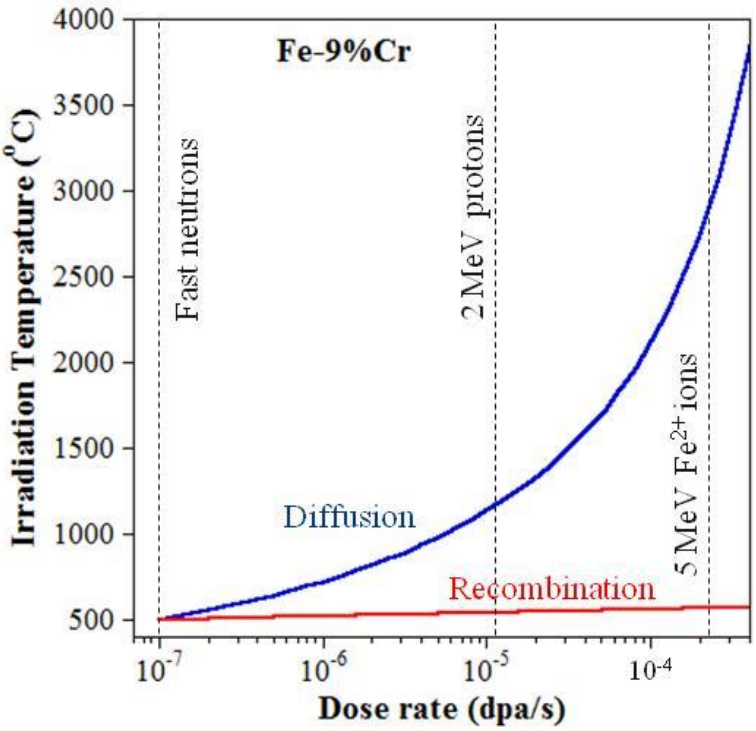

Figure 7.8. Comparison of calculated temperature shifts required for diffusion-driven (blue line) and recombination-driven (solid line) mechanisms to produce consistent defect clusters, from [187,188].

7.3 Limitations of APT Reconstruction and Cluster Analysis

Atom probe tomography (APT) is an emerging technique which is increasingly being utilized in the field of nuclear materials. APT enables atomic-level resolution and provides capability for more objective chemical analysis and characterization of any nanoscale phases present. However, as with other techniques, some inherent limitations and artifacts may be present or introduced during APT analysis which need to be

considered when interpreting data. Also, when reviewing published data resulting from APT analysis, it is important to recognize the inherent limitations and artifacts involved which may influence the conclusions. The following sections will provide a review of these considerations and some context for analysis and interpretation of the results of this study and those found in archival literature.

7.3.1 LEAP Analysis

The procedure for conducted analysis using the local electrode atom probe (LEAP) involves the fabrication of very fine needle-shaped samples with a tip radius of <50 nm. Subsequently, each of the surface atoms at the tip of the needle are sequentially evaporated and collected on a detector. Although the total LEAP process of evaporation may encompass several hours of instrument time, the resulting amount of analysis volume which is typically collected is on the order of 100,000 to 1,000,000 nm^3.The largest data set collected for this thesis had a total volume of 1,465,928 nm3, which is the equivalent to the volume of a cube with sides ~114 nm in length. As result, each collected data set is only a very small sampling of the overall bulk material, making each data set sensitive to inhomogeneities within the microstructure. It is not uncommon for a data set from one specimen to contain a grain boundary or secondary phase, while the next data set from the same specimen does not. Based on this, it is recommended to always collect as many data sets as possible for each specimen so that the combined analysis volume may be maximized, reducing the vulnerability to any inhomogeneities in the microstructure. For this thesis, every possible data set was used for analysis, with the exception of those which clearly encompassed a secondary phase or clearly intersected with a network of grain boundaries.

Another important consideration is the detector efficiency, which typically ranges from 0.36 to 0.50 for most modern LEAP systems. For this thesis, the Cameca LEAP 4000X-HR at CAES, which has a detector efficiency of 0.36, was used for all the sample analyses. This means only 36% of the evaporated atoms from each sample needle were collected at the detector following evaporation. Fortunately, the reconstruction within IVAS accounts for the efficiency when approximating the original location of atoms. The net result is a reduced atomic density within the 3D reconstruction. For the b.c.c. Fe crystal structure, the atomic density is estimated to be 85.2 atoms/nm^3. Therefore, theoretically, the 3D reconstruction atomic density is expected to be ~85.2*0.36 = 30.7 atoms/nm^3.This is consistent with the measured atomic density within each data set of this study, which range from 28.0 to 31.6 atoms/nm^3. Any additional discrepancies between the theoretical and experimental atomic densities are explained by further loss of collected atoms to background noise. Background is evident in the mass spectrum as a level of noise amidst the mass-to-charge ratio peaks. This noise is typically caused by evaporated atoms which departed from the source sample at a time in between the LEAP laser pulses. As a result, the measurement of the time-of-flight of the ion from the sample to the detector is no longer accurate and these ions are typically unable to be identified.

During the evaporation of the sample needles, atoms of different species often evaporate at different rates, depending on the evaporation field (F in Eq. 4.9) present. This difference is relevant when the evaporation sequence encounters an interface between the bulk matrix atoms (i.e. primary Fe atoms) and a secondary phase or nanoparticle. Depending on the relative fields between the matrix and the particle, the surrounding matrix atoms may evaporate more readily than the particle, or vice versa,

leading to local magnification effects [170,177]. One of the known side effects of this phenomenon are trajectory aberrations between the original location of the source ions and their eventual impact location on the detector. These trajectory aberrations can manifest in some of the matrix atoms (i.e. Fe and Cr) surrounding the nanoparticle to be reconstructed in a location within the nanoparticle. As expected, these errantly placed atoms will influence the measurement of chemical composition of the nanoparticle(s) when conducting cluster analysis in IVAS. Some authors have suggested methods to remove Fe from the nanoparticle composition [176], while others publish the composition data as-measured [8,9], or publish both the "uncorrected" and "matrix corrected" compositions [59]. For ODS alloys, observations in archival literature indicate that smaller oxides tend to have non-stoichiometric chemistry, while larger oxides have a pyrochlore Y_2Ti_2O7 or orthorhombic Y_2TiO_5 crystal structure [124,130–134]. In this study, none of the Y:Ti or (Y+Ti):O ratios reflect either of these crystal structures, so there is no evidence to suggest the oxide nanoparticles are single crystals void of any Fe atoms. Therefore, all composition data for the nanoparticles in this thesis have been kept as-measured, without any composition altering. This approach is kept consistent throughout this work, enabling a "like-for-like" comparison between each data point and an evaluation of nanocluster evolution across different irradiation conditions, doses, and temperatures.

7.3.2 Reconstruction and Cluster Analysis in IVAS

One of the most critical parameters to define during the reconstruction of the sample data is the image compression factor (ICF). When using IVAS, the default value for the ICF is 1.65. In addition to the procedure outlined in Section 4.5.2, where an

effective ICF for each data set is selected, an additional iteration of cluster analysis was conducted for all specimens of the Fe-9%Cr ODS and HCM12A alloys using this default ICF value, while all other aspects of the cluster analysis were maintained consistent. Atom distribution maps showing clustering in Fe-9%Cr ODS for each iteration of reconstruction are shown in Figure 7.9 for the same sample with the voltage history in Figure 4.14. In the initial reconstruction using ICF = 1.65 (Figure 7.9a), clusters appear to be more horizontally elongated, particularly towards the outer extremes of the represented volume. This result is inconsistent with the observation of TEM-resolution nanoclusters [8] and in the archival literature [12,84,96,110], in which oxide nanoclusters tend to take a spherical shape. On the other hand, clusters in this latter iteration (Figure 7.9b) appear to be more consistently spherical in shape. The cluster "stretching" effect can be explained by the IVAS reconstruction algorithm, which limits the researcher to utilizing a single ICF value for a data set having an evolving collection voltage history. As the IVAS software is reconstructing the sample, it is attempting to reconcile the detector location of source ions and the prescribed shape of the original sample (as defined either by collection voltage, shank angle, or tip profile). Inevitably, these separate inputs will not match perfectly and the software reconciles these differences by locally varying the atomic density of the source atoms to most closely fit the inputs. These variations are most pronounced at the outer extremes of the represented volume, where the detector ion locations and the user-defined shape of the reconstruction are the most mis-matched.

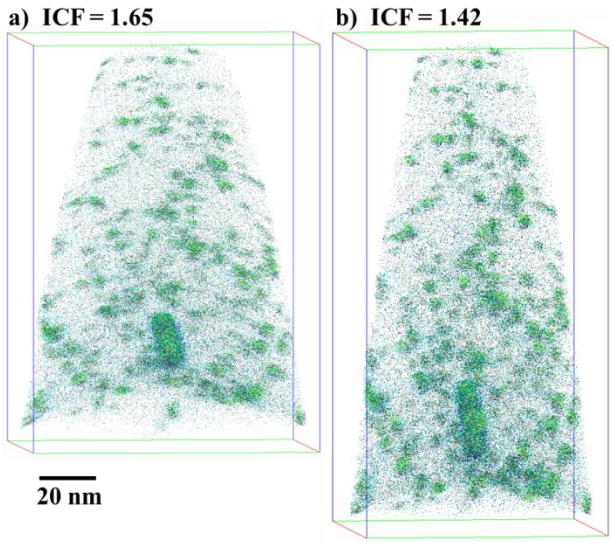

Figure 7.9 Atom distribution maps of Ti, TiO, O, YO, Y, FeO, and CrO atoms in an Fe-9%Cr ODS sample reconstructed with a) ICF = 1.65, and b) ICF = 1.42 selected via the effective voltage (Section 4.5.2).

The default ICF value of 1.65 is most accurate for a collection voltage of ~2800 V, which is well below the collection voltage history of all the samples collected in this study. As a result, the width of the data sets reconstructed using the default ICF tends to be overestimated (Figure 7.9), which then requires the software to overly "decompress" the atomic density (and thus the cluster dimensions) in the lateral direction. This effect is illustrated in Figure 7.10, where the effects of different ICF values on a given sample are illustrated. It is worth noting that selecting an effective ICF based on V_{eff} also does not produce a perfect reconstruction. Nevertheless, the effective ICF method outlined herein produces a more accurate reconstruction than the constant ICF method, with fewer clusters appearing elongated or stretched in any direction. Ideally, if the reconstruction software allowed variation of the ICF as a function of the voltage history (i.e. ICF evolves along with the voltage history during reconstruction), an even more reliable reconstruction of the original cluster geometry would likely result. However, this is not a trivial algorithm to implement within the IVAS software.

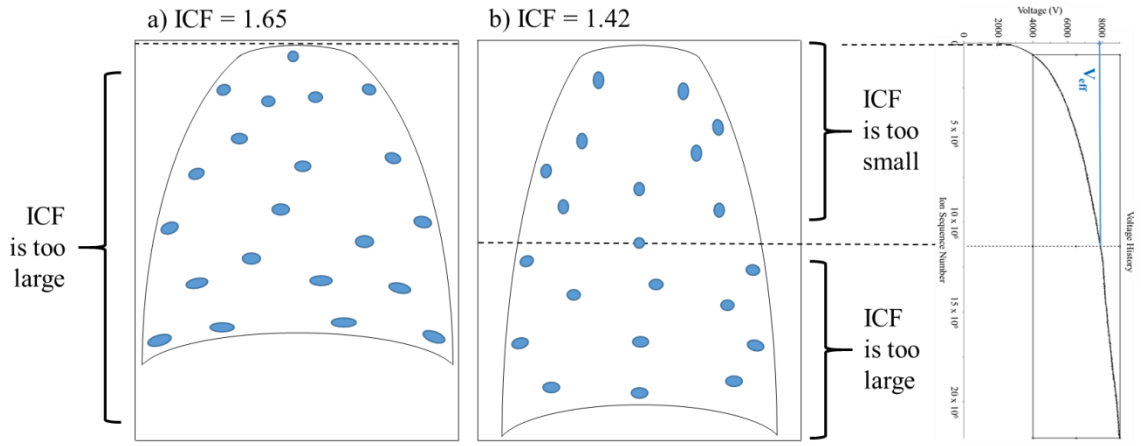

Figure 7.10 Simplified illustration of how selecting different ICF values will influence the reconstruction of clusters within a data set with larger overall ion counts, with ICF values of a) 1.65, and b) 1.42.

The resultant average Guinier diameter for each specimen condition for Fe-9%Cr ODS and HCM12A using ICF = 1.65 and using an "effective" ICF for each data set (Section 4.5.2) are listed in Table 7.1, with values after normalization also provided. Coupling the effective ICF reconstruction technique with normalization of the cluster size measurements (Section 5.2) provides a more credible assessment of the influence of each irradiation condition on the cluster sizes in both ODS and HCM12A. In specimens having data set sizes relatively evenly distributed over a wide span of ranged ions, the average cluster diameter changes very little. In specimens having a narrow range of data set sizes, with one exceptionally large or exceptionally small data set, the normalization changes the average cluster diameter more significantly. This effect is readily observed by comparing the oxide nanocluster diameter in the as-received ODS to that in the Fe^{2+} self-ion irradiated ODS at 3 dpa and 500°C. Using a fixed ICF and without normalization, the irradiation seemingly results in a statistically-significant cluster dissolution (diameters reduce from 5.96 ± 0.14 nm to 5.06 ± 0.13 nm). But using the effective ICF reconstruction technique with normalization to 20 million ions, the average cluster

diameter in the irradiated specimen (5.73± 0.11 nm) is now comparable to that in the as-received specimen (5.71 ± 0.09 nm) within measurement error. This suggests oxide nanoclusters do not dissolve, but rather are relatively stable upon self-ion irradiation up to 3 dpa. In the example just presented, the change from irradiation dissolution to irradiation stability is most considerably influenced by the normalization procedure. The combined effective ICF selection and normalization step thus enables a more reliable measurement of the oxide nanocluster irradiation evolution.

Table 7.1 Average cluster Guinier diameter measurements for two ICF selection approaches, then with normalization (± values are standard deviation of the mean).

ICF		1.65 (default)		Effective		Effective
Data set size		Not normalized		Not normalized		Normalized to 20 million
Material & cluster type	Irradiation conditions	# of clusters	Average Guinier diameter (nm)	# of clusters	Average Guinier diameter (nm)	Average Guinier diameter (nm)
Fe-9%Cr ODS Y-Ti-O nanoclusters	As-Received	486	5.96 ± 0.14	413	5.74 ± 0.09	5.71 ± 0.09
	Neutron (3 dpa, 500°C)	355	3.41 ± 0.09	169	4.84 ± 0.08	5.03 ± 0.08
	Proton (3 dpa, 500°C)	964	4.77 ± 0.06	975	4.83 ± 0.04	5.15 ± 0.05
	Fe^{2+} (3 dpa, 500°C)	232	5.06 ± 0.13	188	5.50 ± 0.11	5.73 ± 0.11
	Fe^{2+}(100 dpa, 500°C)	1578	5.35 ± 0.07	1474	5.47 ± 0.06	5.58 ± 0.06
	Fe^{2+}(50 dpa, 400°C)	93	4.38 ± 0.23	63	5.30 ± 0.24	5.41 ± 0.25
HCM12A Si-Mn-Ni-P nanoclusters	Neutron (3 dpa, 500°C)	335	3.51 ± 0.08	228	4.00 ± 0.05	4.36 ± 0.06
	Proton (3 dpa, 500°C)	73	9.22 ± 0.42	66	10.28 ± 0.43	9.63 ± 0.40
	Fe^{2+}(3 dpa, 500°C)	73	4.65 ± 0.15	75	5.41 ± 0.23	5.71 ± 0.25
HCM12A Cu-rich nanoclusters	Neutron (3 dpa, 500°C)	249	3.61 ± 0.06	213	4.02 ± 0.06	4.37 ± 0.07
	Proton (3 dpa, 500°C)	70	6.69 ± 0.29	66	7.26 ± 0.32	6.82 ± 0.30
	Fe^{2+}(3 dpa, 500°C)	100	5.27 ± 0.14	87	5.91 ± 0.13	6.18 ± 0.14

7.3.3 Archival Studies using APT

Atom probe tomography (APT) is increasingly being used to complement transmission electron microscopy (TEM) to characterize microstructures, particularly for nanofeatured materials containing phases below TEM resolution limits [6,8,9,24,25,40,59,86]. Local electrode atom probe (LEAP) tomographic cluster analysis algorithms provide an objective means to identify and measure the size and number density of these nanoscale phases [167]. However, there is a lack of standardized

methodology for quantifying average cluster size, which presents ambiguities and challenges when attempting to compare nanocluster morphology between different specimens and the results from different studies in archival literature.

In recent years, much effort has been placed on developing a standardized methodology for "best practices" of cluster analysis within the IVAS software, particularly by appropriate selection of analysis parameters d_{max} and N_{min} [171–173,175,200–203] (see Section 4.5.3). However, some aspects of the reconstruction process prior to the cluster analysis still lack standardization. In particular, there are currently no standardized guidelines for selecting the image compression factor (ICF) for each sample reconstruction, and no standard methods to quantify the average size of clusters when the available data sets vary in number and size.

Several studies have been found in archival literature which are aimed at characterizing the morphology of clusters with the alloys and evaluating the evolution of such clusters upon irradiation. A summary of the known publications for such studies on alloys similar to those in this study are listed in Table 7.2. For each study, a survey is conducted to itemize the respective information provided regarding how the reconstruction and cluster analysis parameters were determined. In most cases limited information is available.

Table 7.2 Summary of the APT analysis studies in archival literature and the provided information in each respective publication.

Material	Ref.	Number of Tips	Analysis Volume	Number of clusters	ICF selection	d_{max} selection	N_{min} selection	Normal-ization?
MA957	[86]	-	-	-	-	✓	-	-
9Cr ODS	[6]	-	-	✓	-	✓*	✓*	-
14YWT	[5]	-	✓	✓	-	✓	✓	-
14YT	[89]	-	-	-	-	-	-	-
14YWT	[8]	-	-	-	-	✓*	✓*	-
9Cr ODS	[9]	-	-	-	-	✓*	✓*	-
18Cr ODS	[59]	-	-	-	-	✓	✓	-
MA957	[102]	-	-	-	-	✓*	✓*	-
12YWT	[105]	-	-	-	-	✓*	-	-
14LMT	[107]	-	-	-	-	✓	✓	-
Eurofer 97 ODS	[67,114]	-	-	-	-	✓*	✓*	-
Eurofer 97 ODS	[115]	-	-	-	-	✓*	✓*	-
Eurofer 97 ODS	[116]	-	-	-	-	✓*	✓*	-
13.5Cr ODS	[116]	-	-	-	-	✓*	✓*	-
Eurofer 97 ODS	[122]	-	-	-	-	-	-	-
Fe-Cr alloys	[31]	-	-	-	-	✓	✓	✓
T91, HCM12A, HT9	[204]	-	-	✓	-	-	-	-
HCM12A	[24]	-	-	✓	-	✓	✓	-

*Used the same values for all data sets.

First, the majority of these studies do not provide any information about the quantity of samples analyzed, nor the total analysis volume considered. It has been shown how both factors will influence the relative confidence one may have in the results. For example, the ODS alloy is this study exhibits evidence of an inhomogeneous distribution of oxide nanoclusters (Section 5.2.1). As a result, multiple tips and a higher analysis volume is desirable to achieve more statistical confidence in the results. Similarly, only a handful of the publications in Table 7.2 identify the number of clusters measured in achieving the results. This is also an important consideration when establishing statistical confidence in such measurements. It is not the author's intent to suggest a lack of confidence in each of the studies in Table 7.2, but merely to point out the information is not available in the publication, so it is difficult to compare results of those studies to the results herein.

Next, it is evident that none of these studies have published any description about how the ICF for each reconstruction was selected. It has been shown in Section 7.3.2 how this factor can influence the end result of the nanocluster size measurements, and how this factor should be selected independently for each data set. Since no information is provided for the studies in Table 7.2, it is possible many of these studies are simply using the default ICF value of 1.65 in IVAS. However, this is only speculation, as no additional information is available. Regardless, it is difficult to be certain of an "apples-to-apples" comparison between the results of this thesis to those from an archival study in which a different method of reconstruction was potentially used.

Furthermore, each study in literature provides no information about any means for how the measured cluster sizes are compared between different sizes of data sets. It is

shown in Section 5.2.1 how the size of the data set may also influence the measured size of the clusters, making it potentially misleading to compare clusters measured from one small data set to those measured from a different larger data set. On a different note, one study by Bachav, et at. [31] does acknowledge the influence of the magnification effect in measuring Cr-rich α' clusters due to the varying evaporation fields of Cr and the Fe matrix atoms and takes mitigating steps to ensure cluster size comparisons are still more representative of reality.

Finally, as previously discussed, more effort has recently been placed on the selection of d_{max} and N_{min} for cluster analysis using the maximum separation method. As a result, most publications are providing some indication of how these values were determined and sometimes providing the exact values in the manuscripts. However, many of these studies also indicate the same values of d_{max} and N_{min} have been used for all data sets and specimens studied (indicated by an asterisk in Table 7.2). However, it is shown in Section 4.5.3 how these values should be determined for each individual data set, and certainly for each specimen. The ramifications of this are most evident in the APT data for the Fe-9%Cr ODS alloy in this thesis. In comparing the results across Fe^{2+}, proton, and neutron irradiation to a common dose of 3 dpa at 500°C, the APT results show notable differences in nanocluster enrichment and matrix chemistry between each condition studied (Table 5.5 and Table 5.4, respectively). The optimized selection of d_{max} for cluster analysis in the LEAP data sets (per the procedure in Section 4.5.3) for each condition also provides a cursory indication of the differences in the clustering of the oxide elements. In the as-received ODS data sets, the objective selections for d_{max} ranged from 0.7 to 0.9 nm. Meanwhile, d_{max} selections for Fe^{2+}-, proton-, and neutron-irradiated

specimens were 0.75-0.9 nm, 0.70-0.85 nm, and 0.65-0.70 nm, respectively. A comparison of these figures with the relative average enrichment (f_{en}^{i}) and the matrix compositions for Y, Ti, and O in these specimens is illustrated in Figure 7.11. The most dramatic change in the optimized d_{max} parameters occurs for the neutron-irradiated specimens. Correspondingly, the most dramatic reduction of cluster enrichment and increase in matrix composition of Y, Ti, and O also occurs in the neutron-irradiated specimen.

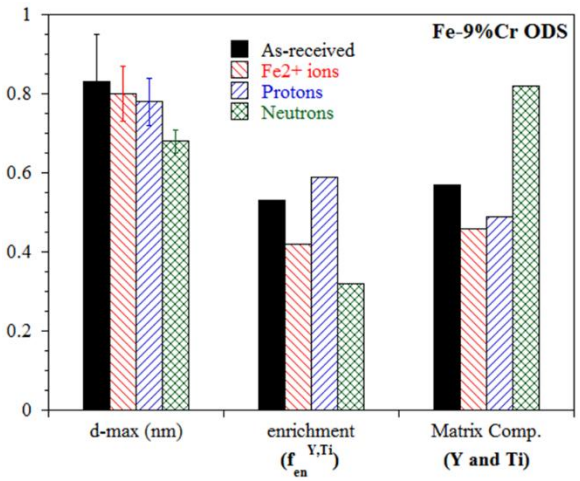

Figure 7.11 Comparison of optimized dmax values, solute enrichment of Y and Ti and clusters, and the matrix composition of Y and Ti in Fe-9%Cr ODS in the as-received specimen and after each respective irradiation to 3 dpa at 500°C.

The evolution of solutes migrating between the matrix and the nanoclusters within the matrix clearly has an influence on the resulting optimized d_{max} required for cluster analysis. This principle is further illustrated in Figure 7.12 showing two different plots generated by IVAS showing how the resulting cluster count depends on the selection of d_{max}. For specimens which have high solute enrichment in the clusters, there is a negligible second "hump" in the data plot (Figure 7.12a), indicating low solute content in the matrix is present. On the other hand, for specimens with higher matrix content, a

bimodal distribution is present (Figure 7.12b). In this latter case, the appropriate d_{max} is selected at the lowest point between these two peaks [175]. If the selected value for d_{max} is too large, additional clusters in the matrix will be spuriously identified, thus overinflating the number density of clusters and potentially influencing the measured average size. On this basis, it is further emphasized that optimization of d_{max} (and N_{min}) is necessary for every sample and data set. It is not always appropriate to use the same d_{max} and N_{min} across all conditions for experimental control, as this may counter-intuitively lead to spurious measurement or detection of clusters.

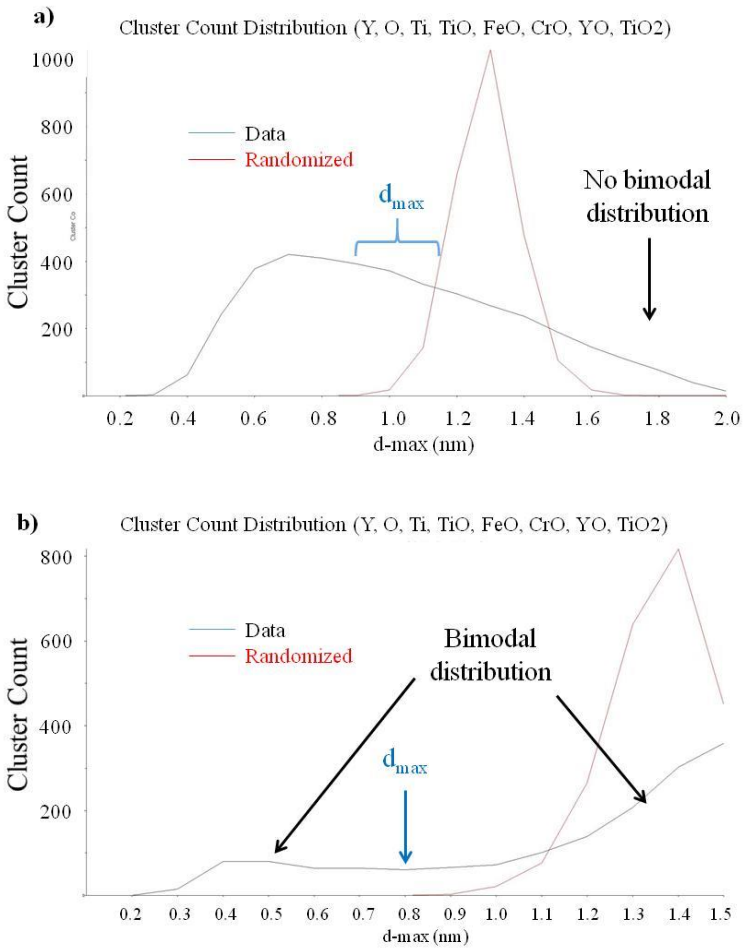

Figure 7.12 Contrasting "Cluster Count Distribution Analysis" results with a) a single mode distribution, and b) a bimodal distribution. Appropriate selection for d_{max} is indicated.

7.3.4 Summary and Recommendations for APT Cluster Analysis

In light of the limited information provided in each of the publications in Table 7.2, one should use some discernment in analyzing each set of respective results and comparing them to the results of this thesis.

To carry out credible APT reconstruction and cluster analysis, it is recommended to use the following methodology to analyze APT data and compare the average cluster size amongst multiple specimens:

1) Collect LEAP data from as many sample tips as possible for each specimen (ideally > 3 samples) and include data from a variety of data set sizes.
2) For the reconstruction of each data set in IVAS, establish the "effective" collection voltage, V_{eff}, at or near the midpoint of the ion collection (similar to Figure 4.15). Use V_{eff} to select the "effective" ICF, for reconstruction (Figure 4.20 as a guideline).
3) Reconstruct each sample in "Voltage" mode for data consisting of gradually evolving voltage history. Avoid sample regions where major fracture events have occurred as these events create localized distortion of the reconstruction data. Consider using "Shank" or "Tip profile" mode for larger samples to ensure the reconstruction most accurately matches the expected tip geometry. Regardless of method, use the "effective" ICF determined in step 2.
4) Confirm the ranging of all peaks in each mass-to-charge ratio histogram are consistent across all data sets for comparison.

5) For an initial estimate of the number of clusters in each data set, construct isosurfaces using the clustering elements in question. Ensure these isosurfaces visually correspond to visible clusters in the reconstruction data.
6) Use the cluster analysis module in IVAS to formally analyze the cluster morphology in the sample. For the selection of the analysis parameters, d_{max} and N_{min}, follow the procedure prescribed by Williams, et al. [173], in which the selected d_{max} yields a minimum number of counted clusters by the analysis. For confidence, confirm the total number of clusters identified through this process is comparable to the total number identified via isosurfaces in step 5.
7) Calculate the average cluster diameter from each data set using Eq. 4.10 and 4.11 (Section 4.5.3) and plot the trend of cluster diameter relative to the number of ranged ions for each data set (similar to Figure 5.22).
8) Normalize the average cluster diameter for each specimen by interpolating (or extrapolating) to a common data set size to create a more dependable comparison of average cluster diameter from one specimen to another.

Furthermore, the following information is recommended for inclusion in future publications involving cluster analysis and diameter measurements, in order to facilitate relevant data comparison between studies by different researchers:

- The method for selecting the ICF for each data set reconstruction.
- The overall number of clusters measured for each specimen and the relative certainty of the mean value reported.
- The method for normalizing data to ensure a robust comparison may be drawn, such as the procedure outlined in this study.

7.4 Nanocluster Evolution

One of the objectives of this study is to evaluate the effects of dose rate and cascade morphology on nanocluster evolution in a model Fe-9%Cr ODS steel and the F-M alloys HCM12A and HT9. Complimentary irradiation types using neutrons, protons, and Fe^{2+} self-ions enable a meaningful investigation. The following sections provide a qualitative description of the measured results for nanocluster evolution in Fe-9%Cr ODS and the commercial F-M alloys HCM12A and HT9, respectively.

7.4.1 ODS Oxides

After applying the procedures to normalize the nanocluster size measurements and accounting for the adjusted volume fraction and number density (Section 5.2.1), one important trend to recognize in the ODS alloy is the evolution of nanocluster size and number density over increasing dose for both Fe^{2+} and proton irradiation (Figure 5.25 and Table 5.5). In both cases, average nanocluster size decreases while number density increases with dose above 1 dpa. The inverse relationship between size and number density has been observed elsewhere in literature [72,84,88,101], and is akin to inverse Ostwald ripening, which has been previously described in the context of ion beam-induced size refinement of embedded metallic nanoparticles [58,75,77,78,205], an emerging research area in nanoelectronics. Through inverse Ostwald ripening, smaller nanoclusters nucleate and grow at the expense of larger nanoclusters, due to the competing mechanisms of ballistic dissolution and diffusion-driven nanocluster growth, with the net result being a reduced average cluster size and increased number density. Finally, it is observed that upon both Fe^{2+} and proton irradiation, the average sizes of the

oxide nanoclusters appear to asymptotically approach steady-states at doses >3 dpa, consistent with previous modeling [57,74,79] and experimental [5,79,84,107,206] efforts.

7.4.2 G-phase and Cu-rich clusters

A common trait in the irradiated HCM12A specimens is the Si-Mn-Ni-rich clusters and Cu-rich clusters are located adjacent to one another. Jiao, et. al [24,25] and Wharry et. al [23] also observed similar behavior in HCM12A and T91, respectively, after irradiation with protons at 400°C and 500°C. However, it is interesting to note after only 1 dpa of proton-irradiation of HCM12A, only Cu-rich clusters are present. This result suggests that Cu-rich clusters first nucleate homogeneously, followed by heterogeneous nucleation of Si-Mn-Ni-P clusters at or near the interface of the Cu-rich clusters and the surrounding matrix. Anderoglu, et. al [20] and Sencer, et. al [18] have also observed evidence suggesting that Si-Mn-Ni clusters nucleate heterogeneously. Additionally, Allen, et. al [16] observed a similar result in HCM12A and estimated the incubation time for Si-Mn-Ni-rich clusters to be between ~1-3 dpa for proton irradiated specimens.

Unlike HCM12A, the HT9 alloy has very low Cu content, and thus none of the irradiated specimens contain any Cu-rich clusters. Consequently, Si-Mn-Ni clusters will either heterogeneously nucleate on alternative interfaces (i.e. dislocations and grain boundaries) or they can nucleate homogeneously within the matrix, which is generally less favorable. However, upon Fe^{2+} irradiation, no clusters are observed after 3 dpa. This result may seem counterintuitive, but is likely related to the relative incubation period for nucleation of Si-Mn-Ni clusters for each irradiation. Contrary to proton-irradiation, the same Allen, et al. [16] study observed an incubation period for Si-Mn-Ni-rich clusters in

HCM12A under self-ion irradiation to be ~7 dpa. The contrast in incubation dose between proton and self-ion irradiations is consistent with the observed low dose Si-Mn-Ni clustering in this study. This discrepancy in the incubation period between Fe^{2+} and proton irradiation is unclear. Nucleation and growth of Si-Mn-Ni clusters are limited by diffusion, so the incubation period is likely related to the relative duration of each of the irradiations. With Fe^{2+} irradiation to 3 dpa, the total irradiation time is only ~4 hours, but is extended to ~9 hours when irradiated to 7 dpa. This increase in duration at which the specimens are held at an elevated temperature enables more solutes to thermally diffuse towards nuclei.

At a higher dose of 100 dpa with Fe^{2+} irradiation, there are no clusters present in either HCM12A or HT9. This result is somewhat inconsistent with the results of Jiao, et. al [25], in which Fe^{2+} irradiation of HCM12A to 100 dpa at 500°C induced clusters with an average radius of 3.9 ± 0.1. However, in the Jiao study, only 2 Si-Mn-Ni clusters and only 19 Cu-rich clusters are identified, with evidence that these clusters formed on grain boundaries, potentially influenced by radiation induced segregation [25]. Although no matrix clusters were found in our study, similar grain boundary segregation was observed in both HCM12A and HT9 after 100 dpa (Figure 5.27 and Figure 5.29). The explanation for clustering in HCM12A following self-ion irradiation to 3 dpa, but not at 100 dpa is not clear. One possible explanation may involve the balance of clustering and radiation-induced segregation to sinks such as grain boundaries, dislocations, or irradiation-induced dislocation loops. At low dose, matrix solutes are readily available to cluster, and likely also begin to segregate towards other sinks. Over longer-term irradiation, it is possible that segregation to other sinks is more favorable due to the higher dose rate of self-ion

irradiation. As more solutes segregate towards other sinks, the matrix is depleted of solute, thus swinging the balance away from favoring clustering, leading to dissolution of the clusters.

7.4.3 α' precipitates

Neutrons are the only irradiating particles that have produced any Cr-rich clusters in both HCM12A and HT9. These alloys contain 10.5 and 12.1 wt% Cr, respectively, which is above the ~9% solubility limit of Cr in α-Fe. In these materials, then, if given enough energy and time, Cr will partially precipitate out of solution. For each of the irradiations conducted in this study, the temperature was kept consistent at 500°C. Therefore, the thermal diffusion rates of Cr would have been consistent across all experiments. Approximate irradiation times were 4 hours, 3.5 days and ~1 year for the self-ion, proton, and neutron irradiations, respectively. Thus, Cr clustering only in the neutron-irradiated specimens may be largely influenced by thermal aging at 500°C over ~1 year.

According to various models summarized in [20], the prediction of α-α' separation is typically around 450-475°C. To the author's best knowledge, irradiation-induced α' separation has only previously been observed in HT9 up to temperatures of 466°C [20]. However, Mathon et al. [165] have also found the kinetics of precipitation are further increased by irradiation over the kinetics of purely thermal aging, supporting the possibility of irradiation-induced precipitation at 500°C. In addition, Mathon et al. also highlights the how increased solute content (such as Mo and Ni) may also influence α-α’ phase separation. The temperature dilation theory of Martin [60] also provides an explanation for why α' precipitation is not observed upon Fe^{2+} or proton irradiation. The

higher dose rate of the charged particle irradiations results in a higher configurational entropy of the system, increasing the solubility limit of Cr in the surrounding Fe matrix.

7.5 Sensitivity of the Advanced NHM Model

The advanced NHM model introduced in this thesis involves a number of parameters which are entered as inputs by the analyst. Each of these parameters require some prior knowledge about the target alloy or the specific irradiation conditions present. Using these parameters, the model conducts a stepwise calculation over finite increments of time, simulating accumulating dose. It has been repeatedly shown in Chapter 6 how the model predicts the evolution of the average size of the nanoclusters asymptotically toward a stable cluster size. Since the desired outcome in developing NFAs such ODS alloys is long-term nanocluster stability, the model calculation stable cluster size, d_{ss}, is one of the key outputs of the routine. Since several input parameters are used to generate this output (Table 7.3), it follows if any one of these parameters are altered, the output is likely to be affected as well.

Table 7.3 Summary of input parameters for the advanced NHM model.

Parameter, P	Definition	Units
K	Dose rate	dpa/s
a	Lattice parameter	nm
$\bar{T}$	Transferred energy to primary knock-on atom	eV
f	Disordering efficiency	-
r	Initial average cluster radius (at 0 dpa)	nm
k^2	Alloy sink strength	cm^{-2}
E_v^f	Vacancy formation energy	eV
E_v^m	Vacancy migration energy	eV
D_i^{th}	Solute thermal diffusion rate	cm^2/s
n_{nc}	Nanocluster number density	m^{-3}
p_i		-
Ci	Solute concentration in target alloy (non-carbide)	-
T	Irradiation temperature	K

To gain a better understanding of how each of these parameters influence the NHM model calculation, a sensitivity analysis is conducted to identify the relative influence of each input parameter, *P*, and identify those parameters with the greatest sensitivity. The sensitivity of the model is specified as the derivative of the output cluster stable size as a function of the input parameter ($\delta d_{ss}/dP$). To simplify the calculation for sensitivity, the approach taken is to vary the input parameter about its reference value and solve for the sensitivity using:

$$\frac{\delta d}{\delta P} = \frac{d'_{ss} - d_{ss}^{ref}}{P' - P^{ref}} \tag{7.1}$$

where d_{ss}^{ref} is the calculated steady-state cluster diameter when the reference input parameter, P^{ref}, is used. Similarly, with P' as the varied parameter, d'_{ss} is the new steady-state cluster diameter when P' is used in the calculation. It is possible to express the

sensitivity as a significance, which gives a more straightforward comparison of the relative influence of each input variable. The significance, S_P^d, is determined by:

$$S_P^d = \frac{d'_{ss} - d_{ss}^{ref}}{P' - P^{ref}} \cdot \frac{P^{ref}}{d_{ss}^{ref}} \tag{7.2}$$

Using this calculation, the variables which exhibit the highest significance are those to which the advanced NHM model is most sensitive.

The significance is calculated for each input variable using the NHM model for proton-irradiation on the Fe-9%Cr ODS alloy at 500°C. The predicted steady-state cluster diameter for this set of conditions is $d_{ss}^{ref} = 5.33\ nm$. The input for each variable was altered individually by entering values higher than the reference value for the parameter. With this P' input, the revised steady-state cluster diameter is recorded and the significance of the varied input is calculated. The significance results for each parameter are provided in Table 7.4 and illustrated in Figure 7.13. The direction of the significance represents the directional influence on the steady-state cluster size. Variables with a negative significance value indicates an increase in the variable value will result in a decrease in the predicted steady-state cluster size.

Table 7.4 Significance of varied input parameters for the NHM model.

Parameter, P	Units	P^{ref}	P'	d'_{ss} (nm)	Significance
K	dpa/s	1.2 x 10^{-5}	5 x 10^{-5}	5.33	0
a	nm	0.286	0.35	5.30	-0.025
$\bar{T}$	eV	200	500	5.01	-0.040
f	-	0.15	0.25	4.74	-0.166
r	nm	2.86	3.50	5.33	0
k^2	cm^{-2}	2.7 x 10^{-12}	5.12 x 10^{-12}	4.34	-0.208
E_v^f	eV	2.2	2.3	6.34	4.169
E_v^m	eV	0.68	0.9	6.66	0.771
D_i^{th}	cm^2/s	3.88 x 10^{-21}	3.88 x 10^{-20}	6.55	0.025
n_{nc}	m^{-3}	443 x 10^{21}	600 x 10^{21}	4.76	-0.302
p_i	-	0.0873	0.1	5.05	-0.361
C_i	-	0.0062	0.01	6.43	0.332
T	K	773	873	5.63	0.435

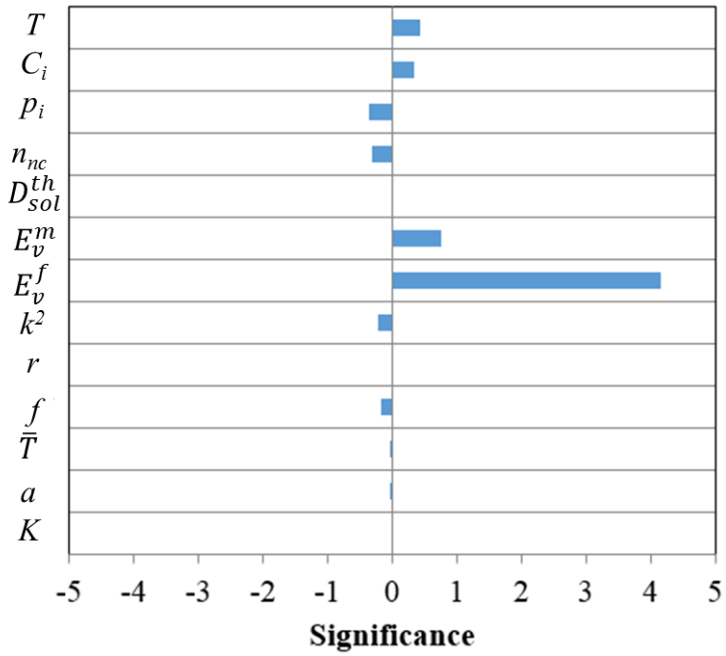

Figure 7.13 Significance of input parameter in the advanced NHM on the outcome of the predicted stable size of nanoclusters.

Some interesting observations are made from this simple exercise. First, the initial cluster size does not have any influence on the irradiation-induced predicted stable cluster size. The model predicts a stable size based on the balance of the other input parameters and will predict evolution toward this stable size, regardless of the initial starting point. This finding is notable because it suggests that in ODS alloy design and development, beginning with an ultrafine oxide nanoparticle distribution may not be necessary if other alloy and irradiation parameters are chosen so as to lead to the desired steady-state particle size.

Similarly, the steady-state particle size is also independent of the irradiation dose rate, although it is dependent on other aspects of the irradiation conditions. This significance seems counterintuitive, and is different than the Martin model (Eq. 6.27). In the NHM model, the dose rate (K) appears in the numerator of each term on the right hand side of Eq. 6.1. In the first term, the flux (ϕ) is directly proportional to K (Section 2.4.6). In the third and fourth terms of Eq. 6.1, the dose rate is proportional to the radiation-enhanced diffusion rate (Eq. 6.4 and 6.7). For the steady-state condition, the influence of these terms are directly offsetting and the dose rate does not directly influence the steady-state cluster size. Therefore, the differences in steady-state cluster size due to different irradiating particle is determined only by its corresponding cascade morphology and efficiency in the NHM model (ψ in Eq. 6.1). The Martin theory takes a different approach in its treatment of the flux (Eq. 6.27). Its impact will be further discussed in Section 7.6.2.

Furthermore, the model is only minutely sensitive to $\bar{T}$, the transferred energy to the primary knock-on atom. The value for this parameter is based on literature estimates

for all three irradiating particle in consideration. In the case of neutron irradiation, a single value for $\bar{T}$ is used for all NHM model calculations, reflecting an assumption of a mono-energetic spectrum of neutron irradiation. The author recognizes the neutron spectrum is likely to not be mono-energetic in a nuclear reactor environment. Therefore, the value for $\bar{T}$ (Table 2.1) used for the neutron irradiation NHM calculations is taken as an estimated average.

The two parameters with the most significance in the NHM model (Figure 7.12) are the energies for vacancy formation (E_v^f) and vacancy migration (E_v^m), respectively. Both terms directly influence the calculation for the radiation-enhanced diffusion of the respective solutes of interest (Eq. 6.5 and Eq. 6.18). Since these values are retrieved from literature, it is important to have reasonable confidence in these numbers, particularly since just a small increase in the formation energy (from 2.2 eV to 2.3 eV) results in a relative large increase in steady-state diameter (from 5.33 nm to 6.34 nm). However, in the context of this study, if an alternate vacancy formation energy is used in the NHM model, different fitted values for f_i and D_i^{th} would result, which would be carried over to the HCM12A fitting procedure, and so on. The model doesn't become invalid, but the resulting fitted values would be different. This fact emphasizes the need for clear communication of the values used for each parameter, as well as underscores the importance of benchmarking the fitting parameters against a robust experimental data set such as that presented herein. Subsequently, consistent input and fitting parameter values may be used for studies of similar alloys systems (i.e. b.c.c. Fe) to enable a direct comparison between the results.

7.6 Advanced NHM Model - Potential as a Predictive Tool

One of the objectives of the modeling effort in this thesis is to provide the framework for developing an adaptive model applicable to any b.c.c. Fe-based alloy (and other systems) for predicting radiation-induced nanocluster evolution. Ideally, the model may be used in the future as a development tool for the morphology or elemental tailoring of alloys to maximize radiation resistance. It is believed the model (in its current state) has the opportunity to serve this objective in the following capacities: 1) as a means to estimate the temperature shift required when conducting high dose irradiations (i.e. charged particles) to emulate the irradiation-induced nanocluster evolution with low dose irradiations (i.e. neutron irradiation), 2) as a means to estimate optimum as-manufactured cluster morphology to maximize long-term irradiation resistance, 3) as a means to estimate the individual clustering behavior of specific solutes in an alloy, and 4) a means to conduct similar cluster evolution analysis on other systems based on elements other than Fe. The following sections will review how the current model emulates cluster evolution found in archival literature, then outline the potential application of the advanced NHM model developed in the context of each of these goals.

7.6.1 Comparison of Model with Literature Results

As discussed in Section 7.5.2, most studies in archival literature provide basic information regarding the results of their respective APT analyses, which is certainly valid and useful to the greater research community. However, most of these studies did not publish all the information necessary to use the advanced NHM model introduced in this thesis. In most cases, the following information is generally not available: a) specific information about the sink strength of the material, b) the fraction of the clusters which

are solute items (variable *p* in Eq. 6.1), and c) the total composition of solutes not included in any other secondary phases such as carbide precipitates (variable *C* in Eq. 6.1). On some occasions, the respective compositions of the clusters and the matrix are provided for conditions before and after irradiation. In such cases, the values of *p* and *C* may be estimated, where *p* is approximated as the composition of the solutes in the clusters, and *C* is calculated using [57]:

$$C = \frac{4}{3}\pi r^3 np + c \tag{7.1}$$

in which *r* is the average cluster radius, *n* is the number density of clusters, and *c* is the matrix composition of the solutes.

One such study in which all of the above information is available was published by Lescoat, et al. [59], evaluating the stability of oxide nanoclusters upon Fe^+ ion irradiation up to 150 dpa at 500°C in an Fe-18%Cr ODS alloy. In this study, the oxides were observed to coarsen as a result of the irradiation, and this effect is attributed to radiation-induced Ostwald ripening, considering the influence of both the ballistic effects of the irradiation and the growth kinetics due to radiation-enhanced diffusion. The parameters provided from this study are used as inputs in the advanced NHM model developed for this thesis (Table 7.5) to confirm if the model predicts a similar result to that measured.

Table 7.5 Initial parameters in the NHM model setup for Fe-18%Cr ODS irradiated in Ref. [59]**.**

Parameter	Fe^{2+} irradiation	Source
$\phi = K \cdot 10^{14}$	6.4 x 10^{11}	K = 6.4 x 10^{-3} dpa/s [59]
N (atoms/nm^3)	85.2	b.c.c. Fe
l (nm)	6.8	Table 2.1
f	0.039	Table 6.13
k^2 (cm^{-2})	4.3 x 10^{11}	[59] and Eq. 6.7
T (K)	773 K (500°C)	[59]
D_{sol}^{th}(cm^2/s)*	3.88 x 10^{-21}	fitted
E_v^f (eV)	2.2	[59]
E_v^m (eV)	0.68	[183]
Calculated D^{irr}(cm^2/s)	1.75 x 10^{-14}	Eq. 6.2
r (nm)	1.50	[59]
n (m^{-3})	2.3 x 10^{23}	[59]
$p_{Y,Ti}$	0.079	[59]
$C_{Y,Ti}$	0.0040	[59]
Δt (s)	90	-

* Used as a fitting parameter

Since the relevant solutes in this alloy (Y and Ti) are the same as those in the Fe-9%Cr ODS alloy of this thesis, the values for the disordering efficiency, f, and the thermal diffusion, D_{sol}^{th}, are initially kept consistent (Table 7.5). A plot of this initial NHM prediction of the cluster evolution compared to the published oxide measurements in [59] is provided in Figure 7.14 (solid line). As with all the calculations in Chapter 6, the predicted average cluster size quickly approaches a steady state value at low dose. The model successfully predicts the direction of the cluster evolution, resulting in an increase in the average size of the clusters. However, the model overestimates the size of

the measured nanoclusters after both 75 and 150 dpa. As a second iteration, the value of the thermal diffusion, D_{sol}^{th}, is reduced by a factor of 4 to a value of 9.71 x 10^{-22} cm^2/s and is plotted in Figure 7.14 (dashed line). This prediction is a much closer match to the cluster size measurements at 150 dpa.

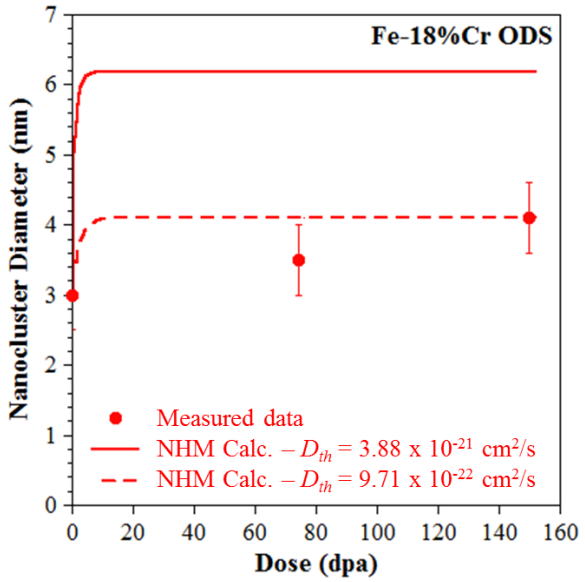

Figure 7.14 Calculations using the NHM model for Fe-18%Cr compared to measured cluster size data in Ref. [59].

The reason for a reduced D_{sol}^{th} value providing a better fit may lie in the nature of the existing oxide nanoclusters of Lescoat's alloy. In Section 6.5.3, the values for each fitted D_{sol}^{th} are hypothesized as a means to characterize the relative affinity for the solutes to diffuse towards the clusters. Since the average initial cluster size in the Fe-18%Cr ODS alloy in the Lescoat, et al. study (3.0 nm) are smaller than those in the Fe-9%Cr ODS alloy of this thesis (5.71 nm), it is plausible that solutes Y and Ti have a slightly weaker affinity for diffusion towards smaller ODS clusters. Larger clusters are also likely to be have higher affinity for solutes due to their reduced surface energy, which results from their larger radius, reducing their respective wetting angle. Observations in the

archival literature also suggest that smaller oxides tend to be more coherent than larger oxides; smaller oxides tend to have non-stoichiometric chemistry with Y:Ti ratio ≈ 0.5 [9,13], while larger oxides trend toward a Y:Ti ≈ 1.3 [9,13] with a pyrochlore $Y_2Ti_2O_7$ or orthorhombic Y_2TiO_5 structure [124,130–134]. As a result, larger clusters with a more incoherent structure may provide slightly more impetus for the Y and Ti solutes to migrate towards the clusters.

Regardless, based on the exercise using the data from the Lescoat, et al. experiment [59], it may be concluded that the advanced NHM model is capable of predicting either oxide dissolution or growth, depending on the target alloy and the irradiation conditions. However, it appears the parameters f and D_{sol}^{th} fitted from one alloy (i.e. Fe-9%Cr ODS) may not necessarily be directly transferred to another alloy. Instead, the advanced NHM alloy likely requires a baseline set of experimental data to calibrate the fitted values for D_{sol}^{th}, and possibly for f as well. Even with this limitation, it is believed the advanced NHM model still offers some predictive capability, which will be outlined in the next sections.

7.6.2 Temperature Shift

Mansur [187,188] theorized a temperature shift is necessary in order to produce consistent defect cluster microstructures when the irradiation dose rate increases. The desired microstructures are bound by two mechanisms of point defect loss: 1) mutual recombination in the matrix, and 2) diffusion to sinks. The temperature shift for recombination-dominant and diffusion-dominant regimes is calculated for a reference condition of 500°C at 10^{-7} dpa/sec (Figure 7.15), conditions comparable to the neutron irradiation experiment in the present study. The vacancy migration and formation

energies are taken to be 0.68 eV [183] and 2.20 eV [59] , respectively, for a b.c.c. Fe-9%Cr steel. But since the temperature is fixed at both dose rates in the present irradiation experiments, the temperature shift curve must have a slope ~0 in order for the proton- and neutron-irradiated void and dislocation loop microstructures to be consistent with one another, as observed in this work. It thus follows that void and loop nucleation and growth are recombination-driven processes (solid purple line, Figure 7.15), so their evolution will be relatively independent of dose rate at a fixed temperature.

Conversely, the evolution of oxide, Si-Ni-Mn-rich, and Cu-rich nanoclusters are all inconsistent between neutron and the charged particle irradiations conducted for this thesis, suggesting that cluster formation and dissolution may not simply be recombination-driven processes. Multiple authors [57,60,74] have hypothesized that oxide nanocluster stability is governed by a balance between two competing effects: 1) ballistic dissolution due to irradiation damage cascades, and 2) thermal diffusion driving solute atoms to re-form into clusters (i.e. Ostwald ripening). The combination of these effects is manifested in the rate of radiation-enhanced diffusion (RED) of solutes. Since the increased solute mobility due to the irradiation-induced vacancy supersaturation is a primary mechanism of solute diffusion in the matrix [42,60], it follows that the highest dose rate will induce the highest rate of RED for vacancy diffusing solutes (per Eq. 6.5 and Eq. 6.2). From this, Martin [60] developed a model to describe nanocluster evolution in the presence of irradiation with differing flux and dose rates. One of the key conclusions from Martin's model is the damage effects resulting from increased irradiation flux lead to an increase in the configurational entropy of the system, which can be equated to a rise in temperature of the system. Consequentially, this theory

suggests that higher dose rate irradiations would need to be conducted at lower temperatures than lower dose rate irradiations in order to attain consistent nanocluster morphologies.

Using Martin's theory, comparable temperature shift estimates are calculated using the same approach as in Section 6.5.1.1 for each type of irradiating particles (neutrons, protons, Fe^{2+} ions) at a range of dose rates. Each irradiating particle follows a slightly different path due to the relative disordering efficiencies for each type of irradiation. The model suggests an increase in downward temperature shift is required as the dose rate increases for all three irradiating particles.

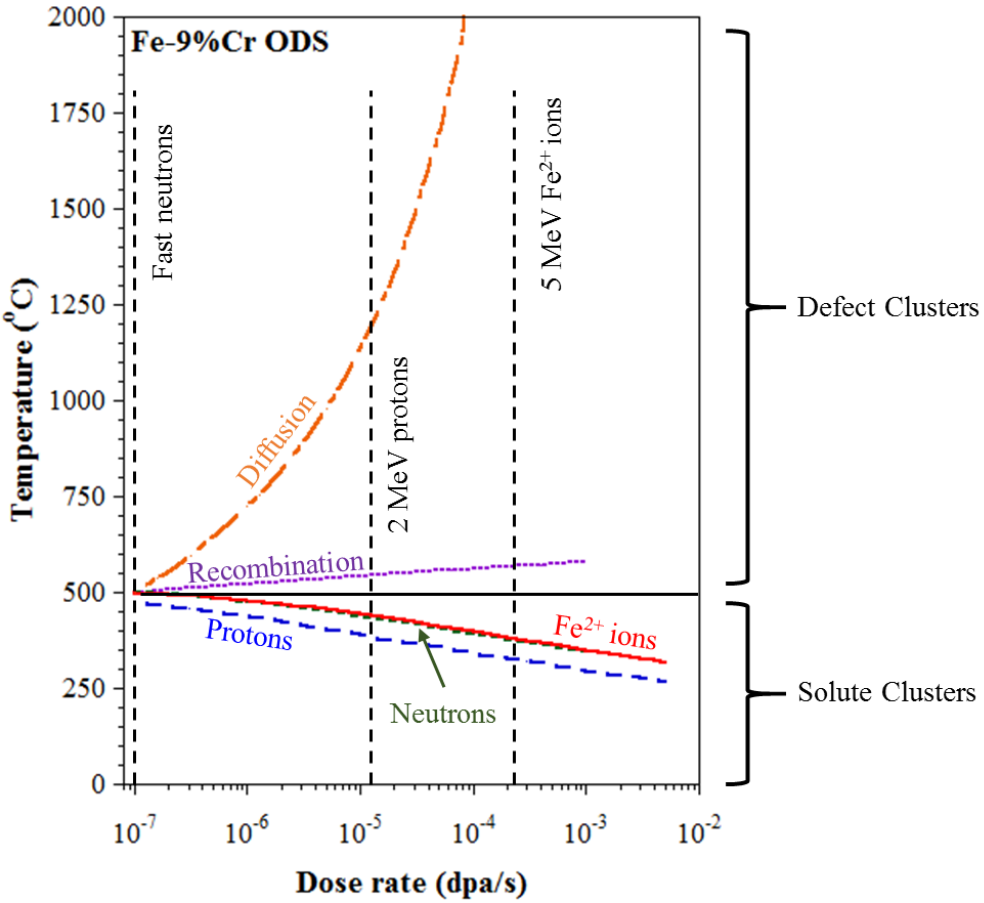

Figure 7.15 Comparison of calculated temperature shifts required for defect clusters with diffusion-driven (dashed orange line) and recombination-driven (solid

purple line) mechanisms [187,188] **and for solute clusters depending on the respective irradiating particles** [60] **in Fe-9%Cr ODS.**

The ramifications of these separate temperature shifts for defect clusters and solute clusters are significant in the context of using charged particle irradiations (at higher dose rates) to emulate the irradiation effects of neutron irradiation on the microstructure. It suggests multiple charged particle irradiation experiments at varying temperatures are required to fully emulate and verify the microstructural evolution of a nanofeatured alloy containing solute nanoclusters. For example, a high dose rate irradiation is required at a higher temperature to isolate and emulate defect cluster (loops and voids) evolution by controlling the concentration of vacancies as defined by the Mansur theory. Another high dose rate irradiation is required at a lower temperature to isolate and emulate solute cluster evolution by controlling the RED of solutes as defined by the Martin theory.

At first glance, these opposing temperature shifts seem counterintuitive, as the common practice for higher dose rate irradiation experiments currently follow the Mansur theology. However, it is important to recognize the Mansur theory is developed in the context of defect clusters (i.e. voids) only. The basis of Mansur's theory is to equate the concentration of vacancies within the microstructure so that formation of defect (i.e. vacancy) clusters will be comparable, despite differences in irradiation dose rate. As a result, since higher dose rate irradiations will result in a denser concentration of defects (with respect to time), this effect must be offset by increasing the temperature. The temperature increase enables the defects to diffuse more rapidly, resulting in more trapping and annihilation at sinks in the microstructure, offsetting the increase in defect production rate.

In Section 6.1.1.2, it was discussed how the majority of solute atoms will migrate by the vacancy diffusion mechanism. This mechanism is thus limited by the concentration of vacancies within the lattice by limiting the amount of opportunities each atom has to make a "jump" from site to site. When irradiating at a higher dose rate and increasing the concentration of vacancies, solutes will have more opportunity to migrate via these vacancies (i.e. radiation-enhanced diffusion). Furthermore, since the solutes migrate via vacancies, their diffusion direction is directly opposite that of the vacancies. Therefore, while vacancies are migrating more quickly toward sinks, the solutes are also migrating more quickly, including toward existing nanoclusters. It follows that, in order to offset the radiation-enhanced diffusion of solutes (and vacancies), higher dose rate irradiations must be conducted at a lower temperature to reduce the mobility of both the defects and solutes, enabling a more comparable influence on the irradiation-induced evolution of the nanoclusters.

7.6.3 Cluster Morphology Tailoring

The extreme performance of ODS steels is attributed to their high density of Ti-Y-O-rich nanoparticles, which: 1) act as localized sinks for point defects, providing resistance to irradiation swelling [4–6,8–10,12], and 2) strengthen the material without significantly compromising ductility. Since the properties and performance of nanofeatured ferritic alloys (NFAs) such as ODS steels are highly dependent upon their nanoparticles, it is desirable for the nanoparticles to remain stable under high temperature irradiation in a nuclear reactor environment. The advanced NHM model introduced in this thesis has the potential to be used as a predictive to aid in the design and optimization of the oxide nanocluster morphology to improve or maximize oxide stability. A flowchart

illustrating an iterative methodology is shown in Figure 7.16, incorporating use of the NHM model to: 1) predict a stable cluster morphology, 2) estimate the temperature shift required for verification using charged particle irradiation(s), and 3) comparing measured results to model predictions to inform future experiments. In this proposed process, theoretical development of an optimized microstructure is coupled with process development for consistently manufacturing an alloy with the target microstructure.

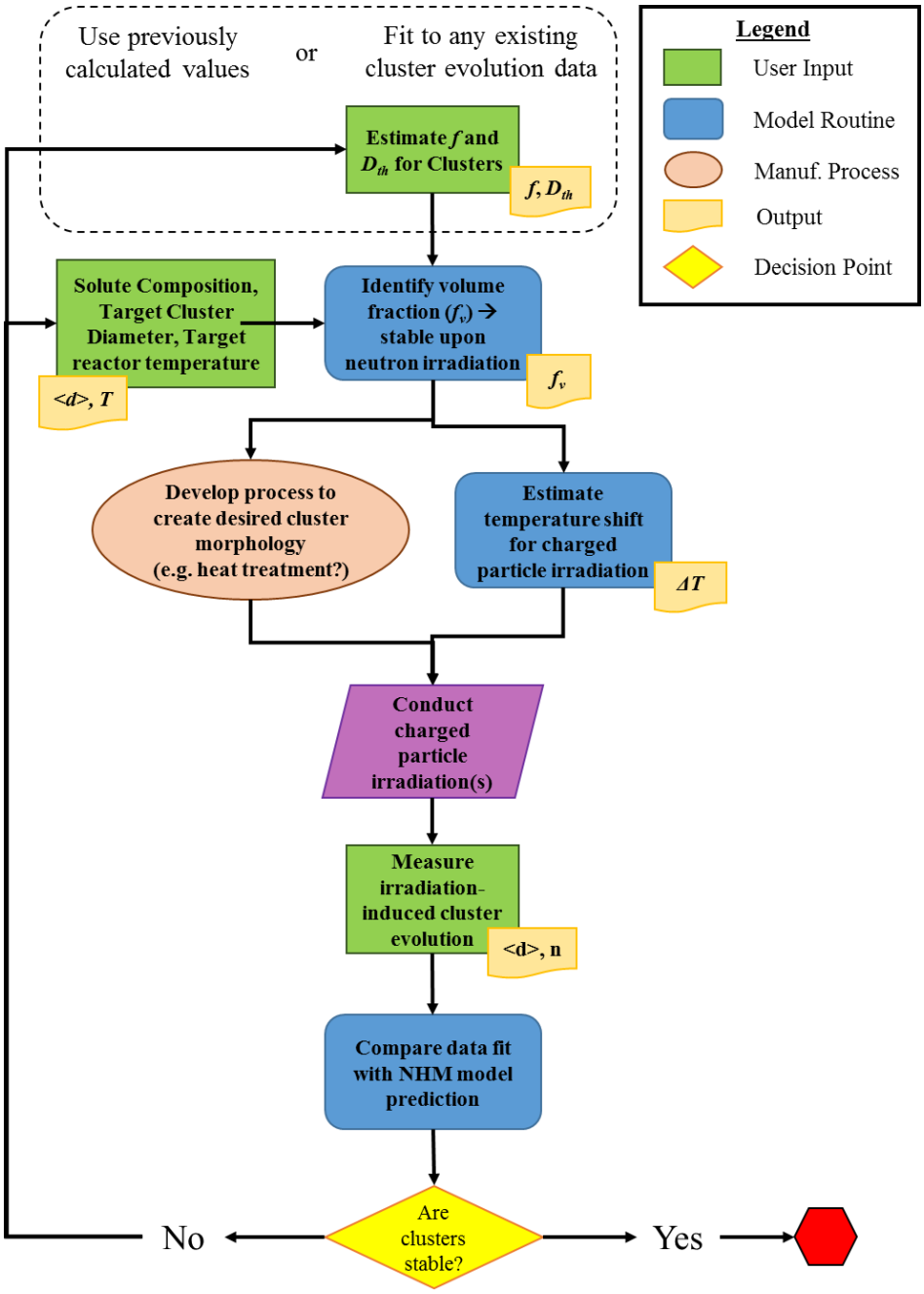

Figure 7.16 Flowchart of process to optimize cluster morphology to maximize cluster size stability upon neutron irradiation.

The application of this process may be illustrated using a hypothetical scenario with the Fe-9%Cr ODS alloy studied in this thesis as a starting point with the following approach: a) use the same solute composition as the Fe-9%Cr ODS in this thesis, b) a target stable nanocluster diameter of 6 nm, c) a target irradiation reactor environment of

500°C, and d) using Fe^{2+} irradiation to conduct initial verification of irradiation-stability of the nanoclusters. Based on the modeling effort in this thesis, the values for f^n, and f^{Fe} are tabulated in Table 6.15 and are 0.046, and 0.039, respectively, and D_{sol}^{th} is determined to be 3.88 x 10^{-21} cm^2/s. Therefore, it is reasonable to start with these inputs into the NHM model.

Using the NHM model results illustrated in the Figure 6.2 for neutron irradiation, the average cluster size is predicted to evolve from the as-received average size of 5.71 nm to an irradiation-induced stable size of 4.97 nm (r_{st} = 2.485 nm). This calculation was conducted using the as-received cluster number density of n = 4.43 x 10^{23} m^{-3}. Based on this, a stable volume fraction (f_v^{st}) of nanoclusters in this alloy is estimated to be:

$$f_v^{st} = \frac{4}{3}\pi r_{st}^3 n \qquad (7.2)$$

Once this stable volume fraction is established, the NHM model predicts the nanoclusters will remain stable, with very little sensitivity to the initial size of the nanocluster in the as-received alloy (Figure 7.17).

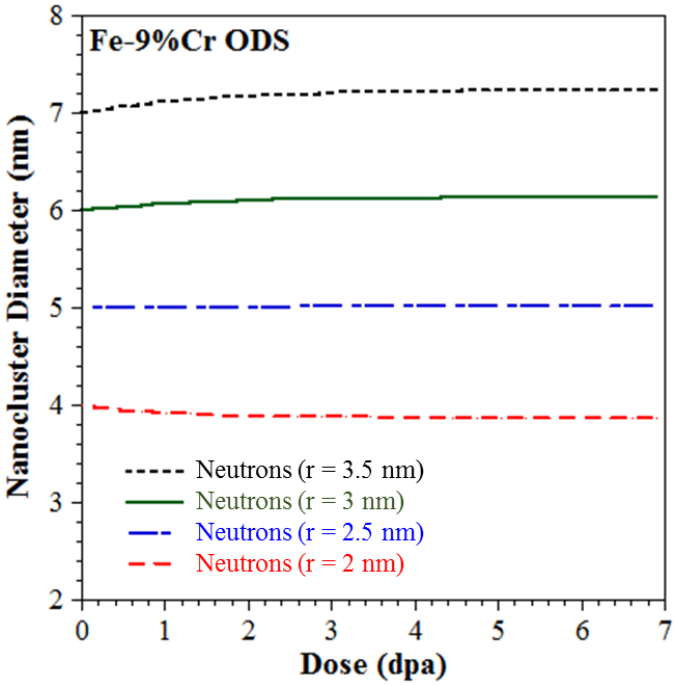

Figure 7.17 NHM model calculations of cluster evolution upon neutron irradiation at various starting cluster size using the stable volume calculated in Eq. 7.2.

Establishing the target diameter of the nanoclusters is also a non-trivial matter. This requires some knowledge of the strengthening mechanisms of the alloy under development and an optimization of the mechanical and other properties, which is beyond the scope of this thesis. Therefore, for the sake of this hypothetical illustration, it is arbitrarily assumed the target oxide diameter, d_t, is 6 nm (r_t = 3 nm). With the stable volume fraction calculated in Eq. 7.2 and the target diameter, one may calculate a target number density (n_{st}) as:

$$n_{st} = \frac{3 f_v^{st}}{4\pi r_t^3} \tag{7.3}$$

In this scenario with d_t = 6 nm, n_{st} is calculated to be ~2.52 x 10^{21} m^{-3}. Of course, developing the process to manufacturing an alloy with this target morphology is not a trivial matter. The intent here is that the NHM model predictions are coupled with efforts

to develop such manufacturing processes. As a result, the calculations and processing steps may need to be iterative to verify an alloy design.

Now, given the target cluster morphology, it is possible to conduct an NHM model calculation to predict the cluster evolution response to a higher dose irradiation such as Fe^{2+} ions. An NHM model prediction of these irradiation conditions on the target alloy are illustrated in Figure 7.18, along with the respective temperature shift required for the Fe^{2+} irradiation to yield stable nanocluster size similar to neutron irradiation. In this case, the calculated temperature shift is -120°C.

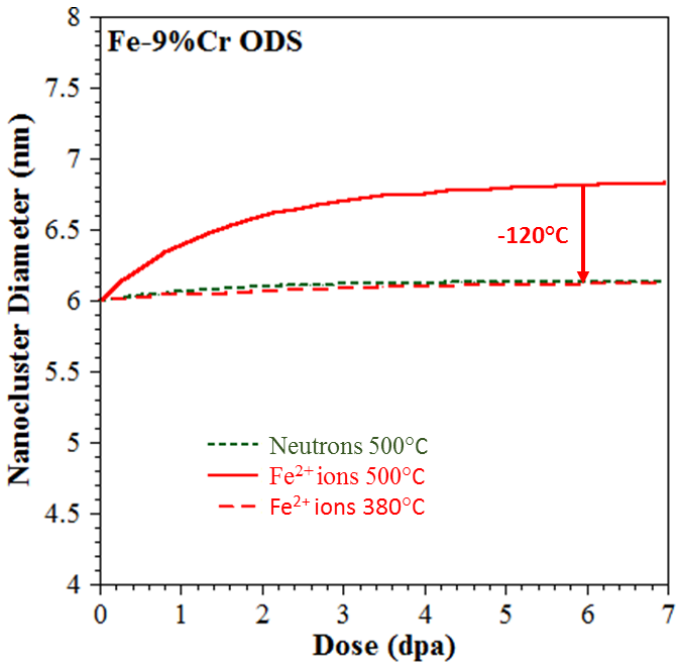

Figure 7.18 NHM model calculations of cluster evolution upon Fe2+ irradiation and the respective temperature shift to emulate neutron irradiation evolution.

Using this information, an Fe^{2+} irradiation experiment may be designed to be conducted at an irradiation temperature 380°C to a single high dose or to a range of doses. Once these irradiations are completed, the analyst would characterize the microstructure following each irradiation to confirm if the nanoclusters are successfully

stable as predicted. If the clusters exhibit stability over a range of doses, the model has been successful. If the clusters do not exhibit stability, the NHM model may be refined using the newly available experimental data and another iteration of development may begin. In the end, the expectation is that eventually the NHM model predictions, the alloy manufacturing process, and the physical irradiation results will converge onto a cluster morphology which exhibits stability and meets all other requirements and mechanical properties for the alloy. Once this is the case, the alloy and the respective stability of the nanoclusters may be tested in a test nuclear reactor environment for validation of its performance.

7.6.4 Elemental Tailoring

Within the background review for this thesis (Chapter 2), the role of different solutes on the processing and mechanical properties of F-M and ODS alloys was discussed. In Section 2.2.2, it was outlined how the alloying solutes influence such important factors as the: a) austenite solubility limit of Cr, b) the transformation temperatures of different phases, c) resulting phases and relative amounts of each phase formed during tempering, d) solid solution strengthening, e) dispersed precipitate strengthening, and f) activation in an irradiation environment. As a result, much effort is underway to tailor the alloying elements of F-M and ODS alloys for an optimized balance of performance and properties. As with any design, this process involves a system of trade-offs as various properties are influenced (either favorably or adversely) by any alloying elements which are added or removed.

The advanced NHM model introduced in this thesis is intended to serve as another informative tool for the elemental tailoring process of F-M and ODS alloys.

However, it is important to recognize some key limitations when attempting to use the NHM model to isolate individual solute species. Most notably, it is required for the analyst to have some prior knowledge of the "clusterability" of different species in the alloy system being modeled. For instance, in the case of analyzing HT9 in this study, the analyst already has prior knowledge of the alloying elements Si, Mn, Ni, and Cr, which have all demonstrated clustering behavior in the Fe-9%Cr ODS and HCM12A, so they may infer these same solutes will also cluster in HT9. In which case, the analyst may use the fitted values for f_i and D_{sol}^{th} of each respective solute (from ODS and HCM12A), along with an estimated value for p (from HCM12A), and make a "semi-prediction" of the projected size evolution of the resulting clusters after each irradiation. It is only when experimental results are available following irradiation that the analyst may confirm such assumptions.

Another limitation of the NHM model is that it provides no information or indication for when the nucleation point for irradiation-induced solute clusters will occur. This is also evident in the analysis of HT9, in which no solute clusters were observed in the specimen irradiated with Fe^{2+} ions to 3 dpa at 500°C, despite the NHM model "prediction" that clustering of Si, Mn, Ni, and P will occur, just as in the proton- and neutron-irradiated specimens experiencing the same dose of 3 dpa at 500°C. This inconsistent result is therefore hypothesized to be due to the relative incubation period of solute clusters in HT9, which has also been observed in literature [16] (Section 7.4.2.1). However, at this time, there is no experimental evidence to yet confirm this hypothesis. Regardless, the NHM model is not capable of predicting when nucleation is likely to

occur. In all cases for HCM12A and HT9, the nucleation of clusters was manually introduced in to the model.

Despite these limitations, the model has shown some remarkable consistency with the results for individual solutes across the alloys evaluated in this study. For all three alloys, the observed clustering of each solute element is able to be replicated by the model, and in each case, realistic values for f_i are fitted. Most notably, these efficiency values all follow a consistent trend, in which f_i^{Fe} is the lowest values, while f_i^n is the highest efficiency (Table 6.14). Furthermore, the fitted disordering efficiency values are shown to follow a generally pattern in Figure 6.19, in which solutes with higher displacement energy, E_d, also tend to have lower disordering efficiencies. These trends may be informative in tailoring alloying solutes and may also explain why heavier solute elements such as W and Mo are not observed to cluster in any of the alloys in this thesis. These solutes are heavier and are estimated to have higher displacement energies of ~90 eV and 60 eV for W and Mo, respectively [191]. As a result, it is expected that the disordering efficiencies for these solutes would be low, while the relative mobility of these solutes would also be low, due to their relative size compared to the surrounding matrix Fe atoms.

Possibly the most valuable insight the advanced NHM model is able to provide is the relative sensitivity of clustering behavior to the composition of each solute species. For each species which favors irradiation-induced clustering, it would be natural to hypothesize how a higher concentration of the solute would result in either larger clusters and/or higher volume fraction. Using the NHM model, a sensitivity study on the clustering evolution prediction of solutes in Fe-9%Cr ODS and HCM12A upon neutron

irradiation at 500°C is illustrated in Figure 7.19 and Figure 7.20, respectively. As expected, the model predicts higher solute content will favor larger clusters to result upon irradiation. It would be further informative to collect experimental data to confirm this trend with solute concentration, as it would be informative to an alloy designer who is considering the trade-offs of adding and removing different solute concentrations to engineer the desired properties of the alloy.

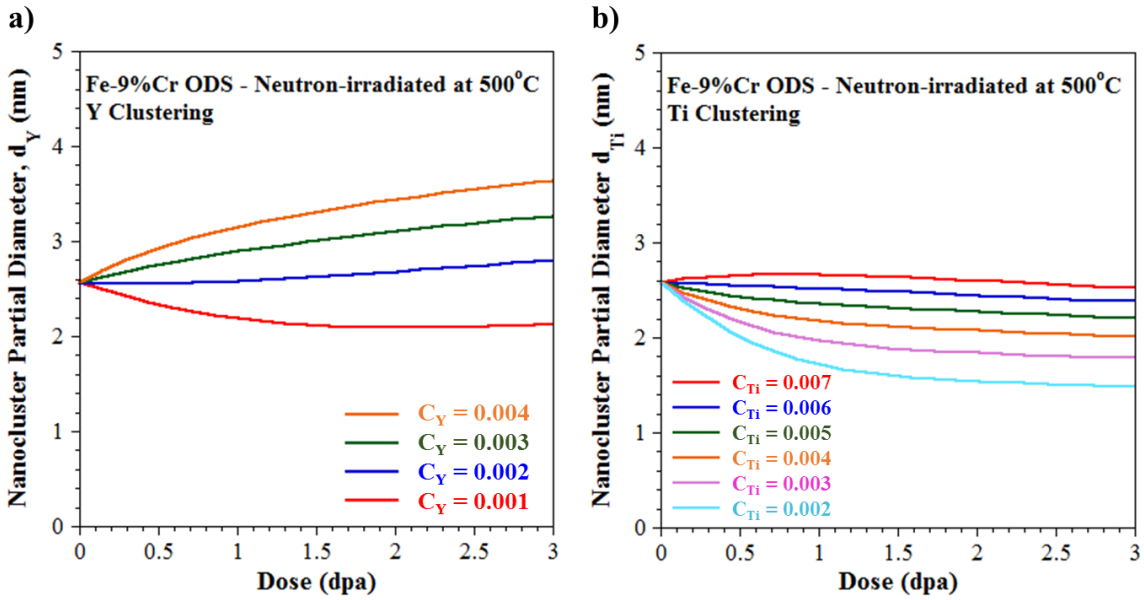

Figure 7.19 NHM model calculations of species specific cluster evolution upon neutron irradiation at 500°C for solutes in Fe-9%Cr ODS: a) Y, and b) Ti.

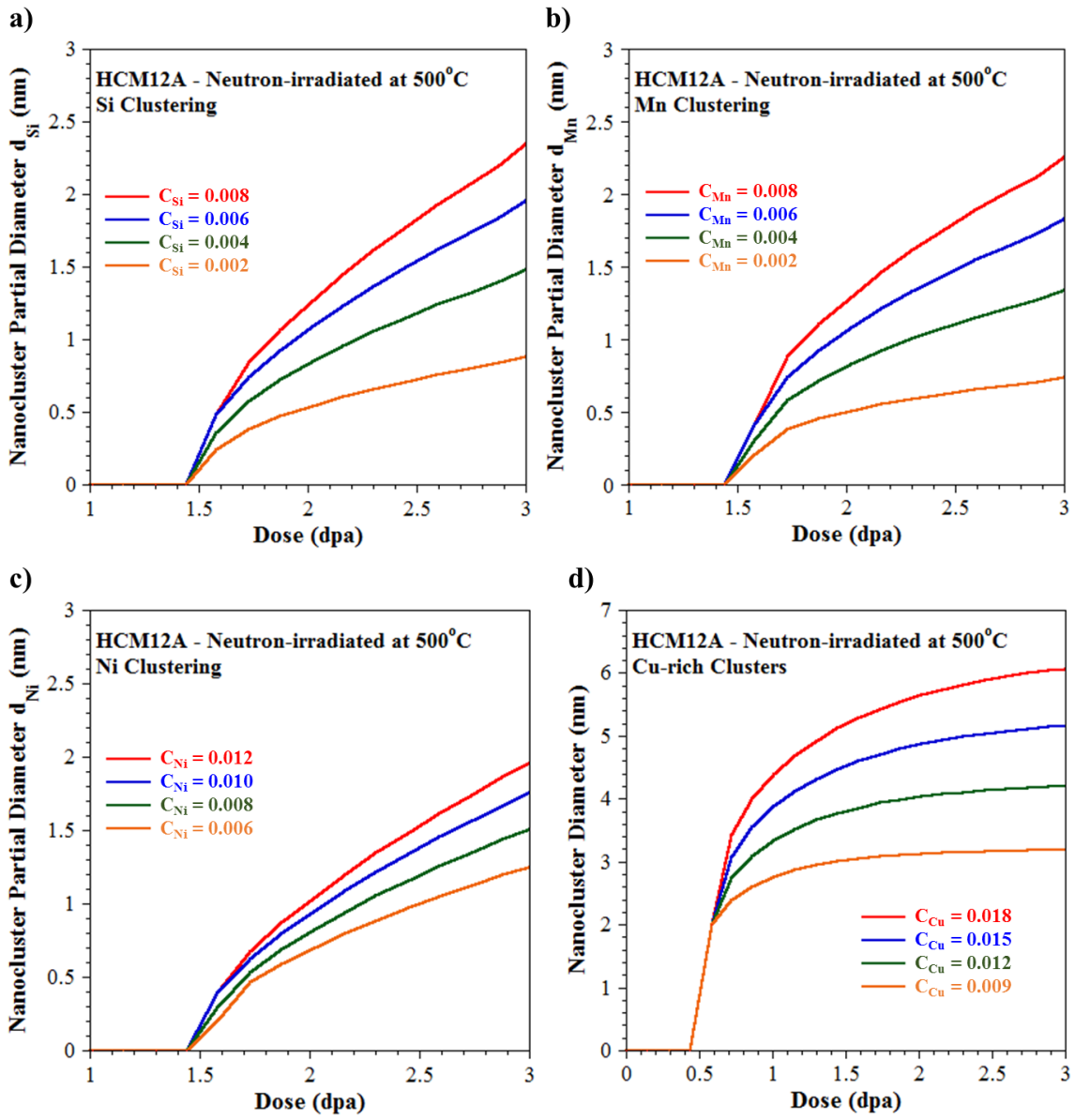

Figure 7.20 NHM model calculations of species specific cluster evolution upon neutron irradiation at 500°C for solutes in HCM12A: a) Si, b) Mn, c) Ni, and d) Cu.

7.6.5 Different Systems

Up to this point, the context of this thesis has been confined to the b.c.c. Fe-based alloy system for F-M and ferritic ODS alloys. Moving forward it is believed the advanced NHM model may be adapted for other b.c.c. Fe-based alloys containing different solute elements. Some logical choices would be to evaluate the clustering behavior of solutes of

Zr and Al in such systems. In ref. [191], the estimated displacement energies for Zr and Al are 40 eV and 25 eV, respectively. This information gives some inclination about their relative disordering efficiencies (i.e. Al should have a higher disordering efficiency based on the relationship illustrated in Figure 6.19), but there is insufficient information to establish a credible estimate for both the disordering efficiencies, f_i, or the relative thermal diffusion rates these solutes would have towards the clusters, D_{sol}^{th}. As a result, some prior knowledge about the clustering behavior of these solutes, in the form of experimental data, is required to model these systems. When experimental data measuring cluster evolution of such solutes upon irradiation is available, it is then possible to use the advanced NHM model to fit values for f_i and D_{sol}^{th} for each solute element. Once this is accomplished, the calculation may be calibrated and capable of providing some informative insight (as discussed in the prior sections).

Inherently, the advanced NHM model could also be adapted to other systems besides b.c.c. Fe-based alloys. In doing so, a whole new set of basic input parameters would need to be calculated. For illustration purposed, an f.c.c. Cu-based alloy system will be considered. As with the Fe-based system, each of the parameters in Eq. 6.1 are to be calculated or estimated. One could use SRIM to estimate the relative damage rate (ϕ) and target analysis region for each respective charged particle irradiation. The atomic density for h.c.p. Zr is estimated as N_{Zr} = 44.0 atoms/nm^3 (assuming an atomic radius of 0.159 nm [73]). Next, following the same approach as outlined in Section 2.1.2, the values for each respective variable and a total estimated effective damage cascade diameter, l, may be calculated for each type of irradiating of interest. A summary of such values are given in Table 7.6. Despite the relative differences in the atomic density and

mass of the target Zr atoms, the estimated effective cascade diameters are still quite similar to those calculated for Fe (see Table 2.1). In addition to these parameters, an analyst would need to estimate all the inputs influencing diffusion rates, including vacancy formation and migration energies, and the respective solute migration energies to calculate the respective RED diffusion rates for solutions (D^{irr}).

Table 7.6 Summary of calculation variables and estimated effective diameter for different irradiating particles upon an h.c.p. Zr-based target alloy.

Irradiating particle	***PKA Energy,T* (eV), from** [42]	***Screening Radius, a* (nm)**	ε_N	k_N	g	***Cascade Damage Energy,* E_D (eV)**	**Estimated effective cascade diameter,** l **(nm)**
1 MeV electrons	60	0.0137	60.00	0.000	75.4	60	1.65
2 MeV protons	200	0.0133	0.014	0.134	1.7	163	2.30
5 MeV Fe^{2+}	5000	0.0087	0.003	0.157	1.26	4173	6.78
Fast neutrons	35000	0.0133	2.442	0.134	7.17	17865	11.01

These steps to get the model functioning are practical. However, the same limitations as previously discussed remain - the analyst requires some prior experimental observation and measured data of cluster evolution upon irradiation. This data enables calibration of the model, through fitting values for f and D_{sol}^{th} for each respective irradiating particle upon the target alloy. Once these values are deduced with reasonable confidence, a more informative analysis may commence including: a) evaluation of potential temperature shifts required using higher dose irradiations (Section 7.6.2), b) Optimization of existing cluster morphology to enhance stability upon irradiation

(Section 7.6.3), or c) tailoring of alloying elements and their respective concentrations (Section 7.6.4).

CHAPTER EIGHT: CONCLUSIONS AND FUTURE WORK

For this thesis, a series of irradiation experiments are conducted on a model Fe-9%Cr ferritic ODS alloy and the commercial F-M alloys HCM12A and HT9. Irradiations with Fe^{2+} ions, protons, or neutrons were executed to damage doses ranging 1-100 dpa, 1-7 dpa, or 3 dpa, respectively. All irradiations are conducted at 500°C, with one exception: irradiation with Fe^{2+} ions to 50 dpa at 400°C on the Fe-9%Cr ODS alloy. Transmission electron microscopy is conducted on each specimen to characterize the overall microstructure, including evaluation of defect cluster evolution after each irradiation. Atom probe tomography is used to characterize the morphology and evolution of any nanoscale phases present in each alloy after irradiation. For the ODS alloy, each specimen is also compared to the nanocluster morphology of the as-received specimen to evaluate cluster stability upon irradiation. Utilizing theoretical calculation models developed by Nelson, Hudson, and Mazey [57] and Martin [60], an advanced model is developed to simulate the observed nanocluster evolution following each irradiation. As a result of this work, the following key trends and conclusions are reported:

1) *When using higher dose rate charged particle irradiations to emulate lower dose rate neutron irradiation, two separate irradiation experiments are required to fully verify the microstructural evolution of a nanofeatured alloy containing solute nanoclusters.* First, a high dose rate irradiation is required at a higher temperature to isolate and emulate defect cluster (loops and voids) evolution. A second high dose rate

irradiation is required at a lower temperature to isolate and emulate solute cluster evolution.

a. *Dislocation loops are present after 1 dpa upon both Fe^{2+} and proton irradiation, with only limited growth at higher doses.* This result is consistent with loop growth observations in various ferritic-martensitic alloys [16,23,138], and it supports the theory of defect cluster saturation developed by Whapham and Makin [136,137].

b. *The average size and number density of dislocation loops and voids are similar in Fe^{2+}, proton- and neutron-irradiated specimens at 3 dpa.* Charged particle irradiations can reproduce the neutron-irradiated loop microstructure with a Mansur-type recombination-driven temperature shift. For the high sink density of the subject alloys, this temperature shift happens to be ~0°C.

c. *Changes to nanocluster number density correlate with damage cascade size, while changes to nanocluster size correlate with damage cascade efficiency.* This is most clearly evidenced with ODS oxide nanoclusters irradiated with neutrons, protons, and Fe^{2+} ions at 3 dpa, 500°C. The reduction in nanocluster number density is most dramatic upon neutron irradiation; larger cascades (i.e. those produced by neutron irradiation) are more likely to have a footprint that overlaps or entirely envelops the oxides, promoting ballistic dissolution of whole nanoclusters. The average nanocluster sizes are largest after Fe^{2+} irradiation (as compared to proton or neutron irradiation), correlating with the low cascade efficiency of heavy ion species such as Fe^{2+}. Hence, although proton irradiation is less effective at dissolving whole clusters, they may be

more effective than Fe^{2+} ions at reducing cluster size by ejection or disordering of clustered atoms.

2) *The advanced NHM model developed may be used as an informative tool to predict the evolution of cluster morphology in ODS and other nanofeatured alloys*. Cluster evolution is governed by the competing influences of ballistic dissolution and diffusion-driven growth of the nanoclusters. For the ODS alloy in this study, the oxide nanocluster diameters converge on steady-state values at doses ≳3 dpa for all irradiating particles and experience the phenomenon of inverse Ostwald ripening over the examined irradiation envelope of 1-100 dpa at 400-500°C (i.e. decrease in size while increasing in density). However, alloys with different cluster morphology will experience differing cluster evolution based on the relative balance of these two mechanisms. Coupled with alloy processing development and physical irradiation experiments, the model can be used to assist alloy composition and process tailoring to optimize morphology and design verification experiments for higher dose irradiations.
3) *The advanced NHM model provides some insight into the relative clusterability of specific solute species, including their respective cascade disordering efficiencies and their rate of diffusion toward existing clusters.* However, for the model to provide such information, some prior cluster evolution measurements from physical irradiation experiments are required to enable fitting of such parameters to calibrate the model.
4) *For publications reporting APT cluster analysis data, key information is required to enable a robust comparison of results between different researchers.* At a minimum,

the following information should be provided: a) the method for selecting the ICF for each data set reconstruction, b) the overall number of clusters measured for each specimen and the relative certainty of the mean value reported, and c) the method for normalizing data to ensure a robust comparison may be drawn, such as the procedure outlined in this study.

5) *In HCM12A, Cu-rich clusters first nucleate homogeneously (prior to 1 dpa with proton irradiation), followed by heterogeneous nucleation of Si-Mn-Ni clusters at or near the Cu cluster-matrix interface (occurs between 1 and 3 dpa with proton irradiation).* Meanwhile, in HT9, no clusters are observed after Fe^{2+} irradiation to 3 dpa. This result is likely related to the relative incubation period for nucleation of Si-Mn-Ni clusters for each irradiation.
6) *Neutrons are the only irradiating particles producing any Cr-rich (α') clusters in both HCM12A and HT9.* Cr clustering in the neutron-irradiated specimens may be largely influenced by thermal aging at 500°C over ~1 year. Furthermore, temperature dilation resulting from higher dose rate of the charged particle irradiations results in a higher configurational entropy of the system, likely increasing the solubility limit of Cr in the surrounding Fe matrix.

Although a significant amount of new insights have been accomplished as a result of the work for this thesis, additional opportunities have emerged for future research to gain further insight into the mechanisms of irradiation-induced nanocluster evolution. The following is a brief overview of items meriting future attention:

A) Conduct charged particle irradiation experiments on each alloy (Fe-9%Cr ODS, HCM12A, and HT9) at lower temperatures to validate the predicted downward

temperature shift theory (e.g. Fe^{2+} irradiation at ~380°C) to emulate neutron irradiation-induced cluster evolution.

B) Conduct a series of Fe^{2+} irradiations of HCM12A and HT9 at intermediate doses (between 3 and 100 dpa) to confirm the nucleation and incubation behavior of Si-Mn-Ni-rich clusters and identify the turning point between cluster growth and cluster dissolution. In HCM12A, clustering was observed after 3 dpa, but absent after 100 dpa. In HT9, clustering was absent after 3 dpa, but is hypothesized to be favorable at a higher dose to the relative incubation period of higher dose Fe^{2+} irradiation.

C) Acquire irradiation-induced cluster evolution data for other b.c.c. Fe-based alloys and verify the transferability of the NHM model predictions. Is there consistency in the cascade disordering efficiencies for each solute and the relative rates of diffusion toward existing clusters? Estimate the temperature shift required for high dose irradiations to inform future charged particle irradiation experiments.

D) Acquire irradiation-induced cluster evolution data for different alloy systems (e.g. Zr-based or Cu-based). Evaluate the required temperature shifts for higher dose irradiations to emulate neutron irradiation induced cluster evolution using the advanced NHM model and validate predictions via further charged particle irradiation experiments.

REFERENCES

[1] S.J. Zinkle, J.T. Busby, Mater. Today 12 (2009) 12.

[2] T. Allen, J. Busby, M. Meyer, D. Petti, Mater. Today 13 (2010) 14.

[3] P. Yvon, F. Carré, J. Nucl. Mater. 385 (2009) 217.

[4] L. Barnard, G.R. Odette, I. Szlufarska, D. Morgan, Acta Mater. 60 (2012) 935.

[5] A. Certain, S. Kuchibhatla, V. Shutthanandan, D.T. Hoelzer, T.R. Allen, J. Nucl. Mater. 434 (2013) 311.

[6] A.G. Certain, K.G. Field, T.R. Allen, M.K. Miller, J. Bentley, J.T. Busby, J. Nucl. Mater. 407 (2010) 2.

[7] P. Dubuisson, Y. De Carlan, V. Garat, M. Blat, J. Nucl. Mater. 428 (2012) 6.

[8] J. He, F. Wan, K. Sridharan, T.R. Allen, A. Certain, V. Shutthanandan, Y.Q. Wu, J. Nucl. Mater. 455 (2014) 41.

[9] J. He, F. Wan, K. Sridharan, T.R. Allen, A. Certain, Y.Q. Wu, J. Nucl. Mater. 452 (2014) 87.

[10] C. Hin, B.D. Wirth, J. Nucl. Mater. 402 (2010) 30.

[11] R.L. Klueh, D.R. Harries, High-Chromium Ferritic and Martensitic Steels for Nuclear Applications, ASTM, 2001.

[12] C. Liu, C. Yu, N. Hashimoto, S. Ohnuki, M. Ando, K. Shiba, S. Jitsukawa, J. Nucl. Mater. 417 (2011) 270.

[13] H. Sakasegawa, L. Chaffron, F. Legendre, L. Boulanger, T. Cozzika, M. Brocq, Y. de Carlan, J. Nucl. Mater. 384 (2009) 115.

[14] D.S. Gelles, 237 (1996) 293.

[15] P.J. Maziasz, J. Nucl. Mater. 169 (1989) 95.

[16] T.R. Allen, J.P. Wharry, K.G. Field, D.L. Morgan, A.T. Motta, B.D. Wirth, Y. Yang, J. Mater. Res. 30 (2015).

[17] J.J. Kai, R.L. K, 230 (1996) 116.

[18] B.H. Sencer, J.R. Kennedy, J.I. Cole, S.A. Maloy, F.A. Garner, J. Nucl. Mater. 414 (2011) 237.

[19] P. Dubuisson, D. Gilbon, D.T.A.C. Dtm, S. De Recherches, M. Appliqukes, C.E. Saclay, 205 (1993) 178.

[20] O. Anderoglu, J. Van Den Bosch, P. Hosemann, E. Stergar, B.H. Sencer, D. Bhattacharyya, 430 (2012) 194.

[21] J. Van Den Bosch, O. Anderoglu, R. Dickerson, M. Hartl, P. Dickerson, J.A. Aguiar, P. Hosemann, M.B. Toloczko, S.A. Maloy, J. Nucl. Mater. 440 (2013) 91.

[22] J.P. Wharry, M.J. Swenson, K.H. Yano, J. Nucl. Mater. 486 (2017) 11.

[23] J.P. Wharry, Z. Jiao, V. Shankar, J.T. Busby, G.S. Was, J. Nucl. Mater. 417 (2011) 140.

[24] Z. Jiao, G.S. Was, J. Nucl. Mater. 425 (2012) 105.

[25] Z. Jiao, V. Shankar, G.S. Was, J. Nucl. Mater. 419 (2011) 52.

[26] V. Kuksenko, C. Pareige, C. Genevois, P. Pareige, J. Nucl. Mater. 434 (2013) 49.

[27] V. Kuksenko, C. Pareige, C. Genevois, F. Cuvilly, M. Roussel, P. Pareige, 415 (2011) 61.

[28] V. Kuksenko, C. Pareige, P. Pareige, J. Nucl. Mater. 425 (2012) 125.

[29] B.H. Sencer, J.R. Kennedy, J.I. Cole, S.A. Maloy, F.A. Garner, J. Nucl. Mater. 393 (2009) 235.

[30] E. Getto, K. Sun, A.M. Monterrosa, Z. Jiao, M.J. Hackett, G.S. Was, J. Nucl. Mater. 480 (2016) 159.

[31] M. Bachhav, G. Robert Odette, E.A. Marquis, Scr. Mater. 74 (2014) 48.

[32] C. Hardie, (2013).

[33] V. Kuksenko, C. Pareige, P. Pareige, J. Nucl. Mater. 432 (2013) 160.

[34] Y.Y. Dai, L. Ao, Q.Q. Sun, L. Yang, J.L. Nie, S.M. Peng, X.G. Long, X.S. Zhou, X.T. Zu, L. Liu, X. Sun, D. Terentyev, F. Gao, 101 (2015) 293.

[35] D. Xu, A. Certain, H.L. Voigt, T. Allen, B.D. Wirth, D. Xu, A. Certain, H.L. Voigt, T. Allen, B.D. Wirth, J. Chem. Phys. 145 (2016).

[36] G.S. Was, Z. Jiao, E. Getto, K. Sun, a. M. Monterrosa, S. a. Maloy, O. Anderoglu, B.H. Sencer, M. Hackett, Scr. Mater. 88 (2014) 33.

[37] X. Wang, A.M. Monterrosa, F. Zhang, H. Huang, Q. Yan, Z. Jiao, G.S. Was, L. Wang, J. Nucl. Mater. 462 (2015) 119.

[38] J.G. Gigax, T. Chen, H. Kim, J. Wang, L.M. Price, E. Aydogan, S.A. Maloy, D.K. Schreiber, M.B. Toloczko, F.A. Garner, L. Shao, J. Nucl. Mater. 482 (2016) 257.

[39] Y. Huang, J.P. Wharry, Z. Jiao, C.M. Parish, S. Ukai, T.R. Allen, 442 (2013) 800.

[40] M.J. Swenson, J.P. Wharry, J. Nucl. Mater. 467 (2015) 97.

[41] M.J. Swenson, C.K. Dolph, J.P. Wharry, J. Nucl. Mater. 479 (2016) 426.

[42] G.S. Was, Fundamentals of Radiation Materials Science: Metals and Alloys, Springer, 2007.

[43] (2007).

[44] J.F. Ziegler, J.P. Biersack, M.D. Ziegler, SRIM - The Stopping and Range of Ions in Matter, 2013.

[45] R.S. Averback, R. Benedek, K.L. Merkle, Phys. Rev. B 18 (1978) 4156.

[46] R.E. Stoller, L.R. Greenwood, J. Nucl. Mater. 271-272 (1999) 57.

[47] R.E. Stoller, J. Nucl. Mater. 276 (2000) 22.

[48] R.E. Stoller, G.R. Odette, B.D. Wirth, J. Nucl. Mater. 251 (1997) 49.

[49] M.J. Norgett, M.T. Robinson, I.M. Torrens, Nucl. Eng. Des. 33 (1975) 50.

[50] B.M. Latta, P.J. Scanlon, Phys. Rev. A 10 (1974) 1638.

[51] R.S. Averback, J. Nucl. Mater. 216 (1994) 49.

[52] R.L. Klueh, J.P. Shingledecker, R.W. Swindeman, D.T. Hoelzer, 341 (2005) 103.

[53] I. Hilger, M. Tegel, M.J. Gorley, P.S. Grant, T. Weißgärber, B. Kieback, J. Nucl. Mater. 447 (2014) 242.

[54] G.R. Odette, M.J. Alinger, B.D. Wirth, Annu. Rev. Mater. Res. 38 (2008) 471.

[55] R. Lindau, 79 (2005) 989.

[56] D.T. Hoelzer, J. Bentley, M. a. Sokolov, M.K. Miller, G.R. Odette, M.J. Alinger, J. Nucl. Mater. 367-370 (2007) 166.

[57] R.S. Nelson, J.A. Hudson, D.J. Mazey, J. Nucl. Mater. 44 (1972) 318.

[58] K.H. Heinig, T. M�ller, B. Schmidt, M. Strobel, W. M�ller, Appl. Phys. A Mater. Sci. Process. 77 (2003) 17.

[59] M.-L. Lescoat, J. Ribis, Y. Chen, E.A. Marquis, E. Bordas, P. Trocellier, Y. Serruys, A. Gentils, O. Kaïtasov, Y. de Carlan, A. Legris, Acta Mater. 78 (2014) 328.

[60] G. Martin, Phys. Rev. 30 (1984) 1424.

[61] J. Li, C. Guo, Y. Ma, Z. Wang, J. Wang, Acta Mater. 90 (2015) 10.

[62] V.M. Burlakov, L. Kantorovich, J. Chem. Phys. 134 (2011) 024521.

[63] R.D. Vengrenovich, A. V. Moskalyuk, S. V. Yarema, Phys. Solid State 49 (2007) 11.

[64] S.G. Kim, Acta Mater. 55 (2007) 6513.

[65] C.J. Kuehmann, P.W. Voorhees, Metall. Mater. Trans. A 27A (1996) 937.

[66] T. Philippe, P.W. Voorhees, Acta Mater. 61 (2013) 4237.

[67] S. V Rogozhkin, A.A. Aleev, A.G. Zaluzhnyi, A.A. Nikitin, N.A. Iskandarov, P. Vladimirov, R. Lindau, A. Möslang, J. Nucl. Mater. 409 (2011) 94.

[68] S. V Rogozhkin, A.A. Aleev, A.G. Zaluzhnyi, N.A. Iskanderov, A.A. Nikitin, P. Vladimirov, R. Lindau, 113 (2012) 98.

[69] J. Ribis, E. Bordas, P. Trocellier, Y. Serruys, Y. de Carlan, A. Legris, J. Mater. Res. 30 (2015) 2210.

[70] D. Menut, J. Béchade, S. Cammelli, S. Schlutig, B. Sitaud, P.L. Solari, (2017).

[71] P. Dubuisson, R. Schill, M.-P. Hugon, I. Grislin, J.-L. Seran, in:, Eff. Radiat. Mater. 18th Int. Symp. ASTM STP 132, 1999, pp. 882–898.

[72] I. Monnet, T. Van den Berghe, P. Dubuisson, J. Nucl. Mater. 424 (2012) 204.

[73] W.D. Callister, D.G. Rethwisch, Materials Science and Engineering: An Introduction, 9th ed., Wiley, 2014.

[74] K.C. Russell, J. Nucl. Mater. 206 (1993) 129.

[75] P. Kluth, B. Johannessen, R. Giulian, C.S.S. andd G. J. Foran D. J. Cookson, A.P.B.M.C. Ridgway, Radiat. Eff. Defects Solids 162 (2007) 501.

[76] D.P. Datta, Y. Takeda, H. Amekura, M. Sasase, N. Kishimoto, Appl. Surf. Sci. 310 (2014) 164.

[77] G.C. Rizza, M. Strobel, K.H. Heinig, H. Bernas, Nucl. Instruments Methods Phys. Res. Sect. B Beam Interact. with Mater. Atoms 178 (2001) 78.

[78] G. Rizza, H. Cheverry, T. Gacoin, A. Lamasson, S. Henry, J. Appl. Phys. 101 (2007).

[79] T. Chen, J.G. Gigax, L. Price, D. Chen, S. Ukai, E. Aydogan, S.A. Maloy, F.A. Garner, L. Shao, Acta Mater. 116 (2016) 29.

[80] C. Wagner, Z. Elektrochemie 65 (1961) 581.

[81] N. Akasaka, S. Yamashita, T. Yoshitake, S. Ukai, A. Kimura, J. Nucl. Mater. 329-333 (2004) 1053.

[82] A. Alamo, V. Lambard, X. Averty, M.H. Mathon, J. Nucl. Mater. 329-333 (2004) 333.

[83] T.R. Allen, J. Gan, J.I. Cole, S. Ukai, Nucl. Sci. Eng. 151 (2005) 305.

[84] T.R. Allen, J. Gan, J.I. Cole, M.K. Miller, J.T. Busby, S. Shutthanandan, S. Thevuthasan, J. Nucl. Mater. 375 (2008) 26.

[85] K. Asano, Y. Kohno, A. Kohyama, T. Suzuki, H. Kusanagi, J. Nucl. Mater. 155-157 (1988) 928.

[86] N.A. Bailey, E. Stergar, M. Toloczko, P. Hosemann, J. Nucl. Mater. 459 (2015) 225.

[87] V. De Castro, M. Briceno, S. Lozano-Perez, P. Trocellier, S.G. Roberts, R. Pareja, J. Nucl. Mater. 455 (2014) 157.

[88] P. Dubuisson, R. Schill, M.-P. Hugon, I. Grislin, J.-L. Seran, in:, R.K. Nanstad, M.L. Hamilton, F.A. Garner, A.S. Kumar (Eds.), Eff. Radiat. Mater. 18th Int. Symp. ASTM STP 1325, American Society for Testing and Materials, West Conshohocken, PA, 1999, pp. 882–898.

[89] P.D. Edmondson, A. London, A. Xu, D.E.J. Armstrong, S.G. Roberts, J. Nucl. Mater. 462 (2015) 369.

[90] K. Hide, N. Sekimura, N. Fukuya, H. Kusangi, H. Taguchi, M. Satake, T. Arai, Y. Iimura, H. Takaku, S. Ishino, in:, N.H. Packan, R.E. Stoller, A.S. Kumar (Eds.), Eff. Radiat. Mater. 14th Annu. Symp. ASTM STP 1046, American Society for Testing and Materials, Philadelphia, PA, 1989, pp. 61–72.

[91] T. Kaito, S. Ohtsuka, Y. Yano, T. Tanno, S. Yamashita, R. Ogawa, K. Tanaka, in:, Fast React. Relat. Fuel Cycles Safe Technol. Sustain. Scenar. (FR13), Proc. an Int. Conf., International Atomic Energy Agency (IAEA), 2015.

[92] D. Kaoumi, A. Motta, M. Kirk, Trans. Am. Nucl. Soc. 98 (2008) 1113.

[93] A. Kimura, H.-S. Cho, N. Toda, R. Kasada, K. Yutani, H. Kishimoto, N. Iwata, S. Ukai, M. Fujiwara, J. Nucl. Sci. Technol. 44 (2007) 323.

[94] H. Kishimoto, K. Yutani, R. Kasada, O. Hashitomi, A. Kimura, J. Nucl. Mater. 367-370 (2007) 179.

[95] H. Kishimoto, R. Kasada, A. Kimura, M. Inoue, T. Okuda, F. Abe, S. Ohnuki, T. Fujisawa, in:, Proc. ICAPP 2009, Tokyo, Japan, 2009, p. 9219.

[96] M.-L. Lescoat, J. Ribis, A. Gentils, O. Kaïtasov, Y. de Carlan, A. Legris, J. Nucl. Mater. 428 (2012) 176.

[97] F. Li, H. Abe, T. Ishizaki, Y. Li, T. Nagasaka, T. Muroga, T. Nagase, H. Yasuda, J. Nucl. Mater. 455 (2014) 724.

[98] E.A. Little, in:, D.S. Gelles, R.K. Nanstad, A.S. Kumar, E.A. Little (Eds.), Eff. Radiat. Mater. 17th Int. Symp. ASTM STP 1270, American Society for Testing and Materials, West Conshohocken, PA, 1996, pp. 739–752.

[99] A.J. London, B.K. Panigrahi, C.C. Tang, C. Murray, C.R.M. Grovenor, Scr. Mater. 110 (2016) 24.

[100] M.-H. Mathon, Y. De Carlan, X. Averty, A. Alamo, C.-H. de Novion, J. ASTM Int. 2 (2005) 1.

[101] D. Menut, J.-L. Béchade, S. Cammelli, S. Schlutig, B. Sitaud, P.L. Solari, J. Mater. Res. 30 (2015) 1392.

[102] M.K. Miller, D.T. Hoelzer, J. Nucl. Mater. 418 (2011) 307.

[103] I. Monnet, C. Grygiel, M.L. Lescoat, J. Ribis, J. Nucl. Mater. 424 (2012) 12.

[104] I. Monnet, P. Dubuisson, Y. Serruys, M.O. Ruault, O. Kaıtasov, B. Jouffrey, J. Nucl. Mater. 335 (2004) 311.

[105] P. Pareige, M.K. Miller, R.E. Stoller, D.T. Hoelzer, E. Cadel, B. Radiguet, J. Nucl. Mater. 360 (2007) 136.

[106] P. Parente, T. Leguey, V. De Castro, T. Gigl, M. Reiner, C. Hugenschmidt, R. Pareja, J. Nucl. Mater. 464 (2015) 140.

[107] S. Pasebani, I. Charit, J. Burns, S. Alsagabi, D.P. Butt, J.I. Cole, L.M. Price, L. Shao, J. Nucl. Mater. 462 (2015) 191.

[108] A. Ramar, N. Baluc, R. Schäublin, J. Nucl. Mater. 367-370 (2007) 217.

[109] J. Ribis, M.L. Lescoat, Y. De Carlan, J.M. Costantini, I. Monnet, T. Cozzika, F. Delabrouille, J. Malaplate, J. Nucl. Mater. 417 (2011) 262.

[110] J. Ribis, S. Lozano-Perez, J. Nucl. Mater. 444 (2014) 314.

[111] J. Ribis, J. Nucl. Mater. 434 (2013) 178.

[112] J. Ribis, E. Bordas, P. Trocellier, Y. Serruys, Y. De Carlan, A. Legris, Nucl. Instruments Methods Phys. Res. Sect. B Beam Interact. with Mater. Atoms 365 (2015) 22.

[113] C. Robertson, B.K.K. Panigrahi, S. Balaji, S. Kataria, Y. Serruys, M.-H. Mathon, C.S. Sundar, J. Nucl. Mater. 426 (2012) 240.

[114] S. V. Rogozhkin, a. a. Aleev, a. G. Zaluzhnyi, N. a. Iskanderov, a. a. Nikitin, P. Vladimirov, R. Lindau, a. Möslang, Phys. Met. Metallogr. 113 (2012) 98.

[115] S.V. Rogozhkin, N.N. Orlov, A.A. Aleev, A.G. Zaluzhnyi, M.A. Kozodaev, R.P. Kuibeda, T.V. Kulevoy, A.A. Nikitin, B.B. Chalykh, R. Lindau, A. Möslang, P. Vladimirov, Phys. Met. Metallogr. 116 (2015) 72.

[116] S. Rogozhkin, A. Bogachev, O. Korchuganova, A. Nikitin, N. Orlov, A. Aleev, A. Zaluzhnyi, M. Kozodaev, T. Kulevoy, B. Chalykh, R. Lindau, J. Hoffmann, A. Möslang, P. Vladimirov, M. Klimenkov, M. Heilmaier, J. Wagner, S. Seils, Nucl. Mater. Energy 0 (2016) 1.

[117] J. Saito, T. Suda, S. Yamashita, S. Ohnuki, H. Takahashi, N. Akasaka, M. Nishida, S. Ukai, J. Nucl. Mater. 258-263 (1998) 1264.

[118] M. Šćepanović, V. de Castro, T. Leguey, M.A. Auger, S. Lozano-Perez, R. Pareja, Nucl. Mater. Energy 0 (2016) 1.

[119] R. Schäublin, A. Ramar, N. Baluc, V. de Castro, M.A. Monge, T. Leguey, N. Schmid, C. Bonjour, J. Nucl. Mater. 351 (2006) 247.

[120] V.A. Skuratov, A.S. Sohatsky, J.H. O'Connell, K. Kornieieva, A.A. Nikitina, V. V. Uglov, J.H. Neethling, V.S. Ageev, Nucl. Instruments Methods Phys. Res. Sect. B Beam Interact. with Mater. Atoms 374 (2016) 102.

[121] V.A. Skuratov, A.S. Sohatsky, J.H. O'Connell, K. Kornieieva, A.A. Nikitina, J.H. Neethling, V.S. Ageev, J. Nucl. Mater. 456 (2015) 111.

[122] C.A. Williams, J.M. Hyde, G.D.W. Smith, E.A. Marquis, J. Nucl. Mater. 412 (2011) 100.

[123] S. Yamashita, K. Oka, S. Ohnuki, N. Akasaka, S. Ukai, J. Nucl. Mater. 307-311 (2002) 283.

[124] S. Yamashita, N. Akasaka, S. Ohnuki, J. Nucl. Mater. 329-333 (2004) 377.

[125] S. Yamashita, N. Akasaka, S. Ukai, S. Ohnuki, J. Nucl. Mater. 367-370 (2007) 202.

[126] C.Z. Yu, H. Oka, N. Hashimoto, S. Ohnuki, J. Nucl. Mater. 417 (2011) 286.

[127] A. Yutani, K, Kasada, R., Kishimoto, H., Kimura, J. ASTM Int. 4 (2007) 323.

[128] Y. Zhanbing, H. Benfu, H. Kinoshita, H. Takahashi, S. Watanabe, J. Nucl. Mater. 398 (2010) 81.

[129] H.J. Jung, D.J. Edwards, R.J. Kurtz, T. Yamamoto, Y. Wu, G.R. Odette, J. Nucl. Mater. 484 (2016) 68.

[130] H. Kishimoto, R. Kasada, O. Hashitomi, A. Kimura, J. Nucl. Mater. 386-388 (2009) 533.

[131] S. Ukai, T. Okuda, M. Fujiwara, T. Kobayashi, S. Mizuta, H. Nakashima, J. Nucl. Sci. Technol. 39 (2002) 872.

[132] Y. Wu, E.M. Haney, N.J. Cunningham, G.R. Odette, Acta Mater. 60 (2012) 3456.

[133] S.Y. Zhong, J. Ribis, V. Klosek, Y. de Carlan, N. Lochet, V. Ji, M.H. Mathon, J. Nucl. Mater. 428 (2012) 154.

[134] M. Klimiankou, R. Lindau, a Möslang, J. Nucl. Mater. 329-333 (2004) 347.

[135] M.L. Lescoat, I. Monnet, J. Ribis, P. Dubuisson, Y. De Carlan, J.M. Costantini, J. Malaplate, J. Nucl. Mater. 417 (2011) 266.

[136] A.D. Whapham, M.J. Makin, Philos. Mag. 5 (1960) 237.

[137] E. Gaganidze, C. Petersen, E. Materna-Morris, C. Dethloff, O.J. Weiß, J. Aktaa, a. Povstyanko, a. Fedoseev, O. Makarov, V. Prokhorov, J. Nucl. Mater. 417 (2011) 93.

[138] C. Topbasi, D. Kaoumi, A.T. Motta, M.A. Kirk, J. Nucl. Mater. 466 (2015) 179.

[139] A. Seeger, J. Diehl, S. Mader, H. Rebstock, Philos. Mag. 2 (1957) 323.

[140] I. Kubena, B. Fournier, T. Kruml, J. Nucl. Mater. 424 (2012) 101.

[141] G.R. Odette, G.E. Lucas, Radiat. Eff. Defects Solids 144 (1998) 189.

[142] J.W. Martin, Micromechanisms in Particle-Hardened Alloys, 1980.

[143] G.E. Lucas, J. Nucl. Mater. 206 (1993) 287.

[144] K.G. Field, X. Hu, K.C. Littrell, Y. Yamamoto, L.L. Snead, J. Nucl. Mater. 465 (2015) 746.

[145] F. Bergner, C. Pareige, M. Hernández-Mayoral, L. Malerba, C. Heintze, J. Nucl. Mater. 448 (2014) 96.

[146] S.I. Porollo, A.M. Dvoriashin, A.N. Vorobyev, Y. V Konobeev, J. Nucl. Mater. 256 (1998) 1.

[147] L. Tan, J.T. Busby, J. Nucl. Mater. 465 (2015) 724.

[148] S. Kotrechko, V. Dubinko, N. Stetsenko, D. Terentyev, X. He, M. Sorokin, J. Nucl. Mater. 464 (2015) 6.

[149] M.J. Alinger, On the Formation and Stability of Nanometer Scale Precipitates in Ferritic Alloys During Processing and High Temperature Service, 2004.

[150] J. Malaplate, F. Mompiou, J.-L. Béchade, T. Van Den Berghe, M. Ratti, J. Nucl. Mater. 417 (2011) 205.

[151] T. Tanno, S. Ohtsuka, Y. Yano, T. Kaito, Y. Oba, M. Ohnuma, S. Koyama, K. Tanaka, J. Nucl. Mater. 440 (2013) 568.

[152] Q. Lu, W. Xu, S. Van Der Zwaag, Comput. Mater. Sci. 84 (2014) 198.

[153] F.B. Pickering, Physical Metallurgy and the Design of Steels, Applied Science Publishers LTD, London, 1978.

[154] W.C. Leslie, Metall. Trans. 3 (1972) 5.

[155] R.W. Cahn, P. Haasen, Physical Metallurgy, Elsevier, Amsterdam, 1996.

[156] S. Ohtsuka, S. Ukai, M. Fujiwara, T. Kaito, T. Narita, Mater. Trans. 46 (2005) 487.

[157] T. Allen, F. Marshall, J. Ulrich, eds., ATR National Scientific User Facility 2012 Annual Report, 2012.

[158] J.P. Wharry, The Mechanism of Radiation-Induced Segregation In Ferritic-Martensitic Steels, University of Michigan, 2012.

[159] R.E. Stoller, M.B. Toloczko, G.S. Was, a. G. Certain, S. Dwaraknath, F. a. Garner, Nucl. Instruments Methods Phys. Res. Sect. B Beam Interact. with Mater. Atoms 310 (2013) 75.

[160] J.F. Ziegler, J.P. Biersack, SRIM - The Stopping and Range of Ions in Matter, 2008.

[161] C.M. Parish, K.G. Field, A.G. Certain, J.P. Wharry, J. Mater. Res. 30 (2015) 1275.

[162] K. Thompson, D. Lawrence, D.J. Larson, J.D. Olson, T.F. Kelly, B. Gorman, Ultramicroscopy 107 (2007) 131.

[163] B. Yao, D.J. Edwards, R.J. Kurtz, J. Nucl. Mater. 434 (2013) 402.

[164] C. Robertson, B.K. Panigrahi, S. Balaji, S. Kataria, Y. Serruys, M.-H. Mathon, C.S. Sundar, J. Nucl. Mater. 426 (2012) 240.

[165] M.H. Mathon, Y. De Carlan, G. Geoffroy, X. Averty, A. Alamo, C.H. De Novion, J. Nucl. Mater. 312 (2003) 236.

[166] V. de Castro, P. Rodrigo, E. a. Marquis, S. Lozano-Perez, J. Nucl. Mater. 444 (2014) 416.

[167] M.K. Miller, R. Forbes, Atom Probe Tomography: The Local Electrode Atom Probe, Springer, New York, 2014.

[168] S.V.N.T. Kuchibhatla, V. Shutthanandan, T.J. Prosa, P. Adusumilli, B. Arey, a Buxbaum, Y.C. Wang, T. Tessner, R. Ulfig, C.M. Wang, S. Thevuthasan, Nanotechnology 23 (2012) 215704.

[169] T.J. Prosa, D. Olson, B. Geiser, D.J. Larson, K. Henry, E. Steel, Ultramicroscopy 132 (2013) 179.

[170] D.J. Larson, T.J. Prosa, R.M. Ulfig, B.P. Geiser, T.F. Kelly, Local Electrode Atom Probe Tomography, Springer, New York, 2013.

[171] J.M. Hyde, E.A. Marquis, K.B. Wilford, T.J. Williams, Ultramicroscopy 111 (2011) 440.

[172] D. Vaumousse, A. Cerezo, P.J. Warren, Ultramicroscopy 95 (2003) 215.

[173] C.A. Williams, D. Haley, E.A. Marquis, G.D.W. Smith, M.P. Moody, Ultramicroscopy 132 (2013) 271.

[174] S. Yamashita, J. Nucl. Mater. 311 (2002) 283.

[175] R.P. Kolli, D.N. Seidman, Microsc. Microanal. 13 (2007) 272.

[176] C.A. Williams, E.A. Marquis, A. Cerezo, G.D.W. Smith, J. Nucl. Mater. 400 (2010) 37.

[177] C.A. Williams, G.D.W. Smith, E.A. Marquis, Ultramicroscopy 125 (2013) 10.

[178] M.J. Swenson, J.P. Wharry, J. Nucl. Mater. Submitted (n.d.).

[179] J.P. Wharry, G.S. Was, Acta Mater. 65 (2014) 42.

[180] A.D. Brailsford, R. Bullough, Philos. Trans. R. Soc. London 302 (1981) 87.

[181] F.A. Nichols, J. Nucl. Mater. 75 (1978) 32.

[182] H. Wiedersich, Radiat. Eff. 12 (1972) 111.

[183] C. Hofer, E. Stergar, S.A. Maloy, Y.Q. Wang, P. Hosemann, J. Nucl. Mater. 458 (2015) 361.

[184] X. Boulnat, M. Perez, D. Fabregue, S. Cazottes, Y. De Carlan, Acta Mater. 107 (2016) 390.

[185] W. Gale, T. Totemeier, Smithells Metals Reference Book, eighth ed., Elsevier, 2004.

[186] M.H. Mathon, Y. De Carlan, G. Geoffroy, X. Averty, A. Alamo, C.H. De Novion, J. Nucl. Mater. 312 (2003) 236.

[187] L.K. Mansur, J. Nucl. Mater. 206 (1993) 306.

[188] L.K. Mansur, J. Nucl. Mater. 78 (1978) 156.

[189] C. Flament, J. Ribis, J. Garnier, Y. Serruys, F. Leprêtre, A. Gentils, C. Baumier, M. Descoins, D. Mangelinck, A. Lopez, K. Colas, K. Buchanan, P. Donnadieu, A. Deschamps, Acta Mater. (2017).

[190] M.D. Rechtin, H.Wiedersich, Radiat. Eff. 31 (1977) 181.

[191] ASTM E521, Standard Practice for Neutron Radiation Damage Simulation by Charged-Particle Irradiation, ASTM International, West Conshohocken, PA, 2003.

[192] L. Barnard, N. Cunningham, G.R. Odette, I. Szlufarska, D. Morgan, Acta Mater. 91 (2015) 340.

[193] J.P. Wharry, G.S. Was, J. Nucl. Mater. 442 (2013) 7.

[194] J.P. Wharry, Z. Jiao, G.S. Was, J. Nucl. Mater. 425 (2012) 117.

[195] A. Aitkaliyeva, J.W. Madden, B.D. Miller, J.I. Cole, J. Gan, J. Nucl. Mater. 459 (2015) 241.

[196] A. Dunn, B. Muntifering, R. Dingreville, K. Hattar, L. Capolungo, J. Nucl. Mater. 480 (2016) 129.

[197] D. Xu, G. Vancoevering, B.D. Wirth, Comput. Mater. Sci. 114 (2016) 47.

[198] E. Getto, G. Vancoevering, G.S. Was, J. Nucl. Mater. 484 (2017) 193.

[199] E. Getto, Z. Jiao, A.M. Monterrosa, K. Sun, G.S. Was, J. Nucl. Mater. 462 (2015) 458.

[200] A. Cerezo, L. Davin, Surf. Interface Anal. Anal. 39 (2007) 184.

[201] E.A. Jägle, P.-P. Choi, D. Raabe, Microsc. Microanal. 20 (2014) 1662.

[202] P.D. Styman, J.M. Hyde, K. Wilford, G.D.W. Smith, Ultramicroscopy 132 (2013) 258.

[203] J.M. Hyde, a Cerezo, T.J. Williams, Ultramicroscopy 109 (2009) 502.

[204] Z. Jiao, G.S. Was, Acta Mater. 59 (2011) 4467.

[205] D.P. Datta, Y. Takeda, H. Amekura, M. Sasase, N. Kishimoto, Appl. Surf. Sci. 310 (2014) 164.

[206] T.R. Allen, J. Gan, J.I. Cole, S. Ukia, S. Shutthanandan, S. Thevuthasan, Nucl. Sci. Eng. 151 (2005) 305.

APPENDIX A:

Transmission Electron Microscopy Image Analysis

TEM Data Files

All measurements and calculations for sizes and number density of microstructural features are captured in Microsoft Excel files. The doi numbers for TEM image sets and links to the analysis file for each specimen are provided in Table A.1.

Table A.1 Summary of specimens analyzed with TEM, with links to data files.

Alloy	Irradiating Particle	Dose	Irradiation Temperature (°C)	doi number for TEM image sets	Link to Analysis File
Fe-9%Cr ODS	As-received	-	-	doi:10.18122/B20K5C	A/R
	Fe^{2+} ions	50	400	doi:10.18122/B2730T	Fe50-400
		1	500	doi:10.18122/B2R30G	Fe1-500
		3		doi:10.18122/B2GK5Q	Fe3-500
		100		doi:10.18122/B2ZK52	Fe100-500
	Protons	1		doi:10.18122/B2FK5D	P1-500
		3		doi:10.18122/B2630H	P3-500
		7		doi:10.18122/B2XK5R	P7-500
	Neutrons	3		doi:10.18122/B2Q305	N3-500
HCM12A	Fe^{2+} ions	3	500	doi:10.18122/B2P30V	Fe3-500
		100		doi:10.18122/B2DK53	Fe100-500
	Protons	1		doi:10.18122/B2WK5F	P1-500
		3		doi:10.18122/B2N30J	P3-500
	Neutrons	3		doi:10.18122/B25306	N3-500
HT9	Fe^{2+} ions	3	500	doi:10.18122/B2CP4F	Fe3-500
		100		doi:10.18122/B24590	Fe100-500
	Protons	1		doi:10.18122/B2M59B	P1-500
		3		doi:10.18122/B2BP44	P3-500
	Neutrons	3		doi:10.18122/B2VP4S	N3-500

APPENDIX B:

Atom Probe Tomography Analysis

APT Data Files

All outputs from cluster analysis in IVAS are exported into Microsoft Excel files for morphology and chemical analysis microstructural. The doi number for LEAP data sets and links to the analysis files for each specimen are provided in Table B.1.

Table B.1 Summary of specimens analyzed with APT, with links to data files.

Alloy	Irradiating Particle	Dose	Irradiation Temperature (°C)	doi number for LEAP data sets	Link to Analysis File
Fe-9%Cr ODS	As-received	-	-	doi:10.18122/B2488N	A/R
	Fe^{2+} ions	50	400	doi:10.18122/B2BS3S	Fe50-400
		1	500	doi:10.18122/B2VS3F	Fe1-500
		3		doi:10.18122/B2M880	Fe3-500
		100		doi:10.18122/B2388B	Fe100-500
	Protons	1		doi:10.18122/B2K88P	P1-500
		3		doi:10.18122/B29W24	P3-500
		7		doi:10.18122/B22C7P	P7-500
	Neutrons	3		doi:10.18122/B2TS34	N3-500
HCM12A	Fe^{2+} ions	3	500	doi:10.18122/B2SW2G	Fe3-500
		100		doi:10.18122/B2JC71	N.M.
	Protons	1		doi:10.18122/B21C7C	P1-500
		3		doi:10.18122/B2RW25	P3-500
	Neutrons	3		doi:10.18122/B28W2T	N3-500
HT9	Fe^{2+} ions	3	500	doi:10.18122/B2HC7Q	N.M.
		100		doi:10.18122/B27W2H	N.M.
	Protons	1		doi:10.18122/B2QW2V	N.M.
		3		doi:10.18122/B2GC7D	P3-500
	Neutrons	3		doi:10.18122/B20C72	N3-500

N.M. = None measured

For each APT sample, the average size and number density is calculated and tabulated. Using this information, the measured cluster sizes were tabulated and plotted, enabling the normalization process (Section 7.3.2) for comparison between multiple specimens. The files listed in Table B.2 provide a summary of the data which informed the normalization.

Table B.2 APT data summary and normalization of cluster size files.

Alloy	Link to File
Fe-9%Cr ODS	ODS-APT
HCM12A	HCM12A-APT
HT9	HT9-APT